FRACTIONALISATION IN SPIN-ORBIT COUPLED MAGNETIC INSULATORS

A Thesis

submitted to the

Tata Institute of Fundamental Research, Mumbai

for

the degree of Doctor of Philosophy in Physics

by

Arnab Seth

International Centre for Theoretical Sciences

Tata Institute of Fundamental Research

Bengaluru, 560097, India

July, 2022
(Final version submitted in October, 2022)

DECLARATION

This thesis is a presentation of my original research work. Wherever contributions of others are involved, every effort is made to indicate this clearly, with due reference to the literature, and acknowledgement of collaborative research and discussions.

The work was done under the guidance of Professor Subhro Bhattacharjee, at the International Centre for Theoretical Sciences, Tata Institute of Fundamental Research, Bangalore.

Arnab Seth

In my capacity as supervisor of the candidate's thesis, I certify that the above statements are true to the best of my knowledge.

Prof. Subhro Bhattacharjee

Date: October 26, 2022

Dedicated to my sister, mother and father

for years of support and keeping confidence in me

&

to Taniya

for endless patience and motivation

PUBLICATIONS

- **"Probing signatures of fractionalization in the candidate quantum spin liquid Cu_2IrO_3 via anomalous Raman scattering,"** Srishti Pal, Arnab Seth, Piyush Sakrikar, Anzar Ali, Subhro Bhattacharjee, D.V.S. Muthu, Yogesh Singh, A. K. Sood, *Phys. Rev. B*, 104, 184420, (2021)
  URL: https://doi.org/10.1103/PhysRevB.104.184420

- **"Probing emergent QED in quantum spin ice via Raman scattering of phonons: shallow inelastic scattering and pair production,"** Arnab Seth, Subhro Bhattacharjee, Roderich Moessner, *Phys. Rev. B*, 106, 054507, 2022
  URL: https://doi.org/10.1103/PhysRevB.106.054507

- **"Spin-3/2 ice,"** Arnab Seth, Subhro Bhattacharjee, Roderich Moessner, *Manuscript under preparation.*

- **"Strong coupling of lattice and orbital excitations in quantum magnet $Ca_{10}Cr_7O_{28}$: Anomalous temperature dependence of Raman phonons,** Srishti Pal, Arnab Seth, Anzar Ali, Yogesh Singh, D.V.S. Muthu, Subhro Bhattacharjee, A. K. Sood, *Manuscript under preparation.*

ACKNOWLEDGEMENTS

TABLE OF CONTENTS

Chapter 5: Anomalous Raman signatures of $Ca_{10}Cr_7O_{28}$

Chapter 6: Spin-$3/2$ Ice

Chapter 7: Conclusions

Appendix A: Signatures of fractionalization in candidate in Kramers Kitaev quantum spin liquids, Cu_2IrO_3 via anomalous Raman scattering of phonons

Appendix B: Probing emergent QED in non-Kramers quantum spin ice via Raman scattering of phonons

References

ABSTRACT

Long-range entanglement in quantum spin liquids (QSLs) leads to novel gauge structures and excitations with fractionalised quantum numbers. However, experimental signatures of such fractionalisation are rare and require more theoretical frameworks to interpret the experimental outcomes. Here we present a theoretical study of possible spectroscopic signatures of fractionalisation via the coupling of spins to Raman-active phonons in candidate QSLs. In the QSL phase, such magnetoelastic interaction leads to coupling between the lattice and the emergent excitations, resulting in renormalisation of the frequency and linewidth of phonons with characteristic frequency and temperature dependence. We particularly emphasise on the role of spin-orbit coupling present in various candidate materials, which on a generic ground gives rise to novel structures to such magnetoelastic interactions. For more concreteness, we calculate the phonon renormalisation in two kinds of QSLs, Kitaev QSL and non-Kramers quantum spin ice. In the Kitaev QSL, the phonon renormalisation captures the essential features of the underlying Majorana excitations arising from the spin fractionalisation. On the other hand, in the non-Kramers spin ice, phonon renormalisation gets contribution from emergent photons, magnetic monopoles and electric charges. Such characterisation is shown to be particularly useful since it allows to naturally separate out their signatures in experiments.

In the second part of the thesis, we address the question of how to obtain newer kinds of frustrated magnets by varying competing microscopic energy scales. Our analysis predicts the existence of a new kind of cooperative paramagnet, S=3/2 classical spin ice (CSI), hosted by the pyrochlore magnets with low-lying crystal field excitations. This model has a richer phase diagram and new kinds of excitations compared to the usual S=1/2 CSI. Interestingly, these models are more prone to fall out-of-equilibrium at low temperatures, even in the absence of long-range interaction or disorder.

CHAPTER 1

INTRODUCTION AND BACKGROUND

Realised on a lattice system of interacting spins–describing the physics of magnetic insulators– quantum spin liquids (QSLs) are prototypes of *long-range many-body entangled* phases of quantum matter [1–3]. The non-trivial long-range many-body entanglement and absence of the long-range ordering forbid description of such phases in terms of the conventional framework of spontaneous symmetry breaking via a local order parameter field [4] on one hand, and *symmetry protected topological phases* on the other [5, 6]. Perhaps the most striking difference is the topological bipartition entanglement of the ground state of a gapped QSL that prevents adiabatically deforming the QSL ground state to a trivial area law state [3, 7–10]. An important fall out of the long-range entanglement is the possibility of symmetry fractionalisation in low energy "elementary" quasiparticles and emergence of effective gauge theories [11–13]. In the QSL phase, the dynamic gauge fields being in the Coulomb or perimeter phase [10, 14–16], the quasiparticles, that carry the gauge charges, are "deconfined". These emergent excitations then constitute the correct low energy degrees of freedom instead of spins. Interestingly, such symmetry fractionalisation in the deconfined phase allows to access solid state realisations of various exotic excitations, such as magnetic monopoles [8,14], Majorana fermions [13], and so on, which are originally conceived earlier in the context of high energy physics. When the QSL undergoes a phase transition to a more conventional magnetic phase, such as thermal paramagnets, trivially polarised or magnetically ordered states, the gauge fields undergo a confinement [17, 18] or Higgs transition [19], leading to restoration of their description in terms of spins.

Over the last two decades, an extensive attempt is being made to explore more and more toy models which gives rise to a zoo of QSLs with various novel structures. Lattice realisation of QED [12] and Z_2 gauge theory [13] are possibly the most common among them. With the advancement of quantum chemistry, more tunability is achieved in designing the competing microscopic interactions, which, in turn, has immensely helped the theoretical community to conceptualise various newer models. Remarkably, such investigations give rise to a wide class of QSLs with more exotic features, such as recent realisations of Einstein's equation of gravity [20], higher rank gauge theories [21], non-abelian anyons [13], and so on.

1

In parallel to various theoretical developments, an extensive experimental program has been developed in search of explicit realisation for the QSL phases in the materials. The major challenges regarding the experiments are mostly two-fold: first to identify the suitable materials which qualify as promising QSL candidates, and then to design experiments that can probe the quasiparticles of a QSL.

Regarding the material realisation of the QSLs, it is now well-understood from the earlier studies of various spin Hamiltonians that the key ingredient is the interplay of various competing interactions [22–24] as well as the geometrical frustration arising from the underlying lattice structure [25–27]. In magnetic insulators, such competitions often suppress the conventional long-range order in favour of QSL ground state. For a generic magnetic material, the competing microscopic energy scales are mostly governed by the Coulomb interaction, spin-orbit coupling (SOC), and the crystal electric field environment of the magnetic ions. The interplay of these interactions often stabilises various effective degrees of freedom in the low energy description, which in turn favors the appearance of QSL phases. It is generically conjectured that the systems with low-spins are more probable to host QSL phases because of the enhanced quantum fluctuations. In various materials with $4d$, $5d$ or $4f$ electrons, due to the interesting hierarchy of the above-mentioned energy scales, often such effective spin-1/2 moment is realised, leading to realisation of Kitaev and U(1) QSLs in these candidates. The most notable examples are materials with rare-earth magnetic ions on a frustrated pyrochlore lattice, such as $Tb_2Ti_2O_7$ [28], $Pr_2Zr_2O_7$ [29], $Yb_2Ti_2O_7$ [30], etc, which are promising candidates for realisation of U(1) QSLs, whereas $4d$ and $5d$ magnetic materials, such as $\alpha-RuCl_3$ [31, 32], Na_2IrO_3 [33], β- and $\gamma-Li_2IrO_3$ [34], Cu_2IrO_3 [35], etc, which are candidates for the Kitaev QSL. However, we would like to note that among these microscopic energy scales, the role of SOC is particularly interesting, which is also one of the central pillars of this thesis work. SOC interlocks the spin and real spaces and therefore, these low-energy coupled degrees of freedom often have newer symmetry implementation favouring interactions that can stabilise a QSL. In many scenarios, the SOC gives rise to the anisotropic spin Hamiltonian [36] by breaking the complete spin rotation symmetry, which allows experimentalists to realise various QSLs like Kitaev materials [23, 37], which are completely based on the bond-dependent spin exchange interactions. In fact, as we will see in this work, the SOC coupled low-energy degrees of freedom plays the central role to obtain newer QSLs [38] and to design the newer probes for QSL phases [39].

Turning to the issue of experimental detection of signatures of QSL excitations, the major conceptual obstruction is the quasiparticles having fractional quantum numbers compared to the electronic excitations, often do not couple to the usual probes or couple in a very different way. Perhaps, the most common observation in this context is the broad continuum of excitations reported in the inelastic neutron scattering experiments [40] of the candidate materials, which is in contrast to the sharp signatures observed for conventional magnetically ordered states. It can be generically attributed to the fact that the experimental probes, such as neutrons, couple to multiple fractionalised quasiparticles of a QSL. Hence the momentum and energy transferred by the probe can be widely redistributed following the conservation laws. The neutron scattering further gives rise to potential implications of the underlying gauge structures in some of the QSL candidates, most notably in the pyrochlore spin ice systems, where the static spin structure factor measurements show a very special pinch-point-like patterns [41, 42] due to the inherent U(1) gauge structure. Apart from the neutron scattering, various thermodynamic and transport measurements also show promising signatures of the QSL phases. The most notable and illuminating observation among these is low-temperature scaling of the specific heat in a QSL with gapped matter fields, which typically arises due to the gapless emergent gauge excitations [19, 21, 43]. On the other hand, for QSLs with spinon Fermi surface, the specific heat shows linear temperature dependence [44, 45]–such metallic behaviour is clearly unexpected in case of a symmetry broken phase with magnon-like excitations, indeed suggesting frcationalisation. Recently, thermal conductivity [44] and thermal hall [46] measurements also show prominent signatures of QSL excitations. The anomalous quantum oscillations seen in the hall measurements of various candidate QSLs is possibly the most striking observation which is currently one of the central debates in the community [46].

More recently, several spectroscopic experiments beyond neutron scattering have shown much promise. Perhaps the most important among them is Raman scattering [31, 34, 47], which is also one of the central interests of this thesis work. Although the neutrons, due to their intrinsic magnetic moment easily couple to the magnetic excitations, it has various drawbacks. For example, the emergent partons having very different symmetry properties than the conventional spins, often cannot couple to the neutrons, sometimes the candidate materials strongly absorb neutrons [23], also the intensity of the neutron scattering due to the gauge bosons becomes significantly low [19] making them very difficult to observe. On the other hand, light couples to the magnetic or lattice degrees of freedom differently than neutrons, which makes it a

complementary approach to neutron scattering. Moreover, due to the high velocity of the probe photons, light scattering essentially occurs at zero momentum transfer [48], which makes the achievable energy resolution in Raman scattering significantly higher than many other probes. Another important advantage of such spectroscopic probes is that their coupling to other conventional electronic excitations of a magnetic material (such as phonons) can be indirectly used to extract the signatures of a QSL, because, in the QSL phase, the conventional excitations also get renormalised due to their scattering with the emergent quasiparticles [31]. However, in spite of such promising advantages, the theoretical principles of such spectroscopic experiments in the context of QSLs need further development in order to create a framework to successfully interpret the experimental results for candidate materials, which is one of the central aspects of this thesis.

We now start with a brief overview of the thesis before delving into the further details of the results.

1.1 Overview of the thesis

In this thesis work, we address some of these related issues which are indicated in the above discussion. The main goals of this thesis are two-fold:

- understanding and developing the theoretical principles of an experimental probe for the QSLs based on the magnetoelastic coupling present in the candidate materials, which can be useful for extracting the possible signatures of the fractionalisation via the Raman spectroscopy on phonons [39, 48]. The particular scope varies with the particular symmetry implementation of which we show three concrete examples.

- exploring the possibility of a new kind of classical spin ice (CSI), called $S = 3/2$ CSI on pyrochlore magnets [38], which at the classical level hosts a much richer phase diagram and excitations, in comparison to the usual CSI [49]. By adding quantum fluctuations, this is a potential candidate for a completely new type of QSL which has very different low-energy spectra and associated phase transitions than that of a more conventional U(1) QSL [12].

In the next chapter of the thesis, we begin by addressing the first issue and develop a theoretical framework of capturing QSL signatures via Raman scattering of phonons, which is

applicable to generic QSL candidates. Typically, in magnetic materials, there are two contributions in the Raman intensity profile coming from the magnetic degrees of freedom and lattice vibrations [31, 48]. These two seemingly independent contributions get correlated in presence of substantial magnetoelastic coupling. Therefore, the phonon excitations can convey information about the underlying QSL as well. We explicitly present the details of both kinds of contributions by giving the relevant vertices for external photon-magnetic degrees of freedom coupling and external photon-phonon coupling. The magnetic part, often dubbed as Loudon-Fleury contribution in literature [50, 51], are more direct probe of spin physics, which has been extensively studied earlier, both theoretically [52–56] and experimentally [31, 57], in the context of various candidate QSLs. On the contrary, the phonon contributions, although reported in some experiments [31, 57], are not very well-characterised in the theoretical studies. Therefore, we particularly focus on this kind of contribution and explicitly discuss the essential theoretical ideas of obtaining the signatures of a QSL via the phonon renormalisation measurements in Raman experiments. Further, we discuss a new kind of interaction vertex between external photons and quasiparticles of a QSL, which is mediated via phonons. We dub this contribution as *phonon mediated Loudon-Fleury* vertex. These are particularly interesting in the subset of QSL candidates, where the spin-phonon coupling is of substantially strong. The explicit experimental relevance of such interaction is discussed. In the following two chapters, we explicitly apply these theoretical frameworks in the context of two kinds of QSLs, Kitaev QSL and U(1) quantum spin ice.

In chapter 3, we discuss the phonon renormalisation in the first example of Kitaev QSL. This is a work done in collaboration with experiments, where the candidate material used is Cu_2IrO_3, a *second generation* Kitaev material. The magnetic moment in the material comes from the odd electron (Kramers) Ir^{4+} ion, which gives rise to S=1/2 moment in the low energy description due to the interesting interplay of CEF and SOC. The spin-phonon coupling in the material is explicitly derived, which is consisted of Kitaev-like bond-dependent spin bilinears and is governed by the spin-exchange coupling constant. In the QSL phase, the spins are further fractionalised into Majorana excitations giving rise to phonon-Majorana coupling. Due to the presence of such emergent scattering channels at low temperatures, the phonons get an anomalous renormalisation in their frequency and linewidth, which we explicitly compute using a diagrammatic perturbation theory. The frequency shift of the phonon is shown to be dependent on the energy density of the Majorana fermions, whereas the broadening of the

phonon linewidth follows the two-particle density of states of these emergent excitations in its frequency dependence. Our theoretical result matches quite well with the experimental observations by our collaborators in the Raman scattering experiment on this compound.

In chapter 4, we discuss the second example of Raman scattering on phonons in the U(1) quantum spin ice. For concreteness of the calculations, we consider a particular material example, $Pr_2Zr_2O_7$. The magnetic atom of the compound, Pr^{3+}, has $4f^2$ electronic configuration in its outer shell, which further gives rise to an effective doublet at the low energy due to the interplay of CEF and SOC. However, being an even electron system, this doublet has a very different transformation property than the usual spin-1/2 doublet. The Pauli matrices formed out of this doublet have two components which are even under time-reversal, whereas the remaining one is odd. This is the famous non-Kramers doublet of the pyrochlore spin ice [24, 58]. The most interesting fall out of such non-trivial symmetry transformation is that the spins can now linearly couple to the time-reversal even phonons. In fact, in these non-Kramers materials, such couplings are expected to be dominant contributions to the magnetoelastic coupling. Further, in the QSL phase, because of the fractionalisation of the spins, phonons–via the linear spin-phonon coupling–are shown to coherently scatter from the excitations of the emergent QED, i.e., gapped magnetic monopoles, electric charges, and photons. We explicitly calculate the phonon linewidth for each scattering channel using diagrammatic perturbation theory, and it is generically shown to depend on the two-particle density of states of the respective quasiparticles. Furthermore, phonon renormalisation is also calculated in the $\pi-$flux phase of a quantum spin ice, where π-electric flux pierces through all the elementary hexagonal plaquettes of the pyrochlore lattice. Remarkably, we show that such non-trivial details of the QSL can also be captured via phonon renormalisation measurements–more precisely, the anomalous linewidth of the phonon is shown to be sensitive to the projective implementation of the symmetry on the QSL quasiparticles. Further, such phonon renormalisation in QSL is explicitly contrasted with the renormalisation effects in the paramagnetic phase. It is shown that in the paramagnetic regime, the phonons scatter from the incoherent spins, resulting in renormalisation of its frequency but not in linewidth, at the leading order.

As a continuation of the investigation of the Raman signatures of QSLs, in chapter 5 we study phonon renormalisation in $Ca_{10}Cr_7O_{28}$, which is a quasi-two-dimensional Heisenberg quantum magnet on bi-layer kagome lattice, and shows QSL phase below the Curie-Weiss (CW) scale of $\Theta_{CW} \approx 4$ K due to the spin-$\frac{1}{2}$ Cr^{5+} ions [59]. Recently, Raman scattering has

been performed in this material down to $\sim$4 K [60]. However, surprisingly it reveals signatures of strong anomalies in the temperature dependence of both phonon frequencies and linewidths, at the crossover temperature of $T_C \sim$100 K, much above the CW scale. Clearly, unlike the scenarios described so far, such effects then cannot arise from the non-trivial spin-phonon coupling, since the spins, for all the experimentally relevant temperatures, are deep inside the thermal paramagnet. The central question we then try to address is how to accommodate this new temperature scale and associated Raman anomalies into the framework of magnetoelastic coupling developed so far. To answer this, we first note that the system contains the Jahn-Teller (JT) active [61] Cr^{5+} ion sites offering moderately distorted $Cr^V O_4$ tetrahedra even at room temperature as reported in the earlier studies [62]. We then theoretically predict a rearrangement of the orbital degrees of freedom of Cr^{5+} ions below the temperature scale of primary JT distortion driven by the orbital fluctuations. We claim that the phonons are sensitive to such orbital reordering via the cooperative JT mechanism, which in turn renormalises the phonon parameters.

In the chapter 6, we turn to the second problem of the thesis, where a new kind of pyrochlore magnet is studied, which might be particularly interesting to realise a new kind of QSL. A particular setting of pyrochlore magnets is analyzed where the CW scale is comparable to the onsite crystal field gap. Hence, the spin-orbit coupled excited crystal field states also participate in the magnetism. We show that the presence of such additional degrees of freedom leads to a richer phase diagram and stabilizes a very different CSI, dubbed here as $S = 3/2$ CSI, which does not conform the conventional $S = 1/2$ CSI. A new parameter regime is unraveled where the lowest excitaions are gauge-neutral objects, unlike the usual magnetic monopoles. They are shown to be very robust under thermal fluctuations, leading to an interesting possibility of the CSI to fall out of equilibrium at low temperatures, even if the interaction is short ranged. Further, the effective entropic interaction between these ultra-localised excitations is calculated. Interestingly, they are shown to be interacting via dipolar interaction, leading to the realisation that they behave as magnetic dipoles at low-temperature regimes. The introduction of the quantum fluctuations into this CSI leads to the dynamics of these excitations, which might ultimately lead to their condensation, making the QSL to undergo a phase transition into more conventional ordered phases. The excitations being gauge neutral, such phase transition is very different from the Higgs or confinement transition of a QSL.

In chapter 7, we finally summarise all the results and conclude. The details of various

calculations are further given in the Appendix.

CHAPTER 2

A BRIEF OVERVIEW OF THE RAMAN SCATTERING OF MAGNETIC INSULATORS

In this chapter, we begin by addressing the first problem of the thesis, i.e., extracting signatures of QSL excitations via Raman scattering of phonons, by deriving the relevant theoretical frameworks which is applicable to a generic QSL phase. We first give a brief review of the conventional Raman scattering mechanism in a magnetic insulator, which is governed by the scattering of external photons in the magnetic channels. This has been studied earlier in the context of various QSLs, both theoretically [34, 47, 52, 53, 57, 63, 64] and experimentally [31, 57]. We then focus on the Raman scattering of the phonons and indicate its usefulness to explore the signatures of QSL quasiparticles.

Historically, Raman scattering was first conceptualized in theory by Smekal in 1923 [65] and soon discovered in experiments by C.V. Raman in the context of organic liquids in 1927 [66, 67]. Gradually, with improved resolutions and laser sources, it was extended to the crystalline and amorphous solids (mostly insulators) [50, 68], and later to high T_c superconductors [69–71], where it revealed a plethora of information about their excitations and also phonons. Particularly, the non-destructive nature of the Raman spectroscopy, easy sample preparation, availability of laser sources of high resolution, and very different coupling mechanism between light and electronic excitations, draw the attention of the wide experimental community to use Raman scattering as a complementary spectroscopic probe to neutrons. More recently, Raman scattering is being given special importance in the context of studying various exotic magnetic insulators including QSLs [31, 34, 47, 52, 53, 57, 63, 64]. Typically, in a magnetic insulator, there are two contributions in the Raman intensity profile, coming from the magnetic degrees of freedom and lattice vibrations [31, 48, 57]. Their spectroscopic signatures are well-separated and easy to extract. However, these two seemingly independent contributions get correlated in presence of substantial magnetoelastic coupling. Therefore, even by studying the phonon excitations, we can obtain information about the underlying magnetic physics, in turn about the QSL. In the following sections, we first briefly discuss the magnetic contribution in the Raman spectra, and then turn to the vibrational part in greater detail.

2.1 The magnetic contribution: Loudon-Fleury vertex

The magnetic part of the Raman spectra, often dubbed as *Loudon-Fleury* contribution in literature [50–56, 64], is a more direct probe of the spin physics than the vibrational component. Such contribution generically appears due to the virtual charge fluctuations of a magnetic insulator and the associated electric polarization in the presence of the external probe electric field [50, 51]. The interaction between the Raman photons and the magnetic degrees of freedom is given by the *Loudon-Fleury vertex* (R_{LF}) which is expressed in terms of the Raman tensor, $R_{\mu\nu}$ – an analogue of the *polarisability tensor* of the materials [52–56]. This is defined as,

$$R_{LF} = \sum_{\mu\nu} \epsilon_{\text{in}}^{\mu} R_{\mu\nu} \epsilon_{\text{out}}^{\nu} \quad \text{where,} \quad R_{\mu\nu} = \sum_{\alpha} d_{\alpha}^{\mu} \mathcal{H}_{\alpha} d_{\alpha}^{\nu} \tag{2.1}$$

Here ϵ_{in} and ϵ_{out} are the polarization of the incident and emitted photons, $\mathbf{d}_{\alpha}$ is the bond vector of the underlying lattice, and $\mathcal{H}_{\alpha}$ is the spin exchange interaction along that bond whose generic form is given by, $\mathcal{H}_{\alpha} = J_{\mathbf{r},\alpha}^{\beta,\gamma} S_{\mathbf{r}}^{\beta} S_{\mathbf{r}+\mathbf{d}_{\alpha}}^{\gamma} + \cdots$, with $\cdots$ denoting all the symmetry allowed terms. The Raman intensity can then be computed from the above using the Fermi's Golden rule [67],

$$I_{LF}(\omega) = \sum_{i,f} \frac{e^{-\beta E_i}}{Z} |\langle f | R_{LF} | i \rangle|^2 \, \delta(\omega - E_f + E_i) \tag{2.2}$$

where $|i\rangle$ and $|f\rangle$ are the initial and final states of the spins with energies E_i and E_f, respectively, and Z is the thermal partition at temperature, $T = 1/k_B \beta$. The structure of the Raman tensor, $R_{\mu\nu}$, is constrained by symmetries, which results in specific polarisation dependence. In fact, it can be shown that only some particular polarisation channels are useful to extract the underlying magnetic information.

In the case of magnetically ordered phases, the spins are better described in terms of the low-energy Goldstone modes of the symmetry broken phase– called *magnons* [72]. Therefore, Eq. 2.1 when rewritten in terms of the magnons, results in the coupling of Raman photons to the two-magnon operators [50, 68]. Therefore, the energy and momentum transferred into/by the system can be redistributed among multiple excitations, giving rise to a continuum of Raman response with characteristic temperature and frequency (Raman shift) dependence of magnons [50, 68].

On the other hand, for a QSL, in the absence of the Goldstone modes, redistribution of

the absorbed energy occurs among the emergent quasiparticles leading to the continuum of response. Hence, the Raman intensity can potentially carry information about spin fractionalisation. Depending upon the underlying emergent excitations and gauge structure, the profile of the scattering continuum can widely change, leading to useful implications about the density of states and statistics of the quasiparticles. This has been extensively studied earlier, both theoretically [52–56, 64] and experimentally [31, 57], in the context of various candidate QSLs.

However, we note that the energy scale of the Loudon-Fleury vertex is governed by the charge fluctuation in the magnetic Mott insulating phase [50, 51], and therefore, it is generically proportional to the spin exchange coupling constant, $J_{\mathbf{r},\alpha}^{\beta,\gamma}$, as can be seen directly from Eq. 2.1. In some materials, such contributions might be significantly suppressed if the electrons are very localised. This is generically expected to happen in magnetic atoms with *4f*-electrons [39]. In such a scenario, the phonon contribution on the other hand might be very useful to analyze. Such signatures have been recently reported in some QSL candidates, such as α-$RuCl_3$ [31], $Ba_4Ir_3O_{10}$ [57] along with the scattering continuum, but their complete characterisation is still lacking in the context of QSLs.

2.2 The vibrational contribution

Having discussed the Loudon-Fleury contribution to the Raman intensity we now turn to the vibrational component of the Raman scattering. For a phonon mode to be Raman active, it is necessary that it should have even parity and the phonon contribution to the rank-2 polarizability tensor (Λ) should oscillate as a function of time [68]. For small amplitude of vibration, we can expand Λ as powers of normal modes.

$$\Lambda = \Lambda_0 + \boldsymbol{\zeta}^{(\bar{p})} \cdot \left[\boldsymbol{\nabla}_{\boldsymbol{\zeta}^{(\bar{p})}} \Lambda \right]_{\boldsymbol{\zeta}^{(\bar{p})}=0} + \cdots \tag{2.3}$$

where $\boldsymbol{\zeta}^{(\bar{p})}$ is the phonon modes belonging to $\bar{p}$ irreducible representation of the lattice symmetry group. We have truncated the Taylor expansion at linear order, assuming the processes involving multiple phonons are suppressed at low temperatures and generically denoted by $\cdots$. Λ_0 is the time-independent part, hence does not contribute to the Raman scattering. The
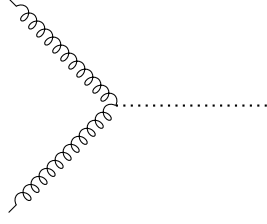
Figure 2.1: **Raman vertex for phonon-Raman photon scattering:** The curly and dotted lines represent probe photons and Raman active phonons, respectively.

coupling between the Raman photons and phonons is then given by,

$$
\begin{aligned}
H_{Raman} &= \int \mathbf{P}(\mathbf{r}) \cdot \mathbf{E}_{ext}(\mathbf{r})\, d^3\mathbf{r} \\
&= \int d\mathbf{k}\, d\mathbf{k}'\, \omega_{\mathbf{k}}^{in}\, \omega_{-\mathbf{k}'}^{out} \left[\nabla_{\zeta^{(\bar{p})}} \Lambda\right]_{\zeta^{(\bar{p})}=0}^{ij} \cdot \zeta^{(\bar{p})}(\mathbf{k} - \mathbf{k}')\mathcal{A}_i^{in}(\mathbf{k})\mathcal{A}_j^{out}(\mathbf{k}') \qquad (2.4)
\end{aligned}
$$

where $\mathbf{P}(\mathbf{r}) = \Lambda \mathbf{E}_{ext}(\mathbf{r})$ is the polarisation of the crystal in presence of external electric field $\mathbf{E}_{ext}(\mathbf{r})$, $\mathcal{A}(\mathbf{r})$ is the vector potential corresponding to $\mathbf{E}_{ext}(\mathbf{r})$. The above Hamiltonian is manifestly gauge invariant, since it can be completely expressed in terms of the electric fields. The Feynman diagram for the above Raman vertex is shown in Fig. 2.1. $\nabla_{\zeta^{(\bar{p})}} \Lambda$ forms a set of symmetric matrices which have the same symmetry properties as $\zeta^{(\bar{p})}$. In other words, this set forms an irreducible representation $(\bar{p})$ of the symmetry group. We dub these matrices as *Raman matrices*. The detailed structure of the matrices can be obtained from the lattice symmetry analysis. In Chapter 4, we will discuss one particular lattice structure and explicitly give the form of the Raman matrices associated with it. The above vertex needs to be contrasted with the previously described Loudon-Fleury vertex where the external photons couple to multiple magnetic excitations of the system. On the contrary, the Raman photons can couple to a single phonon excitation, leading to the appearance of sharp peaks in the scattering spectra.

The differential Raman scattering cross-section for the phonon-photon scattering, which measures the Raman count in the differential solid angle $d\Theta_s$ and frequency window between ω^{out} and $\omega^{out} + d\omega^{out}$, is given by,

$$
\frac{d^2\sigma(\mathbf{q}, \Omega)}{d\Theta_s d\omega^{out}} \propto R(\mathbf{q}, \Omega), \qquad (2.5)
$$

where for a system at thermal equilibrium, by Fermi's Golden rule [67, 68],

$$R(\mathbf{q}, \Omega) = \sum_{i,f} \frac{e^{-\beta E_i}}{Z} \mid \langle f \mid H_{Raman} \mid i \rangle \mid^2 \delta(\Omega - E_f + E_i) \qquad (2.6)$$

This is a similar kind of expression as Eq. 2.2, with only the difference being $\mid i \rangle$ and $\mid f \rangle$ now represent the initial and final state of the phonons, instead of the magnetic states in the earlier case. Here $\mathbf{q} = \mathbf{q_{in}} - \mathbf{q_{out}}$ and $\Omega = \omega^{in} - \omega^{out}$ are respectively the net momentum and energy transferred to the system by the Raman photons. As the speed of light is very large compared to that of the phonons, only the $\mathbf{q} \to 0$ regime of the Brillouin zone can be probed by Raman scattering. Further, E_i and E_f are the energies of the initial and the final phonon states, respectively.

At low temperatures, the initial state can be approximated by the ground state with zero phonons. Also, we can see from the Raman vertex (Eq. 2.4) that the scattering matrix element is non-zero only when $\mid i \rangle$ and $\mid f \rangle$ differ by a single phonon, as multi-phonon processes are suppressed at low temperatures due to the Bose occupation factor. So at this temperature regime, $\mid f \rangle$ should be chosen from the single phonon sector ($\mid f \rangle \approx \mid \mathbf{q} \rangle$) leading to

$$R(\mathbf{q}, \Omega) \propto -\frac{\pi n(\Omega) e^{\beta \Omega}}{Z} e^{-\beta E_0} \lim_{\delta \to 0^+} \mathcal{I}m[D_0(\mathbf{q}, \Omega + i\delta)] \qquad (2.7)$$

where, $n(\Omega) = \frac{1}{e^{\beta\Omega} - 1}$ is the Bose-factor and $D_0(\mathbf{q}, \Omega + i\delta) = -\frac{2\Omega_\mathbf{q}}{(\Omega + i\delta)^2 + \Omega_\mathbf{q}^2}$ is the bare retarded Green's function of the phonon, with $\Omega_\mathbf{q}$ being its bare dispersion. However, in presence of interaction, the single-particle states of the phonons become dressed and the effect can be taken into account by considering the dressed propagators (which has an additional self-energy term with all the effects of interaction encoded into it) instead of the bare Green's function. The dressed Green's function can be calculated from the analytic continuation of the Matsubara Green's function, $D(\mathbf{q}, i\Omega)$, given by

$$D(\mathbf{q}, i\Omega) = -\int_0^\beta d\tau \langle \hat{\mathcal{T}}(\zeta(\mathbf{q}, \tau)\zeta(-\mathbf{q}, 0)) \rangle e^{i\Omega\tau} = -\frac{2\Omega_\mathbf{q}}{\Omega^2 + \Omega_\mathbf{q}^2 + 2\Omega_\mathbf{q}\Sigma(\mathbf{q}, i\Omega)} \qquad (2.8)$$

where $\Sigma(\mathbf{q}, i\Omega)$ is the self-energy of the phonon arising from the interactions. The imaginary part of the dressed Green's function, which is relevant to the Raman scattering cross section

(see Eq. 2.7 with non-interacting Green's function replaced by the interacting one), is given by,

$$\frac{4\Omega_{\mathbf{q}}^2 \mathcal{I}m[\Sigma]}{(\Omega^2 - \Omega_{\mathbf{q}}^2 - 2\Omega_{\mathbf{q}}\mathcal{R}e[\Sigma])^2 + 4\Omega_{\mathbf{q}}^2 \mathcal{I}m[\Sigma]^2} \tag{2.9}$$

The above expression if plotted against phonon frequency, Ω, takes a Lorentzian lineshape, which is the crucial feature of an interacting phonon system (instead of the sharp Dirac delta profile for a non-interacting system). The position of the peak of this curve is shifted from the non-interacting one by

$$\delta\Omega = \mathcal{R}e\left[\Sigma(\mathbf{q}, \Omega + i\delta)\right] \tag{2.10}$$

and the full-width at half maximum of the Lorentzian is given by

$$\Gamma = 2 \mid \mathcal{I}m\left[\Sigma(\mathbf{q}, \Omega + i\delta)\right] \mid \tag{2.11}$$

In the Raman experiments, the frequency shift and the linewidth of the phonon Lorentzian can be measured with a very good resolution. Clearly, such outcomes are then indicative of the underlying scattering channels for the phonon.

In the materials, there are two contributions to the phonon self-energy that are relevant to our case, the anharmonic contribution of the phonons, and the magnetoelastic coupling. The anharmonic contribution is generically present in all the materials due to phonon-phonon scattering, and its effect is more enhanced at higher temperatures [48, 60]. On the other hand, in materials with moderate magnetoelastic coupling, the phonons substantially scatter from the spins. Hence analyzing the renormalisation of the phonon parameters in the magnetic channels, we can extract useful information about the underlying spin physics. In the QSLs, the spins being further fractionalised into emergent excitations, new scattering channels for phonons open up where phonons can coherently decay into those quasiparticles, gaining anomalous renormalisation. In fact, as we are going to discuss in the following sections, the temperature and frequency dependence of these renormalised phonon parameters are extremely useful to extract the density of states and the statistics of the novel quasiparticles of a QSL. We further note that the QSL phase, being stabilised only at low temperatures, such anomalous renormalisation is observed only below the CW scale, which makes it easier to separate out from the anharmonic contribution.
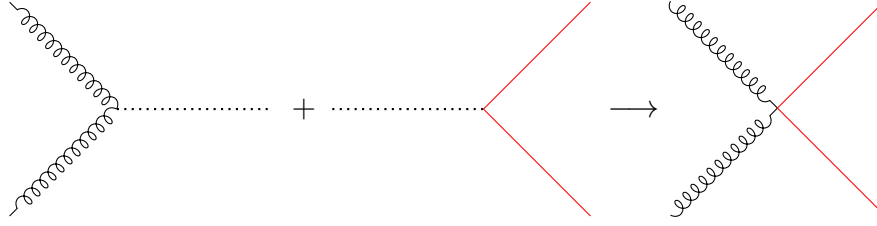
Figure 2.2: **Phonon mediated Loudon-Fleury vertex in magnetically ordered phases:** The red solid lines represent the magnons of a symmetry broken magnetically ordered state. The first and second figure show the coupling of phonons to the Raman photons and magnons, respectively. Integrating out the phonons, the *phonon mediated (Raman) photon-magnon Loudon-Fleury vertex* is obtained which is shown in the rightmost diagram.

A further implication of the underlying spin fractionalisation on the phonon spectra is that the phonon Lorentzian becomes asymmetric in the QSL phase. This is a consequence of the celebrated Fano effect [73, 74] which has been historically discovered in the context of high energy physics. The Raman photons, on one hand, scatter from phonons leading to discrete peaks in the spectroscopic signals, whereas on the other hand, they give rise to a continuum background due to the scattering with multiple magnetic quasiparticles. The interference effect of these two gives rise to such asymmetry, which has been reported earlier in the experiments [31]. However, in our theoretical calculation, we do not focus on such effects and stick to the anomalous phonon renormalisation due to the scattering of phonons from the QSL quasiparticles.

2.3   Phonon mediated Loudon-Fleury vertex

In this section, we introduce the possibility of a rather new kind of Raman vertex, between the Raman photons and the magnetic degrees of freedom, mediated by the phonons in presence of moderate magnetoelastic coupling, which is dubbed as *phonon mediated Loudon-Fleury vertex*. Such interaction is of particular interest when the strength of the usual Loudon-Fleury vertex (mediated by virtual charge fluctuations) is significantly weak. Even in such a scenario, the continuum of Raman response might appear due to these phonon-mediated processes, coupling the probe photon with the magnetic excitations.

Phonon mediated Loudon-Fleury vertex can generically be derived by integrating out the phonons from the magnetoelastic coupling (see Chapters 3 and 4) and the phonon-Raman photon vertex (see Eq. 2.4). This procedure is schematically shown in Fig. 2.2 for the magnetically ordered phases, where the spins are described by the magnon modes. The leading spin-phonon

coupling is taken to be one-phonon-two-magnon vertex [50, 68], which has been mentioned earlier in Sec. 2.1. On the physical ground, such a process can be thought of as follows– the incident Raman photon excites a virtual phonon of the lattice which in turn decays into a magnon pair due to magnetoelastic coupling, leading to effective interaction between Raman photons and magnons (two-magnon operators), very similar to the usual Loudon-Fleury. In the QSLs, instead of the magnons, the phonons scatter into the emergent fractionalised excitations due to the spin-phonon coupling, which effectively opens up the possibility of phonon-mediated coupling between Raman photons and emergent excitations. This in turn results into a scattering continuum very similar to that due to the usual Loudon-Fleury contribution, hence carrying characteristic signatures of the emergent excitations. The explicit examples of such phonon-mediated vertices will be discussed in the context of Kitaev QSL and non-Kramers U(1) quantum spin ice in the next two chapters.

From the Feynman diagram of Fig. 2.2, it can be argued that the coupling strength of the phonon mediated Loudon-Fleury vertex is directly proportional to individual strength of the photon-phonon vertex (left panel), $\left[\nabla_{\zeta^{(\bar{P})}}\Lambda\right]_{\zeta^{(\bar{P})}=0}$, and magnetoelastic coupling (middle panel), J_{sp}, as well as inversely proportional to the frequency of the intermediate virtual phonon, Ω_0. Therefore, such coupling strength can be reasonably approximated as $\propto \frac{J_{sp}\left[\nabla_{\zeta^{(\bar{P})}}\Lambda\right]_{\zeta^{(\bar{P})}=0}}{\Omega_0}$. Interestingly, we will see in the next chapter, J_{sp} is generically proportional to the spin-exchange coupling constant in the case of odd electron Kramers systems, clearly indicating that the phonon-mediated Loudon-Fleury is more suppressed by the phonon frequency than the usual Loudon-Fleury. Therefore, it might not be very useful for the experimental realisation. On the contrary, for even electron non-Kramers system, as will be discussed in chapter 4, due to the non-trivial implementation of the time-reversal symmetry on the low energy magnetic degrees of freedom, the magnetoelastic coupling has an unconventional structure and it is governed by a very different coupling coefficient than the spin-exchange constant. Therefore, the phonon-mediated contributions have a very different energy scale in this case than that of the Kramers one, leading to the possibility of the appearance of a broad scattering continuum even if the usual Loudon-Fleury vertex is significantly weak.

2.4 The focus of our work

In this thesis work, we particularly focus on the phonon contributions to the Raman intensity and prescribe a theoretical framework that can concretely extract the signatures of fractionali-

sation in a QSL from the anomalous phonon spectra. We apply the set of ideas discussed in Sec. 2.2 and 2.3 in the context of two different QSLs– Kramers Kitaev QSL [48] and non-Kramers U(1) quantum spin ice [39], which have direct experimental realisations, and identify various possible signatures of the spin fractionalisation that might be relevant to the experiments.

For Kramers Kitaev QSL, the spins get fractionalised into the Majorana fermions, leading to phonon-Majoana scattering in presence of substantial magnetoelastic coupling. For such interaction channels, we compute the renormalisation of the phonon frequency and linewidth by calculating the real and imaginary part of the phonon self-energy (see Sec. 2.2 above) perturbatively. These are further characterised via their temperature and frequency dependence, which carry direct evidence of the underlying Majorana fermions. Our theoretical results match quite well with the experimental findings of the Raman scattering measurement on candidate Kitaev material, Cu_2IrO_3, performed by our collaborators [48, 75].

For non-Kramers spin ice, the spins are fractionalised into quasiparticles of an emergent QED–gapped magnetic monopoles and electric charges, and gapless photons. Scattering channels of phonons from all these excitations are analyzed to obtain the phonon renormalisation in the QSL phase. For all three cases, the frequency dependence of the linewidth is shown to follow the two-particle density of states of respective excitations. Another interesting scenario is considered, when the QSL is in $\pi-$flux phase, i.e., the elementary hexagons of the pyrochlore lattice contain non-trivial electric fluxes. The presence of such fluxes modifies the dynamics of the underlying magnetic monopoles resulting into their momentum fractionalisation. We show that such non-trivial details of the QSL phase are also captured in the phonon renormalisation measurements. However, the experimental results of the Raman scattering in this class of candidate QSLs are still not available. Therefore, here we provide all the required details necessary for the Raman experiments on such materials and discuss their probable implications in the phonon measurements.

On a similar line of interest, we have analyzed the Raman signature of another magnetic insulator $Ca_{10}Cr_7O_{28}$ [60], which is also a QSL candidate [59]. However, to our surprise, it shows Raman anomaly at much higher temperatures than the CW scale, hence cannot be described by the QSL physics. We theoretically predict the presence of an orbital reordering in this material and show that the onset temperature scale of the Raman anomaly can be associated with this crossover temperature. We note that such anomaly is very different than that has been described in the context of QSLs so far.

In the following three chapters, we are going to describe all the details of our theoretical investigation for these three cases one by one.

CHAPTER 3

SIGNATURES OF FRACTIONALIZATION IN CANDIDATE KRAMERS KITAEV QUANTUM SPIN LIQUIDS, Cu$_2$IrO$_3$ VIA ANOMALOUS RAMAN SCATTERING OF PHONONS

3.1 Introduction

In this chapter, we describe the first example of Kitaev QSL, where the previously described theoretical framework of detecting spin fractionalisation via anomalous phonon renormalisation is explicitly applied. Kitaev QSL is particularly interesting because it is one of the few examples of exactly solvable interacting spin models with QSL ground state, and provides a unique opportunity to realise Majorana excitations along with an emergent Z_2 lattice gauge theory [13]. Raman scattering in various candidate Kitaev materials has already shown promising signatures of spin fractionalisation via observation of characteristic magnetic continuum and various phonon anomalies [31, 57]. However, although the magnetic continuum has been studied extensively in the theory [52, 54, 55, 57], the phonon anomalies are barely understood and have not been characterised enough earlier.

In this experiment-theory collaboration, we particularly analyse the phonon anomalies observed in the candidate Kitaev material Cu$_2$IrO$_3$ [48]. This compound belongs to the recently discovered family of *second generation Kitaev materials* [35] which are expected to be more proximate to the QSL phase than the more conventional *first generation* candidates, such as α-RuCl$_3$ [32], Na$_2$IrO$_3$ [33], etc. The major conceptual obstruction about the first generation materials is that they ultimately order magnetically at much lower temperatures possibly due to additional non-Kitaev interactions in the system, therefore, the realisation of the pristine Kitaev physics remains debatable. On the other hand, for the second-generation materials, the magnetic order is absent all the way to the lowest available temperatures [76–78] due to the fact that the motif formed by the magnetic atoms (for example, Ir^{4+} in Cu$_2$IrO$_3$) is much closer to the ideal honeycomb structure [35], and also possibly due to the smallness of non-Kitaev interactions. Therefore, such candidates have been the central attraction for the experimental community to realise QSL physics. To our knowledge, all of the previously reported Raman scattering experiments have always been performed in the first generation Kitaev materials [31,

57], and thus our work is particularly an important addition in this regard.

The magnetic atom Ir^{4+} in Cu_2IrO_3 has $5d^5$ electronic configuration in the outer shell. In these transition metals, spin-orbit coupling is significantly strong, and due to the interplay of crystal field and SOC, an effective $S = 1/2$ electron shows up in the low energy description. Such SOC coupled low energy theory naturally leads to enhanced spin-lattice coupling as described in the earlier chapters, hence opens up the possibility of detection of spin fractionalisation via studying phonon renormalisation in Raman spectroscopy. Before delving into further details of our results, we first give a brief summary of the $S = 1/2$ Kitaev QSL [13] for the completeness of the discussion.

3.2 Description of Kitaev QSL in terms of Majoranas
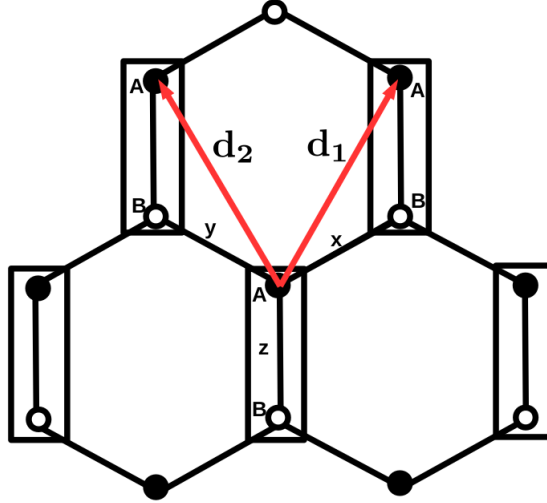
Figure 3.1: **Honeycomb lattice and lattice vectors:** The two-point unit cell has been considered along the z bonds. $\mathbf{d}_1$ and $\mathbf{d}_2$ denotes the two lattice vectors of the Honeycomb lattice.

The Kitaev QSL [13] is governed by the bond-dependent spin exchange Hamiltonian on the honeycomb lattice,

$$H_K = \sum_{i,\alpha} J_{i,\alpha} S_i^\alpha S_{i+\hat{\alpha}}^\alpha \tag{3.1}$$

where α denotes x, y or z type of bonds and $\hat{\alpha}$ denotes the three nearest neighbour vectors of honeycomb lattice (see Fig. 3.1). This model can be exactly solved following Kitaev's prescription [13] of rewriting spins in terms of the Majorana fermions, $S_i^\alpha = \frac{i}{2} b_i^\alpha c_i$, with

b_i^x, b_i^y, b_i^z and c_i being Majoranas. Therefore, we have,

$$S_i^\alpha S_{i+\hat{\alpha}}^\alpha = -\frac{1}{4}u_{i,i+\hat{\alpha}}^\alpha(ic_ic_{i+\hat{\alpha}}) \tag{3.2}$$

Here, $u_{i,i+\hat{\alpha}}^\alpha = ib_i^\alpha b_{i+\alpha}^\alpha$ is the Z_2 gauge field. The physical gauge invariant flux excitations of the gauge fields can be obtained by considering the Wilson loops and taking the product of the gauge connection around the loop. Since the lowest possible loop on the honeycomb lattice is a hexagon, the elementary gauge flux is defined as,

$$W_p = \prod_{i\alpha \in \bigcirc} u_{i,i+\hat{\alpha}}^\alpha \tag{3.3}$$

It is easy to show that these fluxes are conserved quantities of the Hamiltonian dynamics, therefore, the Kitaev model can be solved via restricting to a particular flux configuration [13, 79]. It can then be shown that the Kitaev QSL is consisted of two kinds of excitations– localised Z_2 fluxes (W_p) and itinerant Majorana fermions (c_i) which carries Z_2 gauge charge. Here we consider the isotropic limit of the Kitaev model, where $J_{i,\alpha} = J_K$. At this point, the zero flux sector of the model becomes the lowest energy sector due to Lieb's theorem [80]. Creating the flux excitations above this low-energy manifold requires a finite amount of energy leading to the mass gap of the flux being, $\Delta_{W_p} \approx 0.012J_K$. Due to the mass gap, the flux excitations become relevant only above a characteristic temperature scale of $T_l \sim 0.012J_K$. Below this, it is fairly reasonable to assume the background flux to be zero. The itinerant Majoranas then become non-interacting which is evident if we choose a trivial gauge fixing, $u_{i,i+\hat{\alpha}}^\alpha = 1$, and the free Majorana Hamiltonian can be analytically diagonalised by– first transforming the Majoranas to *complex bond-matter fermions* [13, 81]

$$c_i = \begin{cases} f_i + f_i^\dagger & \forall \; i \in A \\ i(f_i - f_i^\dagger) & \forall \; i \in B \end{cases} \tag{3.4}$$

and then applying a Bogolioubov transformations [13, 81] on the momentum space version of these complex fermionic operators, $f_\mathbf{k}(= \frac{1}{\sqrt{N_b}}\sum_\mathbf{k} e^{i\mathbf{k}\cdot\mathbf{r}_i} f_i)$,

$$\begin{bmatrix} f_\mathbf{k} \\ f_{-\mathbf{k}}^\dagger \end{bmatrix} = \begin{bmatrix} \cos\theta_\mathbf{k} & i\sin\theta_\mathbf{k} \\ i\sin\theta_\mathbf{k} & \cos\theta_\mathbf{k} \end{bmatrix} \begin{bmatrix} a_\mathbf{k} \\ a_{-\mathbf{k}}^\dagger \end{bmatrix} \tag{3.5}$$

21

where, $\tan 2\theta_{\mathbf{k}} = -\frac{\mathcal{I}mS(\mathbf{k})}{\mathcal{R}eS(\mathbf{k})}$ and $S(\mathbf{k}) = \frac{J_K}{4}(1 + e^{i\mathbf{k}\cdot\mathbf{d}_1} + e^{i\mathbf{k}\cdot\mathbf{d}_2})$, with $\mathbf{d}_1$ and $\mathbf{d}_2$ being two lattice vectors of the honeycomb motif as shown in Fig. 3.1. This leads to a graphene-like band structure for the itinerant Majoranas in the zero flux sector,

$$\epsilon_{\mathbf{k}} = \frac{J_K}{4}\sqrt{3 + 2\cos k_x + 4\cos\frac{k_x}{2}\cos\frac{\sqrt{3}k_y}{2}} \tag{3.6}$$

For temperatures, $T > T_l$, the flux excitations thermally proliferate breaking the translation invariance for a generic flux configuration. However, the Majorana Hamiltonian can still be diagonalised in a particular flux sector numerically to obtain the renormalised band structure, in presence of Majorana-flux scattering [82].

One of the most surprising features of the Kitaev model is that in spite of the gapless Majoranas, the spin-spin correlations are ultra-short-ranged [79], in fact, they vanish beyond the nearest neighbours. With increasing temperature, the Kitaev model goes through a crossover temperature scale of $T_h \sim 0.38J_K$ beyond which the spins become completely disordered, and the model goes into a paramagnetic or free spin phase [82].

3.3 Magnetoelastic coupling

To obtain the spin-phonon coupling in Kitaev materials, we note that the exchange couplings, $J_{i,\alpha}$s, are functions of the ionic position as they come from the overlap of the electronic wave functions. Thus, in presence of lattice vibrations, we have [83]

$$J_{i,\alpha} = J_K + \frac{\partial J_{i,\alpha}}{\partial R_{i,\alpha}^a}\delta_{i,\alpha}^a + \frac{1}{2}\frac{\partial^2 J_{i,\alpha}}{\partial R_{i,\alpha}^a \partial R_{i,\alpha}^b}\delta_{i,\alpha}^a\delta_{i,\alpha}^b \tag{3.7}$$

where the expansion is done about the equilibrium ionic positions of the crystal, $\bar{R}_{i,\alpha}^a = r_i^a - r_{i+\hat{\alpha}}^a$ with $\delta_{i,\alpha}^a = R_{i,\alpha}^a - \bar{R}_{i,\alpha}^a$ ($a = x, y$) denoting the deformation of the bond and the derivatives are evaluated at the equilibrium position $\bar{R}_{ij}$. This in the original Kitaev Hamiltonian leads to the spin-phonon Hamiltonian that dictates the coupled dynamics of the optical phonons and the spins.

$$H = H_K + H_{\text{spin-phonon}} + H_{\text{phonon}} \tag{3.8}$$

where H_K is the bare spin Kitaev Hamiltonian of Eq. 3.1 with $J_{i,\alpha} \to J_K$, H_phonon is the bare Harmonic phonon Hamiltonian,

$$H_\mathrm{phonon} = \sum_{i,\alpha} \frac{\mathbf{P}_{i,\alpha}^2}{2m} + \frac{1}{2} \sum_{i,\alpha} \mathcal{D}_{\alpha\beta}^{ab} \delta_{i,\alpha}^a \delta_{i,\beta}^b \tag{3.9}$$

and

$$H_\mathrm{spin-phonon} = H_1 + H_2 \tag{3.10}$$

represents the spin-phonon coupling. The two terms denote the first and second order contributions of Eq. 3.7 and are given by

$$H_1 = \sum_{i,\alpha} \frac{\partial J_{i,\alpha}}{\partial R_{i,\alpha}^a} \delta_{i,\alpha}^a \, S_i^\alpha S_{i+\hat\alpha}^\alpha \tag{3.11}$$

and

$$H_2 = \frac{1}{2} \sum_{i,\alpha} \frac{\partial^2 J_{i,\alpha}}{\partial R_{i,\alpha}^a \partial R_{i,\alpha}^b} \delta_{i,\alpha}^a \delta_{i,\alpha}^b \, S_i^\alpha S_{i+\hat\alpha}^\alpha \tag{3.12}$$

respectively. We note that Ir^{4+}, having odd number of electrons, is a Kramers material, and the low energy $S = 1/2$ doublet is odd under TR, similar to the usual spins. Therefore, on symmetry ground, the spins cannot couple linearly with the phonons, which we see in the above magnetoelastic coupling as well. This is a stark difference between Kramers and non-Kramers materials, which will be more clear in the next chapter, where we will give an explicit example of non-Kramers material. It will be shown that the dominant contribution to the magnetoelastic coupling in the non-Kramers case is generically governed by a very different energy scale, unlike the spin exchange coupling coefficients ($\sim J_K$) in the case of the Kramers material which we are discussing now.

A further basis transformation can be performed on the lattice vibrations to rewrite the bond distortions in the normal mode basis, $\zeta_i^{(\bar{p})}$, which diagonalises the matrix $\mathcal{D}_{\alpha\beta}^{ab}$. The unitary transformation is given by, $\boldsymbol{\delta}_{i,\alpha}$, $\delta_{i,\alpha}^a = \Gamma_{\alpha\bar{p}}^{ab} \zeta_{i,b}^{(\bar{p})}$.

Further, we note that in the insulators, due to the small overlaps of the atomic orbitals the

microscopic forms of the spin exchange coupling constants typically looks like,

$$J_{ij}^\alpha = \bar{J}_{ij}^\alpha e^{-\eta \delta_{ij}} \tag{3.13}$$

where we have assumed a simplified isotropic form where η is the inverse length-scale of decay of overlap. Using the above form, we further define following notations for the compactness of the calculation:

$$\Gamma_{\alpha p}^{ab} \frac{\partial}{\partial R_{i,\alpha}^a} e^{-\eta \delta_{i,\alpha}} \equiv \chi_{p,\alpha}^b$$

$$\frac{1}{2} \Gamma_{\alpha p}^{ac} \Gamma_{\alpha q}^{bd} \frac{\partial^2}{\partial R_{i,\alpha}^a \partial R_{i,\alpha}^b} e^{-\eta \delta_{i,\alpha}} \equiv \lambda_{p,q,\alpha}^{cd} \tag{3.14}$$

With these notations, the spin-phonon coupling, $H_{\text{spin}-\text{phonon}}$, can now be rewritten in terms of the normal mode coordinates as,

$$H_1 = \sum_{i,\alpha} \chi_{\alpha,p}^b \zeta_{i,b}^{(p)} \, S_i^\alpha S_{i+\hat{\alpha}}^\alpha \tag{3.15}$$

$$H_2 = \sum_{i,\alpha} \lambda_{p,q,\alpha}^{cd} \zeta_{i,c}^{(p)} \zeta_{i,d}^{(q)} \, S_i^\alpha S_{i+\hat{\alpha}}^\alpha \tag{3.16}$$

Clearly, the above magnetoelastic couplings generate interaction between different normal modes of the phonons via the spins. However, in the following sections, we perform a single mode approximation by neglecting all possible inter-mode couplings and consider only a particular mode to calculate its frequency shift and linewidth broadening.

Further, to calculate the generic qualitative features of the renormalised phonon parameters, we simplify the above expression by neglecting the matrix structure of the coupling coefficients, assuming $\chi_{\alpha,p}^b = \chi$ and $\lambda_{p,q,\alpha}^{cd} = \lambda$. This assumption removes some of the details of the information, such as mode dependence of phonon renormalisation. However, this still captures the essential signatures of the fractionalisation by giving rise to various scattering channels for the phonons in the QSL phase, which is the central objective of this work. We now obtain the renormalisation of the phonon frequency and linewidth by calculating the self-energy correction to the phonon propagators due to the above spin-phonon interactions within a single mode approximation for the phonons.

(a)   (b)
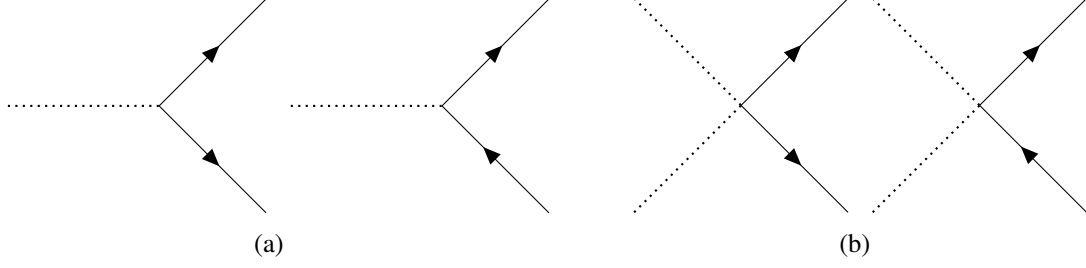
Figure 3.2: **Feynman diagrams representing the interaction between phonons (dotted lines) and bond-matter fermions (solid lines with arrow) in Kitaev QSL**: (a) and (b) denote contributions due to the spin-phonon coupling linear (Eq. 3.11) and quadratic in phonons (Eq. 3.12), respectively.

3.3.1 Phonon-Majorana coupling

Within the Kitaev QSL phenomenology, we now perform the standard Majorana decoupling of the spins to obtain the scattering vertices between the Majoranas and the phonons. Further, it is assumed that the background fluxes through all the hexagonal plaquettes are zero, which is strictly speaking a valid assumption below T_l (see Sec. 3.2). However, this does a huge complexity reduction and allows us to tackle the problem in an analytical approach. Within this assumption, the above spin-phonon coupling is rewritten in terms of the itinerant Majorana-phonon coupling,

$$H_1 = -\frac{\chi J_K}{4} \sum_{i,\alpha,a} \Theta^a_{i,\bar{p}}(ic_i c_{i+\hat{\alpha}}) \tag{3.17}$$

$$H_2 = -\frac{\lambda J_K}{4} \sum_{i,\alpha,c,d} \Theta^c_{i,\bar{p}} \Theta^d_{i,\bar{p}} \left(ic_i c_{i+\hat{\alpha}} \right) \tag{3.18}$$

and in turn bond-matter fermion-phonon coupling using the transformation given in Eq. 3.4,

$$H_1 = \frac{J_K}{4\sqrt{N_b}} \sum_{\mathbf{k},\mathbf{k'}} \chi^a \Theta^a_{\mathbf{k},\bar{p}} \left[\mathcal{A}_{\mathbf{k},\mathbf{k'}} f^\dagger_{\mathbf{k'}} f_{\mathbf{k'}-\mathbf{k}} + \mathcal{B}_{\mathbf{k},\mathbf{k'}} f_{\mathbf{k'}} f_{-\mathbf{k}-\mathbf{k'}} + \mathcal{C}_{\mathbf{k},\mathbf{k'}} f_{\mathbf{k'}} f^\dagger_{\mathbf{k}+\mathbf{k'}} + \mathcal{D}_{\mathbf{k},\mathbf{k'}} f^\dagger_{\mathbf{k'}} f^\dagger_{\mathbf{k}-\mathbf{k'}} \right]$$

$$\tag{3.19}$$

$$H_2 = \frac{J_K}{4N_b} \sum_{\mathbf{k},\mathbf{k'},\mathbf{k''}} \lambda^{cd} \, \Theta^c_{\mathbf{k},\bar{p}} \Theta^d_{\mathbf{k'},\bar{q}} \left[\mathcal{P}_{\mathbf{k},\mathbf{k'},\mathbf{k''}} f^\dagger_{\mathbf{k''}} f_{\mathbf{k''}-\mathbf{k}-\mathbf{k'}} + \mathcal{Q}_{\mathbf{k},\mathbf{k'},\mathbf{k''}} f_{\mathbf{k''}} f_{-\mathbf{k}-\mathbf{k'}-\mathbf{k''}} \right.$$

$$\left. + \mathcal{R}_{\mathbf{k},\mathbf{k'},\mathbf{k''}} f_{\mathbf{k''}} f^\dagger_{\mathbf{k}+\mathbf{k'}+\mathbf{k''}} + \mathcal{S}_{\mathbf{k},\mathbf{k'},\mathbf{k''}} f^\dagger_{\mathbf{k''}} f^\dagger_{\mathbf{k}+\mathbf{k'}-\mathbf{k''}} \right] \tag{3.20}$$

25

Figure 3.3: Leading order contribution to the phonon frequency shift due to the phonon-Majorana interaction

where

$$\mathcal{A}_{\mathbf{k},\mathbf{k}'} = 2 + e^{i(\mathbf{k}'-\mathbf{k})\cdot\mathbf{d}_1} + e^{i(\mathbf{k}'-\mathbf{k})\cdot\mathbf{d}_2}$$

$$\mathcal{B}_{\mathbf{k},\mathbf{k}'} = e^{-i(\mathbf{k}+\mathbf{k}')\cdot\mathbf{d}_1} + e^{-i(\mathbf{k}+\mathbf{k}')\cdot\mathbf{d}_2}$$

$$\mathcal{C}_{\mathbf{k},\mathbf{k}'} = -e^{-i(\mathbf{k}+\mathbf{k}')\cdot\mathbf{d}_1} - e^{-i(\mathbf{k}+\mathbf{k}')\cdot\mathbf{d}_2}$$

$$\mathcal{D}_{\mathbf{k},\mathbf{k}'} = -e^{i(\mathbf{k}'-\mathbf{k})\cdot\mathbf{d}_1} - e^{i(\mathbf{k}'-\mathbf{k})\cdot\mathbf{d}_2}$$

$$\mathcal{P}_{\mathbf{k},\mathbf{k}',\mathbf{k}''} = 2 + e^{i(\mathbf{k}''-\mathbf{k}-\mathbf{k}')\cdot\mathbf{d}_1} + e^{i(\mathbf{k}''-\mathbf{k}-\mathbf{k}')\cdot\mathbf{d}_2}$$

$$\mathcal{Q}_{\mathbf{k},\mathbf{k}',\mathbf{k}''} = e^{-i(\mathbf{k}+\mathbf{k}'+\mathbf{k}'')\cdot\mathbf{d}_1} + e^{-i(\mathbf{k}+\mathbf{k}'+\mathbf{k}'')\cdot\mathbf{d}_2}$$

$$\mathcal{R}_{\mathbf{k},\mathbf{k}',\mathbf{k}''} = -e^{-i(\mathbf{k}+\mathbf{k}'+\mathbf{k}'')\cdot\mathbf{d}_1} - e^{-i(\mathbf{k}+\mathbf{k}'+\mathbf{k}'')\cdot\mathbf{d}_2}$$

$$\mathcal{S}_{\mathbf{k},\mathbf{k}',\mathbf{k}''} = -e^{i(\mathbf{k}''-\mathbf{k}-\mathbf{k}')\cdot\mathbf{d}_1} - e^{i(\mathbf{k}''-\mathbf{k}-\mathbf{k}')\cdot\mathbf{d}_2} \tag{3.21}$$

These interaction vertices are represented by the Feynman diagrams shown in Fig. 3.2, where Fig. 3.2(a) and 3.2(b) denote the interaction vertices arising due to H_1 (Eq. 3.19) and H_2 (Eq. 3.20), respectively. These vertices clearly show that the phonons can decay into the fractionalised excitations of the QSL and this would renormalise both the frequency and the linewidth of the phonon peaks. In regard to the linewidth, we expect an anomalous broadening as the temperature is decreased since on lowering the temperature the fermions become more coherent, and hence the phonon can more efficiently decay into them while obeying all the conservation laws.

3.4 Phonon renormalisation

3.4.1 Frequency renormalisation

The leading order contribution to the renormalisation of the frequency comes from the vertices shown in Fig. 3.2(b) when we integrate over the fermions (see Fig. 3.3). The resultant

frequency renormalisation is given by

$$\delta\omega \propto \frac{1}{N_b} \sum_{i,\alpha} \langle J_K\, S_i^\alpha S_{i+\hat\alpha}^\alpha \rangle_S \tag{3.22}$$

where $\langle \hat{O} \rangle_S = \frac{Tr(\hat{O}e^{-\beta H_{spin}})}{Tr(e^{-\beta H_{spin}})}$ denotes averaging of the equal time spin correlators over the thermodynamic ensemble, and the proportionality constant is given in terms of the first order spin-phonon coupling and the transformation to the phonon soft modes. For the present discussion, we neglect their detail structure and assume it to be a constant, λ.

Within a free Majorana phenomenology restricted to the zero-flux sector, the spin-energy can be calculated leading to the energy density of the free Majorana fermions. The frequency shift can then be rewritten as,

$$\delta\omega \sim \lambda J_K \sum_{\mathbf{k}} \langle \epsilon_{\mathbf{k}} (a_{\mathbf{k}}^\dagger a_{\mathbf{k}} - \frac{1}{2}) \rangle_S \tag{3.23}$$

The above expression being proportional to the total energy of the spin system, is always negative. This is shown in Fig. 3.4. The curve implies that the frequency shift goes to zero at $T \to \infty$ and gradually turns non-zero around $T \sim J_K$ ultimately saturating to a negative constant number at zero temperature corresponding to the ground state energy-density of the spins. Although the deviation from the bare frequency monotonically increases with decreasing temperature, whether it hardens or softens depends on the sign of the coupling constant, λ, of the phonon-Majorana vertex described by Fig. 3.2(b).

Further, numerical calculations exist for finite temperatures including all the flux sectors for the pure Kitaev model [82] which shows that the thermally excited flux excitations renormalises the band structure of the itinerant Majoranas. Therefore, on a general ground, it is expected that the frequency shift is only renormalised via the modified energy density of the Majorana fermions, keeping the expected experimental consequences unchanged. We note that further temperature dependence of the frequency shift can come from the real part of the self-energy bubble due to the interaction vertex H_1. However, this is a second-order effect in perturbation theory and is expected to be subleading.
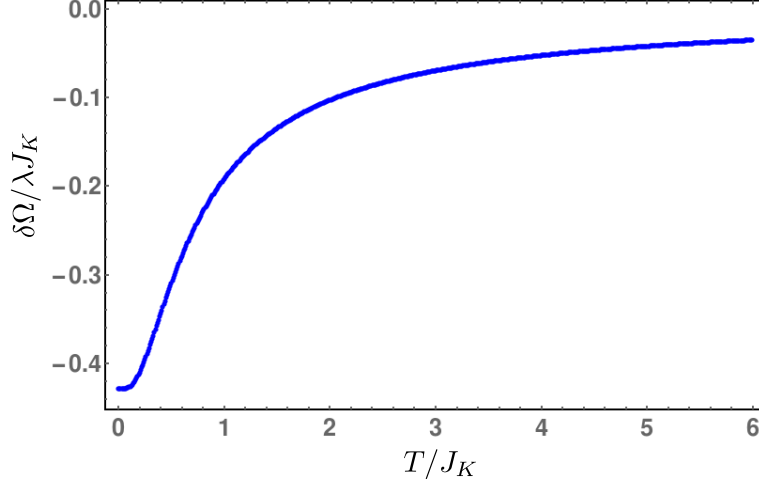
Figure 3.4: Temperature dependence of the frequency shift of the phonons in Kitaev QSL
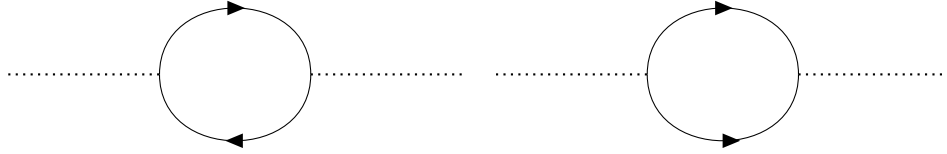
Figure 3.5: Self-energy of the phonon due to the phonon-Majorana interaction

3.4.2 Phonon Linewidth :

The leading contribution to the linewidth comes from the vertices shown in Fig. 3.2(a) in the second order of the perturbation theory by calculating the imaginary part of the self-energy bubble diagram shown in Fig. 3.5. Within the free Majorana phenomenology, the phonon self-energy is given by,

$$\Sigma(\mathbf{q}, i\Omega) \sim \frac{\chi^2 J_K^2}{N_b \beta} \times$$

$$\sum_{m,\mathbf{k}} \Big[M_{\mathbf{k+q,k}} G(\mathbf{k+q}, -i\Omega - i\omega_m) G(-\mathbf{k}, i\omega_m) + M_{-\mathbf{k-q,-k}} G(\mathbf{k+q}, i\Omega - i\omega_m) G(-\mathbf{k}, i\omega_m)$$

$$+ N_{\mathbf{k+q,k}} G(\mathbf{k+q}, i\Omega + i\omega_m) G(\mathbf{k}, i\omega_m) + N_{-\mathbf{k-q,-k}} G(\mathbf{k+q}, -i\Omega + i\omega_m) G(\mathbf{k}, i\omega_m) \Big]$$

$$(3.24)$$

where, $G(\mathbf{k}, i\omega)$ is the time-ordered correlator for the Majorana fermions which is given by,
$G(\mathbf{k}, i\omega) = -\int_0^\beta d\tau \langle \mathcal{T} a_\mathbf{k}(\tau) a_\mathbf{k}^\dagger(0) \rangle_0 e^{i\omega\tau} = \frac{1}{i\omega - \epsilon_\mathbf{k}}$, and

$$M_{\mathbf{k+q},\mathbf{k}} = \bar{\mathcal{A}}_{-\mathbf{q},\mathbf{k}} \bar{\mathcal{D}}_{\mathbf{q},-\mathbf{k}} + \bar{\mathcal{A}}_{-\mathbf{q},-\mathbf{k}-\mathbf{q}} \bar{\mathcal{D}}_{\mathbf{q},-\mathbf{k}} + \bar{\mathcal{D}}_{\mathbf{q},-\mathbf{k}} \bar{\mathcal{A}}_{-\mathbf{q},\mathbf{k}} + \bar{\mathcal{D}}_{\mathbf{q},\mathbf{k}+\mathbf{q}} \bar{\mathcal{A}}_{-\mathbf{q},\mathbf{k}}$$

$$N_{\mathbf{k+q},\mathbf{k}} = \bar{\mathcal{B}}_{-\mathbf{q},-\mathbf{q}-\mathbf{k}} \bar{\mathcal{B}}_{\mathbf{q},-\mathbf{k}} + \bar{\mathcal{C}}_{-\mathbf{q},\mathbf{k}} \bar{\mathcal{B}}_{\mathbf{q},-\mathbf{k}} + \bar{\mathcal{B}}_{-\mathbf{q},\mathbf{k}} \bar{\mathcal{C}}_{\mathbf{q},-\mathbf{k}} + \bar{\mathcal{C}}_{\mathbf{q},\mathbf{k}+\mathbf{q}} \bar{\mathcal{C}}_{-\mathbf{q},\mathbf{k}} \quad (3.25)$$

See the Appendix A.1 for the details of the above coupling constants. Further performing the Matsubara summation in the above expression and calculating its imaginary part (see Appendix A.2 for details of the calculations), we obtain

$$\mathcal{I}m\left[\Sigma(\mathbf{q}=0, \Omega + i0^+)\right] \propto \frac{J_K^2}{N_b} \sum_\mathbf{k} (1 - 2n_F(\epsilon_\mathbf{k}))\left[\delta(\Omega + 2\epsilon_\mathbf{k}) - \delta(\Omega - 2\epsilon_\mathbf{k})\right] \quad (3.26)$$

where $n_F(\epsilon_\mathbf{k})$ denotes the fermionic occupancy with dispersion $\epsilon_\mathbf{k}$ (see Eq. 3.6) in the zero-flux sector. Again, the proportionality constant depends on the magneto-elastic coupling and the normal-mode matrix elements which have been assumed to be a constant (χ) for this calculation. The temperature and the frequency dependence of the above are shown in Figs. 3.6(a) and 3.6(b), respectively. As indicated by the delta functions, the frequency dependence of linewidth closely follows the two-particle density of states of Majoranas which is shown in the inset of Fig. 3.6(b). As $T \to \infty$, the Majorana fermions become incoherent and hence their contribution to linewidth goes to zero, while at low temperatures it reaches a finite value for the completely coherent Majoranas. This effect is completely opposite of the usual temperature related broadening due to anharmonic terms and arises due to the development of a coherent scattering channel for the phonons. Clearly, in absence of any magnetic phase transition, such coherent particles - in case of a Kitaev QSL Majorana fermions - indicate novel low-temperature physics in the spin sector. This is in direct conformity with the experimental outcomes that have been reported in our experiment-theory collaboration on the Raman spectroscopic measurements on the candidate Kitaev material, Cu_2IrO_3 [48, 75].

We note that the zero flux assumption breaks down at the temperature regime of $T > T_l$, which is relevant to the experiment. In this case, the itinerant fermion lines are further renormalised by their scattering with the Z_2 fluxes, which, in turn, provide a finite lifetime to the fermions as well as renormalise their bandwidth [13]. However, it was shown in the earlier numerical calculations [55, 82] that the qualitative features of the itinerant fermionic density of states remain almost intact at finite temperatures almost all the way up to the crossover
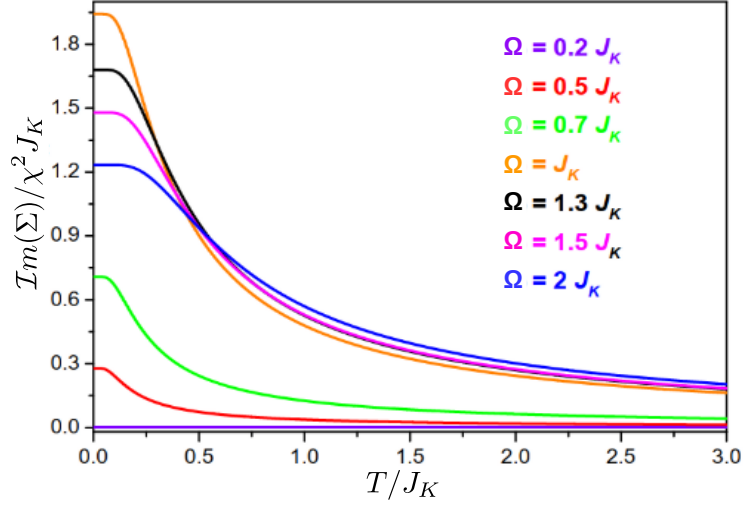
(a)
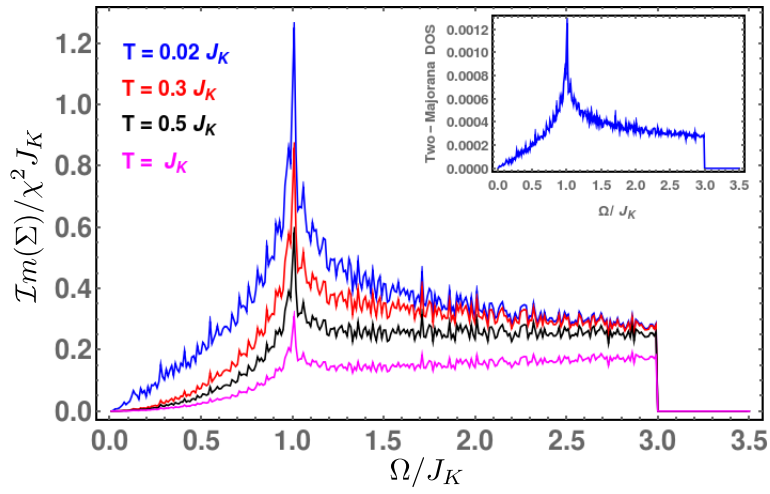
(b)

Figure 3.6: **Renormalisation of the phonon linewidth in Kitaev QSL:** (a) and (b) show temperature and frequency dependence of the linewidth, respectively. Inset of (c) shows two-particle density of states of Majoranas in zero flux sector.
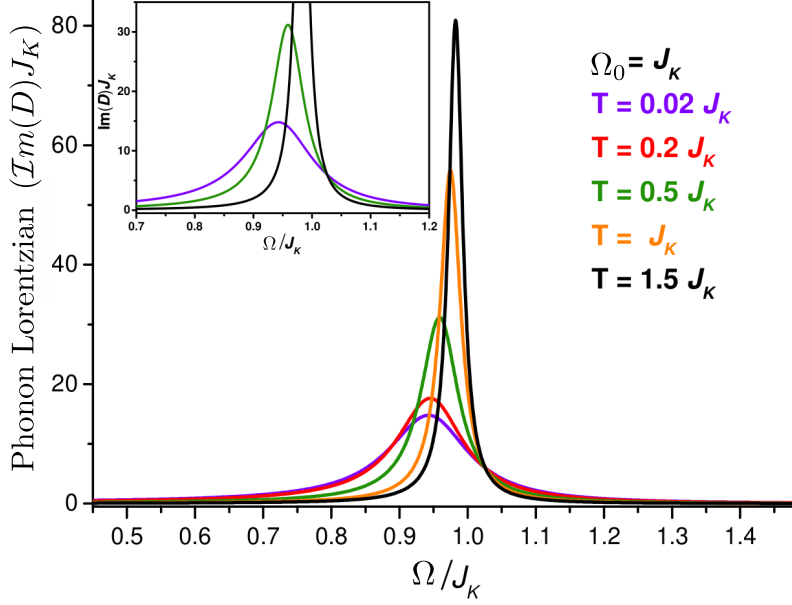
Figure 3.7: **Temperature evolution of the Lorentzians of the phonon peaks:** We plot the imaginary part of the phonon Green's function (D) which gives rise to the Lorentzian lineshape of the phonon spectra with the frequency scaled w.r.t. the Kitaev coupling J_K. Different curves represent different temperatures. The spin-phonon coupling constants are taken to be $\lambda = 0.13$ and $\chi = 0.2$ for the illustrative purpose.

temperature, T_h (see Sec. 3.2), where the itinerant Majoranas start to become incoherent and the QSL goes to the paramagnetic phase by destroying the ultra-short-ranged nearest neighbour spin correlations in favour of conventional CW behaviour. Therefore, although the zero flux assumption is no longer valid at higher temperatures, the qualitative features of our results are still applicable (up to $T < T_h$), with the free itinerant Majorana density of states replaced by the renormalised one.

We further plot the phonon Lorentzian (see Eq. 2.9) at different temperatures for the Stokes lines in Fig. 3.7 using the expression of the Eq. 3.23 and Eq. 3.26 at the limit $\mathbf{q} \to 0$ (which is relevant to the Raman experiments) for some representative values of coupling constants λ and χ, and assuming the band structure of the optical phonons being $\Omega_{\mathbf{q}} \approx \Omega_0$. The temperature evolution of this Lorentzian is in qualitative agreement with the experimental observations as reported in the Ph.D. thesis of Srishti Pal [75].

3.4.3   Comparison with experiments

For completion, a further comparison with the experimental data is obtained by fitting the results to the experimental data (reported in Ph.D. thesis of Srishti Pal [75]) as shown in Fig. 3.8. Here we compare our results with one particular phonon mode seen in the experiments.

The match is quite promising at least to the qualitative level. However, since we do not have detailed information about the mode dependent magnetoelastic coupling constants or particular matrix elements of the transformation from bond distortion to normal modes, precise quantitative comparison is not possible.
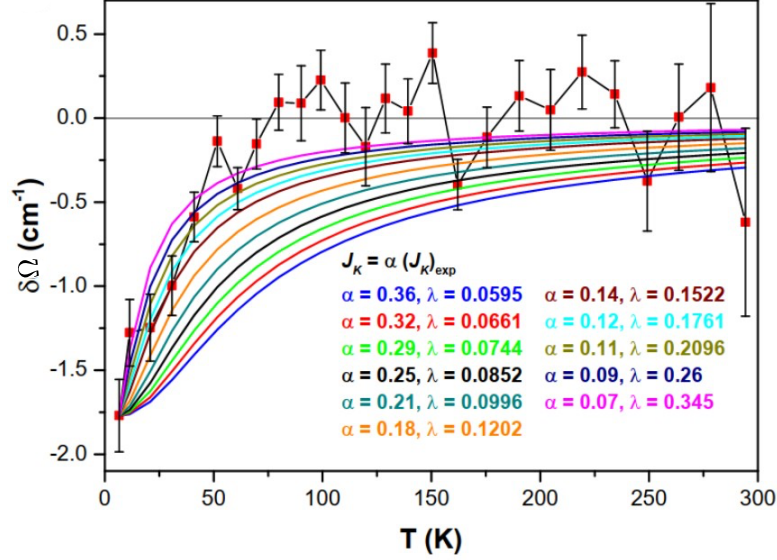
(a)
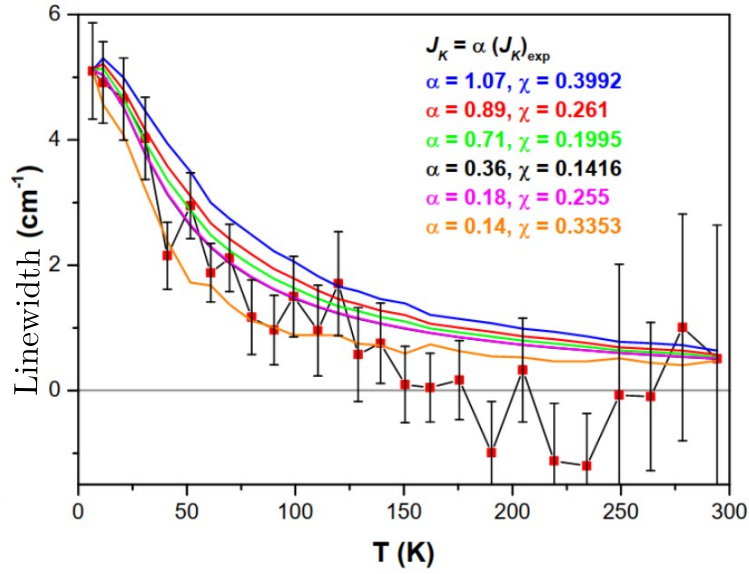
(b)

Figure 3.8: **Comparison for theoretical results and experimental data for a particular phonon mode seen in experimental observation:** Temperature dependence of **(a)** frequency shift and **(b)** linewidth for the phonon mode. Red squares are the experimental data after subtracting the anharmonic contribution. The smooth lines represent the theoretical curves at different values of coupling constant. In **(b)**, we plot only till $J_K = 40K$ considering the finite bandwidth ($\sim 3J_K$) effect as shown in Fig 3.6(b).

In spite of the remarkable similarity of the qualitative features of our theoretical analysis

32

with the experimental data, we should note that a basic assumption of our theory is that the low-temperature phase of Cu_2IrO_3 is governed by the pure Kitaev QSL. However, it is well-known that the nature of the synthesis makes these second-generation Kitaev materials prone to disorder [35]. In fact, Cu_2IrO_3 suffers a valence disorder of Cu^+ converting into Cu^{2+}, and also Cu-Ir site disorder [76]. The generic role of these disorders is to introduce non-magnetic impurities into the honeycomb motif, leading to the possibility of partial freezing at low temperatures [35, 77]. However, the present samples are of much higher quality and do not show any features of a glassy state either in ac magnetic susceptibility [48] or in μSR down to 260 mK [76]. Although in the DC susceptibility measurements, there is a sub-Curie kind of behaviour observed below $\approx$10 K, this temperature region is beyond the scope of this experiment. This justifies the applicability of our theory of pure QSL physics throughout the temperature regime starting from the CW scale to the lowest available experimental temperature. However, understanding the role of disorder on our theoretical analysis still remains an open question and will be very interesting to understand in the future.

3.5 Phonon-mediated Loudon-Fleury vertex

As mentioned previously in the Sec. 2.3, in presence of moderate magnetoelastic coupling, the phonons can mediate an effective coupling between the Raman photons and the magnetic degrees of freedom. In the case of Kitaev materials, such interaction vertices can be obtained by integrating out the phonons from the spin-phonon vertices given by Eq. 3.10 and phonon-Raman photon vertex given by Eq. 2.4. Inside the QSL phase, and with the restriction to the low-temperature zero-flux sector, such interactions then generate a coupling between the probe Raman photons and the Majorana fermions, in turn, bond-matter fermions, which we describe now.

The phonons are integrated out from the vertices shown in Fig. 3.2 and 2.1 within a perturbative framework. At the leading order, this leads to the following interaction vertices,

$$H_{LF}^{\text{fermion}} = \frac{1}{2} \left[-\langle H_{\text{Raman}} H_1 \rangle_\zeta + \langle H_{\text{Raman}}^2 H_2 \rangle_\zeta + \langle H_{\text{Raman}} \left(H_1 H_2 + H_2 H_1 \right) \rangle_\zeta \right] \quad (3.27)$$

where $\langle \hat{O} \rangle_\zeta = \frac{\int D\zeta \, \hat{O} \, e^{-\beta H_\zeta}}{\int D\zeta \, e^{-\beta H_\zeta}}$ is the thermal averaging over the phonons, and H_{Raman} is the Raman vertex for the phonon-external photon coupling as described in the previous chapter (see Eq. 2.4). Using the form of H_1 and H_2 as given in Eqs. 3.19 and 3.20, respectively, the

above vertices are explicitly calculated to obtain,

$$\langle H_{\text{Raman}}H_1\rangle = \frac{J_K\chi}{8N_b\Omega_0}\int d^2\mathbf{k}d^2\mathbf{k}'d^2\bar{\mathbf{k}}d^2\bar{\mathbf{k}}'\left(\nabla_{\zeta_{\bar{p}}}\Lambda\right)^{ij}_{\zeta_{\bar{p}}=0}\omega^{in}_{\bar{\mathbf{k}}}\omega^{out}_{-\bar{\mathbf{k}}'}\delta_{\mathbf{k}+\bar{\mathbf{k}},\bar{\mathbf{k}}'}\mathcal{A}^{in}_i(\bar{\mathbf{k}})\mathcal{A}^{out}_j(\bar{\mathbf{k}}')$$

$$\times\left[\mathcal{A}_{\mathbf{k}\mathbf{k}'}f^\dagger_{\mathbf{k}'}f_{\mathbf{k}'-\mathbf{k}}+\mathcal{B}_{\mathbf{k}\mathbf{k}'}f_{\mathbf{k}'}f_{\mathbf{k}-\mathbf{k}'}+\mathcal{C}_{\mathbf{k}\mathbf{k}'}f_{\mathbf{k}'}f^\dagger_{\mathbf{k}+\mathbf{k}'}+\mathcal{D}_{\mathbf{k}\mathbf{k}'}f^\dagger_{\mathbf{k}'}f^\dagger_{\mathbf{k}-\mathbf{k}'}\right]$$

(3.28)

$$\langle H^2_{\text{Raman}}H_2\rangle = \frac{J_K\lambda}{4N_b\Omega_0^2}\sum_{\mathbf{k},\mathbf{k}',\mathbf{k}'',\bar{\mathbf{k}},\bar{\mathbf{k}}',\bar{\bar{\mathbf{k}}},\bar{\bar{\mathbf{k}}}'}\delta_{\mathbf{k},\bar{\mathbf{k}}'-\bar{\mathbf{k}}}\delta_{\mathbf{k}',\bar{\bar{\mathbf{k}}}'-\bar{\bar{\mathbf{k}}}}\omega^{in}_{\bar{\mathbf{k}}}\omega^{out}_{-\bar{\mathbf{k}}'}\omega^{in}_{\bar{\bar{\mathbf{k}}}}\omega^{out}_{-\bar{\bar{\mathbf{k}}}'}\left(\nabla_{\zeta_{\bar{p}}}\Lambda\right)^{ij}_{\zeta_{\bar{p}}=0}\left(\nabla_{\zeta_{\bar{p}}}\Lambda\right)^{mn}_{\zeta_{\bar{p}}=0}$$

$$\times\mathcal{A}^{in}_i(\bar{\mathbf{k}})\mathcal{A}^{out}_j(\bar{\mathbf{k}}')\mathcal{A}^{in}_m(\bar{\bar{\mathbf{k}}})\mathcal{A}^{out}_n(\bar{\bar{\mathbf{k}}}')\left[\mathcal{P}_{\mathbf{k},\mathbf{k}',\mathbf{k}''}f^\dagger_{\mathbf{k}''}f_{\mathbf{k}''-\mathbf{k}-\mathbf{k}'}+\mathcal{Q}_{\mathbf{k},\mathbf{k}',\mathbf{k}''}f_{\mathbf{k}''}f_{-\mathbf{k}-\mathbf{k}'-\mathbf{k}''}\right.$$

$$\left.+\mathcal{R}_{\mathbf{k},\mathbf{k}',\mathbf{k}''}f_{\mathbf{k}''}f^\dagger_{\mathbf{k}+\mathbf{k}'+\mathbf{k}''}+\mathcal{S}_{\mathbf{k},\mathbf{k}',\mathbf{k}''}f^\dagger_{\mathbf{k}''}f^\dagger_{\mathbf{k}+\mathbf{k}'-\mathbf{k}''}\right]$$

(3.29)

$$\langle H_{\text{Raman}}H_1H_2\rangle = \frac{J_K^2\chi\lambda}{16N_b^{3/2}\Omega_0^2}\sum_{\mathbf{k},\mathbf{k}',\mathbf{k}'',\bar{\mathbf{k}},\bar{\mathbf{k}}',\bar{\bar{\mathbf{k}}},\bar{\bar{\mathbf{k}}}'}\delta_{-\mathbf{k},\bar{\mathbf{k}}}\delta_{\mathbf{k}',\bar{\bar{\mathbf{k}}}'-\bar{\bar{\mathbf{k}}}}\omega^{in}_{\bar{\bar{\mathbf{k}}}}\omega^{out}_{-\bar{\bar{\mathbf{k}}}'}\left(\nabla_{\zeta_{\bar{p}}}\Lambda\right)^{ij}_{\zeta_{\bar{p}}=0}\mathcal{A}^{in}_i(\bar{\bar{\mathbf{k}}})\mathcal{A}^{out}_j(\bar{\bar{\mathbf{k}}}')$$

$$\times\left[\mathcal{P}_{\mathbf{k},\mathbf{k}',\mathbf{k}''}f^\dagger_{\mathbf{k}''}f_{\mathbf{k}''-\mathbf{k}-\mathbf{k}'}+\mathcal{Q}_{\mathbf{k},\mathbf{k}',\mathbf{k}''}f_{\mathbf{k}''}f_{-\mathbf{k}-\mathbf{k}'-\mathbf{k}''}\mathcal{R}_{\mathbf{k},\mathbf{k}',\mathbf{k}''}f_{\mathbf{k}''}f^\dagger_{\mathbf{k}+\mathbf{k}'+\mathbf{k}''}+\mathcal{S}_{\mathbf{k},\mathbf{k}',\mathbf{k}''}f^\dagger_{\mathbf{k}''}f^\dagger_{\mathbf{k}+\mathbf{k}'-\mathbf{k}''}\right]$$

$$\times\left[\mathcal{A}_{\bar{\mathbf{k}},\bar{\mathbf{k}}'}f^\dagger_{\bar{\mathbf{k}}'}f_{\bar{\mathbf{k}}'-\bar{\mathbf{k}}}+\mathcal{B}_{\bar{\mathbf{k}},\bar{\mathbf{k}}'}f_{\bar{\mathbf{k}}'}f_{-\bar{\mathbf{k}}-\bar{\mathbf{k}}'}+\mathcal{C}_{\bar{\mathbf{k}},\bar{\mathbf{k}}'}f_{\bar{\mathbf{k}}'}f^\dagger_{\bar{\mathbf{k}}+\bar{\mathbf{k}}'}+\mathcal{D}_{\bar{\mathbf{k}},\bar{\mathbf{k}}'}f^\dagger_{\bar{\mathbf{k}}'}f^\dagger_{\bar{\mathbf{k}}-\bar{\mathbf{k}}'}\right]$$

(3.30)

where the optical phonon band structure is approximated as $\Omega_{\mathbf{q}}\approx\Omega_0$. Clearly, the first term (Eq. 3.28), which is obtained in the second order perturbation theory, contributes to the two-photon-two fermion vertices, whereas, the last two terms (Eqs. 3.29 and 3.30), obtained in the third order perturbation, contribute to four-photon-two-fermion and two-photon-four-fermion vertices, respectively. Feynman diagram for Eqs. 3.28, 3.29 and 3.30 are shown in Figs. 3.9(a), 3.9(b), and 3.9(c) respectively. As can be seen from the prefactors, the first type of vertices is suppressed by $1/\Omega_0$ compared to the usual Loudon-Fleury vertex, whereas the last two types are suppressed by $1/\Omega_0^2$. Therefore, generically their contributions to the scattering continuum are expected to be significantly low in comparison to that due to Eq. 2.1. However, we note that since in the Raman intensity profile, the leading phonon-mediated vertices contribute exactly the same way as usual Loudon-Fleury via the two-Majorana density of states, these contributions might be difficult to separate in the experiments.
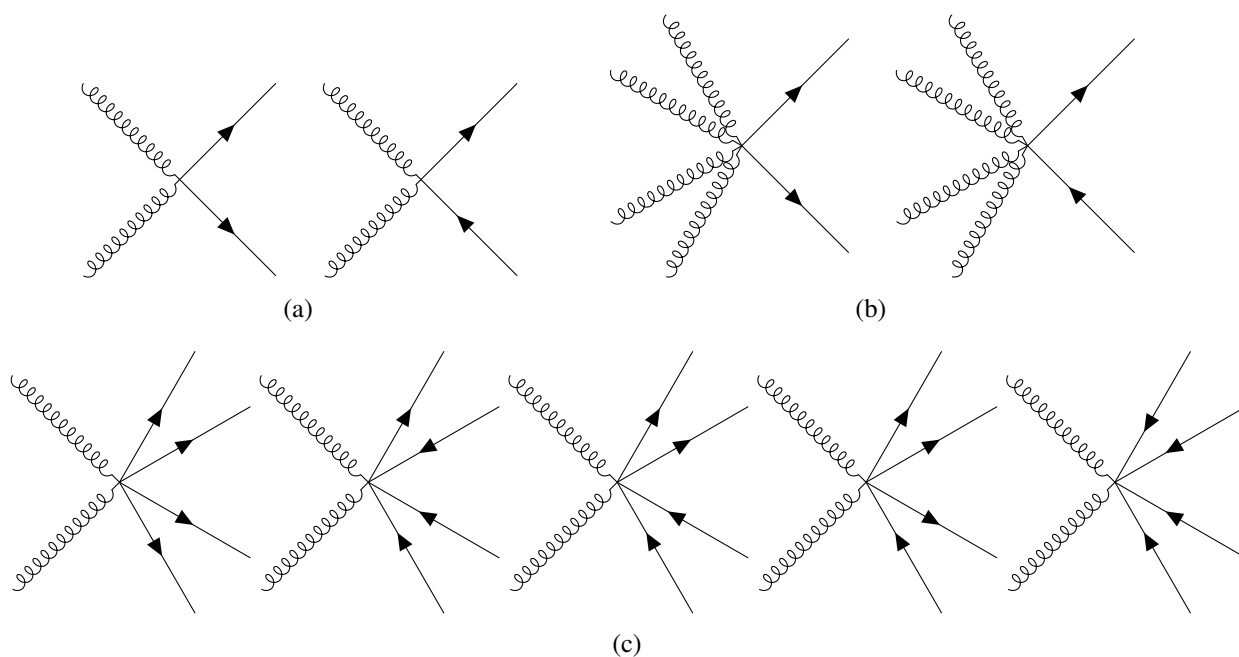
Figure 3.9: **Feynman diagram for phonon mediated Loudon-Fleury vertex for bond-matter fermions:** Vertices shown in (a) and (b) comes from the linear (3.2(a)) and quadratic (3.2(b)) spin-phonon coupling. Vertices shown (c) comes from the combination of linear and quadratic contribution. See the main text for further details.
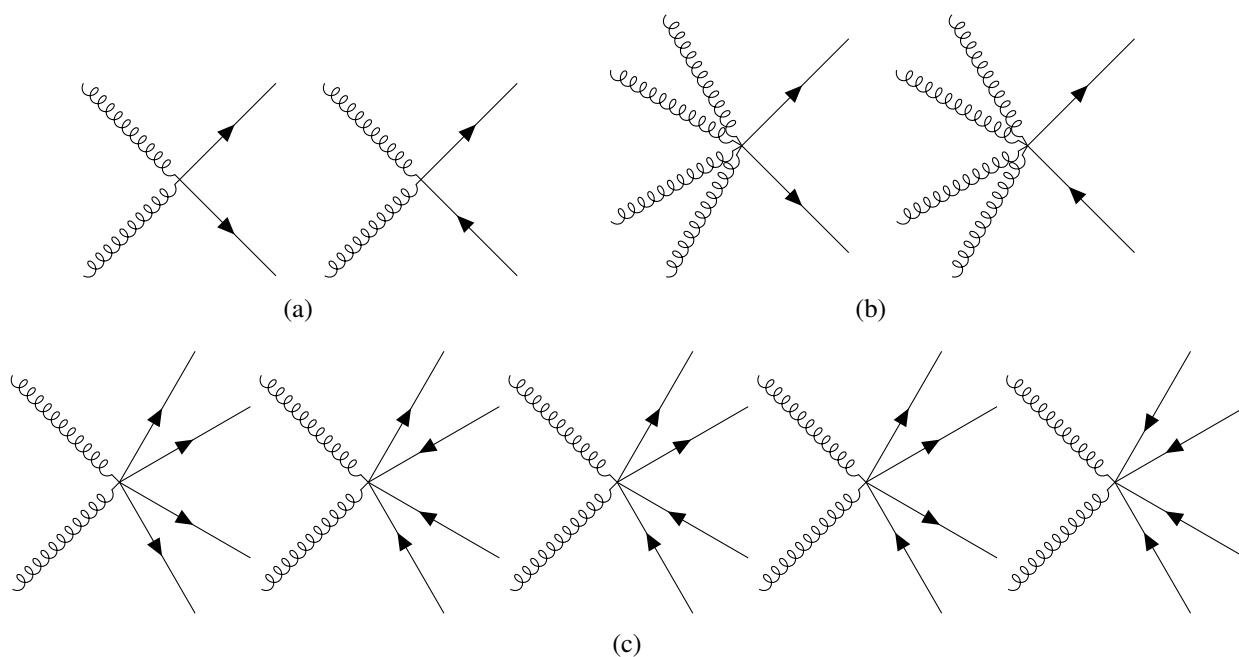
Figure 3.9: **Feynman diagram for phonon mediated Loudon-Fleury vertex for bond-matter fermions:** Vertices shown in (a) and (b) comes from the linear (3.2(a)) and quadratic (3.2(b)) spin-phonon coupling. Vertices shown (c) comes from the combination of linear and quadratic contribution. See the main text for further details.

CHAPTER 4

PROBING EMERGENT QED IN NON-KRAMERS QUANTUM SPIN ICE VIA RAMAN SCATTERING OF PHONONS

4.1 Introduction

Having discussed the experimental implications of the fractionalisation in a Z_2 QSL, we now turn to the case of U(1) QSL. As it is well-known from the work on the gauge theories due to Polyakov [84], the compact U(1) QSLs with gapped matter fields are unstable to instanton effects for spatial dimension D$\leq$ 2, hence, the essential choice to search for their candidates are restricted in 3D materials. So far, one of the most promising family of candidates reported in this regard are spin-orbit coupled rare-earths pyrochlores, where the magnetic moments sit on a three-dimensional network of corner sharing tetrahedra and interact via strongly anisotropic antiferromagnetic spin exchanges [12, 24, 85, 86]. Due to the geometrical frustration inherent to such lattice structures [25, 87], the magnetic ordering is significantly suppressed in these compounds, naturally paving the way for realising the cooperative paramagnets both classical [41, 42, 49, 85, 87–92] and quantum [12, 19, 29, 30, 86, 93–96].

In the classical limit, the model contains a macroscopically degenerate ground state manifold which can be shown to be in a one-to-one correspondence with the water ice with a similar zero temperature entropy counting. Hence these models are dubbed as *classical spin ice* [41, 42, 49, 85, 87–92]. Interestingly, due to such huge residual entropy, the low temperature regime of these models is particularly interesting and can be described entirely by the entropic rearrangements of the spin ice configurations. It can be shown that it naturally leads to a description of such lattice models at low temperatures in terms of the lattice magnetostatics along with a notion of magnetic monopoles defined in terms of the microscopic spin degrees of freedom, which are the excitations of the spin model[49, 97, 98]. With increasing temperature, the monopoles thermally proliferate, eventually leading to a paramagnetic phase without encountering any crossovers or phase transitions [26, 91, 92, 99].

Incorporation of the quantum fluctuations to the classical spin ice becomes way more interesting, which is referred as *quantum spin ice*[12, 19, 29, 30, 86, 93–96] in the literature. As a consequence of the third law of thermodynamics, the system tries to quench the residual

entropy of the ice manifold at zero temperature via quantum tunneling between different degenerate ice configurations, leading to emergence of a lattice QED with gapless photons, and resulting into the long-range entangled resonating QSL ground state [8, 12, 19, 30, 86, 95, 96, 100]. Apart from the magnetic monopoles and the photons, the lattice QED also has another low energy excitation, electric charges, which are the point defects of the compact U(1) gauge field [12, 86]. [1] Various spectroscopic [29, 101] and thermodynamic [43] measurements have been reported so far on the spin ice candidates to ascertain the existence of these exotic magnetic excitations. However, the signatures are not very clear, and more attention is required to develop various unconventional probes to pinpoint their characteristic features.

In this regard, we present here the possibility of detecting signatures of fractionalisation from the anomalous phonon spectra in the quantum spin ice, which further can be detected in the Raman scattering experiments on these compounds [39]. In fact, the spin-phonon coupling gets enhanced in these compounds due to the presence of $4f$ electrons with strong spin-orbit coupling, which in turn favors the possibility of such observations. Such magnetoelastic effects become more significant in an interesting subset of the rare-earth pyrochlores which are the so-called *non-Kramers* spin ice materials such as $Pr_2Zr_2O_7$ [29, 63, 102], $Pr_2Hf_2O_7$ [101], $Tb_2Ti_2O_7$ [103–105], $Ho_2Ti_2O_7$ [104] etc. In these cases, the low-energy spin-1/2 magnetic moments arise from even-electron wave functions [102–104]. The degeneracy of such a non-Kramers doublet is protected by lattice symmetry, the D_{3d} symmetry at the pyrochlore lattice site, instead of the usual time reversal symmetry for Kramers doublets. Therefore under time reversal, $\mathcal{T}$, the transformation of the low-energy doublets, s^α ($\alpha = x, y, z$), made out of spin-orbit coupled wave functions is given by

$$\mathcal{T} \; : \; \{s^x, s^y, s^z\} \rightarrow \{s^x, s^y, -s^z\} \tag{4.1}$$

This is in stark difference from the usual Kramers case as realised in, *e.g.*, $Dy_2Ti_2O_7$, $Yb_2Ti_2O_7$, where all the components of the resultant spin-1/2s are odd under time reversal. Such non-trivial implementation of time reversal symmetry immediately suggests that the transverse components $\{s^x, s^y\}$ can linearly couple to the lattice vibrations of the appropriate space-group

---

[1] We note that there are two different assignments of gauge charges found in the literature. In the first assignment and the one that we use here, the magnetic monopoles of a QSL are obtained by violations of the ice-rule on a tetrahedron which are obtained by spin-flips. The electric charges, on the other hand, are the point defects of the compact U(1) gauge field [49, 96]. In the other convention, the violations of the ice-rule give rise to electric charges (often referred to as spinons in the associated literature) while the point defects associated with the gauge field are dubbed as magnetic monopoles [12].

symmetry, such that this linear coupling makes the above materials ideal candidates to explore the spin physics through the spin-phonon coupling in vibrational Raman spectroscopy of the relevant phonons.

Before delving into further details of the calculations, we first give a brief review on the various candidate materials for the non-Kramers quantum spin ice, and try to indicate the most relevant class of materials that will be prospective candidates for realising our theoretical results.

4.2   A brief overview on the magnetism in non-Kramers rare-earth compounds

Possibly, the most striking example of non-Kramers rare-earth with substantial spin-lattice coupling is $Tb_2Ti_2O_7$ [28, 103, 105–110]. This material is particularly interesting for its very small onsite crystal field gap ($\sim$10 K) and recent neutron scattering experiments suggest that a vibronic bound state arises due to the coupling between acoustic phonon modes and crystal field levels which is absent in the high temperature regimes [105, 111]. However, the exact role of the excited states and the applicability of quantum spin ice physics are currently being debated. In fact, as we will discuss in the later in Chapter 6, these low-lying exctations can potentially lead to realisation of a very different kind of QSL in these frustrated magnets with new exotic excitations that do not conform the quasiparticles of a usual U(1) QSL. $Ho_2Ti_2O_7$, on the other hand, is a classical spin ice [104] with a large crystal field gap, although it is interesting to note that on integrating out the lattice vibrations, their linear coupling with the transverse spins can induce (presumably very weak) quantum tunneling terms within the classical spin ice.

The praseodymium pyrochlores, unlike the above extremes, belong to an interesting intermediate regime, where the crystal field gap is reasonably large, but quantum fluctuations are not insignificant [29]. Inelastic neutron scattering by Wen et al. reveals that the existence of quenched structural disorder in $Pr_2Zr_2O_7$ can act as a transverse field on the non-Kramers Pr^{3+} ion and might lift the degeneracy of the non-Kramers doublet [112], although X-ray diffraction does not show evidence of any structural distortions. More recently, magnetoelastic experiments on ultra-pure samples of $Pr_2Zr_2O_7$ show possibilities of substantial spin-phonon coupling and coupled spin-lattice dynamics [63, 113]. Further, high resolution Raman scattering on the same samples at relatively high temperatures (6 K-100 K) reveals that both the ground state and excited crystal field doublets show a temperature dependent splitting. The splitting grows more pronounced as temperature is increased and can be accounted for by the dynamical
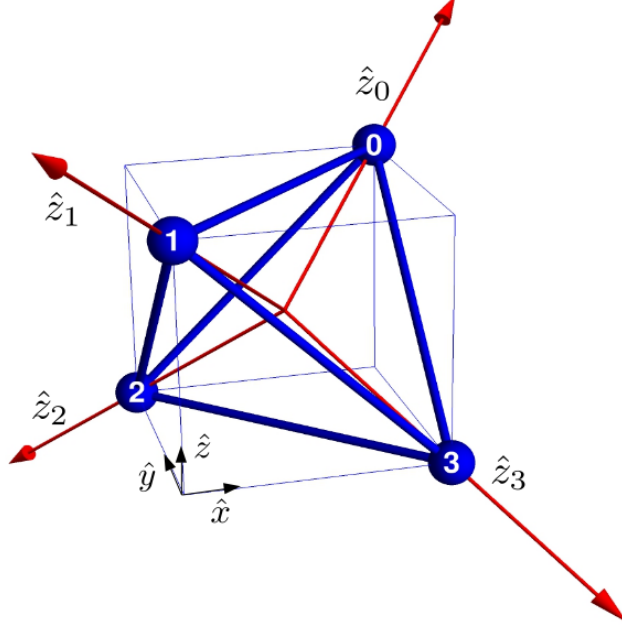
Figure 4.1: **Sublattices of an up tetrahedron:** 0,1,2,3 denote the four sublattices and $\hat{z}_0$, $\hat{z}_1$, $\hat{z}_2$, $\hat{z}_3$ represent the four respective local quantization axes (see Eq. B.2 in Appendix B.1.1).

coupling of spins to the phonons [63]. However, the Raman scattering in the much low temperature QSL regime still remains unexplored. Further experimental development in this area would be very interesting for the direct verification of our theoretical predictions.

Therefore, to be concrete, we build our theory using $Pr_2Zr_2O_7$ as an example, although the results are generically applicable to any non-Kramers quantum spin ice. In $Pr_2Zr_2O_7$, the magnetic ion is the rare-earth element Pr^{3+}, which is in the $4f^2$ electronic configuration. The ground state manifold is a doublet and given by [29, 102],

$$| \pm \rangle = a \, | \pm 4 \rangle \mp b \, | \pm 1 \rangle - c \, | \mp 2 \rangle \tag{4.2}$$

where the different states belong to the $J = 4$ multiplet, arising from the strong spin-orbit coupling, with $J^z \, | \, m \rangle = m \, | \, m \rangle$. Notably, characteristic to spin ice, the natural axis of quantization for the spins is along the local $[111]$ axis (see Fig. 4.1 and Appendix B.1.1). The ground state doublet is separated from the next crystal field state by almost 10 meV [29]. Due to this large gap, the low-temperature magnetic physics is dominated by the above non-Kramers doublet. The effective low-energy magnetic degrees of freedom are then obtained by projecting all the spin operators to the low-energy doublet manifold, and written in terms of the effective pseudo spin-$\frac{1}{2}$ operators as $s^\mu (\equiv \frac{1}{2}\sigma^\mu)$ [102].

A central feature of the doublets in Eq. 4.2 is that under time reversal ($\mathcal{T}$) they transform

as $|\pm\rangle \to |\mp\rangle$ such that the pseudo-spins transform as shown in Eq. 4.1.

4.2.1 The spin exchange physics of non-Kramers quantum spin ice

The pseudo-spins at different sites interact via regular spin exchanges and the minimal symmetry allowed spin Hamiltonian for non-Kramers spin ice is given by [24, 114, 115]

$$H_0 = \sum_{\langle ij \rangle} \left[J_{zz} s_i^z s_j^z - J_\pm (s_i^+ s_j^- + s_i^- s_j^+) \right] + \cdots \tag{4.3}$$

where $\cdots$ denote other symmetry allowed terms (including further neighbour ones) which do not immediately destabilise the QSL. In fact, their main effect in the QSL phase is to renormalise the dispersion of the excitations of the quantum spin ice [94, 116]. We neglect them here and their effects can be taken into account systematically along the lines discussed in the rest of this work.

Experiments reveal the exchange coupling to be strongly anisotropic ($J_{zz} \gg J_\pm$). Also, $J_{zz} \approx 1.6$K, [29] which is two orders of magnitude smaller than the single ion crystal field gap. This justifies the use of single ion crystal field states to treat the problem perturbatively.

Interestingly, the transformation of the non-Kramers doublet under $\mathcal{T}$ in Eq. 4.1 leads to an unusual Zeeman coupling in such materials. The external magnetic field, being odd under time reversal, can couple linearly only with s^z but not with s^x and s^y. The latter, however, can couple to the magnetic field quadratically. The complete onsite Zeeman Hamiltonian can be found in Ref. [58].

4.3 Non-Kramers rare earth and unusual magnetoelastic coupling

Having discussed the spin physics, we now turn to the linear magnetoelastic coupling in non-Kramers systems which is the central idea of this work. From the point of view of symmetry analysis, the structure of such a linear coupling is quite straightforward. For a single tetrahedron, the linear coupling can be obtained starting with the eight-dimensional vector space spanned by the time reversal even transverse components, (s_i^x, s_i^y), of the spins on four corners of a tetrahedron (see Fig. 4.1). This is then decomposed into the irreducible representations of the tetrahedral group, T_d, as [58]

$$\mathbf{e} \oplus \mathbf{t}_1 \oplus \mathbf{t}_2 \tag{4.4}$$

where e denotes the doublet and $\mathbf{t_1}$, $\mathbf{t_2}$ represent two triplets with different symmetry transformations (see Table B.1 in Appendix B.1.3). These irreducible operators are often characterised by their classical correlations [58], e.g., the e sector forms the ferroquadrupolar states, whereas $\mathbf{t_1}$ and $\mathbf{t_2}$ both forms two different antiferroquadrupolar states in case of non-Kramers pyrochlore. Similarly, the (optical) normal vibrational modes of bond distortions of a tetrahedron are decomposed as [117, 118],

$$\mathbf{a_1} \oplus \mathbf{e} \oplus \mathbf{t_2} \tag{4.5}$$

where $\mathbf{a_1}$ is the singlet. It is evident from the above decomposition that e and $\mathbf{t_2}$ vibrational (optical) modes of a tetrahedron can linearly couple to the transverse components of the non-Kramers doublet. Since the complete symmetry of the pyrochlore is $T_d \times \mathcal{I}$ (with $\mathcal{I}$ being the inversion), the complete representation is obtained by taking symmetric and antisymmetric combinations of the previous representations to form the 'g' and 'u' modes, which are even and odd under spatial inversion, respectively.

As Raman scattering is insensitive to inversion-odd modes, we only consider the $\mathbf{e_g}$ and $\mathbf{t_{2g}}$ modes. Hence, the symmetry allowed magnetoelastic coupling for the Raman active modes is given by

$$H_{sp}^{(e)} = \sum_{\mathbf{r},p=1,2} J_{sp}^{(e)} \zeta_{p,g}^{(e)}(\mathbf{r}) \left(Q_p^{(e)}(\mathbf{r}, A) + Q_p^{(e)}(\mathbf{r}, B) \right) \tag{4.6}$$

for the $\mathbf{e_g}$ modes and

$$H_{sp}^{(t_2)} = \sum_{\mathbf{r},p=1,2,3} J_{sp}^{(t_2)} \zeta_{p,g}^{(t_2)}(\mathbf{r}) \left(Q_p^{(t_2)}(\mathbf{r}, A) + Q_p^{(t_2)}(\mathbf{r}, B) \right) \tag{4.7}$$

for the $\mathbf{t_{2g}}$ modes. Here $\mathbf{r}$ denotes the centre of an up tetrahedron and A/B denotes the two sublattices of the underlying diamond lattice, dual to the pyrochlore. $Q_p^{(e)}(\mathbf{r}, A/B)$ and $Q_p^{(t_2)}(\mathbf{r}, A/B)$ respectively span the e and $\mathbf{t_2}$ irreducible sector for the spins. For a single up tetrahedron (see Fig. 4.1), they are given by

$$
\begin{aligned}
Q_1^{(e)} &= s_0^x + s_1^x + s_2^x + s_3^x \\
Q_2^{(e)} &= s_0^y + s_1^y + s_2^y + s_3^y
\end{aligned}
\tag{4.8}
$$

and

$$Q_1^{(t_2)} = \frac{1}{2}(-s_0^x + s_1^x + s_2^x - s_3^x)$$

$$Q_2^{(t_2)} = \frac{1}{4}(-s_0^x - s_1^x + s_2^x + s_3^x) + \frac{\sqrt{3}}{4}(s_0^y + s_1^y - s_2^y - s_3^y)$$

$$Q_3^{(t_2)} = \frac{1}{4}(s_0^x - s_1^x + s_2^x - s_3^x) + \frac{\sqrt{3}}{4}(s_0^y - s_1^y + s_2^y - s_3^y) \tag{4.9}$$

Finally, $\zeta_{p,g}^{(e)}(\mathbf{r})$ and $\zeta_{p,g}^{(t_2)}(\mathbf{r})$ are the $\mathbf{e_g}$ and $\mathbf{t_{2g}}$ normal modes of pyrochlore lattice. These normal modes are given by, $\zeta_{p,g}^{(\rho)}(\mathbf{k}) = b_{p,\mathbf{k}}^{(\rho)} + b_{p,-\mathbf{k}}^{(\rho)\dagger}$ where $b_{p,\mathbf{k}}^{(\rho)\dagger}$ is the creation operator of the phonons of the ρ irreducible representation, with the bare phonon Hamiltonian given by

$$H_\zeta = \sum_\rho \sum_{\mathbf{k},p} \omega_{\mathbf{k}}^{(\rho)} \left(b_{p,\mathbf{k}}^{(\rho)\dagger} b_{p,\mathbf{k}}^{(\rho)} + \frac{1}{2} \right). \tag{4.10}$$

The above linear coupling makes the non-Kramers spin ice materials susceptible to *spin Jahn-Teller* distortions, where the spin entropy can be quenched by distorting the lattice and thereby splitting the doublet. Indeed, in some samples of $Pr_2Zr_2O_7$, signatures of such splitting have been observed [112, 119], accompanied with random lattice distortions. However, more recent higher quality samples appear devoid of such distortions, suggesting controlled suppression of Jahn-Teller distortions in better quality single crystals [113]. In the absence of static deformation of the crystal field environment, the above linear spin-phonon coupling helps to enhance the transverse fluctuations in the spin ice manifold, which could stabilise a U(1) QSL phase in $Pr_2Zr_2O_7$ [113].

To further study the effects of the linear magnetoelastic coupling (Eq. 4.6 and Eq. 4.7) on quantum spin ice, we need to re-write the above spin-phonon coupling in terms of the coupling of the phonon to the low-energy excitations of the U(1) QSL. To derive this, for completeness we first give a briefl overview of the well-known mapping between the spins and low-energy gauge theory for quantum spin ice [12, 17, 19, 94].

4.4 A brief review of quantum spin ice

The description of the quantum spin ice is obtained starting with a magnetic monopole charge density operators [19, 94, 97] $\mathcal{Q}_\mathbf{r}$, defined at the centre of a tetrahedron at $\mathbf{r}$, as

$$\mathcal{Q}_\mathbf{r} = \eta_\mathbf{r} \sum_\mu s^z_{\mathbf{r}, \mathbf{r}+\eta_\mathbf{r}\mathbf{e}_\mu} \tag{4.11}$$

where, $\eta_\mathbf{r} = 1$ (-1) for $\mathbf{r} \in$ up (down) tetrahedra of the pyrochlore lattice and $\mathbf{e}_\mu$ is the vector connecting centres of the two nearest neighbour tetrahedra directed from up to down (see Appendix B.1.2). We call the positively charged particles monopoles and negatively charged ones antimonopoles. The creation operators for the monopoles with positive (negative) charge are defined as $\phi_\mathbf{r}^\dagger$ ($\phi_\mathbf{r}$) such that it satisfies, $[\mathcal{Q}_\mathbf{r}, \phi_{\mathbf{r}'}^\dagger] = \delta_{\mathbf{r}, \mathbf{r}'}\phi_\mathbf{r}^\dagger$, and it is subject to the hard-core constraint

$$\phi_\mathbf{r}^\dagger \phi_\mathbf{r} = 1 \tag{4.12}$$

arising from the spin-1/2 Hilbert space dimension of the non-Kramers doublet. The relation between the monopole and spin operators is given by

$$s^+_{\mathbf{r}, \mathbf{r}+\mathbf{e}_\mu} = \frac{1}{2}\phi_\mathbf{r}^\dagger \, e^{iA_{\mathbf{r},\mu}} \phi_{\mathbf{r}+\mathbf{e}_\mu} \tag{4.13}$$

where $\mathbf{r} \in$ up tetrahedron and $A_{\mathbf{r},\mu}$ represents the compact U(1) dual gauge field on the bond joining $\mathbf{r}$ and $\mathbf{r} + \mathbf{e}_\mu$ (In other words, they live on the links of the dual diamond lattice). The spin operators remain invariant under the following U(1) gauge transformation.

$$\phi_\mathbf{r} \to \phi_\mathbf{r} e^{-i\theta_\mathbf{r}}, \qquad A_{\mathbf{r},\mu} \to A_{\mathbf{r},\mu} + (\theta_{\mathbf{r}+\mathbf{e}_\mu} - \theta_\mathbf{r}) \tag{4.14}$$

The compactness of the gauge field allows for dual electric charge excitations [12] which are gapped in the QSL. Using the above mapping, the spin Hamiltonian of Eq. 4.3 can be written in terms of the gauge fields and monopoles to obtain the lattice gauge theory description of

quantum spin ice. This is given by

$$H_0 = \sum_{\mathbf{r}} \frac{J_{zz}}{2}(\mathcal{Q}_{\mathbf{r},A}^2 + \mathcal{Q}_{\mathbf{r},B}^2) - \frac{J_\pm}{4} \sum_{\mathbf{r},\mu \neq \nu} \phi_{\mathbf{r}+\mathbf{d}_\mu,B}^\dagger \, e^{i(A_{\mathbf{r},\nu} - A_{\mathbf{r},\mu})} \, \phi_{\mathbf{r}+\mathbf{d}_\nu,B}$$
$$- \frac{J_\pm}{4} \sum_{\mathbf{r},\mu \neq \nu} \phi_{\mathbf{r}-\mathbf{d}_\mu,A}^\dagger \, e^{i(A_{\mathbf{r}-\mathbf{d}_\mu,\mu} - A_{\mathbf{r}-\mathbf{d}_\nu,\nu})} \phi_{\mathbf{r}-\mathbf{d}_\nu,A} \quad (4.15)$$

where A, B denote two sublattices of the diamond lattice. $\mathbf{d}_\mu$s ($\mu = 1, 2, 3$) are the lattice vectors and $\mathbf{d_0} = 0$ (see Appendix B.1.2). Solving the above model, we obtain various excitations of the U(1) QSL, as we discuss in the following.

4.4.1 The gapless emergent photons

In the limit $J_{zz} \gg J_\pm$, the magnetic monopoles have a gap of $\mathcal{O}(J_{zz})$ and can be integrated out. The low-energy Hamiltonian is obtained in terms of the fluctuations of the dual U(1) gauge field $A_{\mathbf{r},\mu}$. This leads to the well-known ring-exchange Hamiltonian that can be obtained either via degenerate perturbation theory of Eq. 4.3 [12] or equivalently integrating out the magnetic monopoles from Eq. 4.15. This is given by

$$H_{eff} = \frac{U}{2} \sum_{\mathbf{r},\mu} B_{\mathbf{r},\mu}^2 - \frac{K}{2} \sum_{\bigcirc} \cos\left(\sum_{\mathbf{r},\mu \in \bigcirc} A_{\mathbf{r},\mu}\right) \quad (4.16)$$

where $B_{\mathbf{r},\mu}(= s_{\mathbf{r},\mathbf{r}+\mathbf{e}_\mu}^z, \mathbf{r} \in$ up tetrahedron) is the emergent magnetic field that is canonically conjugate to the dual vector potential, i.e., $[A_{\mathbf{r},\mu}, B_{\mathbf{r}',\nu}] = i\delta_{\mathbf{r},\mathbf{r}'}\delta_{\mu,\nu}$, U is a Lagrange multiplier imposing the half-integer constraint on magnetic fields, and $K \sim \frac{J_\pm^3}{J_{zz}^2}$. The emergent electric field is given by $\mathbf{E}_{\bigcirc} = \sum_{\mathbf{r},\mu \in \bigcirc} A_{\mathbf{r},\mu}$ where $\sum_{\mathbf{r},\mu \in \bigcirc}$ denotes the lattice curl around the hexagonal loops of the pyrochlore.

The QSL corresponds to the deconfined phase ($\mid K \mid \gg U$) of the above Hamiltonian. In this limit, the energy for the pure gauge theory can be minimized by setting up zero (π) electric flux through all the elementary hexagonal plaquettes for $K > 0$ ($K < 0$) [94]. These we shall term as *zero and π-flux phases, respectively, since the magnetic monopoles hopping on the diamond lattice (see below) see this electric flux.*

The low-energy excitations of the gauge theory can then be captured by expanding the *cosine* term up to quadratic order about these static electric flux configurations. This gives rise to a free Maxwell theory with two transverse polarised gapless photon excitations and their

dispersion is given by [64],

$$\varepsilon_{\mathbf{k}} = c_e \mid \mathbf{k} \mid \tag{4.17}$$

where $c_e = \sqrt{UK}$ is the speed of emergent light.

4.4.2 The gapped magnetic monopole

The dynamics of the bare magnetic monopoles, on the other hand can be obtained in a *gauge-mean-field* approximation of Eq. 4.15 by freezing the gauge fluctuation [19] (see Appendix B.2 for details).

For $K > 0$, the ground state of the pure gauge theory is in the zero electric flux sector (see above) where the gauge mean field ansatz can be chosen as $A_{\mathbf{r},\boldsymbol{\mu}} = 0$. The bare band structure for the two flavours (A and B) of magnetic monopoles is then given by [19]

$$\epsilon_{\mathbf{k}}^0 = \sqrt{2J_{zz}\left(\lambda - \frac{J_\pm}{2}\sum_{\mu>\nu}\cos\left(\mathbf{k}\cdot(\mathbf{d}_\mu - \mathbf{d}_\nu)\right)\right)} \tag{4.18}$$

where λ is a Lagrange multiplier introduced to take into account the unitary constraint of the monopole operators (see Appendix B.2.1) at the mean-field level.

For $K < 0$ on the other hand, the monopoles hop in a π-flux background per hexagonal plaquette. This can be implemented by choosing a suitable gauge [94] (also see Fig. B.1 in Appendix B.2) which doubles the size of magnetic unit cell, leading to four flavours of monopoles. The details of their band structure is summarized in Appendix B.2.2. In contrast to the zero flux phase, two non-degenerate bands (denoted as $\epsilon_+^\pi(\mathbf{k})$ and $\epsilon_-^\pi(\mathbf{k})$) appear due to the presence of non-trivial background flux. It will be shown in Sec. 4.6.2 that this leads to a very different Raman response of these two QSL phases.

The bare band structure of monopoles gets further renormalised due to the gauge fluctuations [120]. However, in the following discussion, we will assume the monopole-gauge coupling constant to be small, so that these only lead to a sub-leading corrections of the gauge mean field results (see Sec. 4.6.4). We shall comment on the merits/shortcomings of this approximation in the summary.

4.4.3 The gapped electric charge

The electric charges or the point defects of the gauge field appear due to the 2π ambiguity of defining the compact vector potential [12, 17]. The fluctuations of the electric field are not small near these excitations and the expansion of the *cosine* term (see Sec. 4.4.1) is not possible. Unlike the magnetic monopoles and the photons, these excitations are non-local in terms of the underlying spins and their properties are better captured in the dual description [12, 17, 18, 121] of the emergent gauge theory describing the bosonic electric charges, Ψ_r, hopping on the dual diamond lattice, r, via [17, 18]

$$H_{charge} = -\sum_{\langle r,r' \rangle} t\, e^{-i2\pi a_{r,r'}} \Psi_r^\dagger \Psi_{r'} + m \sum_r \Psi_r^\dagger \Psi_r \tag{4.19}$$

where $a_{r,r'}$ is the vector potential dual to $A_{r,\mu}$; t is the effective hopping strength and m is the chemical potential for the electric charges. The vector potential admits only integer values and is defined by,

$$(\nabla \times a_{r,r'})_{\bigcirc^*} = \sum_{rr' \in \bigcirc^*} a_{r,r'} = B_{r,\mu} - B^0_{r,\mu}$$

$\bigcirc^*$ denotes the dual elementary hexagonal plaquettes and $B^0_{r,\mu}$ is a static divergenceless background field. Since there is a single spin-$1/2$ on every pyrochlore site, the gauge field has a background π-flux in every dual hexagonal plaquette [18] such that in the gauge mean-field limit (where we ignore the fluctuations of $a_{r,r'}$ around the background), the dynamics of electric charges reduces to the problem of bosons hopping on the diamond lattice subject to the background π-flux in every hexagonal plaquette. This can be solved using a proper gauge choice and gives rise to 12 soft modes [17, 18]. We denote the soft modes as $\psi_i(i = 1, ..., 12)$. The energy gap of the electric charges, Δ_c, in the QSL phase is $\sim| J_\pm |^3 /J_{zz}^2$. Within the hopping model, Eq. 4.19, minimum gap of the electric charges is $\Delta_c = m - 2\sqrt{2}t$.

The band structure of the electric charges gets further renormalised due to the gauge fluctuations. Compared to magnetic monopoles, they have a much smaller energy gap, and hence on general grounds, their coupling with the emergent photon is expected to be relatively much stronger. However, in order to keep our analysis tractable, we neglect such effects within our gauge mean field approach and only take them into account perturbatively.
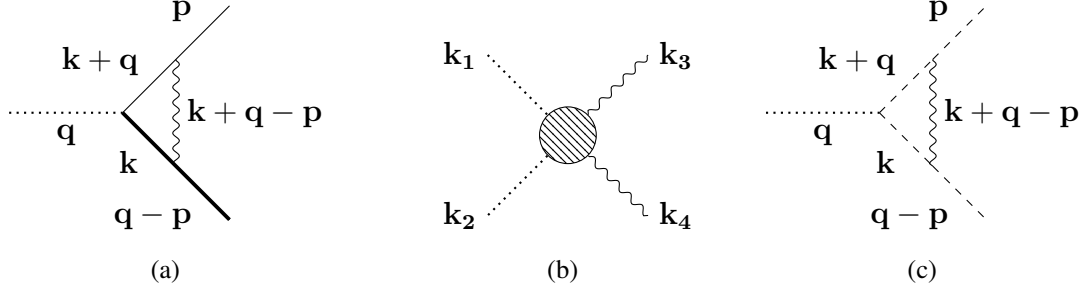
Figure 4.2: **Feynman diagrams for the interactions between the excitations of the quantum spin ice and the Raman active phonons in a non-Kramers system due to the linear spin-phonon coupling (Eqs. 4.6 and 4.7) :** (a) The vertex corresponds to the phonon-magnetic monopole interaction described by Eq. 4.20 and 4.21. Dotted, solid and curly line denote phonon, monopole and *emergent* photon, respectively. Thin and thick solid lines represent two flavours of monopoles, A and B, respectively. (b) Vertex for the phonon-(emergent) photon interaction described by Eq. 4.27. The circle represents the dipolar form factors (see Eq. 4.28) that makes the vertex gauge invariant. (c) Vertex for the phonon and electric charge interaction. The dashed line denotes the electric charge.

4.5 Magnetoelastic coupling in quantum spin ice

The effect of the magnetoelastic coupling in the QSL phase can be analyzed by studying the coupling of the phonon to the emergent excitations using the mapping from spins to gauge charges discussed above. For the linear coupling in Eqs. 4.6 and 4.7, the resultant interactions are given below.

4.5.1   The magnetic monopole-phonon coupling

Here we obtain the direct coupling between the phonon and the magnetic monopole. From Eq. 4.6, we get, for the $\mathbf{e_g}$ phonons :

$$H_{sp}^{(e)} = \frac{J_{sp}^{(e)}}{2} \sum_{\mathbf{r}} \sum_{\mu=0}^{3} \zeta_{-,g}^{(e)}(\mathbf{r}) \left[\phi_{\mathbf{r},A}^{\dagger} e^{iA_{\mathbf{r},\mu}} \phi_{\mathbf{r}+\mathbf{d_\mu},B} + \phi_{\mathbf{r}-\mathbf{d_\mu},A}^{\dagger} e^{iA_{\mathbf{r}-\mathbf{d_\mu},\mu}} \phi_{\mathbf{r},B} \right] + h.c. \qquad (4.20)$$

where, $\zeta_{\pm,g}^{(e)}(\mathbf{r}) = \zeta_{1,g}^{(e)}(\mathbf{r}) \pm i\zeta_{2,g}^{(e)}(\mathbf{r})$ are the displacement fields and from Eq. 4.7 for the $\mathbf{t_{2g}}$ phonons,

$$H_{sp}^{(t_2)} = \frac{J_{sp}^{(t_2)}}{2} \sum_{\mathbf{r}} \sum_{\mu=0}^{3} \sum_{p=1}^{3} \left(\zeta_{p,g}^{(t_2)}(\mathbf{r}) L_{p,x,\mu}^{(t_2)} - i\zeta_{p,g}^{(t_2)}(\mathbf{r}) L_{p,y,\mu}^{(t_2)} \right)$$
$$\times \left[\phi_{\mathbf{r},A}^{\dagger} e^{iA_{\mathbf{r},\mu}} \phi_{\mathbf{r}+\mathbf{d_\mu},B} + \phi_{\mathbf{r}-\mathbf{d_\mu},A}^{\dagger} e^{iA_{\mathbf{r}-\mathbf{d_\mu},\mu}} \phi_{\mathbf{r},B} \right] + h.c.$$
$$(4.21)$$

47
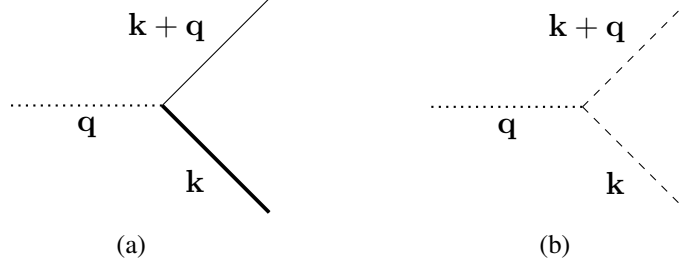
Figure 4.3: (a) Gauge mean field Feynman diagram for phonon and magnetic monopole interaction (described by Eqs. 4.22 and 4.23) in the zero flux phase and (b) phonon and electric charge interaction (described by Eq. 4.29).

The form factors $L_{p,\alpha,\mu}^{(t_2)}$ are obtained via the relation $Q_p^{(t_2)} = \sum_{\alpha=x,y} \sum_{\mu=0}^{3} L_{p,\alpha,\mu}^{(t_2)} s_\mu^\alpha$, their explicit forms can then follow from Eq. 4.9.

Both these interactions give rise to a Yukawa type coupling between the phonons and the monopole bilinear of the form $\zeta\phi^\dagger e^{iA}\phi$, albeit with different form factors. The corresponding bare vertex is shown in Fig. 4.2(a). It is clear from the interaction that the above coupling allows for a phonon to decay into a monopole-antimonopole pair: new low-energy scattering channels for the phonons inside the QSL phase open up. Note that while the bare monopole hopping preserves the sub-lattice flavour of the monopole, the above vertex mixes them, keeping only the total monopole number preserved.

Within gauge mean field theory, we assume that the gauge fluctuations are weak and can be taken into account perturbatively. Thus, within gauge mean field theory, the bare vertex for the magnetic monopole-phonon interaction is given by Fig. 4.3(a), where the gauge fluctuations have been neglected. Indeed, we shall show that within a perturbative treatment of the gauge field, the temperature dependence of the corrections due to gauge fluctuations are sub-leading compared to the mean-field results at low temperatures (see Sec. 4.6.4). In momentum space, gauge mean field vertices are given by

$$H_{sp}^{(e)} = \frac{J_{sp}^{(e)}}{2\sqrt{N}} \sum_{\mathbf{k},\mathbf{k}'} \left[(\alpha_{\mathbf{k}}^{(e)} + \alpha_{\mathbf{k}'}^{(e)})\zeta_{-,g}^{(e)}(\mathbf{k} - \mathbf{k}')\phi_{\mathbf{k},A}^\dagger \phi_{\mathbf{k}',B} + h.c. \right] \tag{4.22}$$

$$H_{sp}^{(t_2)} = \frac{J_{sp}^{(t_2)}}{2\sqrt{N}} \sum_{\mathbf{k},\mathbf{k}'} \sum_{p=1}^{3} \left[(\alpha_{p,\mathbf{k}}^{(t_2)} + \alpha_{p,\mathbf{k}'}^{(t_2)})\zeta_{p,g}^{(t_2)}(\mathbf{k} - \mathbf{k}')\phi_{\mathbf{k},A}^\dagger \phi_{\mathbf{k}',B} + h.c. \right] \tag{4.23}$$

where N is the total number of unit cells, while $\alpha_{\mathbf{k}}^{(e)}$ and $\alpha_{p,\mathbf{k}}^{(t_2)}$s are vertex functions of the $\mathbf{e_g}$

and t_{2g} coupling, respectively, whose forms are given by,

$$
\begin{aligned}
\alpha_{\mathbf{k}}^{(e)} &= \frac{1}{2} \sum_{\mu} e^{i\mathbf{k}\cdot\mathbf{d}_{\mu}} \\
\alpha_{1,\mathbf{k}}^{(t_2)} &= \frac{1}{4}\left(-e^{i\mathbf{k}\cdot\mathbf{d_0}} + e^{i\mathbf{k}\cdot\mathbf{d_1}} + e^{i\mathbf{k}\cdot\mathbf{d_2}} - e^{i\mathbf{k}\cdot\mathbf{d_3}}\right) \\
\alpha_{2,\mathbf{k}}^{(t_2)} &= \frac{e^{i\frac{\pi}{3}}}{4}\left(-e^{i\mathbf{k}\cdot\mathbf{d_0}} - e^{i\mathbf{k}\cdot\mathbf{d_1}} + e^{i\mathbf{k}\cdot\mathbf{d_2}} + e^{i\mathbf{k}\mathbf{d_3}}\right) \\
\alpha_{3,\mathbf{k}}^{(t_2)} &= \frac{e^{-i\frac{\pi}{3}}}{4}\left(e^{i\mathbf{k}\cdot\mathbf{d_0}} - e^{i\mathbf{k}\cdot\mathbf{d_1}} + e^{i\mathbf{k}\cdot\mathbf{d_2}} - e^{i\mathbf{k}\cdot\mathbf{d_3}}\right)
\end{aligned}
\tag{4.24}
$$

4.5.2 The (emergent) photon-phonon coupling

To obtain the coupling between phonon and emergent photon, once again we integrate out the gapped magnetic monopoles (as in Sec. 4.4.1) in presence of the magnetoelastic coupling described by Eq. 4.20 and 4.21. The leading coupling between phonon and gauge field is obtained in fourth-order of the perturbation theory [122]. For the e_g phonons, this gives rise to

$$
H_{phonon-photon} = -\frac{J_{sp}^{(e)2} J_{\pm}^2}{2 J_{zz}^3} \sum_{\bigcirc} \left(\sum_{\mathbf{r}\in\Diamond} \boldsymbol{\zeta}_g^{(e)}(\mathbf{r}) \cdot \boldsymbol{\zeta}_g^{(e)}(\mathbf{r}) \right) \cos\left[\mathbf{E}_{\bigcirc}\right]
\tag{4.25}
$$

A similar treatment for the t_{2g} phonons is possible starting from Eq. 4.7, leading to similar results as for the eg phonons, and hence not presented explicitly. In the deconfined QSL phase, the *cosine* term in the above Hamiltonian can be expanded up to quadratic order as $\cos \mathbf{E} \approx 1 - \mathbf{E}^2/2$. At low energies, the constant term in the expansion leads to a quadratic term in the phonon. This renormalises the frequency of the phonon by a constant shift without affecting its linewidth.

The leading order coupling between the phonon and the emergent photon, in the continuum limit is given by

$$
\mathcal{H}_{phonon-photon} = J_{ph-ph} \int d^3\mathbf{r}\, \boldsymbol{\zeta}_g^{(e)}(\mathbf{r}) \cdot \boldsymbol{\zeta}_g^{(e)}(\mathbf{r})\, \mathbf{E}^2(\mathbf{r})
\tag{4.26}
$$

where $J_{ph-ph} \sim \frac{J_{sp}^{(e)2} J_{\pm}^2}{4 J_{zz}^2 l^3}$ with l being the lattice length-scale. As expected, the phonons cannot simply couple to the dual gauge field since they do not carry the emergent gauge charge. Instead, they couple to the gauge invariant electric field. Further, since the Raman active phonons are even under inversion, they can only couple to the electric field at quadratic order. We note,

in passing, that the antisymmetric phonon modes ('u' modes) on the other hand are allowed to couple linearly to the emergent electric field. Such interaction effects can be probed using infrared spectroscopy [122, 123].

In momentum space, Eq. 4.26 takes the form

$$\mathcal{H}_{phonon-photon} = \int \prod_{i=1}^{4} d^3\mathbf{k}_i \, \mathcal{G}^{\alpha\beta}(\mathbf{k_1}, \mathbf{k_2}, \mathbf{k_3}, \mathbf{k_4}) \left(\boldsymbol{\zeta}_g^{(e)}(\mathbf{k_1}) \cdot \boldsymbol{\zeta}_g^{(e)}(\mathbf{k_2}) \right) A_{\mathbf{k_3}}^{\alpha} A_{\mathbf{k_4}}^{\beta} \quad (4.27)$$

where the interaction vertex is given by

$$\mathcal{G}^{\alpha\beta}(\mathbf{k_1}, \mathbf{k_2}, \mathbf{k_3}, \mathbf{k_4}) = \frac{J_{ph-ph}}{N} \left[-\mathbf{k_3} \cdot \mathbf{k_4} \delta_{\alpha\beta} + k_3^{\beta} k_4^{\alpha} \right] \delta(\mathbf{k_1} + \mathbf{k_2} + \mathbf{k_3} + \mathbf{k_4}) \quad (4.28)$$

The above interaction is shown in Fig. 4.2(b), where the circle represents the gauge invariant dipolar vertex function, $\mathcal{G}^{\alpha\beta}$. Such decay processes for phonons in a QSL phase give rise to an additional contribution to the phonon linewidth similar to that due to the monopoles, albeit at a different energy-scale.

4.5.3   The electric charge-phonon coupling

Similar to the phonon-magnetic monopole coupling, the phonons also interact with the electric charges via a Yukawa coupling as shown in Fig. 4.2(c) (again, the electric charge creation/annihilation operators are not gauge invariant and hence cannot couple to the phonons linearly).

To derive the coupling between the phonons and the electric charges, we construct the bilinears of the soft electric charge modes with appropriate symmetry that can couple to a particular polarisation of the phonon. Here we analyse only the $\mathbf{e_g}$ couplings and the interaction is given by,

$$H_{phonon-charge} = J_{ph-ch}^{(e)} \sum_{\mathbf{r}} \left(\zeta_{1,g}^{(e)}(\mathbf{r})\Theta_1(\mathbf{r}) + \zeta_{2,g}^{(e)}(\mathbf{r})\Theta_2(\mathbf{r}) \right) \quad (4.29)$$

where (Θ_1, Θ_2) forms an $\mathbf{e_g}$ doublet and is given by,

$$\Theta_1 = \psi_1^*\psi_1 + \psi_{11}^*\psi_{11} - \psi_3^*\psi_3 - \psi_9^*\psi_9$$
$$\Theta_2 = -\psi_1^*\psi_1 - \psi_{11}^*\psi_{11} - \psi_3^*\psi_3 - \psi_9^*\psi_9 + 2(\psi_5^*\psi_5 + \psi_7^*\psi_7) \quad (4.30)$$
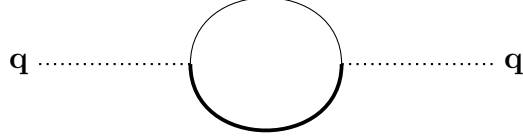
Figure 4.4: Self-energy of the phonon due to the phonon-magnetic monopole interaction (see Fig. 4.3(a))

where ψ_i $(i = 1, 2, \cdots 12)$ are the soft modes of the electric charges as obtained in Ref. [18] and discussed in the previous section. The above interaction is shown in Fig. 4.3(b). A similar kind of coupling between $\mathbf{t_{2g}}$ phonons and electric charges can be obtained via symmetry analysis. However, such coupling produces similar kind of Raman response as $\mathbf{e_g}$ phonons, and is not considered here separately.

Due to the above magnetoelastic coupling, phonons acquire a finite lifetime by scattering with the excitations of the QSL. In the next three sections (Sec. 4.6, 4.7 and 4.8), we compute the lifetime of the phonons and their typical low-temperature behaviour in order to probe the non-Kramers U(1) QSLs.

4.6 Self-energy of the phonon due to phonon-magnetic monopole coupling

We now calculate the self-energy of the phonons and hence the broadening of the phonon peaks due to the phonon-monopole interaction. We calculate the effect of the coupling in a perturbative approach both in the zero and π-flux phases.

4.6.1 Zero flux phase

The first non-zero contribution to the self-energy comes at second order, $\mathcal{O}(J_{sp}^{(\rho)2})$, by computing the bubble diagram of Fig. 4.4. Within gauge mean field theory, for the zero flux phase, the self-energy is given by,

$$\Sigma_{\zeta^{(\rho)}}^0(\mathbf{q}, i\Omega) = -\frac{J_{sp}^{(\rho)2}}{4N\beta} \sum_{\mathbf{k},\omega} \mid \alpha_{\mathbf{k}}^{(\rho)} + \alpha_{\mathbf{k+q}}^{(\rho)} \mid^2 G_\phi^0(\mathbf{k}, A, i\omega) G_\phi^0(\mathbf{k} + \mathbf{q}, B, i(\omega + \Omega)) \quad (4.31)$$

where the time ordered Green's function (G_ϕ^0) for monopoles in the zero flux phase is defined as (see Eq. B.9 in Appendix B.2.1),

$$G_\phi^0(\mathbf{k}, A/B, i\omega) = \int_0^\beta d\tau \langle \hat{\mathcal{T}} \left(\phi_{\mathbf{k},A/B}(\tau) \phi_{\mathbf{k},A/B}^\dagger(0) \right) \rangle e^{i\omega\tau} = \frac{2J_{zz}}{\omega^2 + (\epsilon_{\mathbf{k}}^0)^2} \quad (4.32)$$

51

To obtain the broadening of the Raman peaks, we calculate the imaginary part of $\Sigma^0_{\zeta(\rho)}(\mathbf{q}, i\Omega \rightarrow \Omega + i\delta)$. Performing the frequency summation using standard Matsubara summation techniques [124], we get

$$
\begin{aligned}
\lim_{\delta \rightarrow 0} \mathcal{I}m[\Sigma^0_{\zeta(\rho)}(\mathbf{q}, \Omega + i\delta)] =& \frac{\pi J_{sp}^{(\rho)2} J_{zz}^2}{4N} \sum_{\mathbf{k}} \mid \alpha_{\mathbf{k}}^{(\rho)} + \alpha_{\mathbf{k+q}}^{(\rho)} \mid^2 \\
& \times \left[\frac{n(\epsilon_{\mathbf{k}}^0) - n(\epsilon_{\mathbf{k+q}}^0)}{\epsilon_{\mathbf{k}}^0 \epsilon_{\mathbf{k+q}}^0} \Big(\delta(\Omega + \epsilon_{\mathbf{k+q}}^0 - \epsilon_{\mathbf{k}}^0) - \delta(\Omega + \epsilon_{\mathbf{k}}^0 - \epsilon_{\mathbf{k+q}}^0) \Big) \right. \\
& \left. + \frac{n(\epsilon_{\mathbf{k}}^0) + n(\epsilon_{\mathbf{k+q}}^0) + 1}{\epsilon_{\mathbf{k}}^0 \epsilon_{\mathbf{k+q}}^0} \Big(\delta(\Omega + \epsilon_{\mathbf{k}}^0 + \epsilon_{\mathbf{k+q}}^0) - \delta(\Omega - \epsilon_{\mathbf{k}}^0 - \epsilon_{\mathbf{k+q}}^0) \Big) \right]
\end{aligned}
$$

$$(4.33)$$

where, $n(\epsilon_{\mathbf{k}}^0) = \frac{1}{e^{\beta\epsilon_{\mathbf{k}}^0} - 1}$ is the Bose occupation for the magnetic monopole with $\epsilon_{\mathbf{k}}^0$ being the single-particle dispersion within gauge mean field theory as given by Eq. 4.18.

The first two delta functions of Eq. 4.33 imply processes where a monopole scatters by absorption of a phonon (*absorption* process). The prefactor $(n(\epsilon_{\mathbf{k}}^0) - n(\epsilon_{\mathbf{k+q}}^0))$ represents the net probability of such processes. On the other hand, the last two delta functions in Eq. 4.33 arise due to the conversion of a phonon into a monopole-antimonopole pair or vice-versa (*pair production* process, Fig. 4.7(b)). The prefactor $(1 + n(\epsilon_{\mathbf{k}}^0) + n(\epsilon_{\mathbf{k+q}}^0))$ represents the net probability of two competing processes- the first(second) is the annihilation (creation) of a phonon followed by creation (annihilation) of the monopole-antimonopole pair.

Eq. 4.33 is one of the central results of this work. It shows that the self-energy correction of the phonons arises from its coupling to the magnetic monopoles. We now analyse the self-energy, in particular, its frequency dependence, which can be detected in Raman scattering experiments. For Raman scattering, only the $\mathbf{q} \approx 0$ regime of the Brillouin zone is accessible. In this limit, clearly the probability of the absorption process of the phonons vanishes since the difference of the two Bose factors go to zero as $\mathbf{q} \rightarrow 0$, leading to

$$
\begin{aligned}
\Gamma(\Omega, T) =& 2 \mid \mathcal{I}m[\Sigma^0_{\zeta(\rho)}(\mathbf{q} = 0, \Omega)] \mid \\
=& \frac{2\pi J_{sp}^{(\rho)2} J_{zz}^2}{N} \sum_{\mathbf{k}} \mid \alpha_{\mathbf{k}}^{(\rho)} \mid^2 \left[\frac{2n(\epsilon_{\mathbf{k}}^0) + 1}{(\epsilon_{\mathbf{k}}^0)^2} \mid \Big(\delta(\Omega + 2\epsilon_{\mathbf{k}}^0) - \delta(\Omega - 2\epsilon_{\mathbf{k}}^0) \Big) \mid \right] \quad (4.34)
\end{aligned}
$$

From Eq. 4.18, we see that the bare monopole band structure is gapped with its minima

at $\mathbf{k} = 0$ and the energy gap, $\Delta_0 = \sqrt{2J_{zz}(\lambda - 3J_\pm)}$. It is evident from Eq. 4.34 that the splitting of phonons into a monopole-antimonopole pair occurs only if the phonon frequency is larger than the pair creation energy ($2\Delta_0$) such that $\Gamma \sim \Theta(|\Omega| - 2\Delta_0)$. This is visible in Fig. 4.5, where we plot the linewidth, $\Gamma(\Omega, T)$ versus the frequency, Ω, for various temperatures, T, for both the $\mathbf{e_g}$ and the $\mathbf{t_{2g}}$ modes, for $\Delta_0 = 1.26 J_{zz}$ as an illustrative example for plotting. The profile of the curve remains qualitatively same as long as the constraint $\lambda > 3J_\pm$ is satisfied, which defines the extent of the QSL. Apart from the dependence on the form factors, $\alpha_{\mathbf{k}}^{(\rho)}$, and the Bose factor, both these curves reflects the two-particle density of states profile of monopoles, shown in the inset of Fig. 4.5(b). The effect of the form factors can be noted from the qualitative difference of the two plots. Since $\alpha_{\mathbf{k}}^{(t_2)} \to 0$ as $\mathbf{k} \to 0$ (from Eq. 4.24), the linewidth for $\mathbf{t_{2g}}$ smoothly vanishes for $\Omega \to 2\Delta_0$. By contrast, for $\mathbf{e_g}$, the vertex function $(\alpha_{\mathbf{k}}^{(e)})$ tends to a nonzero constant as $\mathbf{k} \to 0$ (from Eq. 4.24) and the linewidth shows a sharp behaviour even at zero momentum.

4.6.2 $\pi-$flux phase

The phonon-magnetic monopole coupling in the $\pi-$flux phase is obtained from the linear spin-phonon coupling of Eq. 4.6 and Eq. 4.7 via parton decomposition of the spins and freezing the gauge fluctuations to a suitable gauge mean field ansatz as described in Sec. 4.4.2. Focusing only on the $\mathbf{e_g}$ phonons, the phonon-monopole coupling is given by,

$$H_{sp}^{(e)} = \frac{J_{sp}^{(e)}}{2\sqrt{N}} \sum_{\mathbf{k}} \sum_{\mu,\nu=1,2} \left(M_{\mathbf{k}}^{\mu\nu} \zeta_{-,g}^{(e)}(\mathbf{q} = 0) \phi_{\mathbf{k},A\mu}^\dagger \phi_{\mathbf{k},B\nu} + h.c. \right) \tag{4.35}$$

The details of the vertex functions $M_{\mathbf{k}}^{\mu\nu}$ are given in Appendix B.4.1. The Feynman diagram of the above interaction is again represented by the Yukawa vertex which is very similar to Fig. 4.3(a) except for the fact that *four* distinct diagrams are possible due to the extended sublattice structure. The phonon self-energy in this phase is given by,

$$\Sigma_{\zeta^{(e)}}^\pi(\mathbf{q} = 0, i\Omega) = -\frac{J_{sp}^{(e)2}}{4N\beta} \sum_{\mathbf{k},\omega} \sum_{\mu,\nu,\alpha,\beta} M_{\mathbf{k}}^{\mu\alpha} M_{-\mathbf{k}}^{\nu\beta} \left[G_\phi^\pi \right]_{\mu\nu}(\mathbf{k}, A, i\Omega + i\omega) \left[G_\phi^\pi \right]_{\alpha\beta}(\mathbf{k}, B, i\omega)$$

$$\tag{4.36}$$
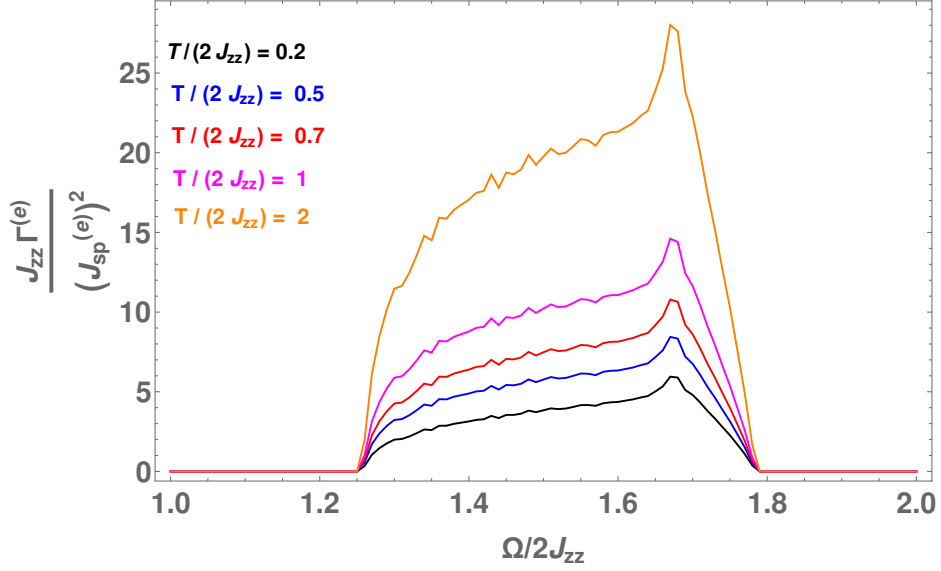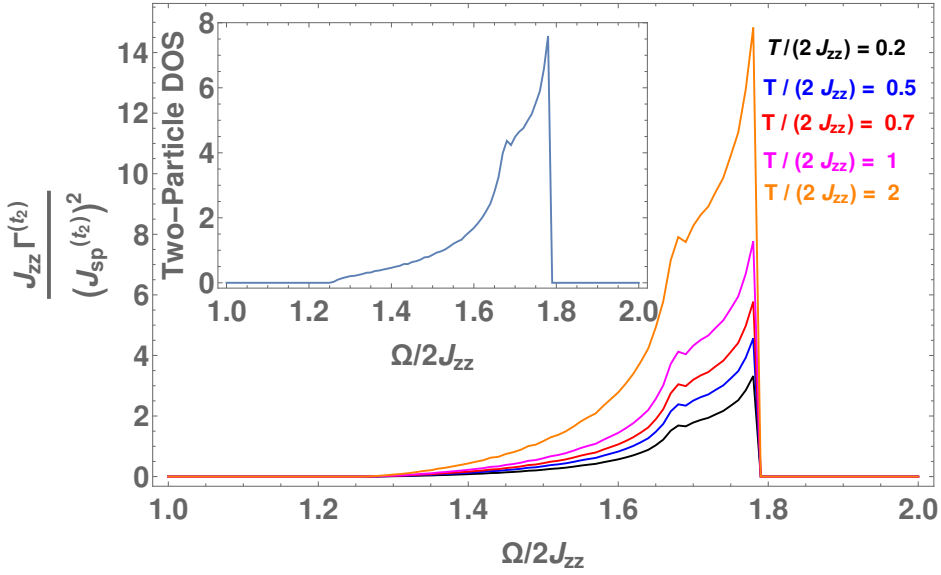
Figure 4.5: **Frequency dependence of linewidth of (a) e$_\mathbf{g}$ and (b) t$_\mathbf{2g}$ phonons in the zero flux phase due to the phonon-magnetic monopole coupling:** For both plots, we have chosen $\frac{\lambda}{2J_{zz}} = 0.7$ and $\frac{J_\pm}{2J_{zz}} = 0.1$ for illustrative purpose. The inset of (b) shows the two-particle density of states (DOS) of magnetic monopoles for the same values of $\lambda/2J_{zz}$ and $J_\pm/2J_{zz}$.

where, $[G_\phi^\pi]_{\mu\nu}(\mathbf{k}, A/B, i\omega)$ is the Green's function for the A/B monopoles in the π-flux phase (see Eq. B.16 in Appendix B.2.2 for the detailed expressions). Computing the imaginary part of the above expression, we obtain the linewidth of the phonons in the $\pi-$flux phase. The contribution where the phonon splits into two monopoles, is given by,

$$
\begin{aligned}
\Gamma(\Omega, T) \\
= \frac{\pi J_{sp}^{(e)2}}{2N} \sum_{\mathbf{k}} \Bigg[& \frac{1 + 2n(\epsilon_+^\pi(\mathbf{k}))}{\epsilon_+^\pi(\mathbf{k})^2} \mathcal{P}_1(\mathbf{k}) \delta\left(\Omega - 2\epsilon_+^\pi(\mathbf{k})\right) + \frac{1 + 2n(\epsilon_-^\pi(\mathbf{k}))}{\epsilon_-^\pi(\mathbf{k})^2} \mathcal{P}_2(\mathbf{k}) \delta\left(\Omega - 2\epsilon_-^\pi(\mathbf{k})\right) \\
& + (\mathcal{P}_3(\mathbf{k}) + \mathcal{P}_4(\mathbf{k})) \left(\frac{1 + n(\epsilon_+^\pi(\mathbf{k})) + n(\epsilon_-^\pi(\mathbf{k}))}{\epsilon_+^\pi(\mathbf{k})\epsilon_-^\pi(\mathbf{k})} \delta\left(\Omega - \epsilon_+^\pi(\mathbf{k}) - \epsilon_-^\pi(\mathbf{k})\right) \right. \\
& \left. + \frac{n(\epsilon_+^\pi(\mathbf{k})) - n(\epsilon_-^\pi(\mathbf{k}))}{\epsilon_+^\pi(\mathbf{k})\epsilon_-^\pi(\mathbf{k})} \delta\left(\Omega + \epsilon_+^\pi(\mathbf{k}) - \epsilon_-^\pi(\mathbf{k})\right) \right) \Bigg]
\end{aligned}
$$

$$(4.37)$$

where, $\mathcal{P}_1(\mathbf{k}), \mathcal{P}_2(\mathbf{k}), \mathcal{P}_3(\mathbf{k}), \mathcal{P}_4(\mathbf{k})$ are real functions of momentum whose detailed forms are given by Eq. B.23 in Appendix B.4.2 and $\epsilon_\pm^\pi(\mathbf{k})$ are the bare monopole dispersions in the π-flux phase as discussed above. The detailed forms are given by Eq. B.13 and B.14 in Appendix B.2.2.

The above expression should be contrasted with that for zero flux (Eq. 4.34). There are four distinct delta functions appearing in the expressions. The first two terms are closely related to the two-particle density of states for the $\epsilon_+^\pi(\mathbf{k})$ and $\epsilon_-^\pi(\mathbf{k})$ bands, implying the decay of a phonon into monopole-antimonopole pair with respective energy in the two bands, $\pm$. On the other hand, the last two entries represent the processes where a phonon scatters into monopole-antimonopole pair of different energy bands. Consequently, unlike the zero flux case, both the pair production and absorption processes show non-zero amplitude even at $\mathbf{q} = 0$.

In Fig. 4.6, we plot various contributions to the two-particle density of states of magnetic monopoles in the $\pi-$flux phase, which represent the four distinct delta functions of Eq. 4.37. The phonon linewidth is obtained from the sum of these delta functions weighted by appropriate momentum dependent form factors ($\mathcal{P}_1(\mathbf{k}), \mathcal{P}_2(\mathbf{k}), \mathcal{P}_3(\mathbf{k}), \mathcal{P}_4(\mathbf{k})$) and the Bosonic distribution functions at finite temperature. It is evident from the figure that, unlike the zero flux case, the Raman linewidth shows a non-zero signal even at very low energy compared to the monopole gap. Availability of the two non-degenerate bands allow a non-zero probability of the process where a monopole (say with energy $\epsilon_-^\pi(\mathbf{k})$) absorbs the phonon and converts into another monopole of different band structure ($\epsilon_+^\pi(\mathbf{k})$) even at $\mathbf{q} = 0$. Also, the enlargement
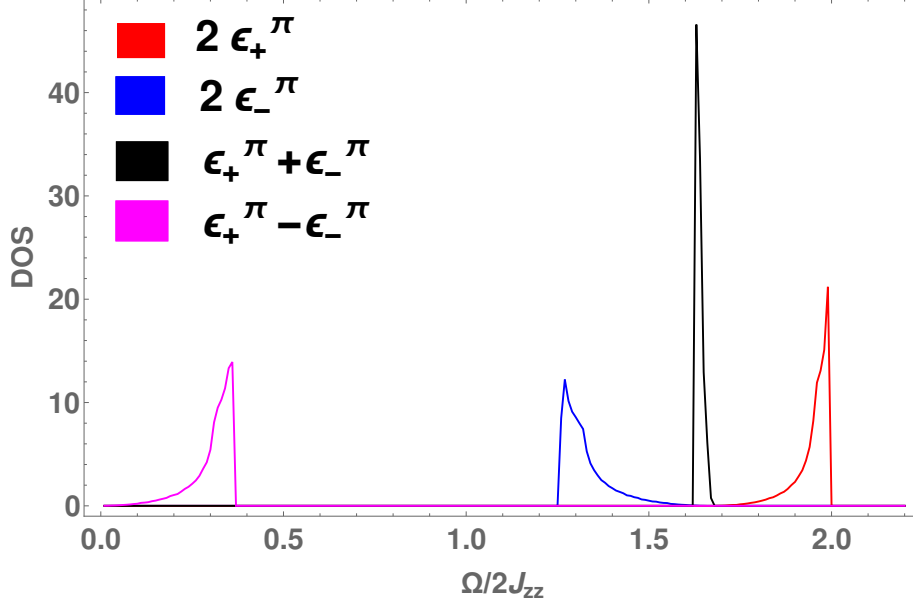
Figure 4.6: **Density of states of different bands contributing to the phonon linewidth in the π-flux phase:** We have chosen $\lambda/2J_{zz} = 0.7$, $J_{\pm}/2J_{zz} = 0.3$ for illustrative purpose. Red and blue curves denote the two-particle density of states for upper(ϵ_+^π) and lower(ϵ_-^π) bands, respectively. Black and magenta curves denote density of states of $\epsilon_+^\pi + \epsilon_-^\pi$ and $\epsilon_+^\pi - \epsilon_-^\pi$, respectively.

of the magnetic unit cell compared to that of the zero flux case– leading to the momentum fractionalisation– is very well captured in such a Raman response profile, which is a signature of the non-trivial projective implementation of symmetry. Hence, the phonon linewidth measurements via Raman experiments can be an extremely useful tool to identify the non-trivial projective symmetry group of a QSL phase.

4.6.3 A correspondence between the phonon-monopole scattering and the scattering processes in QCD

At this point, we would like to note that probing the magnetic monopoles of the QSL via the Raman scattering of the phonons in zero and π-flux phase is quite similar to– (a) high energy pair production (Fig. 4.7(a)), and, (b) the *deep inelastic scattering* [125, 126] of quarks in quantum chromodynamics (QCD) by the leptons, respectively, as described by the standard model of high-energy particle physics (Fig. 4.7(c)). The corresponding two relevant vertices are shown side-by-side in Fig. 4.7(b) and (d), respectively for comparison. In QCD, the quarks become asymptotically free at high energies and the high energy lepton can then probe them on sub-hadron length-scales [127, 128]. In a QSL, however, the non-trivial entanglement leading to fractionalised novel excitations is a low-energy/long-wavelength emergent phenomenon which the phonons probe via "shallow" inelastic scattering.

(a) High energy pair production

(b) Pair Production in quantum spin ice

(c) Deep Inelastic scattering of hadrons

(d) Shallow inelastic scattering in quantum spin ice
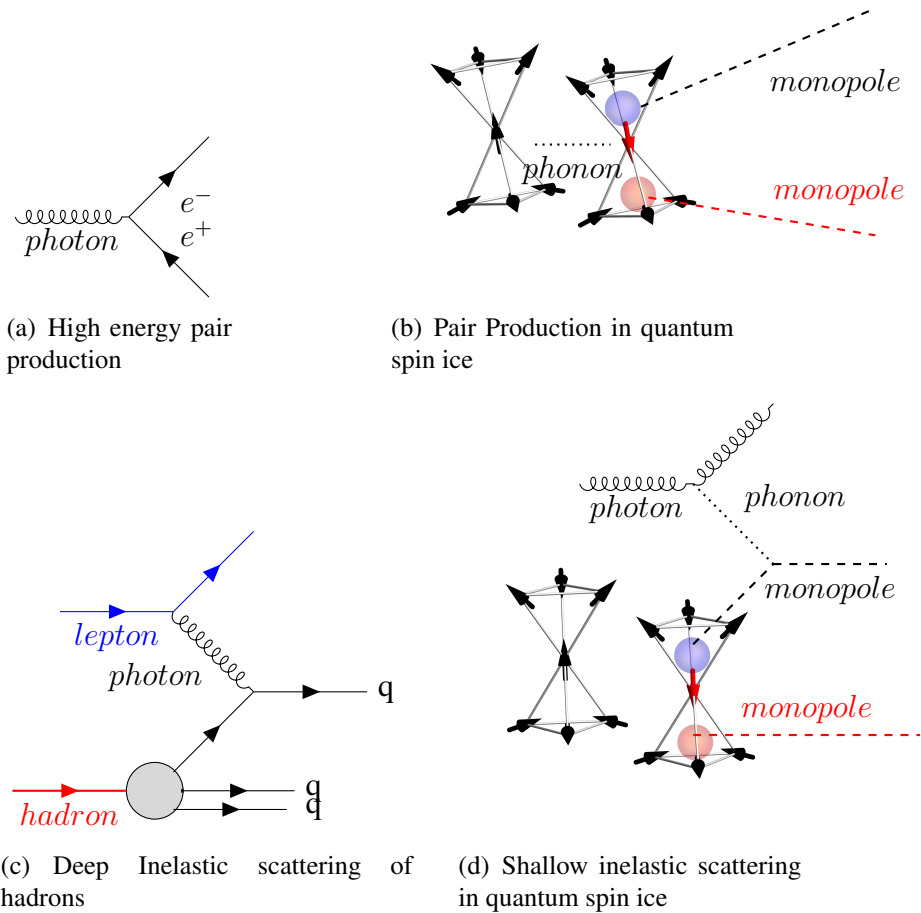
Figure 4.7: **Correspondence of scattering diagrams**: (a) The high energy photon can lead to creation of a positron and an electron via pair production, (b) In non-Kramers quantum spin ice, the phonon flips a spin and creates two magnetic monopoles of opposite charges, (c) In deep inelastic scattering, a photon emitted from a lepton scatters off a parton, a quark q, contained in the hadron, a $q\bar{q}$-pion as a free particle at high energies, and (d) In shallow inelastic scattering, an optical phonon emitted from a photon scatters off a parton, a magnetic monopole or electric charge, emerging from the spin degrees of freedom from fractionalisation at low energies.

4.6.4   Beyond gauge mean field theory : Gauge fluctuations

Coming back to the calculations of Raman cross-section, we note that the previous results (described by Eqs. 4.34 and 4.37) was obtained within gauge mean field theory neglecting the gauge fluctuations. We now consider the effect of long-wavelength gauge fluctuations within a weak-coupling approach for the emergent electrodynamics. At present, it is not clear that such a weak-coupling approach is valid for treating the gauge fluctuations. In fact the coupling parameter– the fine structure constant– for the emergent electrodynamics is generically expected to be sizeable. However, recent numerical calculations [120] on quantum spin ice (via Eq. 4.16) suggest that the emergent fine-structure constant is $\lesssim 0.1$ which may suggest that the perturbative expansion could still provide an estimate of the effect of gauge fluctuations.

For the zero flux case, this is captured by the expansion, $e^{\pm iA_{\mathbf{r},\mu}} \approx (1 \pm iA_{\mathbf{r},\mu})$. Hence, (from Eq. 4.15) the interaction between monopole and gauge field is given by,

$$H_{GF} = \frac{iJ_\pm}{4\sqrt{N}} \sum_{\mathbf{k},\mathbf{k}',\mu\neq\nu} \left[\gamma_B^{\mu\nu}(\mathbf{k},\mathbf{k}') A_{\mathbf{k}-\mathbf{k}',\mu} \phi_{\mathbf{k},B}^\dagger \phi_{\mathbf{k}',B} + \gamma_A^{\mu\nu}(\mathbf{k},\mathbf{k}') A_{\mathbf{k}-\mathbf{k}',\mu} \phi_{\mathbf{k},A}^\dagger \phi_{\mathbf{k}',A} \right] \quad (4.38)$$

where $A_{\mathbf{k},\mu} = \frac{1}{\sqrt{N}} \sum_{\mathbf{r}\in I} A_{\mathbf{r},\mu} e^{i\mathbf{k}\cdot\mathbf{r}}$. The details of the vertex functions, $\gamma_{A/B}^{\mu\nu}(\mathbf{k},\mathbf{k}')$, are given in Appendix B.5 for the zero flux phase. The π-flux phase can be treated in a similar way. There are two (related by Ward identities) effects of the gauge fluctuations– renormalisation of the vertex (Fig. 4.2(a)) and renormalisation of the monopole propagator (Fig. 4.8)– which we discuss in turn.

In presence of such gauge fluctuations, the vertex functions for the bare phonon-monopole interactions get dressed via the virtual photon exchange processes as described by Fig. 4.2(a). This effect can be taken into account by calculating the modified vertices, $\alpha_{\mathbf{k}}^{(\rho)} + \delta\alpha_{\mathbf{k}}^{(\rho)}$. We compute the leading order corrections by expanding the bare monopole energy about the band minima at $\mathbf{k} = 0$ (Eq. B.28). Similarly, all the bare vertex functions ($\alpha_{\mathbf{k}}^{(e)}, \alpha_{\mathbf{k}}^{(t_2)}, \gamma_{A/B}^{\mu\nu}(\mathbf{k},\mathbf{k}')$) are also Taylor expanded in polynomials of momentum and only the leading terms are considered. We note that the terms with higher powers of momentum contribute to more sub-leading (in temperature) corrections to the mean-field vertices at low temperatures. With the above approximations, the leading frequency independent corrections to the $\mathbf{e_g}$ and $\mathbf{t_{2g}}$ vertices are obtained as (see Appendix B.5 for further details),
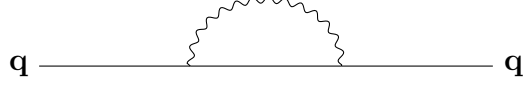
Figure 4.8: Self-energy of the magnetic monopoles due to the gauge fluctuation.

$$\delta\alpha_{\mathbf{k}}^{(e)} \approx a_0 + \frac{a_1}{\beta^4} + \frac{a_2 e^{-\beta\Delta_0}}{\beta^{\frac{3}{2}}} + k^2\left(\frac{a_3}{\beta^2} + \frac{a_4 e^{-\beta\Delta_0}}{\beta^{\frac{1}{2}}}\right)$$

$$\delta\alpha_{\mathbf{k}}^{(t_2)} \approx \tilde{a}_0 + \frac{\tilde{a}_1}{\beta^5} + \frac{\tilde{a}_2 e^{-\beta\Delta_0}}{\beta^2} + k^2\left(\frac{\tilde{a}_3}{\beta^3} + \frac{\tilde{a}_4 e^{-\beta\Delta_0}}{\beta}\right) \tag{4.39}$$

where a_i and $\tilde{a}_i$ are temperature independent constants. The correction to the linewidth can now be obtained by incorporating these vertex corrections to Eq. 4.34. We note that such contributions do not change the dependence of the Raman response on the two-particle density of states of the monopoles. Instead, they modify the temperature dependence and overall profile of the linewidth vs frequency plots (see Fig. 4.5) obtained from the gauge mean field ansatz by renormalisation of the form factors. However, since the QSL phase is stabilised only at low temperatures, the temperature dependent vertex corrections merely give rise to a sub-leading correction to Eq. 4.34 as $T \to 0$.

Apart from the vertex corrections, the virtual photon exchange due to the gauge fluctuations also renormalises the monopole self-energy, via processes shown in Fig. 4.8. Such contributions renormalise the bare monopole linewidth as well as its band structure. The broadening of the linewidth is sub-leading in the low-temperature regime. On the other hand, the renormalisation of the band structure modifies the two-particle density of states of monopoles by an amount proportional to the speed of emergent light (c_e). As a result, the Raman linewidth gets renormalised compared to the gauge mean field results described in Fig. 4.5 via the dressed two-monopole density of states. However, since the large anisotropy of the exchange coupling ($J_{zz} \gg J_\pm$) ensures $\Delta_0 \gg c_e$ [64, 96, 120], such effects are small. The large gap of the magnetic monopoles in QSL phase preserves the essential features of the Raman response obtained in the gauge mean field ansatz.

4.7 Self-energy of the phonon due to phonon-photon coupling

Similar to the Raman response due to the phonon-monopole coupling, the leading contribution to the phonon linewidth due to phonon-photon interaction (see Eq. 4.27) can be computed from
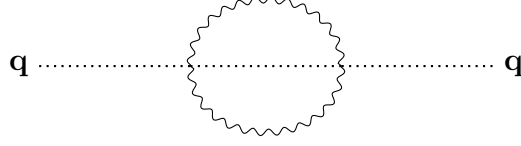
Figure 4.9: Self-energy of the phonon due to the phonon-(emergent) photon interaction (see Fig. 4.2(b)).

the Feynman diagram shown in Fig. 4.9 appearing in the second-order perturbation theory. However, we note that the presence of the background electric flux does not change the low energy photon dispersion, hence the phonon linewidth due to the photons remains similar in both the zero and $\pi-$flux QSLs discussed above. The self-energy of the phonon is given by,

$$\Sigma_{\zeta^{(e)}}(\mathbf{q}, i\Omega) = \frac{1}{\beta^2} \sum_{\mathbf{k_2}, \mathbf{k_3}, \mathbf{k_4}} \sum_{\Omega_2 \Omega_3 \Omega_4} \mathcal{G}^{\beta\gamma}(\mathbf{q}, \mathbf{k_2}, \mathbf{k_3}, \mathbf{k_4}) \mathcal{G}^{\mu\nu}(\mathbf{q}, \mathbf{k_2}, \mathbf{k_3}, \mathbf{k_4}) \delta(\Omega + \Omega_2 + \Omega_3 + \Omega_4)$$
$$\times \ G_\zeta(\mathbf{k_2}, \Omega_2) D_{\beta\mu}(\mathbf{k_3}, \Omega_3) D_{\gamma\nu}(\mathbf{k_4}, \Omega_4) \delta(\mathbf{q} + \mathbf{k_2} + \mathbf{k_3} + \mathbf{k_4}) \qquad (4.40)$$

Here $D_{\mu\nu}(\mathbf{q}, i\omega)$ denotes the photon propagator which can be calculated from the effective low-energy Hamiltonian of the pure gauge theory given in Eq. 4.16, *i.e.*,

$$D_{\mu\nu}(\mathbf{q}, i\Omega) = -\int_0^\beta d\tau \langle \hat{\mathcal{T}} \left(A_{\mathbf{q},\mu}(\tau) A_{-\mathbf{q},\nu}(0) \right) \rangle e^{i\Omega\tau} = -\frac{U\delta_{\mu\nu}}{\Omega^2 + \varepsilon_{\mathbf{q}}^2} \qquad (4.41)$$

Eq. 4.40 can be further simplified by performing the frequency summation [124]. For the Raman scattering experiments discussed earlier, we consider only the $\mathbf{q} \to 0$ limit and focus on the imaginary part. Typically, the dispersion for the optical phonon can be approximated as, $\Omega_{\mathbf{q}} \approx \Omega_0$. Also, the energy scale of the emergent photon is much smaller than the optical phonon excitations of the pyrochlores [64, 129, 130]. Hence, at the low temperatures of the QSL phase, it is fair to consider $n(\Omega_0) \ll n(\varepsilon_{\mathbf{k}})$. Setting $n(\Omega_0) = 0$ in the leading approximation, the contribution to the phonon linewidth is obtained as,

$$\Gamma(0, E) = \frac{\pi(J_{ph-ph}U)^2}{2N} \sum_{\mathbf{k}} \left[\mathbf{k} \cdot \mathbf{k}\delta_{\beta\gamma} - k^\beta k^\gamma\right]^2 \frac{1}{4\varepsilon_{\mathbf{k}}^2} \Bigg[\delta(E + \varepsilon_{\mathbf{k}}) \left[n(-E)\right]^2$$

$$+ \delta(E - \varepsilon_{\mathbf{k}}) \left[1 + n(E)\right]^2 + \delta(E) \left\{2[n(\varepsilon_{\mathbf{k}})][n(\varepsilon_{\mathbf{k}}) + 1]\right\}\Bigg],$$

(4.42)

where $E = (\Omega - \Omega_0)/2$. It is clear from the above expression that the Raman response occurs around $\Omega = \Omega_0$ due to the gaplessness of the photons, which is different from the frequency window at which the magnetic monopole signatures occur. For small positive energies E, the above expression is further simplified to,

$$\Gamma(0, E) \propto E^4(1 + n(E))^2.$$

(4.43)

For the higher energy regime, the photon band structure starts deviating from the linear behaviour and the above form is no longer valid. The complete energy dependence of the above contribution to the linewidth is shown in Fig. 4.10 for different temperatures, where we have used the lattice regularized dispersion for the emergent photons [64, 96]. Apart from the usual dipolar form factor, the linewidth profile is mostly sensitive to the photon density of states, which is shown in the inset of Fig. 4.10.

4.8 Self-energy of the phonon due to phonon-electric charge coupling

The final contribution to the phonon self-energy in the QSL phase arises from scattering of the phonons off the electric charges. Again, assuming weak coupling between the charges and the gauge field, we compute the phonon linewidth due to Eq. 4.29 using gauge mean field theory. As we have already seen, this interaction is very similar to that between phonons and monopoles. Hence, the contribution to the phonon self-energy also comes from similar Feynman diagrams as shown in Fig. 4.11. There are two possible scattering channels for electric charge-phonon interactions– absorption of a phonon by a charge, or, annihilation of a phonon followed by pair production of charges (with charge ± 1). Similar to monopoles, only the second process is relevant here. Therefore, $\Gamma \sim \Theta(\mid \Omega \mid -2\Delta_c)$, and the linewidth vs frequency profile closely follows the two-particle density of states of the electric charges. This is shown
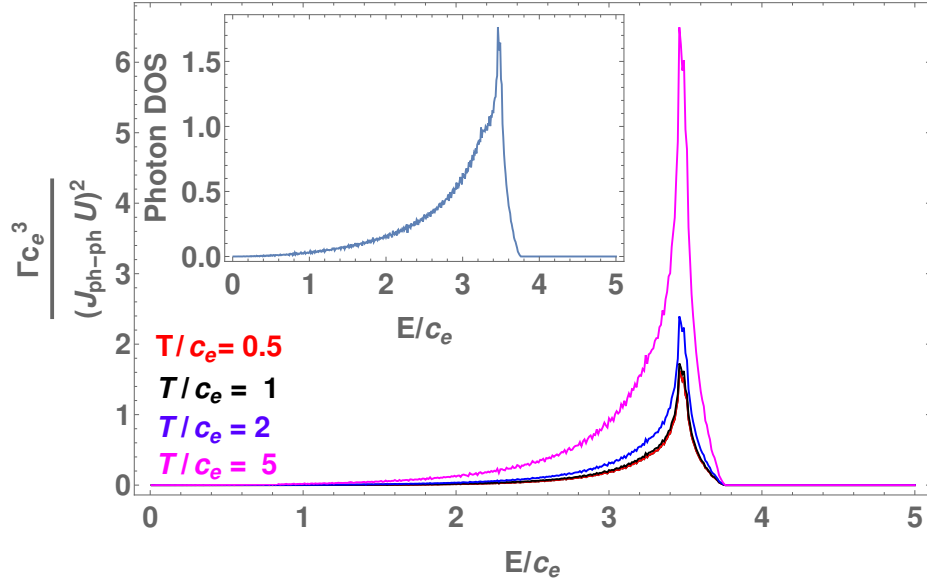
Figure 4.10: **Energy dependence of the linewidth of the e_g phonons due to phonon-(emergent) photon coupling:** The energy dependence is shown at different temperatures. $c_e = \sqrt{UK}$ is the velocity of the emergent photons and its density of states is plotted in the inset.
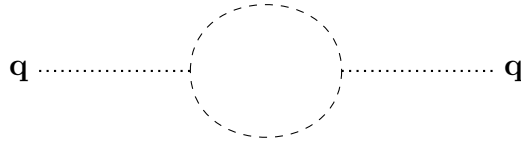
Figure 4.11: Self-energy of the phonon due to the phonon-electric charge interaction (see Fig. 4.3(b))

in Fig. 4.12 for $t/m = 0.2$ as an illustrative example (However, it can be chosen from any value that satisfies, $m > 2\sqrt{2}t$, defining the validity of the QSL description, and the profile remains qualitatively unchanged). Clearly, the Raman response due to the phonon-charge coupling has a threshold energy scale of $\sim 2\Delta_c$ which is a different energy scale compared to the response due to magnetic monopoles and photons.

Perhaps, the most crucial observation in the above discussion of the Raman response due to different spin ice excitations is that in all the cases the phonon linewidth is typically sensitive to the density of states of the respective excitations, and due to the natural separation of the energy scale of these excitations, such renormalisation appear at very different frequency window. We particularly emphasise this feature by depicting the Raman response of the quantum spin ice in the schematic of Fig. 4.13. Such observation might be particularly interesting for the experiments to detect the signatures of the emergent quasiparticles of the quantum spin ice separately in the Raman spectrum.
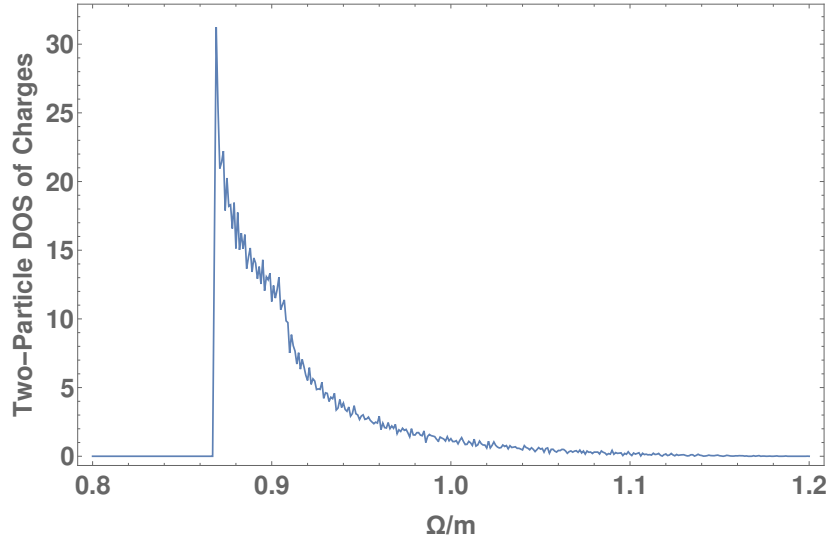
Figure 4.12: **Two-particle density of states of the charges**: For illustrative purpose, we have chosen $t/m = 0.2$ where $\Delta_c/m = 0.43$.
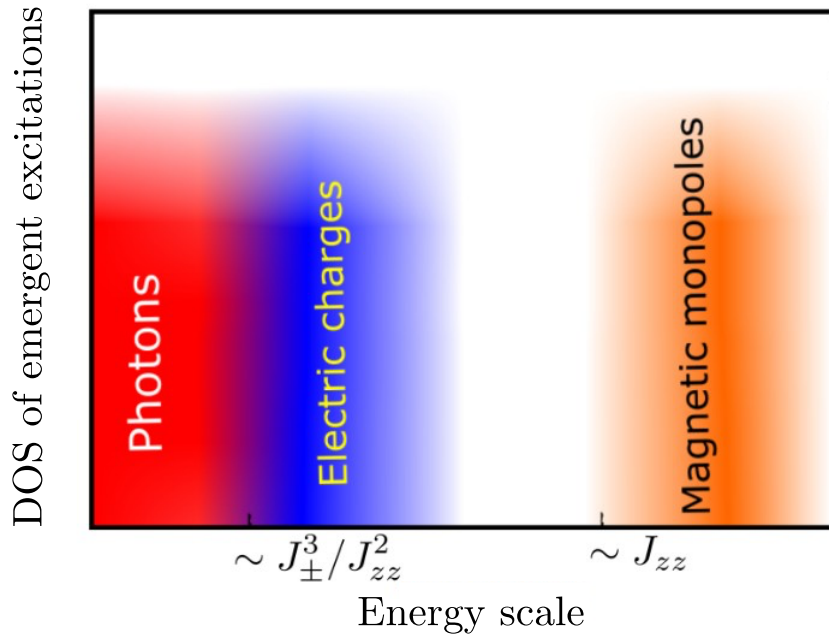
Figure 4.13: Schematic of the energy scales of different density of states (DOS) of the emergent excitations contributing to the phonon linewidth.

4.9 Bilinear coupling

Having discussed the effects of the linear magnetoelastic coupling in the QSL phase, we now briefly discuss the more familiar contribution to the Raman response of the phonons arising due to the bilinear magnetoelastic interaction. This is present both in Kramers and non-Kramers systems, as it arises due to modulation of the spin-exchange interactions via the phonons and can be obtained from the bare spin Hamiltonian of Eq. 4.3 by Taylor expanding the exchange coupling constants in powers of lattice displacements ($\delta_{\mu\nu}$) from the ionic equilibrium position ($\bar{\mathbf{R}}_{\mu\nu}$) [83] as

$$J_\alpha^{\mu\nu}(\mathbf{r}) = J_\alpha + \frac{\partial J_\alpha^{\mu\nu}(\mathbf{r})}{\partial R_{\mu\nu}^a}\delta_{\mu\nu}^a(\mathbf{r}) + \frac{1}{2}\frac{\partial^2 J_\alpha^{\mu\nu}(\mathbf{r})}{\partial R_{\mu\nu}^a \partial R_{\mu\nu}^b}\delta_{\mu\nu}^a(\mathbf{r})\delta_{\mu\nu}^b(\mathbf{r}) \tag{4.44}$$

Here, $J_\alpha^{\mu\nu}(\mathbf{r})$ denotes the generic bond dependent exchange coupling constant on the bond of the pyrochlore connecting the sites $(\mathbf{r}, \boldsymbol{\mu})$ and $(\mathbf{r}, \boldsymbol{\nu})$. Here, $(\mathbf{r}, \boldsymbol{\mu})$ denotes the position vector of the four spins sitting on the corners of the tetrahedron with its centre at $\mathbf{r}$ for $\mu = 0, 1, 2, 3$, with α representing zz or $\pm$ interactions, and,

$$R_{\mu\nu}^a = (\mathbf{r}, \boldsymbol{\mu})^a - (\mathbf{r}, \boldsymbol{\nu})^a, \qquad (a = x, y, z)$$
$$\delta_{\mu\nu}^a = R_{\mu\nu}^a - \bar{R}_{\mu\nu}^a$$

Substituting Eq. 4.44 in the spin-Hamiltonian of Eq. 4.3, we get the coupling between the phonons and spin-bilinears,

$$H_{sp}^{quad} = H_1 + H_2 \tag{4.45}$$

where

$$H_1 = \sum_{\mathbf{r},\mu,\nu}\left(\frac{\partial J_{zz}}{\partial R_{\mu\nu}^a}\delta_{\mu\nu}^a(\mathbf{r})s_{\mathbf{r},\mathbf{r}+\mathbf{e}_\mu}^z s_{\mathbf{r},\mathbf{r}+\mathbf{e}_\nu}^z - \frac{\partial J_\pm}{\partial R_{\mu\nu}^a}\delta_{\mu\nu}^a(\mathbf{r})\left(s_{\mathbf{r},\mathbf{r}+\mathbf{e}_\mu}^+ s_{\mathbf{r},\mathbf{r}+\mathbf{e}_\nu}^- + h.c.\right)\right) \tag{4.46}$$

$$H_2 = \sum_{\mathbf{r},\mu,\nu}\left(\frac{1}{2}\frac{\partial^2 J_{zz}}{\partial R_{\mu\nu}^a \partial R_{\mu\nu}^b}\delta_{\mu\nu}^a(\mathbf{r})\delta_{\mu\nu}^b(\mathbf{r})s_{\mathbf{r},\mathbf{r}+\mathbf{e}_\mu}^z s_{\mathbf{r},\mathbf{r}+\mathbf{e}_\nu}^z\right.$$
$$\left. - \frac{1}{2}\frac{\partial^2 J_\pm}{\partial R_{\mu\nu}^a \partial R_{\mu\nu}^b}\delta_{\mu\nu}^a(\mathbf{r})\delta_{\mu\nu}^b(\mathbf{r})\left(s_{\mathbf{r},\mathbf{r}+\mathbf{e}_\mu}^+ s_{\mathbf{r},\mathbf{r}+\mathbf{e}_\nu}^- + h.c.\right)\right). \tag{4.47}$$

A unitary transformation can be performed on the displacement operators, $\delta_{\mu\nu}(\mathbf{r})$, to re-

write it in the normal mode coordinates, $\zeta^{(\rho)}(\mathbf{r})$, described in Sec. 4.3. The above interaction is re-written in terms of the fractionalised degrees of freedom in a QSL phase using the parton decomposition of spins as described in Sec. 4.4. Within gauge mean field theory, the quadratic magnetoelastic coupling between the phonons and emergent excitations of the QSL is given by,

$$
\begin{aligned}
H_1 = \sum_{\mathbf{r},\mu,\nu} \bigg(& \frac{\partial J_{zz}}{\partial R_{\mu\nu}^a} \delta_{\mu\nu}^a(\mathbf{r},A) B_{\mathbf{r},\boldsymbol{\mu}} B_{\mathbf{r},\boldsymbol{\nu}} + \frac{\partial J_{zz}}{\partial R_{\mu\nu}^a} \delta_{\mu\nu}^a(\mathbf{r},B) B_{\mathbf{r}-\mathbf{d}_{\boldsymbol{\mu}},\boldsymbol{\mu}} B_{\mathbf{r}-\mathbf{d}_{\boldsymbol{\nu}},\boldsymbol{\nu}} \\
& - \frac{\partial J_{\pm}}{\partial R_{\mu\nu}^a} \delta_{\mu\nu}^a(\mathbf{r},A) \left(\phi_{\mathbf{r}+\mathbf{d}_{\boldsymbol{\nu}},B}^{\dagger} \phi_{\mathbf{r}+\mathbf{d}_{\boldsymbol{\mu}},B} + h.c. \right) - \frac{\partial J_{\pm}}{\partial R_{\mu\nu}^a} \delta_{\mu\nu}^a(\mathbf{r},B) \left(\phi_{\mathbf{r}-\mathbf{d}_{\boldsymbol{\nu}},A}^{\dagger} \phi_{\mathbf{r}-\mathbf{d}_{\boldsymbol{\mu}},A} + h.c. \right) \bigg)
\end{aligned}
$$
(4.48)

$$
\begin{aligned}
H_2 = \sum_{\mathbf{r},\mu,\nu} \bigg(& \frac{1}{2} \frac{\partial^2 J_{zz}}{\partial R_{\mu\nu}^a \partial R_{\mu\nu}^b} \delta_{\mu\nu}^a(\mathbf{r},A) \delta_{\mu\nu}^b(\mathbf{r},A) B_{\mathbf{r},\boldsymbol{\mu}} B_{\mathbf{r},\boldsymbol{\nu}} \\
& + \frac{1}{2} \frac{\partial^2 J_{zz}}{\partial R_{\mu\nu}^a \partial R_{\mu\nu}^b} \delta_{\mu\nu}^a(\mathbf{r},B) \delta_{\mu\nu}^b(\mathbf{r},B) B_{\mathbf{r}-\mathbf{d}_{\boldsymbol{\mu}},\boldsymbol{\mu}} B_{\mathbf{r}-\mathbf{d}_{\boldsymbol{\nu}},\boldsymbol{\nu}} \\
& - \frac{1}{2} \frac{\partial^2 J_{\pm}}{\partial R_{\mu\nu}^a \partial R_{\mu\nu}^b} \delta_{\mu\nu}^a(\mathbf{r},A) \delta_{\mu\nu}^b(\mathbf{r},A) \left(\phi_{\mathbf{r}+\mathbf{d}_{\boldsymbol{\nu}},B}^{\dagger} \phi_{\mathbf{r}+\mathbf{d}_{\boldsymbol{\mu}},B} + h.c. \right) \\
& - \frac{1}{2} \frac{\partial^2 J_{\pm}}{\partial R_{\mu\nu}^a \partial R_{\mu\nu}^b} \delta_{\mu\nu}^a(\mathbf{r},B) \delta_{\mu\nu}^b(\mathbf{r},B) \left(\phi_{\mathbf{r}-\mathbf{d}_{\boldsymbol{\nu}},A}^{\dagger} \phi_{\mathbf{r}-\mathbf{d}_{\boldsymbol{\mu}},A} + h.c. \right) \bigg)
\end{aligned}
$$
(4.49)

The above vertices are described by the Feynman diagrams as shown in Fig. 4.14 and 4.15.

The phonon-magnetic monopole vertex arising from the quadratic coupling is shown in Fig 4.14 where (a) and (b) panels show the contribution from H_1 , and, (c) and (d) panels show the contribution from H_2. It is clear from these diagrams that such magnetoelastic coupling gives rise to the hopping of the monopoles which preserves the monopole flavour, i.e., monopoles on A and B sublattices do not mix under this dynamics. This feature can be contrasted with the monopole dynamics due to the linear magnetoelastic coupling described earlier in Eq. 4.22 and 4.23.

The quadratic coupling also generates a coupling between phonons and emergent photons which is shown in Fig. 4.15 with (a) and (b) panels depicting contributions from H_1 and H_2, respectively. In contrast to the linear coupling case, the phonons now couple to the gauge invariant magnetic field. As expected from time reversal invariance of the phonons, the magnetic field appears only at quadratic order in such couplings. We also note that the process shown in Fig. 4.15(a) is in the single phonon scattering channel, which was not present in the previous case.
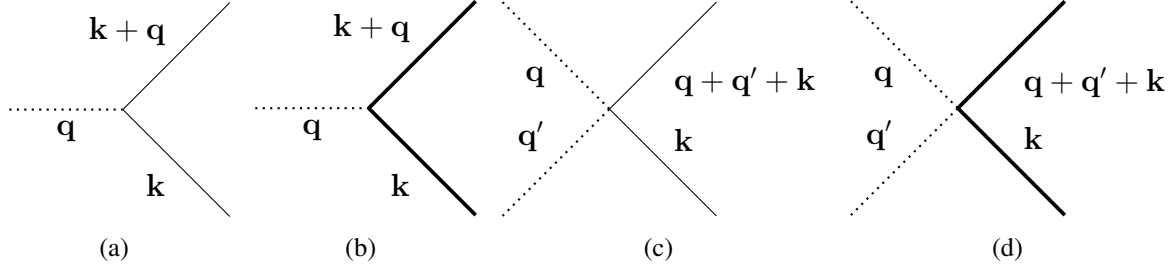
Figure 4.14: **Feynman diagram for phonon and magnetic monopole interaction due to the spin-phonon coupling quadratic in spin operators:** (a) and (b) are the contributions from H_1, and, (c) and (d) are the contributions from H_2 (see Eq. 4.48 and 4.49).
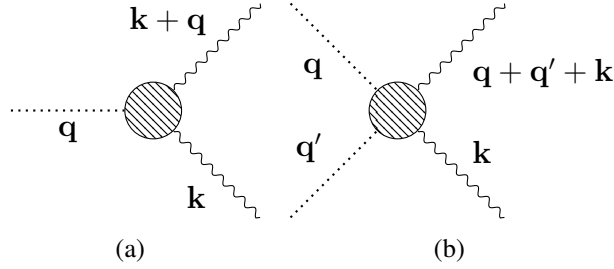
Figure 4.15: **Feynman diagram for phonon and photon interaction due to the spin-phonon coupling quadratic in spin operators:** The circles represent the form factor that makes the vertex gauge invariant. (a) and (b) are contributions due to H_1 and H_2, respectively (see Eq. 4.48 and 4.49).

Similar to the linear magnetoelastic interaction, the quadratic coupling also renormalises the phonon frequency and linewidth by opening up the decay channels for phonons depicted in Fig. 4.14 and 4.15. However, these new scattering channels do not change the essential features of the Raman linewidth, and its frequency dependence on the density of states of emergent excitations remains unchanged. In the non-Kramers materials, this contribution is expected to be sub-dominant compared to the phonon renormalisation due to the linear spin-phonon coupling. However, we note that the quadratic coupling is the only component of the magnetoelastic coupling present in the Kramers materials.

4.10 Self-energy calculation in (thermal) paramagnetic regime

Finally, to contrast the case of the QSL to an ordinary paramagnet, we compute the self-energy of phonon in the high-temperature paramagnetic regime, where $T \gg J_{zz}$ such that the thermal fluctuations predominate. In this thermal paramagnet, due to the presence of abundant thermally excited both electric charges and magnetic monopoles, they cease to be well-defined (sparse) quasiparticles, instead presenting randomly fluctuating background fields. In such a case, individual monopoles or charges cannot propagate coherently, and, the deconfined U(1)

gauge theory no longer is a valid description of the system. Instead of using the emergent excitations, the dressed self-energy due to the spin-phonon interaction (as described in Eq. 4.6 and 4.7) is now computed in terms of the original short-range correlated spin degrees of freedom. The phonon self-energy due to the linear spin-phonon coupling is given, *e.g.* for $\mathbf{e_g}$ modes, by

$$\Sigma_{\zeta^{(e)}}(\mathbf{q}, i\Omega) = -J_{sp}^{(e)2} \sum_{\alpha=x,y} \sum_{\mu,\nu=0}^{3} \left[\eta_{\mu\nu}^{(e)}(\mathbf{q})\kappa_{\mu\nu}^{\alpha\alpha}(\mathbf{q}, i\Omega) + \eta_{\mu\nu}^{(e)}(-\mathbf{q})\kappa_{\mu\nu}^{\alpha\alpha}(-\mathbf{q}, -i\Omega) \right] \quad (4.50)$$

where $\kappa_{\mu\nu}^{\alpha\beta}(\mathbf{q}, i\omega) = \int_0^\beta d\tau \langle \hat{\mathcal{T}} \left(s_\mu^\alpha(\mathbf{q}, \tau) s_\nu^\beta(-\mathbf{q}, 0) \right) \rangle_0 e^{i\omega\tau}$ is the time ordered spin correlation function and $\eta_{\mu\nu}^{(e)}(\mathbf{q})$ is the form factor for the $\mathbf{e_g}$ mode. Similar expressions hold for $\mathbf{t_{2g}}$ modes as discussed in Appendix B.6.

From the bare spin Hamiltonian, we expect the spin-correlations to be diagonal in the spin indices (defined using the local quantisation axes given by Eqs. B.1 and B.2), *i.e.*, $\kappa_{\mu\nu}^{\alpha\beta}(\mathbf{q}, i\omega) = \delta_{\alpha\beta}\kappa_{\mu\nu}^{\alpha\beta}(\mathbf{q}, i\omega)$. Further, in this thermal paramagnetic phase, the spins are incoherent and, therefore, the spin correlations are dominated by the short time values which we replace by the equal time correlators, which in turn can be computed from the high-temperature expansion using the bare spin-exchange Hamiltonian. The leading contribution is given by,

$$\langle s_{\mathbf{r}}^x s_{\mathbf{r'}}^x \rangle_0 = \langle s_{\mathbf{r}}^y s_{\mathbf{r'}}^y \rangle_0 \approx e^{-\frac{|\mathbf{r}-\mathbf{r'}|}{\xi}} \quad (4.51)$$

where $\xi \sim l/\ln\left(\frac{T}{J_\pm}\right)$ is the finite correlation length in the paramagnetic phase. Taking the Fourier transform and substituting it in Eq. 4.50, we obtain,

$$\Sigma_{\zeta^{(\rho)}}(\mathbf{q}, i\Omega) \propto -\frac{J_{sp}^{(\rho)2}\xi^3\beta}{(1 + q^2\xi^2)^2} \quad (4.52)$$

The above expression is purely real, and hence contributes only to a Raman frequency shift that decays inversely with temperature.

Therefore the leading effect of the spin-phonon coupling is to renormalise the phonon energy while its lifetime receives sub-leading contributions. Therefore, the Raman linewidth for the phonons acquires an anomalous broadening while going from the high-temperature paramagnetic phase to the low-temperature QSL. This leads to the question what happens to the linewidth at the thermal confinement-deconfinement phase transition between the low-temperature quantum and high-temperature thermal paramagnets? This is an interesting and

experimentally relevant question which will be very useful to understand in the future.

4.11 Phonon mediated Loudon-Fleury vertex

In addition to the renormalisation of optical phonons, the magnetoelastic coupling can further mediate interaction between the external Raman photons and the magnetic degrees of freedom via phonon mediated Loudon-Fleury vertex as discussed in Sec. 2.3. Such interactions are of particular interest in those materials where the phonon has a very different energy scale compared to the QSL excitations [130, 131].

As explained in the earlier sections, the external photons of the Raman experiment probe the phonons of the system (via Eq. 2.4), which further couple to the fractionalised excitations via the magnetoelastic coupling (see Eq. 4.22, 4.23, 4.27, 4.29). Therefore, integrating out the phonons leads to an interaction between the external photons and the emergent electrodynamics. The leading order interaction vertices are obtained as follows,

$$H_{LF}^{\phi} = \langle H_{Raman} H_{sp} \rangle_{\zeta} \tag{4.53}$$

$$H_{LF}^{A} = \langle H_{Raman}^2 H_{phonon-photon} \rangle_{\zeta} - \langle H_{Raman}^2 \rangle_{\zeta} \langle H_{phonon-photon} \rangle_{\zeta} \tag{4.54}$$

where $\langle \hat{O} \rangle_{\zeta} = \frac{\int D\zeta \, \hat{O} \, e^{-\beta H_{\zeta}}}{\int D\zeta \, e^{-\beta H_{\zeta}}}$ and $H_{sp} = H_{sp}^{(e)} + H_{sp}^{(t_2)}$. Simplifying the above expressions, we get,

$$H_{LF}^{\phi} = \frac{J_{sp}^{(\rho)}}{2\Omega_0} \int \prod_{i=1}^{4} d^3 k_i \left[\nabla_{\zeta^{(\rho)}} \Lambda \right]_{\zeta^{(\rho)}=0}^{ij} \omega_{\mathbf{k_1}}^{in} \omega_{\mathbf{k_2}}^{out} (\alpha_{\mathbf{k_3}} + \alpha_{\mathbf{k_4}}) \mathcal{A}_i^{in}(\mathbf{k_1}) \mathcal{A}_j^{out}(\mathbf{k_2}) \phi_{\mathbf{k_3},A}^{\dagger} \phi_{\mathbf{k_4},B}$$

$$\times \, \delta(\mathbf{k_1} + \mathbf{k_2} + \mathbf{k_3} + \mathbf{k_4}) + h.c. \tag{4.55}$$

$$H_{LF}^{A} = \frac{1}{2\Omega_0^2} \int \prod_{i=1}^{8} d^3 k_i \left[\nabla_{\zeta^{(\rho)}} \Lambda \right]_{\zeta^{(\rho)}=0}^{ij} \left[\nabla_{\zeta^{(\rho)}} \Lambda \right]_{\zeta^{(\rho)}=0}^{mn} \mathcal{G}^{\alpha\beta}(\mathbf{k_1}, \mathbf{k_2}, \mathbf{k_3}, \mathbf{k_4})$$

$$\times \, A_{\mathbf{k_3}}^{\alpha} A_{\mathbf{k_4}}^{\beta} \mathcal{A}_i^{in}(\mathbf{k_5}) \mathcal{A}_j^{out}(\mathbf{k_6}) \mathcal{A}_m^{in}(\mathbf{k_7}) \mathcal{A}_n^{out}(\mathbf{k_8}) \delta(\mathbf{k_5} - \mathbf{k_6} + \mathbf{k_1}) \delta(\mathbf{k_7} - \mathbf{k_8} + \mathbf{k_2}) \tag{4.56}$$

where the optical phonon band structure is approximated as $\Omega_{\mathbf{q}} \approx \Omega_0$. Clearly, the above contributions are suppressed by the optical phonon energy scale compared to the usual Loudon-
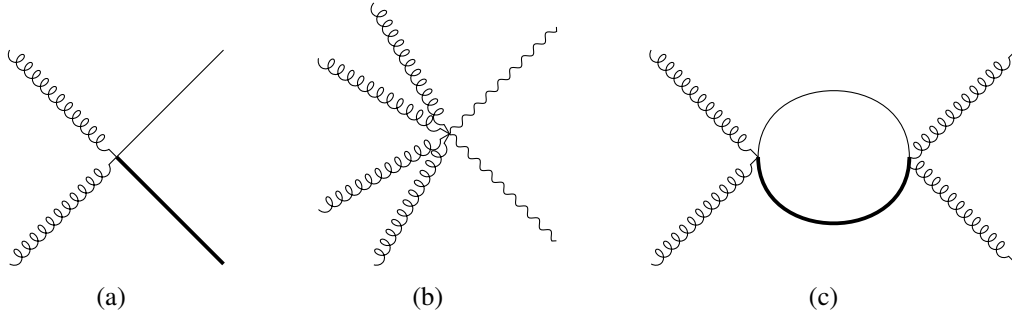
Figure 4.16: Feynman diagram for the phonon mediated Loudon-Fleury vertex in quantum spin ice for (a) magnetic monopoles (see Eq. 4.55) and (b) photons (see Eq. 4.56). (c) Feynman diagram contributing to Raman intensity due to the phonon mediated Loudon-Fleury vertex for magnetic monopoles.

Fleury vertex [64]. Feynman diagram for Eqs. 4.55 and 4.56 are shown in Figs. 4.16(a) and 4.16(b), respectively.

Raman intensity due to these processes is obtained by calculating the imaginary part of the bubble diagrams which comes in the second order perturbation theory. The bubble due to the monopoles is shown in Fig. 4.16(c). It is clear from the diagram that the resulting monopole bubble is exactly same as the one obtained (see Fig. 4.4) earlier. Therefore, the Raman intensity due to the phonon mediated Loudon-Fleury processes are sensitive to the two-monopole density of states in the QSL phase and it can in principle also characterise the physics of spin fractionalisation even if the phonon is off-resonant to the quasiparticles of the QSL phase.

CHAPTER 5

ANOMALOUS RAMAN SIGNATURES OF $Ca_{10}Cr_7O_{28}$

5.1 Introduction

In this chapter, we present vibrational Raman signatures of another exotic quasi-two-dimensional material, $Ca_{10}Cr_7O_{28}$ [59, 132, 133], which is a quantum Heisenberg magnet on bi-layer kagome lattice. This work is an experiment-theory collaboration, where we tried to develop a theory for the anomalous phonon spectra observed in the Raman scattering on the polycrystalline samples. We will soon see that this effect is very different from the Raman anomaly observed in the QSL phases described earlier. Renormalisation of the phonons in $Ca_{10}Cr_7O_{28}$ originates from an intricate reordering of the orbital degrees of freedom of the magnetic atom, instead of the spin fractionalisation of a QSL phase.

The actual stoichiometry of the compound, $Ca_{10}(Cr^V O_4)_6(Cr^{VI}O_4)$ [134], contains magnetically isolated distorted kagome bilayers of spin-$\frac{1}{2}$ Cr^{5+} ions with both ferromagnetic (FM) and antiferromagnetic (AFM) isotropic Heisenberg exchange couplings [132, 135]. The magnetic Hamiltonian, constructed from the experimental phenomenology and first principle calculations, accounts for the inequivalent FM (significantly stronger) and AFM isotropic Heisenberg couplings ($\Sigma J \lesssim 1$ meV) [133] and results in a mean-field CW temperature of $\theta_{CW} \approx 4$ K [59, 135]. However, the system shows no sign of long-range magnetic order or any spin freezing down to 19 mK, implying the presence of a fluctuating spin liquid ground state as confirmed from bulk susceptibility, heat capacity, μSR, or neutron scattering measurements [59, 132, 133, 136, 137] as well as from theoretical studies [137–139].

Surprisingly, the Raman scattering experiment performed by our collaborators on this system down to $\sim$4 K, reveals strong anomalies in the temperature dependence of phonon frequencies and linewidths, at the crossover temperature $T_C \sim$100 K, much above the temperature scale ($\sim$10 K) associated with the spin-exchange interactions. Hence this cannot arise from the non-trivial spin-phonon coupling, because for all practical purposes, spins are deep inside the thermal paramagnet, *i.e.*, effectively at infinite temperature ($T/\Theta_{CW} \gg 1$). On the other hand, these Raman anomalies also do not arise from the temperature-driven magnetic ordering transitions [140, 141], which are strictly absent in this frustrated system [132]. This raises the central

question about the origin of the new crossover energy scale and the associated Raman-active phonon renormalisation.

To answer this question, we first note that the system contains the Jahn-Teller (J-T) active [61] Cr^{5+} ion sites offering moderately distorted $Cr^V O_4$ tetrahedra even at room temperature as reported in the earlier studies [62]. Clearly, the phonon anomaly then cannot be attributed to the static to dynamic J-T crossover [142–144]. Therefore, we turn our focus on the co-operative J-T effects driven by the interaction between localized orbitals and the crystal lattice [145]. In fact, we theoretically predict a rearrangement of the orbital degrees of freedom of Cr^{5+} ions below the temperature scale of primary J-T distortion driven by the orbital fluctuations. We claim that the phonons are sensitive to such orbital reordering via the cooperative JT mechanism, which in turn renormalises the phonon parameters.
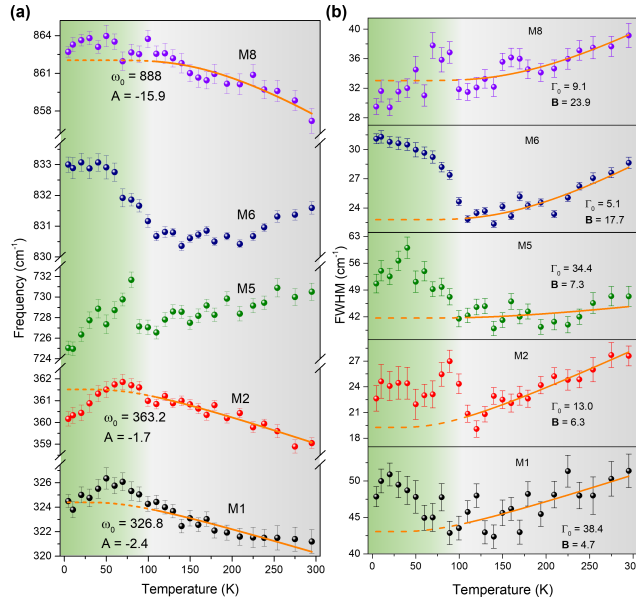
Figure 5.1: **Temperature dependence of (a) frequencies and (b) linewidths of selected phonon modes:** The orange curves are fits to cubic anharmonic model given by Eq. 5.2. Values of the fitting parameters for different modes are mentioned in the plot.

5.2   Experimental observations

In this section, we briefly describe the experimental observations regarding the phonon spectra in $Ca_{10}Cr_7O_{28}$, which is reported in the Ph.D. thesis of our collaborator, Srishti Pal [75].

The temperature evolution of frequencies and linewidths for various phonon modes observed in the experiments are shown in Fig. 5.1(a) and (b), respectively. The solid orange lines are fits for the phonon parameters between 100 K and 295 K determined from the simple cubic

anharmonic model [146]. These fitting equations are given by,

$$\omega^{(p)} = \omega_0 + A\left[1 + 2n_B\left(\frac{\omega_0}{2}\right)\right] \tag{5.1}$$

$$\Pi_{anh}^{(p)} = \Gamma_0 + B\left[1 + 2n_B\left(\frac{\omega_0}{2}\right)\right] \tag{5.2}$$

where ω_0 is the bare frequency, Γ_0, A and B are constants, and $n_B(\omega)$ is the Bosonic distribution at temperature T. The dashed lines are the extensions of the fits to the lower temperature regimes. Clearly, except for M8, frequencies and linewidths of all other modes exhibit anomalous behaviour with temperatures. The frequencies of M1, M2 and linewidths of M1, M2, M5, and M6 show clear deviations from the expected cubic anharmonicity below $\sim$100 K. The frequencies of M5 and M6 remain anomalous throughout the entire temperature range and hence, cannot be fitted with the cubic anharmonic model.

In the following sections, we construct the theoretical model to explain the possible origin of these anomalous behaviours in greater detail by carefully taking into account the J-T effects in the material, which naturally gives rise to a new crossover energy scale, and can be attributed to $\sim$100 K.

5.3 Theoretical model

A minimal model that captures the J-T distortion includes the spin-1/2s, S_i^α, and the two e_g-orbitals $((|d_{3z^2-r^2}\rangle, |d_{x^2-y^2}\rangle) \equiv (|+\rangle, |-\rangle))$ τ_i^α on the Cr^{5+} sites as well as the Raman active phonons, $\zeta_i^{(p)}$ (p denotes the normal modes) with appropriate symmetries. The associated spin-orbital-phonon Hamiltonian is given by $H = H_{S,\tau,\zeta} + H_\zeta$, where H_ζ is the harmonic phonon Hamiltonian:

$$H_\zeta = \sum_p \left[\frac{1}{2}\left(\pi^{(p)}\right)^2 + \frac{1}{2}C_p(\zeta^{(p)})^2\right] \tag{5.3}$$

with $\pi^{(p)}$ representing the momentum conjugate to the mode $\zeta^{(p)}$, and $H_{S,\tau,\zeta}$ governs the coupled dynamics of spin, orbit and phonons:

$$H_{S,\tau,\zeta} = \sum_{\langle ij\rangle,\alpha\beta}\left[K_{ij}^{\alpha\beta} + J_{ij}^{\alpha\beta}\mathbf{S}_i\cdot\mathbf{S}_j\right]\tau_i^\alpha\tau_j^\beta + \sum_{i,p,\beta}\Gamma^{p,\beta}\zeta_i^{(p)}\tau_i^\beta \tag{5.4}$$

72

with $J_{ij}^{\alpha\beta}$ and $K_{ij}^{\alpha\beta}$ denoting the bare spin-spin and orbital-orbital exchange interactions respectively between two neighbouring Cr^{5+} ions; $\Gamma^{p,\beta}$ is the coupling of the orbitals with the phonon modes. Note that, due to the absence of atomic spin-orbit coupling (expected to be small for 3d transition metals), the spin-spin interactions are rotationally symmetric while the dependence on the orbital labels is constrained by lattice symmetries. The second term in the above equation is the symmetry allowed linear coupling between the orbitals and the phonon modes that is present in a J-T active ion and is responsible for the distortion of the lattice. The spins being in the thermal paramagnetic phase, at the experimentally relevant temperatures, they only modify the orbital exchange interaction via short-range spin correlations, $K_{ij}^{\alpha\beta} \rightarrow \mathcal{K}_{ij}^{\alpha\beta} = K_{ij}^{\alpha\beta} + J_{ij}^{\alpha\beta}\langle S_i \cdot S_j \rangle$.

5.3.1 The primary J-T distortion

The primary distortion of the $Cr^V O_4$ tetrahedra is theoretically captured by considering the minima of the J-T potential, $H_{JT} = \sum_{p,\beta} \Gamma^{p,\beta} \zeta^{(p)} \tau^\beta + \frac{1}{2}\sum_p C_p (\zeta^{(p)})^2$, with respect to $\zeta^{(p)}$, which occurs at

$$\zeta^{(p)} = -\sum_\beta \frac{\Gamma^{p,\beta}}{C_p} \tau^\beta \tag{5.5}$$

This is lower in energy when $\langle \tau^\beta \rangle \neq 0$, *i.e.* the orbital degeneracy is lifted, and thereby the tetrahedra is distorted. This is nothing but the single-ion JT distortion. Substituting the above minima in the H_{JT}, we obtain the energy gain due to the J-T distortion. For more than one mode, it is given by,

$$E_{JT} = -\sum_{p,\beta} \frac{\Gamma^{p,\beta}\Gamma^{p,\beta}}{2C_p}. \tag{5.6}$$

Clearly, the above expression is always negative suggesting the fact that the reduction of the symmetry via lattice distortion is always favourable. The maximum energy gain occurs for the mode with the largest J-T coupling, $\Gamma^{p,\beta}$ and minimum elastic constant, C_p. This in turn dictates the specifics of orbital splitting, $\langle \tau^\beta \rangle$.

5.3.2 Orbital reordering at intermediate temperatures

Below the temperature scale of primary J-T splitting, the other J-T coupling constants, as well as the orbital fluctuations can induce a reorientation of the orbital ordering, which was already set by the primary J-T. Such effects are typically expected to be governed by the orbital exchange energy scale, $\mathcal{K}_{ij}^{\alpha\beta}$, and might lead to an appearance of a cross-over energy scale which we are going to explain now in detail.

Consider the intermediate temperature range where the Raman anomalies are observed: $\Theta_{CW}(\sim 10 \text{ K}) \ll T < T_H(> 300 \text{ K})$, where $\Theta_{CW} \sim 10$ K and T_H are respectively the CW and the primary J-T transition temperatures. At this regime, the orbital ordering has already set in due to the primary J-T effect. Let us assume that this ordering is along τ^z (we do not know the actual direction of distortion from the powder samples). Therefore, the effective Hamiltonian in the intermediate temperature range is given by

$$\tilde{H} = \sum_{\langle ij \rangle, \alpha\beta} \mathcal{K}_{ij}^{\alpha\beta}\, \tau_i^\alpha \tau_j^\beta + \Delta_1 \sum_i \tau_i^z + \sum_{i,p} \Gamma^{p,\beta} \zeta_i^{(p)} \tau_i^\beta + \tilde{H}_\zeta \tag{5.7}$$

where Δ_1 characterises the splitting of the orbitals due to the primary J-T effect, $\tilde{H}_\zeta$ is the harmonic phonon Hamiltonian in the distorted lattice. The sum p now runs over the other phonon modes that can potentially lead to co-operative J-T. In principle, there will also be a symmetry allowed term of the form $\Delta_2 \sum_i \tau_i^x$ coming from the lattice distortion at the primary J-T transition, but the effect of such terms is straightforward– they smear out sharp features of phase transitions arising from Eq. 5.7 and makes way for smooth crossover. Assuming a single secondary mode favouring the orbital reordering along a particular direction, the mean-field phase diagram of the orbital part of the above Hamiltonian is easy to work out which we show now.

At the mean-field level, approximating orbitals by their expectation values– $\langle \tau^\beta \rangle$, the Hamiltonian of Eq. 5.7 can be written as,

$$\tilde{H}_{orb}^{MF} = \sum_{\langle ij \rangle, \alpha\beta} \mathcal{K}_{ij}^{\alpha\beta}\, \tau_i^\alpha \langle \tau_j^\beta \rangle + \Delta_1 \sum_i \tau_i^z + \sum_{i,p,\alpha} \Gamma^{p,\alpha} \langle \zeta_i^{(p)} \rangle \tau_i^\alpha \tag{5.8}$$

Then we can use Eq. 5.5 to replace $\langle \zeta^{(p)} \rangle = -\frac{\Gamma^{p,\beta}}{C_p} \langle \tau^\beta \rangle$ to obtain

$$\tilde{H}_{orb}^{MF} = \sum_{\langle ij \rangle, \alpha\beta} \mathcal{K}_{ij}^{\alpha\beta} \, \tau_i^\alpha \langle \tau_j^\beta \rangle + \Delta_1 \sum_i \tau_i^z - \sum_{i,\alpha\beta} \mu^{\alpha\beta} \langle \tau_i^\beta \rangle \tau_i^\alpha \tag{5.9}$$

where, $\mu^{\alpha\beta} = \sum_p \frac{\Gamma^{p,\alpha}\Gamma^{p,\beta}}{C_p}$. Considering a simplified case where the cooperative JT tries to align the orbitals in τ^x direction, the above mean field Hamiltonian can be further simplified as

$$\tilde{H}_{orb}^{MF} = \sum_{\langle ij \rangle, \alpha\beta} \mathcal{K}_{ij}^{xx} \, \tau_i^x \langle \tau_j^x \rangle + \Delta_1 \sum_i \tau_i^z - \sum_{i,\alpha\beta} \mu^{xx} \langle \tau_i^x \rangle \tau_i^x \tag{5.10}$$

where we have neglected other $\mathcal{K}^{\alpha\beta}$ terms, and write down the minimal orbital exchange term that gives rise to the reordering along τ^x. Assuming the orbital exchange coupling constants to be uniform, i.e, $\mathcal{K}_{ij}^{xx} = \mathcal{K}^{xx}$, and defining the effective onsite average CW field to be $\sum_j \mathcal{K}_{ij}^{xx} = \mathcal{K}^{xx} D \equiv \tilde{\mathcal{K}}^{xx}$ (where D is the coordination number of the lattice), the above Hamiltonian can now be solved as a single onsite spin problem. At finite temperature, it then gives rise to

$$\langle \tau^z \rangle = -\frac{\Delta_1}{E} \tanh[E/T] \tag{5.11}$$

$$\langle \tau^x \rangle = \frac{(\mu^{xx} - \tilde{\mathcal{K}}^{xx})\langle \tau^x \rangle}{E} \tanh[E/T] \tag{5.12}$$

where $E = \left[\left(\tilde{\mathcal{K}}^{xx} - \mu^{xx} \right)^2 \langle \tau^x \rangle^2 + \Delta_1^2 \right]^{1/2}$. This in turn translates into

$$T > T_c : \quad \langle \tau^z \rangle = -\tanh[\Delta_1/T] \quad \text{and} \quad \langle \tau^x \rangle = 0 \tag{5.13}$$

and

$$T < T_c : \quad \langle \tau^z \rangle = -\frac{\Delta_1}{E} \tanh[E/T] \quad \text{and} \quad E = (\mu^{xx} - \tilde{\mathcal{K}}^{xx}) \tanh[E/T] \tag{5.14}$$

where the transition temperature, T_c, is determined from, $\delta = \tanh[\delta/t_c]$, with $\delta = \frac{\Delta_1}{\left(\mu^{xx} - \tilde{\mathcal{K}}^{xx} \right)}$ and $t_c = T_c / \left(\mu^{xx} - \tilde{\mathcal{K}}^{xx} \right)$. This equation has a finite solution as long as $\delta \leq 1$ (see Fig. 5.2). Clearly, this implies that the orbitals rearrange themselves via the intersite orbital exchange interaction below the temperature scale of T_c. The reorientation of the orbitals are shown in Fig. 5.3(a) and (b). Our central idea is to associate T_c with ~ 100 K, the experimentally observed onset temperature scale for the phonon anomalies.
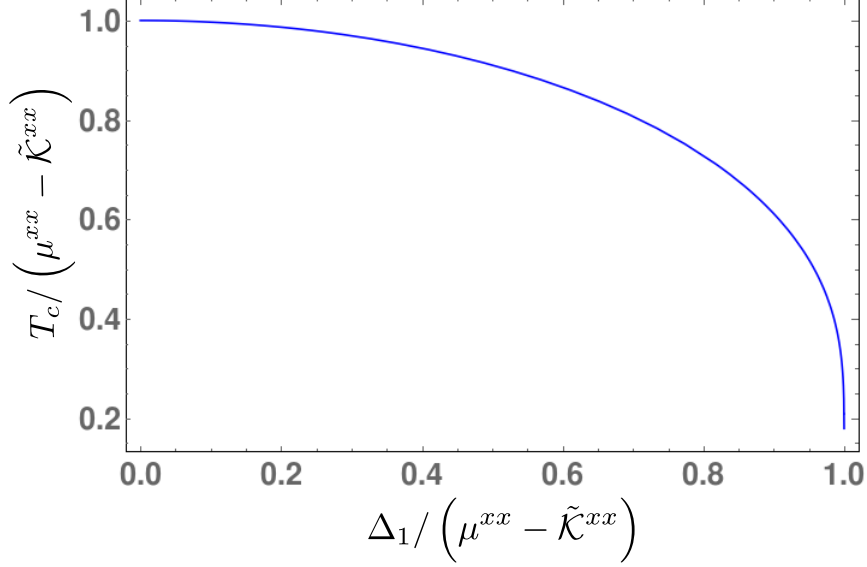
Figure 5.2: Temperature scale for the secondary cooperative Jahn-Teller ordering transition

5.4 Phonon renormalisation due to the orbital reordering

In the intermediate temperature regime, the phonon anomalies observed in the vibrational Raman scattering experiments can be taken into account by considering the fact that phonons are coupled to the orbital degrees of freedom, hence the reordering of the orbitals, in turn, renormalises the phonons via co-operative effects. For this, we note that in addition to $\Gamma^{p,\beta}$, the orbital-phonon coupling has another source *i.e.*, the coupling constants, $\mathcal{K}_{ij}^{\alpha\beta}$, which are dependent on the dynamic distortions of the tetrahedra. Hence we have, similar to the usual magnetoelastic coupling,

$$\mathcal{K}_{ij}^{\alpha\beta} = \bar{\mathcal{K}}_{ij}^{\alpha\beta} + \sum_p A_{ij}^{\alpha\beta;p}(\zeta_i^{(p)} + \zeta_j^{(p)}) + \sum_{p,q} B_{ij}^{\alpha\beta;pq}\zeta_i^{(p)}\zeta_j^{(q)} \tag{5.15}$$

where $A_{ij}^{\alpha\beta;p}$ and $B_{ij}^{\alpha\beta;pq}$ are coupling constants whose different components are constrained by the residual symmetries. Using this in the Eq. 5.7, we obtain the complete orbital-phonon coupling that is central to the vibrational Raman scattering.

$$H_{orb-ph} = \sum_{i,p,\beta}\left[\Gamma^{p,\beta}\tau_i^{\beta} + \sum_{j,\alpha} A_{ij}^{\alpha\beta;p}\tau_i^{\alpha}\tau_j^{\beta}\right]\zeta_i^{(p)} + \sum_{ij}\sum_{\alpha\beta,pq} B_{ij}^{\alpha\beta;pq}\tau_i^{\alpha}\tau_j^{\beta}\zeta_i^{(p)}\zeta_j^{(q)} \tag{5.16}$$

The phonon renormalistion can then be computed perturbatively due these interactions.
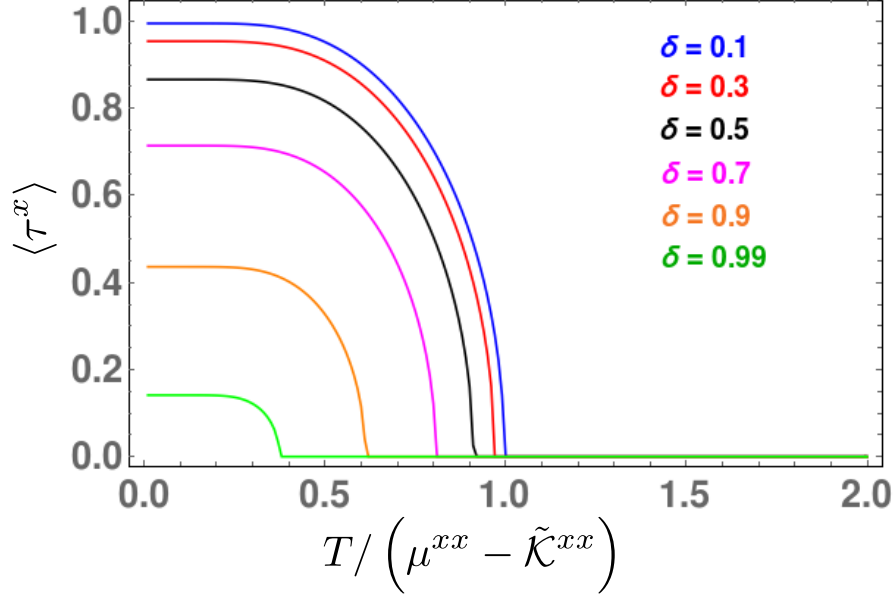
(a)
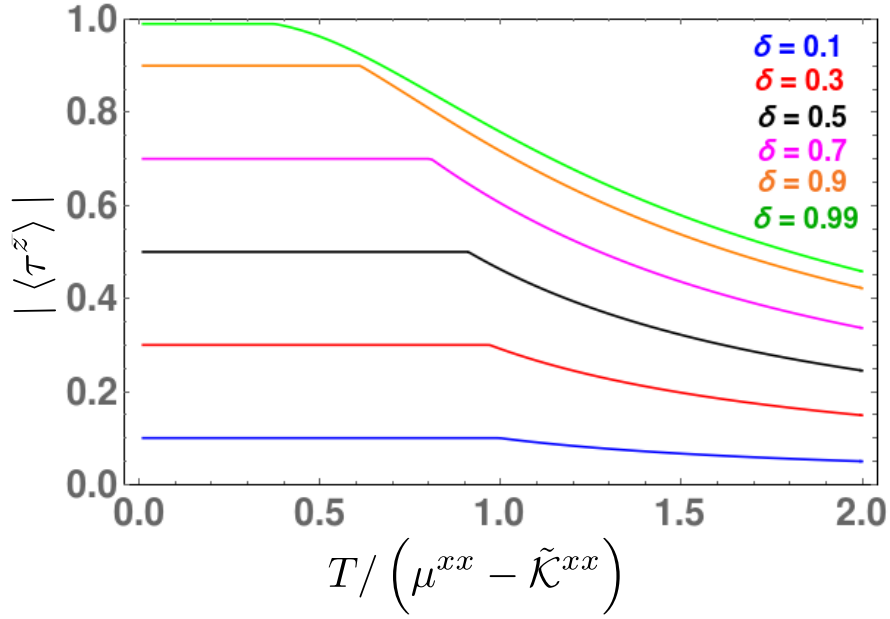
(b)

Figure 5.3: Orbital reordering due to the orbital fluctuations below T_c

The renormalised phonon parameters generically get contribution from both the anharmonic effects and orbital reordering, hence we write

$$\Delta\omega^{(p)} = \omega^{(p)} - \omega_0 = \Delta\omega^{(p)}_{anh} + \Delta\omega^{(p)}_{orb} \tag{5.17}$$

$$\Pi^{(p)} = \mid \Pi^{(p)}_{anh} + \Pi^{(p)}_{orb} \mid \tag{5.18}$$

where the subscript "*anh*" and "*orb*" represent the contributions due to the anharmonic effects and orbital reordering, respectively. While the anharmonic contribution to the phonon parameters are usually determined from the fitting of the experimental data at high temperatures (see Eq. 5.2), the orbital contributions are computed here due to the orbital-phonon coupling which we present now.

The leading order renormalisation of the frequency is is given by

$$\Delta\omega_{orb}^{(p)} \propto B_{ij}^{\beta\gamma;pp}\langle\tau_i^\beta\tau_j^\gamma\rangle \tag{5.19}$$

Clearly, the frequency renormalization due to orbital reordering is determined by the equal-time spin-correlators on nearest neighbours. Within our minimal model, approximating $\langle\tau_i^\alpha\tau_j^\beta\rangle \approx \langle\tau^\alpha\rangle\langle\tau^\beta\rangle$ below T_c, we obtain the results that are plotted in Fig. 5.4(a) as a function of temperature for various representative choices of the coupling constants. In particular, it is clear from these plots that the softening or hardening of the phonon is determined by the sign of the coupling $B_{ij}^{\beta\gamma;pp}$. We see both these behaviours for different phonons that are consistent with the experimental observation [see Fig. 5.1(a)]. An estimate of these coupling constants, however, requires a more microscopic calculation which is beyond the purview of the present symmetry-based arguments.

Turning to the linewidths, we calculate it via diagrammatic perturbation theory from the imaginary part of the phonon self-energy arising due to its scattering of phonons with τ_i^αs. To the leading order of perturbation theory, it is given by,

$$\Pi_{orb}^{(p)} \propto \mathcal{I}m\left(\int_0^\beta d\tau\, e^{i\omega_n\tau}\langle\langle\hat{T}\left[\Gamma^{(p)\beta}\tau_i^\beta(\tau) + \sum_j A_{ij}^{\beta\gamma;(p)}\tau_i^\beta(\tau)\tau_j^\gamma(\tau)\right]\right.$$
$$\left.\times\left[\Gamma^{(p)\beta'}\tau_i^{\beta'}(0) + \sum_k A_{ik}^{\beta'\gamma';(p)}\tau_i^{\beta'}(0)\tau_k^{\gamma'}(0)\right]\rangle\rangle\right)_{i\omega_n\to\omega+i0^+} \tag{5.20}$$

The expression can further be simplified which is shown in the Appendix C.1. The resultant leading order Raman linewidth is given by

$$\Pi_{orb}^{(p)}(\omega) \sim \sum_{\mu,\nu=x,z} \mathcal{M}_{\mu\nu}\mathcal{I}m\left[\tilde{\mathcal{C}}_{\mu\nu}\left(\mathbf{k}=0,\omega+i0^+\right)\right] \tag{5.21}$$

where $\tilde{\mathcal{C}}_{\mu\nu}(\mathbf{k}, i\omega_n)$ is the Fourier transform of the time-ordered orbital correlation functions,

$\mathcal{C}_{\mu\nu}(\mathbf{r}, \tau) = \langle \hat{T} (\tau_{\mathbf{r}}^{\mu}(\tau) \tau_{\mathbf{0}}^{\nu}(0)) \rangle - \langle \tau_{\mathbf{r}}^{\mu}(\tau) \rangle \langle \tau_{\mathbf{0}}^{\nu}(0) \rangle$, and $M_{\mu\nu}$ is a constant whose form can be found in Appendix C.1. The correlation functions for the orbital degrees of freedom are explicitly calculated within a quadratic approximation (see Appendix C.2 for details). We plot the temperature dependence of the linewidth in Fig. 5.4(b). For simplicity, we also assume the coupling coefficients, $\mathcal{M}_{\mu\nu}$, to be temperature independent, and therefore this is now completely controlled by the two-point dynamic correlators of the orbitals. We note that such behaviour is in direct conformity with the experimental observation [see Fig. 5.1(b)].

At this point, we would like to note that the phonon anomalies which were described in the earlier chapters arise due to the opening up of new scattering channels due to the fractionalistion in a QSL phase, hence such effects are quite generic and expected to happen in any QSL phase with moderate magnetoelastic coupling. However in this case, in addition to the orbital-phonon coupling, a central role behind such anomaly is played by the non-trivial interplay of the J-T effects and the orbital fluctuations, which are strongly material dependent. Thus on a generic ground, such effects are not expected to be universal and their experimental realisation in other contexts might be more challenging.
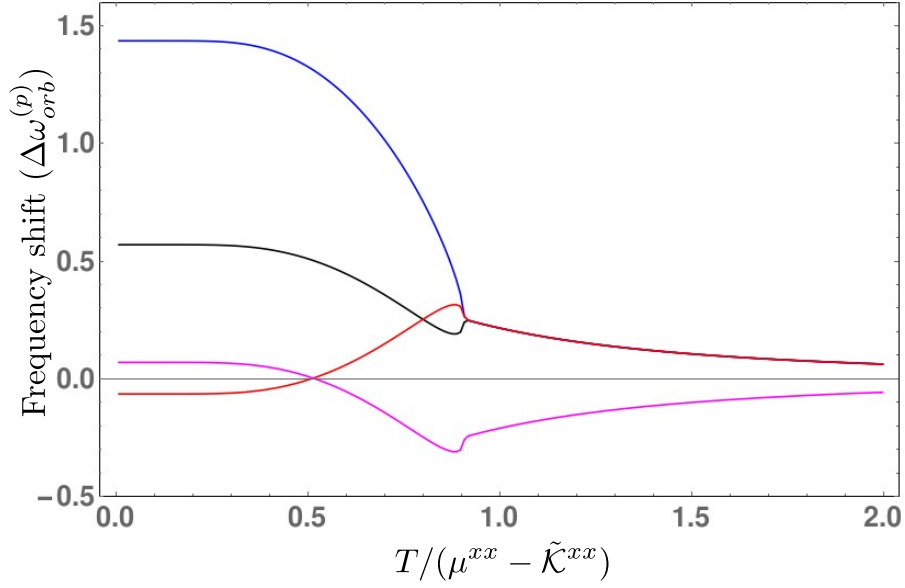
(a)
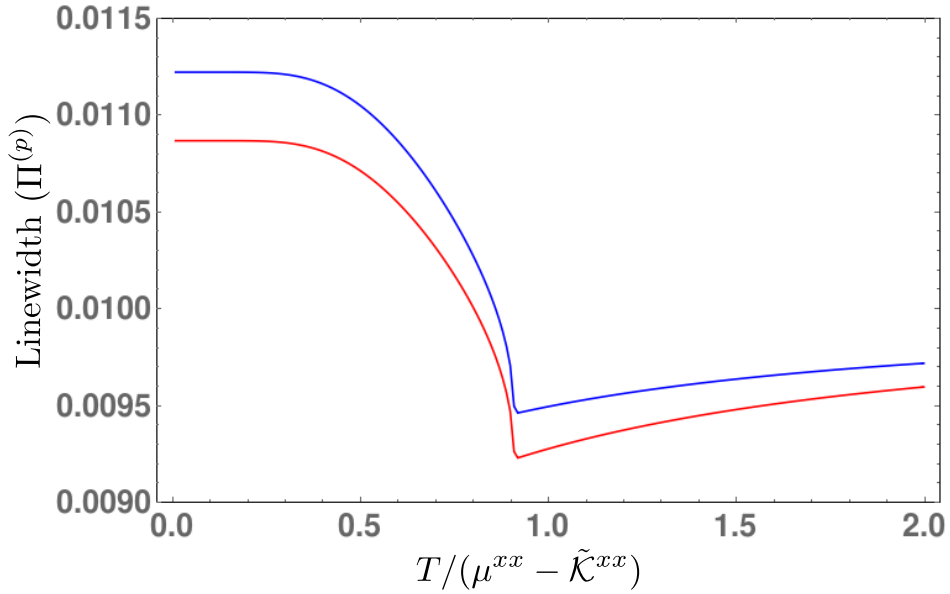
(b)

Figure 5.4: **Frequency and linewidth renormalisation from theoretical calculations: (a)** Frequency shift due to the orbital reordering. Blue, black, red and magenta curves are obtained by choosing $(B^{xx;pp}, B^{zz;pp}, B^{xz;pp})$ to be $(1, 1, 1)$, $(1, 1, -1)$, $(-1, 1, -1)$ and $(1, -1, -1)$, respectively. **(b)** Linewidth renormalisation of phonon. For blue and red curves, we choose $\Gamma_0 = 0.01$, $\mathcal{M}_{xx} = \mathcal{M}_{xz} = -1$ and $\Gamma_0 = 0.01$, $\mathcal{M}_{xx} = -0.7$, $\mathcal{M}_{xz} = -1$, respectively and set all other parameters to zero. For both the panels, $\delta = 0.5$.

CHAPTER 6

SPIN-$3/2$ ICE

6.1 Introduction

In this chapter, we describe the possibility of realising new kinds of frustrated magnets including low-energy magnetic excitations beyond the lowest energy magnetic doublet. This approach has already been proven to be very insightful in several cases, with the novel features reported both in classical [147, 148] and quantum [20, 149] versions of these models. Interestingly, the understanding of these systems allows us to explore more exotic gauge structures, and associated fractionalisations in the solid state set ups [20, 21, 147–149], as well as to realise various unconventional phases and associated phase transitions.

In the search for novel QSL phases in magnetic insulators, the primary focus has been on spin-1/2 systems where the quantum fluctuations are significantly strong. For systems with higher spins ($S > 1/2$), it is generically expected that the spins are more prone to order magnetically. However, there are interesting exceptions to this, starting with the symmetry protected topological AKLT phases for $S = 1$ chains [150] and its higher dimensional analogues [150, 151], as well as $S = 1$ QSLs [152, 153]. This has received particular attention in recent times with several examples of multiorbital magnets with the spin moments $S > 1/2$ [154, 155]. In most of these cases, the large spin representations arise primarily in two ways – (1) due interplay of orbital degeneracy whence the electrons align in order to reduce Coulomb interactions (via Hund's rules) typically in 3d transition metals, or, (2) due to spin-orbit coupling (SOC) such that the total moment of each electron $J = L + S$ is larger than $1/2$. The low energy spin physics is then described in terms of the degenerate $(2S + 1)$ states at every site which interacts via symmetry-allowed interactions.

In this work, we show an alternate novel route for stabilising frustrated $S = 3/2$ magnets with novel paramagnetic phases where the large spin occurs due to almost degenerate crystal electric field (CEF) doublets that arise in rare-earth pyrochlore magnets due to the intricate interplay of electron-electron Coulomb interactions, SOC and CEF [12, 24, 85, 86]. Remarkably, the splitting of the doublets is already known to be low in several candidate pyrochlore magnets [104, 156]. We further show that the splitting can be tuned via phonons due to the
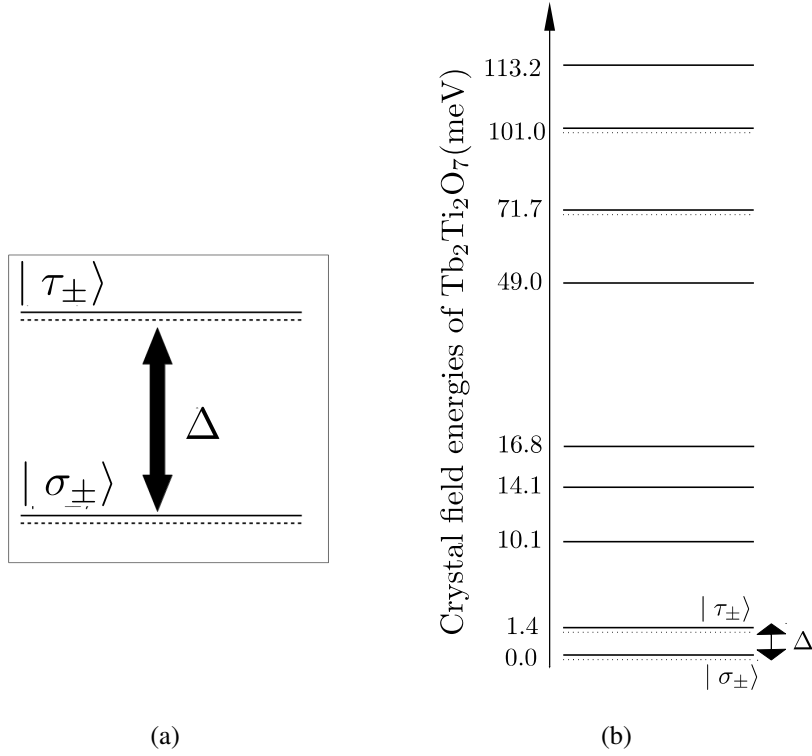
Figure 6.1: (a) **Onsite low energy CEF doublets of our model**, (b) **Onsite CEF energy levels of $Tb_2Ti_2O_7$ [156]:** In the low-energy theoretical formulation, we only consider the lowest two doublets denoted by $|\sigma_\pm\rangle$ and $|\tau_\pm\rangle$, separated by an energy gap of Δ (Eq. 6.1).

magnetoelastic coupling present in these compounds, leading to the interesting possibility of observing both $S = 3/2$ and $S = 1/2$ [12, 19, 42, 49, 88] ice in various candidate materials with small and large CEF splitting, respectively, along with a rich physics in the intermediate regime as well. In fact, here we discover a particular scenario where the lowest excitations of the model are very different from the excitations of a $S = 1/2$ ice [12, 42, 49], which are akin to the magnetic monopoles of the emergent magnetostatics. These new excitations are shown to have no gauge charges under the emergent gauge transformation, which in turn results into a drastic consequence on their dynamics – they become unusually immobile and robust under thermal fluctuations. This leads to an interesting possibility of a very slow equilibration process of the $S = 3/2$ ice at low temperatures via *dynamical arrest* of these excitations.

In the following sections, we now first give the details of our lattice model and then go into the discussion of various interesting features associated with it.

6.2 Theoretical model

Here we consider the pyrochlore geometry with a different CEF scheme. The onsite low-lying CEF energy levels of our model are shown in the schematic of Fig. 6.1(a) where $| \sigma_{\pm} \rangle$ and $| \tau_{\pm} \rangle$ denote the ground state doublet and first excited doublet respectively of the onsite Hilbert space separated by a small energy scale Δ. All other CEF levels are well separated from these low-energy doublets, hence, ignored in the low-energy description. The central attempt of this work is to understand what kind of new features such model gives rise to, due to the presence of such low-lying excitations.

A natural description of such model can be obtained in terms of effective $S = 3/2$ operators, where $S^z = \pm 1/2$ and $S^z = \pm 3/2$ denote the σ and τ doublets respectively. The CEF splitting Hamiltonian for this manifold is then given by (the local [111] direction that forms the natural axis of these materials)

$$H_0 = \frac{\Delta}{2} \sum_i \left((S_i^z)^2 - \frac{1}{4} \right) , \tag{6.1}$$

while the leading order AFM Ising interactions between nearest neighbours are of the form,

$$H^{cl} = J_{zz} \sum_{\langle ij \rangle} S_i^z S_j^z . \tag{6.2}$$

Together they lead to a novel generalisation of the "Ice rules"– the spin-3/2 Ice – with new consequences both at the classical and quantum level.

Remarkably, in the experiments, such models have a concrete realisation in the rare-earth pyrochlore, $Tb_2Ti_2O_7$. The CEF levels for the Tb^{3+} ion in $Tb_2Ti_2O_7$ are schematically depicted in Fig. 6.1(b) [156] to indicate its proximity to our model (also see Appendix D.1). The higher levels can be safely ignored due to their large gap, below the Curie-Weiss temperature scale of the compound, which is ≈ 19 mK [156]. We note that for further material realisations, the ideal candidates would be the non-Kramers [29, 101, 104, 156] subclass of the rare earth pyrochlores (note that $Tb_2Ti_2O_7$ also belongs to this category). In this subclass, as we have already shown in Chapter 4, the magnetoelastic coupling is significantly large, leading to the possibility of hybridisation of the two CEF levels via phonons and renormalisation of the CEF gap. With this added tunability in the CEF scheme, such candidates are the natural choice for realising our theoretical model. In the following section, we explicitly show the phonon-

mediated hybridisation of the CEF levels considering their coupling to the dynamical phonons.

6.3 Magnetoelastic coupling and tunability of the CEF gap

In Chapter 4 of this thesis, we have already given a derivation of the linear magnetoelastic coupling in the non-Kramers pyrochlores, using detailed symmetry analysis. Here we discuss another derivation of the same but from a more microscopic point of view. As we will see, this naturally generalises the linear coupling to the higher non-Kramers CEF doublets, and takes care of the possibility of the hybridisation of CEF levels as well.

To start with the derivation, we first introduce a microscopic description of spins using parton decomposition technique. Two flavours of hard-core bosons are introduced to represent each doublet which are as follows.

$$| \pm \rangle = b_\pm^\dagger \, | \, 0 \rangle \ , \quad | \pm \rangle = d_\pm^\dagger \, | \, 0 \rangle \ . \tag{6.3}$$

Now the effective spin-1/2s (σ^μ and τ^μ), obtained by projecting the angular momentum in these two doublets, can be represented by these hard-core bosonic operators via the well-known spin-1/2 to hard-core boson mapping:

$$\sigma^\mu = \frac{1}{2} b_\alpha^\dagger \eta_{\alpha\beta}^\mu b_\beta \ , \quad \tau^\mu = \frac{1}{2} d_\alpha^\dagger \eta_{\alpha\beta}^\mu d_\beta \ . \tag{6.4}$$

where η^μ denotes three Pauli matrices for $\mu = x, y, z$. The magnetoelastic coupling can now be obtained by writing symmetry allowed coupling between $\mathbf{e_g}$ phonons and microscopic parton degrees of freedom. This is given by,

$$H_{\text{sp}-\text{ph}} = H_{\sigma-ph} + H_{\tau-ph} + H_{\sigma-\tau-ph} \ , \tag{6.5}$$

where,

$$H_{\sigma-ph} = \Gamma_\sigma (\zeta_x \sigma^x + \zeta_y \sigma^y) \ ,$$
$$H_{\tau-ph} = \Gamma_\tau (\zeta_x \tau^x + \zeta_y \tau^y) \ ,$$
$$H_{\sigma-\tau-ph} = \Gamma [\zeta_x (d_\uparrow^\dagger b_\downarrow + d_\downarrow^\dagger b_\uparrow) - i\zeta_y (d_\uparrow^\dagger b_\downarrow - d_\downarrow^\dagger b_\uparrow) + h.c.] \ , \tag{6.6}$$

where, (ζ_x, ζ_y) are two normal modes of the pyrochlore lattice which forms $\mathbf{e_g}$ irreducible
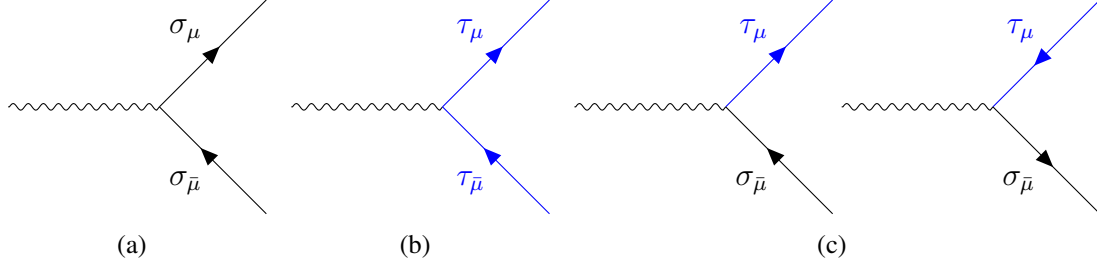
Figure 6.2: **Feynman diagram of the magnetoelastic coupling of Eq. 6.6:** (a), (b) and (c) represent the interaction due to $H_{\sigma-ph}$, $H_{\tau-ph}$ and $H_{\sigma-\tau-ph}$ respectively. Black and blue solid lines denote the particles in the ground state and first excited doublet. The curly line stands for the phonon excitations. $\mu \in (+, -)$ and $\bar{\mu}$ represents the opposite flavour of μ.

representation. It is evident from the above expression that $H_{\sigma-ph}$ and $H_{\tau-ph}$ give the linear coupling between the low energy doublets and phonons, whereas $H_{\sigma-\tau-ph}$ produces a coupling between ground state doublet, the excited doublet, and the phonon. These are represented in the Feynman diagrams given by Fig. 6.2.

The energy gap (Δ) of the CEF levels being small in our model, the phonons can now dynamically generate significant coupling between the two doublets. Treating the magnetoelastic coupling as the smallest energy scale of the problem, we integrate out the optical phonons considering second-order processes (see Fig. 6.3), where a virtual photon is exchanged between the two doublets. This leads to an effective hybridisation of the doublets, which is given by,

$$H_{\sigma-\tau} = \frac{1}{4\Omega} \left[\Gamma_\sigma^2 (n_{b_\uparrow} + n_{b_\downarrow}) + \Gamma_\tau^2 (n_{d_\uparrow} + n_{d_\downarrow}) + \Gamma_1 (\sigma_x \tau_x + \sigma_y \tau_y) + \Gamma_2 (b_\uparrow^\dagger d_\uparrow + b_\downarrow^\dagger d_\downarrow + h.c.) \right] ,$$

(6.7)

where, $\Gamma_1 = 2\Gamma_\sigma \Gamma_\tau$, $\Gamma_2 = \Gamma(\Gamma_\sigma + \Gamma_\tau)$, $n_{b_\mu} = b_\mu^\dagger b_\mu$, $n_{d_\mu} = d_\mu^\dagger d_\mu$ and Ω is energy of the optical $e_{\mathbf{g}}$ mode. We note that the higher order processes involving multiple phonons are suppressed in the relevant low temperature regime. The first two terms of the above Hamiltonian only contributes to the renormalisation of the CEF gap, but does not change anything else. The third term of the Hamiltonian has no matrix element in the physical CEF Hilbert space, which has the single particle constraint given by, $n_{b_\uparrow} + n_{d_\downarrow} + n_{d_\uparrow} + n_{d_\downarrow} = 1$. The only relevant effective coupling between ground state doublet and excited doublet is given by the last term of Eq. 6.7.

Further rewriting the above Hamiltonian in terms of the $S = 3/2$ operators, we obtain,

$$H_{\sigma-\tau} = \sum_i \left[\Gamma_1 (S_i^z)^2 + \Gamma_2 \left(\frac{10}{3} S_i^x - T_i^{xxx} - T_i^{yyx} \right) \right] ,$$

(6.8)

85
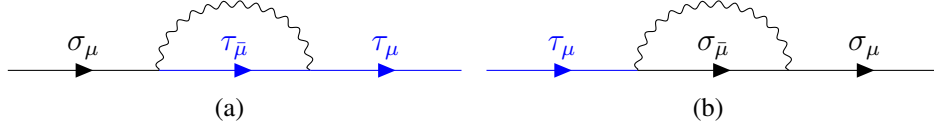
Figure 6.3: Hybridisation of ground state and first excited doublet via virtual phonon exchange process

(a)

(b)
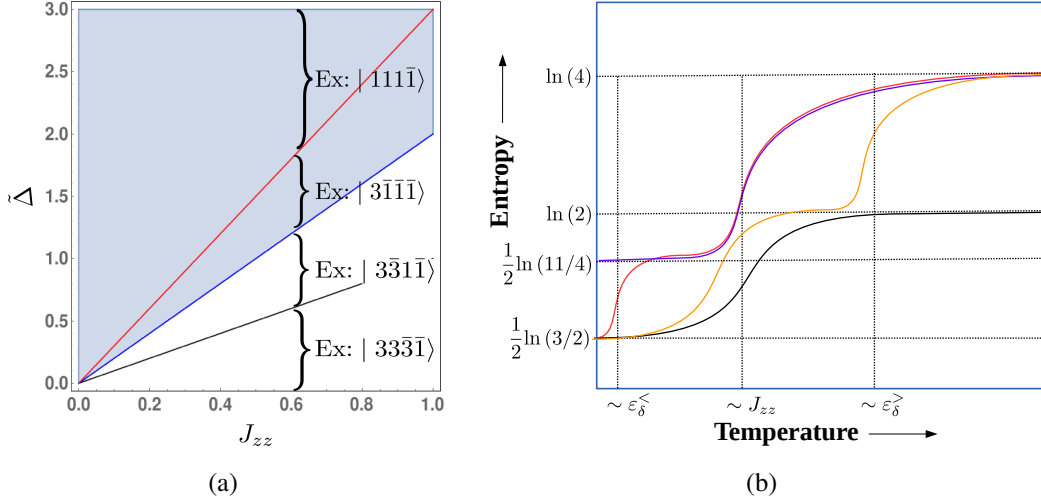
Figure 6.4: **(a) Ground state (GS) and the first excited state (Ex) in different parameter regime :** Red, blue and black line correspond to $\tilde{\Delta} = 3J_{zz}$, $\tilde{\Delta} = 2J_{zz}$, $\tilde{\Delta} = J_{zz}$ respectively. The ground state configurations in the blue region and the white region are given by $|11\bar{1}\bar{1}\rangle$ and $|33\bar{3}\bar{3}\rangle$, respectively. The first excited states (denoted by Ex in the figure) at different region is explicitly shown in the plot.

Clearly, the effect of the first term is to renormalise the CEF gap, $\Delta \to \tilde{\Delta} = \Delta + 2\Gamma_1$ resulting in the possibility of the tunability of the CEF gap in suitable materials. In the last term, $T^{\alpha\beta\gamma} = \frac{1}{6}\mathcal{S}\left[S^\alpha S^\beta S^\gamma\right]$ is the S=3/2 octupole operator ($\mathcal{S}[\cdot]$ denotes symmetrisation with respect to the spin indices $\alpha, \beta, \gamma = x, y, z$). This term induces quantum fluctuations and is responsible for the mixing of σ and τ. Momentarily, we shall assume that such mixing is small and shall return to them along with other symmetry allowed higher rank operators below.

6.4 Phase diagram

With the renormalised CEF gap, $\tilde{\Delta}$, consider the full classical spin-3/2 ice problem given by Eqs. 6.1 and 6.2, which can be rewritten as

$$H = \sum_{\boxtimes} \left[\frac{\left(\tilde{\Delta} - 2J_{zz}\right)}{4} \sum_{i \in \boxtimes} (S_i^z)^2 + \frac{J_{zz}}{2} \left(\mathcal{Q}_{\boxtimes}\right)^2 \right] , \tag{6.9}$$

86

where $\mathcal{Q}_{\boxtimes} = \eta_{\boxtimes} \sum_{i \in \boxtimes} S_i^z$ with $\eta_{\boxtimes} = 1(-1)$ for $\boxtimes \in A(B)$ tetrahedra. According to the standard magnetostatic [88] description of the classical spin ice (CSI), $\mathcal{Q}_{\boxtimes}$ measures the charge of magnetic monopoles on a tetrahedron. We now discuss various aspects of the model, stabilized at different regions of $\tilde{\Delta} - J_{zz}$ plane.

It is instructive to start with the special limit of $\tilde{\Delta} = 2J_{zz}$ denoted by the blue line in Fig. 6.4(a). Compared to the $S = 1/2$ CSI, the ground state ice-manifold obeying $\mathcal{Q}_{\boxtimes} = 0$ per tetrahedron now consists of 44 configurations at single tetrahedron level out of the 256 states. These *3/2-ice* states are given by $| 11\bar{1}\bar{1}\rangle$, $| 33\bar{3}\bar{3}\rangle$, $| 3\bar{1}\bar{1}\bar{1}\rangle$, $| 1\bar{1}3\bar{3}\rangle$ and all the other configurations are generated by applying TR and lattice symmetries. A Pauling-like estimate of the extensively degenerate ground state manifold leads to ground state entropy of $\frac{1}{2} \ln \frac{11}{4}$ per spin which is $\approx 36\%$ of the total entropy and is marginally larger than the CSI case ($\approx 29\%$). Therefore, one expects the zero temperature entropy per spin to saturate at $\frac{1}{2} \ln \frac{11}{4}$ as shown by the blue line in Fig. 6.4(b). Long distance spin correlations in the extended ice manifold can be calculated using the standard mapping of the problem to magnetostatics [49, 97, 98] where $\mathcal{Q}_{\boxtimes} = 0$ leads to Gauss's law resulting in dipolar form ($\langle S_{\mathbf{r}}^z S_{\mathbf{r'}}^z \rangle \sim \frac{1}{|\mathbf{r}-\mathbf{r'}|^3}$) as in CSI. In addition, higher spin representation lead to non-trivial power-law quadrupolar and octupolar correlations and are given by $- \langle\langle Q_{\mathbf{r}}^{zz} Q_{\mathbf{r'}}^{zz}\rangle\rangle \sim \frac{1}{|\mathbf{r}-\mathbf{r'}|^6}$, $\langle\langle T_{\mathbf{r}}^{zzz} T_{\mathbf{r'}}^{zzz}\rangle\rangle \sim \frac{1}{|\mathbf{r}-\mathbf{r'}|^3}$. Here $\langle\langle ...\rangle\rangle$ denotes the connected part of the correlator in the ice manifold. Note that the octupolar correlations are dipolar since they receive parasitic contributions from the spin correlations while the quadrupolar correlations only receive contributions that are square of the $\langle S_{\mathbf{r}}^z S_{\mathbf{r'}}^z \rangle$.

The excitations above the spin-$3/2$ ice manifold are *magnetic monopoles* with integer charge, $\mathcal{Q}_{\boxtimes} = -6, \cdots, +6$ with the lowest excitations ($\mathcal{Q}_{\boxtimes} = \pm 1$) being 80-fold degenerate for a single tetrahedron. These states are given by $| 111\bar{1}\rangle$, $| 3\bar{3}11\rangle$, $| 1\bar{1}3\bar{1}\rangle$, $| 33\bar{3}\bar{1}\rangle$, and others generated by TR and lattice symmetries.

Departure from the $\tilde{\Delta} = 2J_{zz}$ line splits the above extended ground state degeneracy in favour of the regular spin-ice manifold whence the ground state degeneracy becomes 6 for a single tetrahedron and a Pauling entropy of $\frac{1}{2} \ln \frac{3}{2}$ – as is well known for a CSI. In fact, depending on the relative values of J_{zz} and $\tilde{\Delta}$, there is a multi-step partial quenching of entropy, as shown in Fig. 6.4(b). Similar partial quenching of the entropy is observed earlier in the spin-1/2 ice via the application of a magnetic field along the easy axis ([111]) direction [49, 157].

For $\tilde{\Delta} > 2J_{zz}$ ($\tilde{\Delta} < 2J_{zz}$), the ground state is given by the $| 11\bar{1}\bar{1}\rangle$ ($| 33\bar{3}\bar{3}\rangle$) configuration which is shown in Fig. 6.4(a) which is a CSI in the $S = \pm 1/2$ ($\pm 3/2$) manifold with the other
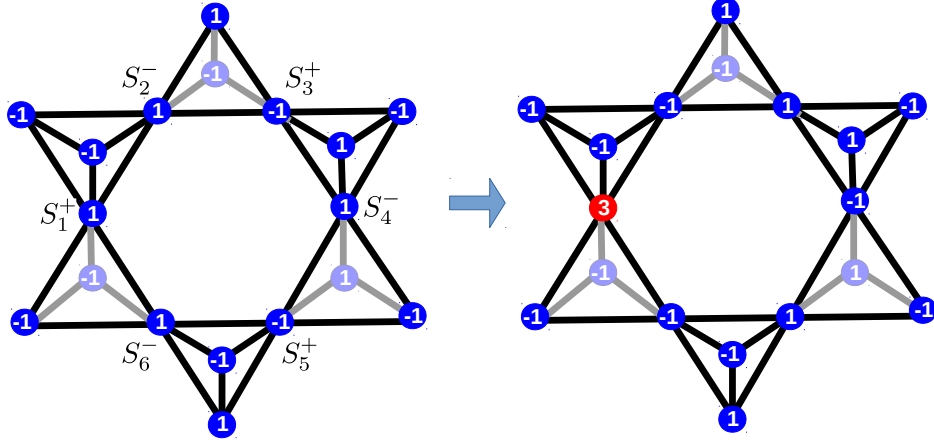
Figure 6.5: **Creation of a δ-excitation** requires at least six spin-flips on a elementary hexagonal loop: A representative operator shown here is $S_1^+ S_2^- S_3^+ S_4^- S_5^+ S_6^-$. Blue (red) discs represent $S^z = \pm 1/2$ ($S^z = \pm 3/2$) with red being the sites of δ-excitations.

states of the extended ground state manifold now forming excitations. In the more physical limit of $\tilde{\Delta} > 2J_{zz}$ these excitations, which we call δ-excitations, are comprised of states of the form $|3\bar{1}\bar{1}\bar{1}\rangle$ and $|\bar{3}111\rangle$ with an energy cost of $\varepsilon_\delta = \frac{\tilde{\Delta} - 2J_{zz}}{2}$. In fact, for $3J_{zz} > \tilde{\Delta} > 2J_{zz}$, the δ-excitations cost less than the lowest $\mathcal{Q}_{\boxtimes} = \pm 1$ magnetic monopoles and are the lowest energy excitations in the system– as indicated in Fig. 6.4(a). It is easy to see that the δ-excitations reside on the sites of the pyrochlore lattice as shown in the right-hand diagram of Fig. 6.5. Foremost, both the tetrahedra associated with the site individually have zero *magnetic* charge, *i.e.*, $\mathcal{Q}_{\boxtimes} = 0$. In this sense, they are a new class of low energy *gauge* neutral excitations not present in spin-1/2 ice. Due to the gapping out of the δ-excitations, the correlations at low temperature now acquire an exponential decay of the form $e^{-\varepsilon_\delta/T}$.

6.5 Creation and annihilation of the δ-excitations

The δ-excitation (as indicated in Fig. 6.5), unlike the magnetic monopoles, cannot be created or annihilated by a single spin flip operation out of an ice manifold, but require a minimum set of six-spin flips over a hexagonal loop of the pyrochlore lattice. Hence, creating them out of incoherent local thermal fluctuations at finite temperature is less probable than the magnetic monopoles even though the latter is energetically more costly. In fact, the process of creating a single δ-excitation is in a one-to-one correspondence with the so-called non-contractible monopoles [158] in spin-1/2 ice although they are different branches of excitations. Alternatively, the annihilation of a single δ-excitation by such thermal fluctuations as single spin-flip

protocol requires a two-step process: first, it splits into a oppositely charged non-contractible magnetic monopole pair and then the monopole pair gets annihilated upon recombination through a series of spin-flips. Clearly, the first step requires activation energy which makes the annihilation of the δ-excitations exponentially suppressed at low temperatures leading to long-lived δ-excitations in quenches [158].

6.6 Entropic interaction between the δ-excitations in the low temperature regime

In the temperature regime, $T \leq \varepsilon_\delta$, the magnetic monopoles are extremely rare and we have a dilute concentration of δ-excitations. At these low temperatures, as argued above, these long-lived metastable states are almost frozen at the sites in a background sea of thermally fluctuating $S = 1/2$ ice rule preserving states.

In absence of such δ-excitations altogether, starting with the well-known spin ice to magnetostatics mapping – $\mathbf{B} \cdot \hat{\mathbf{e}}_{\mathbf{r}\mu} = \eta_\boxtimes S^z_{\mathbf{r}\mu}$ (where $S^z_i = \pm 1/2$) – the entropic contribution to the free energy, $\mathcal{F}$, for a CSI is obtained as $\mathcal{F}/T = \frac{\kappa}{2} \int d^3\mathbf{r} \, \mathbf{B}^2$ with the ice-rules implemented via $\boldsymbol{\nabla} \cdot \mathbf{B} = 0$.

The δ-excitations locally pin the magnetic field as $\mathbf{B} \cdot \hat{\mathbf{e}}_{i\alpha} = \mu_{i\alpha} 3/2$, where $\mu_{i\alpha} = \text{sgn}\left(S^z_{i\alpha}\right)$ at the frozen locations. This can be implemented at low energy via incorporating a cost term $U \sum_{i \in "\delta"} (\mathbf{B} \cdot \hat{\mathbf{e}}_{i\alpha} - \mu_{i\alpha} 3/2)^2$ where the sum runs over only the sites of the excitations and where $U > 0$ is a large number. Expanding the square and coarse-graining, we find that the free energy in presence of the δ-excitations is given by

$$\mathcal{F} = \int d^3\mathbf{r} \left(\frac{\tilde{U}}{2} \mathbf{B}^2 - U\mathbf{M} \cdot \mathbf{B} \right) , \tag{6.10}$$

where $\tilde{U}$ is the renormalised *magnetic permeability* and very suggestively, we have used $\mathbf{M}$ to define new *magnetisation* arising from the δ-excitations as, $\mathbf{M}(\mathbf{r}) = \sum_{i\alpha \in "\delta"} 3\mu_{i\alpha}\delta\left(\mathbf{r} - \mathbf{r}_i\right) \hat{\mathbf{e}}_{i\alpha}$.

The δ-excitations can therefore serve as *magnetization* of the emergent magnetostatics. The entropic interaction between them can then be easily obtained by integrating out the background spin fluctuations, *i.e.*, $\mathbf{B}$ (see Appendix D.5) leading to effective interactions between the δ-excitations is given by

$$\mathcal{F}_\delta = \frac{9U^2}{16\pi\tilde{U}} \sum_{i\alpha, j\beta \in "\delta"} \mathcal{V}^{\alpha\beta}_{ij} \mu_{i\alpha}\mu_{j\beta} , \tag{6.11}$$
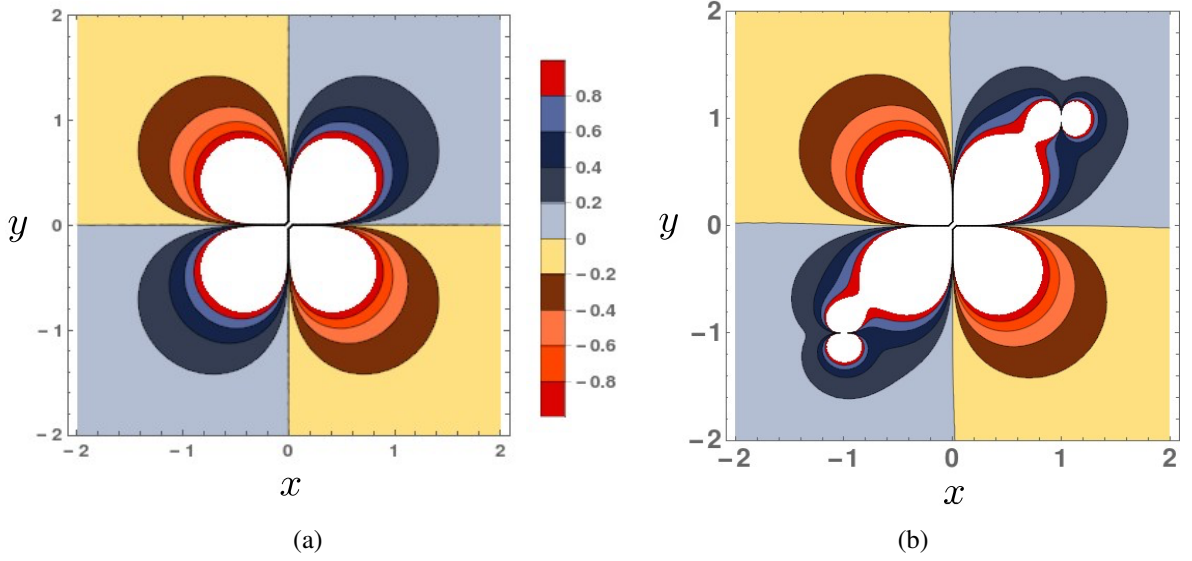
Figure 6.6: **Spin correlation function** between spins sitting at $\{0,0,0\}_{\mathbf{e_0}}$ and $\{x,y,z\}_{\mathbf{e_0}}$ in **(a)** absence of the δ-excitations, **(b)** presence of two δ-excitations sitting at $\{1,1,0\}$ and $\{-1,-1,0\}$.

where $\mathcal{V}_{ij}^{\alpha\beta} = \frac{r_{ij}^2 \hat{\mathbf{e}}_{i\alpha}\cdot\hat{\mathbf{e}}_{j\beta} - 3(\mathbf{r}_{ij}\cdot\hat{\mathbf{e}}_{i\alpha})(\mathbf{r}_{ij}\cdot\hat{\mathbf{e}}_{j\beta})}{r_{ij}^5}$ is the usual dipolar kernel. This long-range dipolar interaction is purely due to the interaction mediated via the emergent magnetic field and is similar to that between the *ghost-spins* in a dipolar-CSI with site dilutions [159]. In fact Eq. 6.11 is exactly the Hamiltonian arrived by Sen *et. al.* in Ref. [159] for dilute site impurities in $S = 1/2$ dipolar CSI and it was subsequently shown [160] to harbour a *topological spin spin-glass* phase for i and j being random. The crucial difference here, however, is there is no quenched disorder in the Hamiltonian in Eq. 6.9, but, it is self-generated via localised and possibly randomly placed metastable δ-excitations.

6.7 Spin-spin correlations

The free energy in Eq. 6.10 readily gives way to calculate the spin-spin correlations in presence of a dilute set of δ-excitations. As detailed in the Appendix D.5, this is given by:

$$\langle S_{\mathbf{r}\alpha}^z S_{\mathbf{r}'\beta}^z \rangle = \frac{C_1}{2\tilde{U}}\mathcal{V}_{\mathbf{r}\mathbf{r}'}^{\alpha\beta} + \frac{C_2 U^2}{4\tilde{U}^2}\sum_{i\mu,j\nu\in"\delta"}\mathcal{V}_{\mathbf{r}i}^{\alpha\mu}\mathcal{V}_{\mathbf{r}'j}^{\beta\nu}\mu_{i\mu}\mu_{j\nu} \,, \tag{6.12}$$

where C_1 and C_2 are two positive constants and the first term denotes the usual dipolar spin-correlations in CSI via $\mathcal{V}_{\mathbf{r}\mathbf{r}'}^{\alpha\beta}$ that results in pinch-points in momentum space observed in neutron scattering. The effect of δ-excitations is given by the second term, which arises from an

effective scattering of the usual spin-1/2s from the $\delta-$excitations due to possible entropic rearrangements in the ice manifold, and gives correction to the dipolar spin correlations. However, since $\mathcal{V}_{\mathbf{rr'}}^{\alpha\beta}$ falls off as $\sim \frac{1}{|\mathbf{r}-\mathbf{r'}|^3}$, the effect of the frozen δ-excitations become significant only near the frozen locations, the spin correlation remains mostly unaffected in the other places (see Fig. 6.6).

6.8 Other symmetry allowed interactions

We now briefly study the effect of other symmetry-allowed interactions in addition to Eq. 6.9. These additional interactions are primarily of two types– (1) classical interactions only involving S_i^z and its higher multipoles, and, (2) quantum which involves the spin-flip terms involving the transverse components.

6.8.1   Classical interactions

For the classical interactions, while there is no symmetry-allowed on-site terms there are bilinear terms given by

$$\Delta H^{cl} = \sum_{\langle ij \rangle} \left(J_Q Q_i^{zz} Q_j^{zz} + J_T T_i^{zzz} T_j^{zzz} \right) \ . \tag{6.13}$$

Here, $Q^{\alpha\beta} = \frac{1}{2} \mathcal{S} \left[S^\alpha S^\beta \right] - \frac{5}{4} \delta^{\alpha\beta} \mathcal{I}$ are the quadrupolar operators. Since, we have $S = 3/2$, the on-site Hilbert space allows for 15 operators that includes three spin, S_i^α, five quadrupole, $Q^{\alpha\beta}$, and seven octupole $T^{\alpha\beta\gamma}$ (also see Appendix D.3).

With $J_{zz} = 0$, the $J_Q > 0$ ($J_T > 0$) only model drives the system into the degenerate manifolds composed of : $| \pm 3 \pm 3 \pm 1 \pm 1 \rangle$ ($| 33\bar{3}\bar{3} \rangle$) configurations characterised by zero quadrupolar (octupolar) charge, i.e., $\mathcal{Q}_{\boxtimes}^Q = \eta_{\boxtimes} \sum_{i \in \boxtimes} Q_i^{zz} = 0$ ($\mathcal{Q}_{\boxtimes}^T = \eta_{\boxtimes} \sum_{i \in \boxtimes} T_i^{zzz} = 0$). While $| 33\bar{3}\bar{3} \rangle$ are usual spin ice configurations with $S^z = \pm 3/2$, the other one is more exotic with enhanced ground state degeneracy of 96 at single tetrahedron level resulting in significant enhancement of entropy per spin $\approx 65\%$. We dub it as *classical quadrupolar ice*.

Turning back to the above regime of our interest where $\varepsilon_\delta < J_{zz}$, for $\frac{J_Q}{J_{zz}} \ll 1$, the extended degeneracy of the special $\tilde{\Delta} = 2J_{zz}$ line is partially lifted from (at the single tetrahedron level) 44 to 24 comprised of the subset $| 3\bar{3}1\bar{1} \rangle-$ comprised of the 2-δ-excitations. In Fig 6.7, we show the energy dependence on J_Q/J_{zz} of different classes of low energy excitations for a representative point in the region $3J_{zz} > \tilde{\Delta} > 2J_{zz}$. The spin ice described above
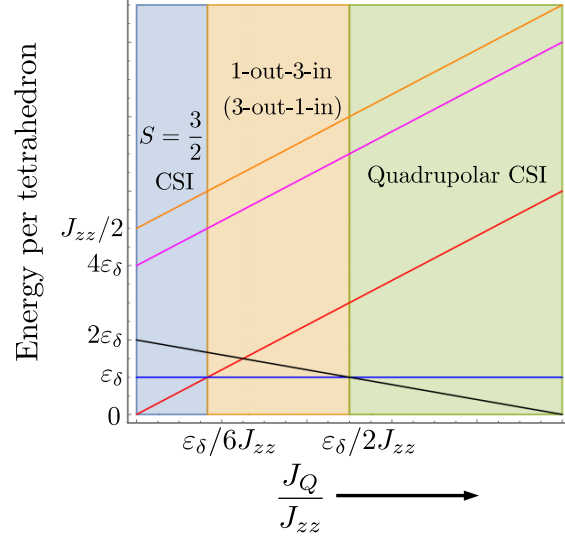
Figure 6.7: **Energy dependence of different states with quadrupolar exchange constant** (J_Q)**:** The octupolar interaction is set to $J_T = 0$. Red, blue, black, magenta and orange lines represent energy for $|\,11\bar{1}\bar{1}\rangle$, $|\,3\bar{1}\bar{1}\bar{1}\rangle$, $|\,33\bar{1}\bar{1}\rangle$, $|\,3\bar{3}\bar{3}\bar{3}\rangle$ and $|\,111\bar{1}\rangle$, respectively. Different colored regions represent various possible phases as mentioned in the figure.

survives along with its properties for $J_Q \ll \varepsilon_\delta$ as shown in the figure. However, in the regime $\frac{\varepsilon_\delta}{6} > J_Q > \frac{\varepsilon_\delta}{2}$, the δ-excitations condense resulting in a generalised version of 1-out-3-in (1-in-3-out) state, with minority spin being $S^z = 3/2\,(-3/2)$, comprised of states such as $|\,3\bar{1}\bar{1}\bar{1}\rangle$ $(|\,\bar{3}111\rangle)$. Such a state breaks both TR symmetry as well as point-group symmetries. For even larger $J_Q > \frac{\varepsilon_\delta}{2}$, the quadrupolar ice is obtained that is characterised by $\mathcal{Q}_\boxtimes^Q = 0$. Therefore, the phase diagram has two different classical Coulomb phases separated by a symmetry-broken one and presents a rather interesting situation. The effect of J_T in the same limit is much less interesting and only renormalises the special line of extensive degeneracy.

6.8.2 Quantum interactions

For the quantum interaction, we have both the on-site contributions with the on-site terms arising from coupling to phonons as discussed above in $H_{\sigma,\tau}$. The full onsite Hamiltonian $H_0 + H_{\sigma,\tau}$ can be fully diagonalised to obtain the eigenstates of a *rotated* S_i^z operator (See Appendix D.4). The bilinear spin-spin exchange terms (Eqs. 6.2 and 6.13) when written in this basis give rise to additional transverse exchange terms of the form

$$H^{qm} = J_\perp \sum_{\langle ij \rangle} \left(S_i^+ S_j^- + h.c. \right) + \cdots \tag{6.14}$$

92

where $\cdots$ refer to other symmetry allowed terms. For small, $\Gamma_2/\Delta \ll 1$– typically expected– the *rotation* is small and all the above analysis of the classical Hamiltonian remains completely valid albeit in the rotated basis.

This leads us to the effect of the intersite spin flip terms in Eq. 6.14 whose generic effect is to introduce quantum dynamics of various excitations leading to the quantum spin ice– a U(1) QSL – via resonating loops of spin flips [12]. They also provide dynamics of the emergent magnetic and electric monopoles and the gapless photons.

Here, however, we focus on the new δ-excitations which also become dynamic in presence of the spin-flip terms. However, because of their gauge neutrality, they hop only via the loop operators generated at higher order perturbation theory in Eq. 6.14– unlike the hopping of magnetic monopoles via single spin flip operations that leaves behind a gauge string. We find that to the lowest order, i.e., applying a single hexagonal loop operator– the smallest loop in a pyrochlore– the δ-excitation can hop only to the second or third nearest neighbour (see Fig. 6.8). Note that the nearest neighbour hopping is not forbidden but is allowed via a two-loop operator that is suppressed in perturbation theory.

Defining the creation (annihilation) operators for the δ-excitations as $a_{\mathbf{r}}^{\dagger}$ ($a_{\mathbf{r}}$), the hopping Hamiltonian for the δ excitations is written as,

$$H_\delta = -t \sum_{\mathbf{rr'}\in 2nn,3nn} \left(e^{i \oint \mathbf{A} \cdot d\mathbf{r}} a_{\mathbf{r}}^{\dagger} a_{\mathbf{r'}} + h.c. \right) , \tag{6.15}$$

where 2nn and 3nn represent second and third (sitting diagonally opposite on a hexagon) nearest neighbour site, $\oint \mathbf{A} \cdot d\mathbf{r}$ implies lattice curl of the emergent U(1) gauge field in the quantum spin ice calculated over the hexagonal loop of which both $\mathbf{r}$ and $\mathbf{r'}$ are a part of. Clearly, the δs being gauge neutral do not couple to the vector potential, but couples to the emergent electric flux, $\oint \mathbf{A} \cdot d\mathbf{r}$. Therefore the dispersion of the δ-excitations depends on the flux pattern. For the two well-known *zero* and π-flux quantum spin ice, this leads to relatively inverted band structures which are shown in Fig. 6.9 (see Appendix D.6 for details of the calculations). The minima of their energy occur at Γ and K points of the BZ, for zero and π-flux, respectively. Softening of the mode at Γ point leads to a *1-out-3-in* type state with the minority spin being in the $S^z = \pm 3/2$ state for the *zero*-flux state while that for the π-flux state leads to a modulated ordered pattern. This transition from the quantum spin ice appears to be different from Higgs's transition in usual quantum spin ice [17, 19].
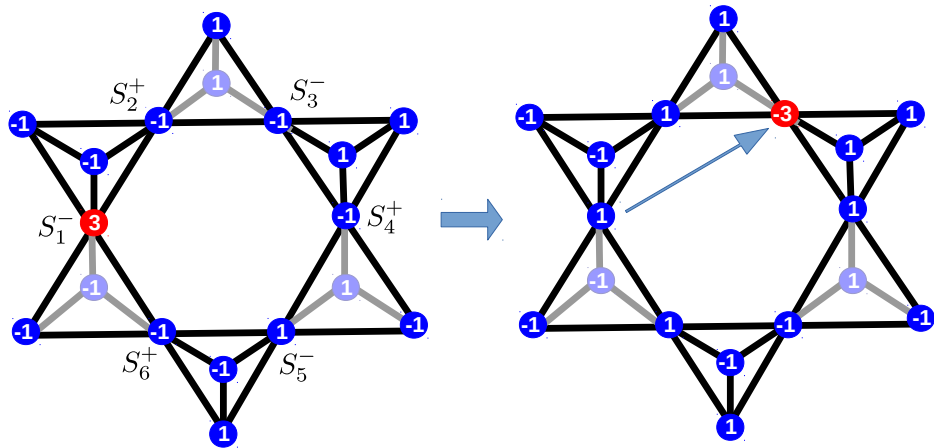
(a) Second nearest neighbour hopping of δ-excitations
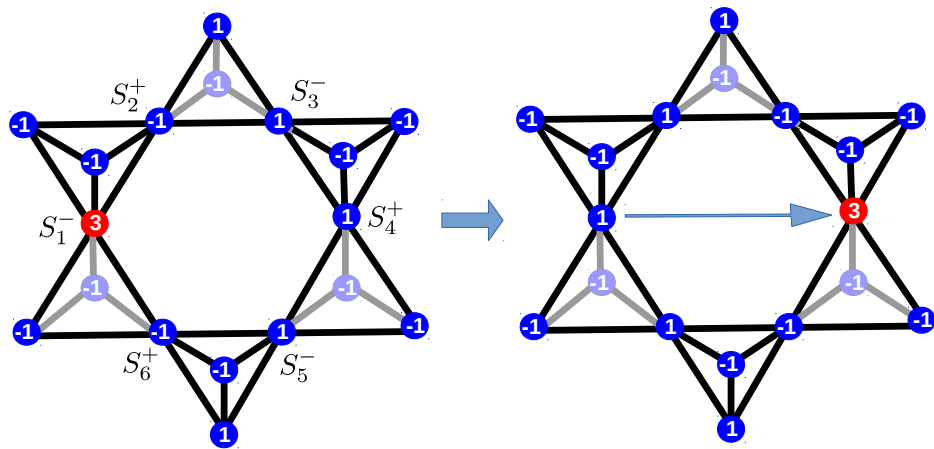
(b) Third nearest neighbour hopping of δ-excitations

Figure 6.8: Hopping process of the δ-excitations.
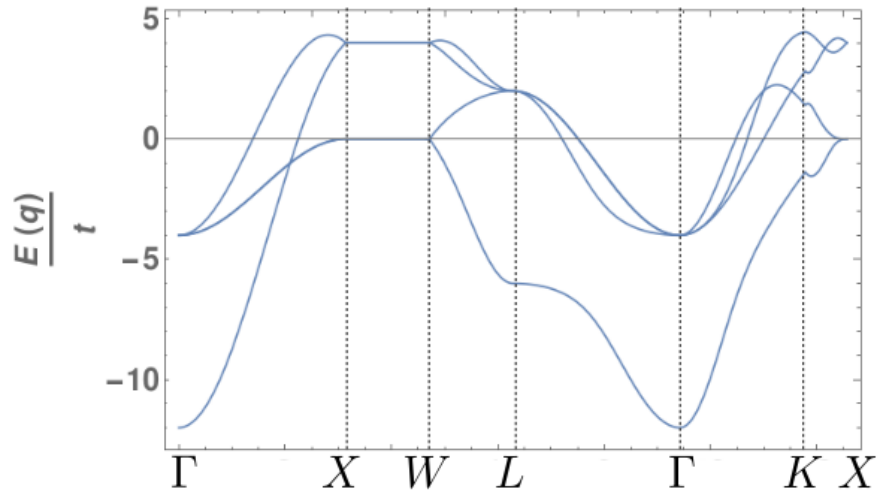
(a)
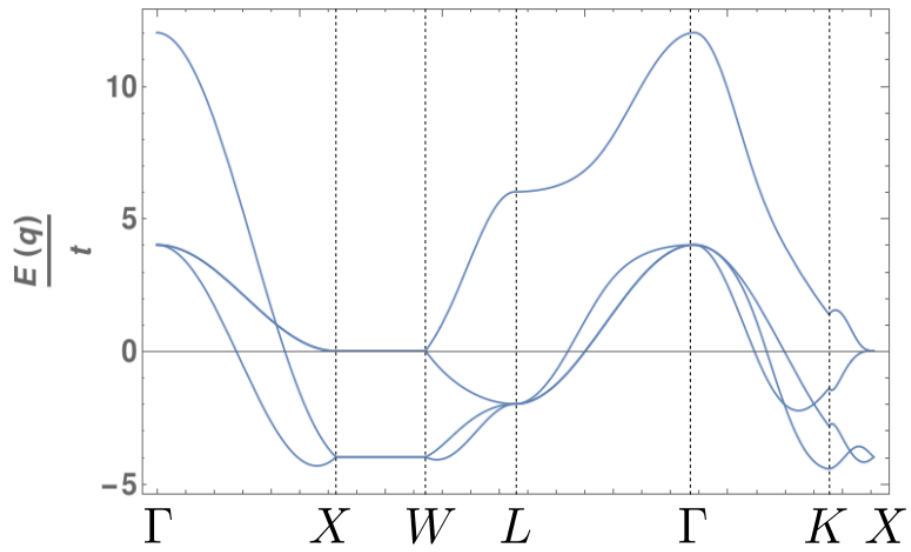
(b)

Figure 6.9: **Band structure of the** δ**-excitations** in the **(a)** zero-flux and **(b)** $\pi-$flux phase. Γ, X, W, L, K are the high symmetry points of the FCC Brillouin zone.

CHAPTER 7

CONCLUSIONS

To summarize, this thesis work addresses two central but complementary aspects of QSL physics in the spin-orbit coupled magnetic insulators.

In the first case, anomalous Raman signatures in the phonon spectra are analyzed in the context of various QSL candidates. It is shown that due to the magnetoelastic coupling, which is generically expected to be substantial in spin-orbit coupled magnetic systems, such anomaly carries signatures of underlying spin fractionalisation that results from the long-range entanglement of a QSL. The phonon renormalisation is explicitly calculated via computing its self-energy perturbatively. The real and imaginary parts of the self-energy are shown to be directly proportional to the frequency shift and the linewidth of the phonons, which can be measured explicitly in the Raman experiments. The signatures of the emergent excitations in a QSL are characterised by the temperature and frequency dependence of these quantities. While the temperature dependence generically conveys information about the statistics of the underlying quasiparticles, the frequency dependence carries information about their density of states. We have explicitly shown the application of our theoretical framework in two examples of Kitaev QSL and non-Kramers quantum spin ice.

In the Kitaev QSL, we identify the signatures of the fractionalised Majorana particles in the phonon anomalies, which are in direct conformity with the experimental observations performed on the second generation candidate material, Cu_2IrO_3. Although for the sake of the simplicity of the calculations, we neglected the flux excitations in the theoretical framework, our results are argued to be robust even if the fluxes get thermally excited.

In case of non-Kramers quantum spin ice, it is shown that the spin-phonon interaction is possibly enhanced due to the presence of *linear* magnetoelastic coupling, which is an essential consequence of the non-Kramers nature of the low-energy magnetic degrees of freedom. We show that in the U(1) QSL phase of the quantum spin ice, all the emergent excitations–the emergent gapped magnetic and electric charges as well as gapless emergent photons–interact with the phonons leading to identification of all three types of excitations by studying the phonon anomaly. Interestingly, since in the quantum spin ice phase, the magnetic sectors and the electric sectors are naturally separated in energy, the Raman response also appears in dif-

ferent energy windows for these degrees of freedom alongside the gapless emergent photon to which both the charges couple. Moreover, it is further shown that the phonon as a probe is particularly interesting, because it can also distinguish between zero flux and $\pi-$flux phases of a QSL, and hence the PSG implementation realised in the QSL. Given the recent development in synthesising high-quality single crystals of $Pr_2Zr_2O_7$ and obtaining their Raman response, albeit so far only at high temperatures, we hope that our work will contribute to the uncovering of the experimental signatures of QSLs in the context of the search for fractionalised quantum phases of matter in D=3.

As a related work, we have also explored the Raman anomalies in polycrystalline samples of the Heisenberg quantum magnet $Ca_{10}Cr_7O_{28}$ which is observed at a temperature scale much higher than the one associated with the spin-exchange interactions of the system. Clearly, in this case, the phonon anomaly does not arise from the fractionalisation physics inside a QSL, but possibly arises due to a unique interplay of J-T distortion and orbital fluctuations. We theoretically predict the presence of an orbital reordering crossover, driven by the co-operative J-T effects, in the already J-T distorted lattice. The phonon renormalisation associated with this reordering is explicitly calculated and shown to be in direct conformity with the experiments.

In the second problem, we present a rather novel and yet unexplored possibility in spin ice systems where the crystal field gap is relatively much smaller, hence, the magnetism of the material is controlled by the ground state manifold as well as by the first excited states to reveal a new set of phenomena related to novel gauge neutral excitations. The effect of these rather localised excitations affects the low-energy spin-correlators measurable in experiments. These low-lying δ-excitations are metastable since they can only decay via creating a pair of magnetic monopoles. Such metastable states in presence of quench disorder have been suggested to drive glassy dynamics [161] in spin systems. The present situation of such metastable gauge invariant excitations in an otherwise fluctuating background of a coulomb liquid in a (quenched) disorder-free system is rather new and can lead to dynamical slowing down [158] and an interesting *topological spin-glass* phase [159, 160] at low temperatures $T/J_{zz} \ll 1$. Numerical confirmation of such a phase would be extremely interesting. While the most likely candidate for such observations are the non-Kramers pyrochlore magnets such as $Pr_2Zr_2O_7$ [29, 39], $Ho_2Ti_2O_7$ [49, 162] and in particular $Tb_2Ti_2O_7$ [103], where the tunability of the crystal field gap is possible via a soft phonon, the basic physics of the δ-excitations can also be realised

in Kramers systems, albeit with lesser tunability.

Appendices

SIGNATURES OF FRACTIONALIZATION IN CANDIDATE IN KRAMERS KITAEV QUANTUM SPIN LIQUIDS, Cu$_2$IrO$_3$ VIA ANOMALOUS RAMAN SCATTERING OF PHONONS

A.1 Details of the Majorana fermion- (optical) phonon coupling

To calculate the phonon renormalisation due to the Majorana-phonon coupling, we first need to rewrite the magnetoelastic couplings in terms of the Bogolioubov particles since the free Majorana Hamiltonian becomes diagonal in this basis. Applying the Bogolioubov transformation given by Eq. 3.5 on the phonon-bond matter fermion coupling Hamiltonian of Eqs. 3.19 and 3.20, we obtain,

$$H_1 = \frac{J_K}{4\sqrt{N_b}} \sum_{\mathbf{k},\mathbf{k}'} \chi^a \Theta^a_{\mathbf{k},\bar{p}} \left[\bar{\mathcal{A}}_{\mathbf{k},\mathbf{k}'} \, a_{-\mathbf{k}'} a_{\mathbf{k}'-\mathbf{k}} + \bar{\mathcal{B}}_{\mathbf{k},\mathbf{k}'} \, a_{-\mathbf{k}'} a^\dagger_{\mathbf{k}-\mathbf{k}'} + \bar{\mathcal{C}}_{\mathbf{k},\mathbf{k}'} \, a^\dagger_{\mathbf{k}'} a_{\mathbf{k}'-\mathbf{k}} + \bar{\mathcal{D}}_{\mathbf{k},\mathbf{k}'} \, a^\dagger_{\mathbf{k}'} a^\dagger_{\mathbf{k}-\mathbf{k}'} \right]$$

(A.1)

$$H_2 = \frac{J_K}{4N_b} \sum_{\mathbf{k},\mathbf{k}',\mathbf{k}''} \lambda^{cd} \, \Theta^c_{\mathbf{k},\bar{p}} \Theta^d_{\mathbf{k}',\bar{q}} \left[\bar{\mathcal{P}}_{\mathbf{k},\mathbf{k}',\mathbf{k}''} a_{-\mathbf{k}''} a_{\mathbf{k}''-\mathbf{k}-\mathbf{k}'} + \bar{\mathcal{Q}}_{\mathbf{k},\mathbf{k}',\mathbf{k}''} a_{-\mathbf{k}''} a^\dagger_{\mathbf{k}+\mathbf{k}'-\mathbf{k}''} \right.$$

$$\left. + \bar{\mathcal{R}}_{\mathbf{k},\mathbf{k}',\mathbf{k}''} a^\dagger_{\mathbf{k}''} a_{\mathbf{k}''-\mathbf{k}-\mathbf{k}'} + \bar{\mathcal{S}}_{\mathbf{k},\mathbf{k}',\mathbf{k}''} a^\dagger_{\mathbf{k}''} a^\dagger_{\mathbf{k}+\mathbf{k}'-\mathbf{k}''} \right]$$

(A.2)

where the vertex functions are given by,

$$\bar{\mathcal{A}}_{\mathbf{k},\mathbf{k}'} = i \sin\theta_{-\mathbf{k}'} \cos\theta_{\mathbf{k}'-\mathbf{k}} \mathcal{A}_{\mathbf{k},\mathbf{k}'} + \cos\theta_{-\mathbf{k}'} \cos\theta_{\mathbf{k}'-\mathbf{k}} \mathcal{B}_{\mathbf{k},-\mathbf{k}'} + i \cos\theta_{-\mathbf{k}'} \sin\theta_{\mathbf{k}'-\mathbf{k}} \mathcal{C}_{\mathbf{k},-\mathbf{k}'}$$

$$- \sin\theta_{-\mathbf{k}'} \sin\theta_{\mathbf{k}'-\mathbf{k}} \mathcal{D}_{\mathbf{k},\mathbf{k}'}$$

$$\bar{\mathcal{B}}_{\mathbf{k},\mathbf{k}'} = - \sin\theta_{-\mathbf{k}'} \sin\theta_{\mathbf{k}'-\mathbf{k}} \mathcal{A}_{\mathbf{k},\mathbf{k}'} + i \cos\theta_{-\mathbf{k}'} \sin\theta_{\mathbf{k}'-\mathbf{k}} \mathcal{B}_{\mathbf{k},-\mathbf{k}'} + \cos\theta_{-\mathbf{k}'} \cos\theta_{\mathbf{k}'-\mathbf{k}} \mathcal{C}_{\mathbf{k},-\mathbf{k}'}$$

$$+ i \sin\theta_{-\mathbf{k}'} \cos\theta_{\mathbf{k}'-\mathbf{k}} \mathcal{D}_{\mathbf{k},\mathbf{k}'}$$

$$\bar{\mathcal{C}}_{\mathbf{k},\mathbf{k}'} = \cos\theta_{-\mathbf{k}'} \cos\theta_{\mathbf{k}'-\mathbf{k}} \mathcal{A}_{\mathbf{k},\mathbf{k}'} + i \sin\theta_{-\mathbf{k}'} \cos\theta_{\mathbf{k}'-\mathbf{k}} \mathcal{B}_{\mathbf{k},-\mathbf{k}'} - \sin\theta_{-\mathbf{k}'} \sin\theta_{\mathbf{k}'-\mathbf{k}} \mathcal{C}_{\mathbf{k},-\mathbf{k}'}$$

$$+ i \cos\theta_{-\mathbf{k}'} \sin\theta_{\mathbf{k}'-\mathbf{k}} \mathcal{D}_{\mathbf{k},\mathbf{k}'}$$

$$\bar{\mathcal{D}}_{\mathbf{k},\mathbf{k}'} = i\cos\theta_{-\mathbf{k}'}\sin\theta_{\mathbf{k}'-\mathbf{k}}\mathcal{A}_{\mathbf{k},\mathbf{k}'} - \sin\theta_{-\mathbf{k}'}\sin\theta_{\mathbf{k}'-\mathbf{k}}\mathcal{B}_{\mathbf{k},-\mathbf{k}'} + i\sin\theta_{-\mathbf{k}'}\cos\theta_{\mathbf{k}'-\mathbf{k}}\mathcal{C}_{\mathbf{k},-\mathbf{k}'}$$
$$+ \cos\theta_{-\mathbf{k}'}\cos\theta_{\mathbf{k}'-\mathbf{k}}\mathcal{D}_{\mathbf{k},\mathbf{k}'}$$

$$\bar{\mathcal{P}}_{\mathbf{k},\mathbf{k}',\mathbf{k}''} = i\sin\theta_{-\mathbf{k}''}\cos\theta_{\mathbf{k}''-\mathbf{k}-\mathbf{k}'}\mathcal{P}_{\mathbf{k},\mathbf{k}',\mathbf{k}''} + \cos\theta_{-\mathbf{k}''}\cos\theta_{\mathbf{k}''-\mathbf{k}-\mathbf{k}'}\mathcal{Q}_{\mathbf{k},\mathbf{k}',-\mathbf{k}''}$$
$$+ i\cos\theta_{-\mathbf{k}''}\sin\theta_{\mathbf{k}''-\mathbf{k}-\mathbf{k}'}\mathcal{R}_{\mathbf{k},\mathbf{k}',-\mathbf{k}''} - \sin\theta_{-\mathbf{k}''}\sin\theta_{\mathbf{k}''-\mathbf{k}-\mathbf{k}'}\mathcal{S}_{\mathbf{k},\mathbf{k}',\mathbf{k}''}$$

$$\bar{\mathcal{Q}}_{\mathbf{k},\mathbf{k}',\mathbf{k}''} = -\sin\theta_{-\mathbf{k}''}\sin\theta_{\mathbf{k}''-\mathbf{k}-\mathbf{k}'}\mathcal{P}_{\mathbf{k},\mathbf{k}',\mathbf{k}''} + i\cos\theta_{-\mathbf{k}''}\sin\theta_{\mathbf{k}''-\mathbf{k}-\mathbf{k}'}\mathcal{Q}_{\mathbf{k},\mathbf{k}',-\mathbf{k}''}$$
$$+ \cos\theta_{-\mathbf{k}''}\cos\theta_{\mathbf{k}''-\mathbf{k}-\mathbf{k}'}\mathcal{R}_{\mathbf{k},\mathbf{k}',-\mathbf{k}''} + i\sin\theta_{-\mathbf{k}''}\cos\theta_{\mathbf{k}''-\mathbf{k}-\mathbf{k}'}\mathcal{S}_{\mathbf{k},\mathbf{k}',\mathbf{k}''}$$

$$\bar{\mathcal{R}}_{\mathbf{k},\mathbf{k}',\mathbf{k}''} = \cos\theta_{-\mathbf{k}''}\cos\theta_{\mathbf{k}''-\mathbf{k}-\mathbf{k}'}\mathcal{P}_{\mathbf{k},\mathbf{k}',\mathbf{k}''} + i\sin\theta_{-\mathbf{k}''}\cos\theta_{\mathbf{k}''-\mathbf{k}-\mathbf{k}'}\mathcal{Q}_{\mathbf{k},\mathbf{k}',-\mathbf{k}''}$$
$$- \sin\theta_{-\mathbf{k}''}\sin\theta_{\mathbf{k}''-\mathbf{k}-\mathbf{k}'}\mathcal{R}_{\mathbf{k},\mathbf{k}',-\mathbf{k}''} + i\cos\theta_{-\mathbf{k}''}\sin\theta_{\mathbf{k}''-\mathbf{k}-\mathbf{k}'}\mathcal{S}_{\mathbf{k},\mathbf{k}',\mathbf{k}''}$$

$$\bar{\mathcal{S}}_{\mathbf{k},\mathbf{k}',\mathbf{k}''} = i\cos\theta_{-\mathbf{k}''}\sin\theta_{\mathbf{k}''-\mathbf{k}-\mathbf{k}'}\mathcal{P}_{\mathbf{k},\mathbf{k}',\mathbf{k}''} - \sin\theta_{-\mathbf{k}''}\sin\theta_{\mathbf{k}''-\mathbf{k}-\mathbf{k}'}\mathcal{Q}_{\mathbf{k},\mathbf{k}',-\mathbf{k}''}$$
$$+ i\sin\theta_{-\mathbf{k}''}\cos\theta_{\mathbf{k}''-\mathbf{k}-\mathbf{k}'}\mathcal{R}_{\mathbf{k},\mathbf{k}',-\mathbf{k}''} + \cos\theta_{-\mathbf{k}''}\cos\theta_{\mathbf{k}''-\mathbf{k}-\mathbf{k}'}\mathcal{S}_{\mathbf{k},\mathbf{k}',\mathbf{k}''}$$
$$\text{(A.3)}$$

A.2 Linewidth of phonon

Using the form of the Green's function for the Majorana fermions, $G(\mathbf{k}, i\omega) = \frac{1}{i\omega - \epsilon_{\mathbf{k}}}$, the self-energy of the phonons given in Eq. 3.24 can be rewritten as,

$$\Sigma(q, i\omega) \sim -\frac{\chi^2 J_K^2}{N_b \beta} \times$$
$$\sum_{\mathbf{k}}\sum_{\omega_m}\left[M_{\mathbf{k}+\mathbf{q},\mathbf{k}}\frac{1}{i\omega + i\omega_m + \epsilon_{\mathbf{k}+\mathbf{q}}}\frac{1}{i\omega_m - \epsilon_{\mathbf{k}}} - M_{-\mathbf{k}-\mathbf{q},-\mathbf{k}}\frac{1}{i\omega - i\omega_m - \epsilon_{\mathbf{k}+\mathbf{q}}}\frac{1}{i\omega_m - \epsilon_{\mathbf{k}}} \right.$$
$$\left. - N_{\mathbf{k}+\mathbf{q},\mathbf{k}}\frac{1}{i\omega + i\omega_m - \epsilon_{\mathbf{k}+\mathbf{q}}}\frac{1}{i\omega_m - \epsilon_{\mathbf{k}}} + N_{-\mathbf{k}-\mathbf{q},-\mathbf{k}}\frac{1}{i\omega - i\omega_m + \epsilon_{\mathbf{k}+\mathbf{q}}}\frac{1}{i\omega_m - \epsilon_{\mathbf{k}}} \right]$$
$$\text{(A.4)}$$

To perform the Matsubara frequency summation, we first define

$$I_1 = \lim_{R\to\infty}\frac{1}{2\pi i}\oint \frac{1}{e^{\beta z} + 1}\frac{1}{z + i\omega + \epsilon_{\mathbf{k}+\mathbf{q}}}\frac{1}{z - \epsilon_{\mathbf{k}}} \tag{A.5}$$

$$I_2 = \lim_{R\to\infty}\frac{1}{2\pi i}\oint \frac{1}{e^{\beta z} + 1}\frac{1}{z + i\omega - \epsilon_{\mathbf{k}+\mathbf{q}}}\frac{1}{z - \epsilon_{\mathbf{k}}} \tag{A.6}$$

Here, the contour is chosen to be the circle with radius R and the radius is sent to ∞. The poles and residues of the complex integrals are listed in the following table.

I_1		I_2	
Poles	Residue	Poles	Residue
$i\omega_m$	$-\frac{1}{\beta}\sum_{\omega_m}\frac{1}{i\omega+i\omega_m+\epsilon_{k+q}}\frac{1}{i\omega_m-\epsilon_k}$	$i\omega_m$	$-\frac{1}{\beta}\sum_{\omega_m}\frac{1}{i\omega+i\omega_m-\epsilon_{k+q}}\frac{1}{i\omega_m+\epsilon_k}$
ϵ_k	$\frac{n_F(\epsilon_k)}{i\omega+\epsilon_k+\epsilon_{k+q}}$	ϵ_k	$\frac{n_F(\epsilon_k)}{i\omega+\epsilon_k-\epsilon_{k+q}}$
$-i\omega-\epsilon_{k+q}$	$-\frac{1-n_F(\epsilon_{k+q})}{i\omega+\epsilon_{k+q}+\epsilon_k}$	$-i\omega+\epsilon_{k+q}$	$-\frac{n_F(\epsilon_{k+q})}{i\omega+\epsilon_k-\epsilon_{k+q}}$

Now, both I_1 and I_2 vanishes as $R \to \infty$. Therefore, from the above table it is straightforward to see that

$$-\frac{1}{\beta}\sum_{\omega_m}\frac{1}{i\omega+i\omega_m+\epsilon_{\mathbf{k+q}}}\frac{1}{i\omega_m-\epsilon_{\mathbf{k}}} = \frac{1-n_F(\epsilon_{\mathbf{k+q}})-n_F(\epsilon_{\mathbf{k}})}{i\omega+\epsilon_{\mathbf{k}}+\epsilon_{\mathbf{k+q}}} \qquad (A.7)$$

$$\frac{1}{\beta}\sum_{\omega_m}\frac{1}{i\omega+i\omega_m-\epsilon_{\mathbf{k+q}}}\frac{1}{i\omega_m+\epsilon_{\mathbf{k}}} = \frac{n_F(\epsilon_{\mathbf{k}})-n_F(\epsilon_{\mathbf{k+q}})}{i\omega+\epsilon_{\mathbf{k}}-\epsilon_{\mathbf{k+q}}} \qquad (A.8)$$

Hence, we have,

$$\Sigma(\mathbf{q}, i\omega) \sim \frac{\chi^2 J_K^2}{N_b}\sum_{\mathbf{k}}\left[\left(1-n_F(\epsilon_{\mathbf{k}})-n_F(\epsilon_{\mathbf{k+q}})\right)\left(\frac{M_{\mathbf{k+q},\mathbf{k}}}{i\omega+\epsilon_{\mathbf{k}}+\epsilon_{\mathbf{k+q}}}-\frac{M_{\mathbf{-k-q},\mathbf{-k}}}{i\omega+\epsilon_{\mathbf{k}}+\epsilon_{\mathbf{k+q}}}\right)\right.$$
$$\left.+\left(n_F(\epsilon_{\mathbf{k}})-n_F(\epsilon_{\mathbf{k+q}})\right)\left(\frac{N_{\mathbf{k+q},\mathbf{k}}}{i\omega+\epsilon_{\mathbf{k}}-\epsilon_{\mathbf{k+q}}}-\frac{N_{\mathbf{-k-q},\mathbf{-k}}}{i\omega+\epsilon_{\mathbf{k+q}}-\epsilon_{\mathbf{k}}}\right)\right]$$
$$(A.9)$$

In this work, we consider the $\mathbf{q}\to 0$ limit which is relevant to the Raman scattering. At this limit, the second part of the above expression with the factor $(n_F(\epsilon_{\mathbf{k}})-n_F(\epsilon_{\mathbf{k+q}}))$ vanishes. Finally, we Taylor expand $M_{\mathbf{k+q},\mathbf{k}}$ in powers of momentum and truncate the series upto the first non-zero term which is momentum independent. This gives the leading temperature dependence of the self-energy. We take the imaginary part of the above expression after doing the analytic continuation. Using the identity $\mathcal{I}m\left[\frac{1}{x-x_0+i0^+}\right]=-\pi\delta(x-x_0)$, we obtain the expression for the linewidth which is given in Eq. 3.26 of the main text.

APPENDIX B

PROBING EMERGENT QED IN NON-KRAMERS QUANTUM SPIN ICE VIA RAMAN SCATTERING OF PHONONS

B.1 Details of the pyrochlore lattice

B.1.1 Local basis for the spins

The spins on a tetrahedron are described by,

$$\mathbf{s}_i = s_i^x \hat{x}_i + s_i^y \hat{y}_i + s_i^z \hat{z}_i \tag{B.1}$$

where, $(\hat{x}_i, \hat{y}_i, \hat{z}_i)$ is the set of local basis defined at site i of a tetrahedron (see Fig. 4.1). In terms of the global coordinates, these local basis vectors for an up tetrahedron are given by,

$$\begin{aligned}
\hat{z}_0 &= \frac{(1,1,1)}{\sqrt{3}} &,&\quad \hat{x}_0 = \frac{(\bar{2},1,1)}{\sqrt{6}} &,&\quad \hat{y}_0 = \frac{(0,\bar{1},1)}{\sqrt{2}} \\
\hat{z}_1 &= \frac{(\bar{1},\bar{1},1)}{\sqrt{3}} &,&\quad \hat{x}_1 = \frac{(2,\bar{1},1)}{\sqrt{6}} &,&\quad \hat{y}_1 = \frac{(0,1,1)}{\sqrt{2}} \\
\hat{z}_2 &= \frac{(\bar{1},1,\bar{1})}{\sqrt{3}} &,&\quad \hat{x}_2 = \frac{(2,1,\bar{1})}{\sqrt{6}} &,&\quad \hat{y}_2 = \frac{(0,\bar{1},\bar{1})}{\sqrt{2}} \\
\hat{z}_3 &= \frac{(1,\bar{1},\bar{1})}{\sqrt{3}} &,&\quad \hat{x}_3 = \frac{(\bar{2},\bar{1},\bar{1})}{\sqrt{6}} &,&\quad \hat{y}_3 = \frac{(0,1,\bar{1})}{\sqrt{2}}
\end{aligned} \tag{B.2}$$

B.1.2 Lattice vectors

The four nearest neighbour vectors, which connect the centre of an up tetrahedron to that of its adjacent down tetrahedra, are given by,

$$\mathbf{e_0} = \frac{(1,1,1)}{\sqrt{3}} \ , \quad \mathbf{e_1} = \frac{(\bar{1},\bar{1},1)}{\sqrt{3}} \ , \quad \mathbf{e_2} = \frac{(\bar{1},1,\bar{1})}{\sqrt{3}} \ , \quad \mathbf{e_3} = \frac{(1,\bar{1},\bar{1})}{\sqrt{3}} \tag{B.3}$$

The FCC lattice vectors are given by,

$$\mathbf{d}_\mu = \mathbf{e_0} - \mathbf{e}_\mu \ , \quad for \ \ \mu = 1,2,3 \tag{B.4}$$

The tetrahedral group, T_d, is made out of 24 symmetry elements which can further be classified into 5 conjugacy classes. To decompose the vector space of (s_i^x, s_i^y) operators into the irreducible representations (see Sec. 4.3), we compute their transformations under one representative symmetry transformation from each non-trivial class : $C_3[111]$ (three-fold rotation about the global $(1,1,1)$ axis), $C_2[\hat{z}]$ (two-fold rotation about the global $\hat{z}$ axis), $\sigma_d[x = y]$ (reflection about the $x = y$ plane) and $S_4[\hat{z}]$ (reflection about the $z = 0$ plane followed by four-fold rotation about the global $\hat{z}$ axis). This is given in Table B.1 for the transverse spin components, s_i^x and s_i^y. Here we do not consider time reversal odd s_i^z operators, since these are not relevant to the linear magnetoelastic coupling.

Symmetry	Transformation of spin operators
$C_3[111]$	$s_0^x \to -\frac{1}{2}s_0^x + \frac{\sqrt{3}}{2}s_0^y$; $s_0^y \to -\frac{\sqrt{3}}{2}s_0^x - \frac{1}{2}s_0^y$ $s_1^x \to -\frac{1}{2}s_2^x + \frac{\sqrt{3}}{2}s_2^y$; $s_1^y \to -\frac{\sqrt{3}}{2}s_2^x - \frac{1}{2}s_2^y$ $s_2^x \to -\frac{1}{2}s_3^x + \frac{\sqrt{3}}{2}s_3^y$; $s_2^y \to -\frac{\sqrt{3}}{2}s_3^x - \frac{1}{2}s_3^y$ $s_3^x \to -\frac{1}{2}s_1^x + \frac{\sqrt{3}}{2}s_1^y$; $s_3^y \to -\frac{\sqrt{3}}{2}s_1^x - \frac{1}{2}s_1^y$
$C_2[\hat{z}]$	$s_0^x \to s_1^x$; $s_0^y \to s_1^y$ $s_1^x \to s_0^x$; $s_1^y \to s_0^y$ $s_2^x \to s_3^x$; $s_2^y \to s_3^y$ $s_3^x \to s_2^x$; $s_3^y \to s_2^y$
$\sigma_d[x = y]$	$s_0^x \to -\frac{1}{2}s_0^x - \frac{\sqrt{3}}{2}s_0^y$; $s_0^y \to -\frac{\sqrt{3}}{2}s_0^x + \frac{1}{2}s_0^y$ $s_1^x \to -\frac{1}{2}s_1^x - \frac{\sqrt{3}}{2}s_1^y$; $s_1^y \to -\frac{\sqrt{3}}{2}s_1^x + \frac{1}{2}s_1^y$ $s_2^x \to -\frac{1}{2}s_3^x - \frac{\sqrt{3}}{2}s_3^y$; $s_2^y \to -\frac{\sqrt{3}}{2}s_3^x + \frac{1}{2}s_3^y$ $s_3^x \to -\frac{1}{2}s_2^x - \frac{\sqrt{3}}{2}s_2^y$; $s_3^y \to -\frac{\sqrt{3}}{2}s_2^x + \frac{1}{2}s_2^y$
$S_4[\hat{z}]$	$s_0^x \to -\frac{1}{2}s_2^x - \frac{\sqrt{3}}{2}s_2^y$; $s_0^y \to -\frac{\sqrt{3}}{2}s_2^x + \frac{1}{2}s_2^y$ $s_1^x \to -\frac{1}{2}s_3^x - \frac{\sqrt{3}}{2}s_3^y$; $s_1^y \to -\frac{\sqrt{3}}{2}s_3^x + \frac{1}{2}s_3^y$ $s_2^x \to -\frac{1}{2}s_1^x - \frac{\sqrt{3}}{2}s_1^y$; $s_2^y \to -\frac{\sqrt{3}}{2}s_1^x + \frac{1}{2}s_1^y$ $s_3^x \to -\frac{1}{2}s_0^x - \frac{\sqrt{3}}{2}s_0^y$; $s_3^y \to -\frac{\sqrt{3}}{2}s_0^x + \frac{1}{2}s_0^y$
$\mathcal{T}$	$s_0^x \to s_0^x$; $s_0^y \to s_0^y$ $s_1^x \to s_1^x$; $s_1^y \to s_1^y$ $s_2^x \to s_2^x$; $s_2^y \to s_2^y$ $s_3^x \to s_3^x$; $s_3^y \to s_3^y$

Table B.1: Transformation of the transverse components of spins under lattice symmetries and time reversal

B.2 Details of the gauge mean field theory of quantum spin ice

B.2.1 Gauge mean field theory of monopole dynamics in the zero-flux phase

To implement the unitary constraint of the monopole operators described by Eq. 4.12, we introduce a new term to the Hamiltonian with a global Lagrange multiplier, λ.

$$\lambda \sum_{\mathbf{r}} \left(\phi_{\mathbf{r}}^{\dagger} \phi_{\mathbf{r}} - 1 \right) \tag{B.5}$$

The constraint is imposed softly if we consider λ to be a large number (more precisely, it needs to be the largest energy scale of the problem). With this term, the constraint can be relaxed by rewriting monopole operators as $\phi_{\mathbf{r}}^{\dagger} = e^{i\chi_{\mathbf{r}}}$ (where $\chi_{\mathbf{r}}$ takes real eigenvalues from $(0, 2\pi]$ and satisfies $[\chi_{\mathbf{r}}, \mathcal{Q}_{\mathbf{r}'}] = i\delta_{\mathbf{r},\mathbf{r}'}$) and expanding it up to linear order of $\chi_{\mathbf{r}}$.

$$\phi_{\mathbf{r}}^{\dagger} \approx 1 + i\chi_{\mathbf{r}} \tag{B.6}$$

Substituting the above expansion in the bare monopole Hamiltonian (obtained by freezing the dual gauge fluctuations in Eq. 4.15) along with the Lagrange multiplier term, we obtain,

$$H_0 \approx \frac{J_{zz}}{2} \sum_{\mathbf{r}} \mathcal{Q}_{\mathbf{r},B}^2 - \frac{J_{\pm}}{4} \sum_{\mathbf{r},\mu \neq \nu} \chi_{\mathbf{r}+\mathbf{d}_{\mu},B}\chi_{\mathbf{r}+\mathbf{d}_{\nu},B} + \lambda \sum_{\mathbf{r}} \chi_{\mathbf{r},\mathbf{B}}\chi_{\mathbf{r},B} + \quad B \to A$$

$$= \sum_{\mathbf{k}} \left[\frac{J_{zz}}{2} \mid \mathcal{Q}_{\mathbf{k},B} \mid^2 + \frac{(\epsilon_{\mathbf{k}}^0)^2}{2J_{zz}} \mid \chi_{\mathbf{k},B} \mid^2 \right] \quad + \quad B \to A \tag{B.7}$$

where $\epsilon_{\mathbf{k}}^0$ is the bare monopole dispersion in the zero flux sector and given by Eq. 4.18. In the above equation, we ignore the unimportant additive constant. We note that the above Hamiltonian describes a bunch of decoupled Harmonic oscillators which can be easily diagonlised using the standard ladder operator formalism.

$$\mathcal{Q}_{\mathbf{k},A/B} = -i\sqrt{\frac{\epsilon_{\mathbf{k}}^0}{2J_{zz}}}(a_{\mathbf{k},A/B} - a_{-\mathbf{k},A/B}^{\dagger})$$

$$\chi_{\mathbf{k},A/B} = \sqrt{\frac{J_{zz}}{2\epsilon_{\mathbf{k}}^0}}(a_{\mathbf{k},A/B} + a_{-\mathbf{k},A/B}^{\dagger})$$

The monopole Hamiltonian is simplified to,

$$H_0 = \sum_{\mathbf{k}} \epsilon_{\mathbf{k}}^0 \left(a_{\mathbf{k},A}^\dagger a_{\mathbf{k},A} + a_{\mathbf{k},B}^\dagger a_{\mathbf{k},B} + 1 \right) \tag{B.8}$$

Action for the magnetic monopoles

We can obtain the action for the monopoles corresponding to the mean field Hamiltonian H_0 using standard Trotter decomposition technique and implementing the unitary constraint of $\phi_{\mathbf{r}}$ field via the Lagrange multiplier term in the path integral formulation. We note that since A and B monopoles are decoupled in the mean field Hamiltonian, their action is additive.

$$S_0 = S_0^A + S_0^B$$

$$S_0^A = \sum_{\mathbf{k},\omega} \phi_{\mathbf{k}\omega,\mathbf{A}}^* \left[\frac{\omega^2}{2J_{zz}} + \lambda - \frac{J_\pm}{2} \sum_{\mu > \nu} \cos\left(\mathbf{k} \cdot (\mathbf{d}_\mu - \mathbf{d}_\nu)\right) \right] \phi_{\mathbf{k}\omega,\mathbf{A}}$$

$$S_0^B = \sum_{\mathbf{k},\omega} \phi_{\mathbf{k}\omega,\mathbf{B}}^* \left[\frac{\omega^2}{2J_{zz}} + \lambda - \frac{J_\pm}{2} \sum_{\mu > \nu} \cos\left(\mathbf{k} \cdot (\mathbf{d}_\mu - \mathbf{d}_\nu)\right) \right] \phi_{\mathbf{k}\omega,\mathbf{B}} \tag{B.9}$$

We can further compute the Green's function for monopoles from the above action which is given by Eq. 4.32 of the main text.

B.2.2 GMFT of monopole dynamics in the $\pi-$ flux phase

The bare dynamics of the magnetic monopoles in the π-flux phase can be obtained by choosing a suitable gauge fixing condition shown in Fig. B.1. It can further be written as $A_{\mathbf{r},\mu} = \epsilon_\mu \mathbf{Q} \cdot \mathbf{r}$ with $\epsilon_\mu = \{0, 1, 1, 0\}$ and $\mathbf{Q} = \frac{\sqrt{3}\pi}{2}(1, 0, 0)$. Similar to the zero flux case, the monopoles can hop only inside the A or B sublattice. Hence, the monopole dynamics can be expressed in terms of the following action.
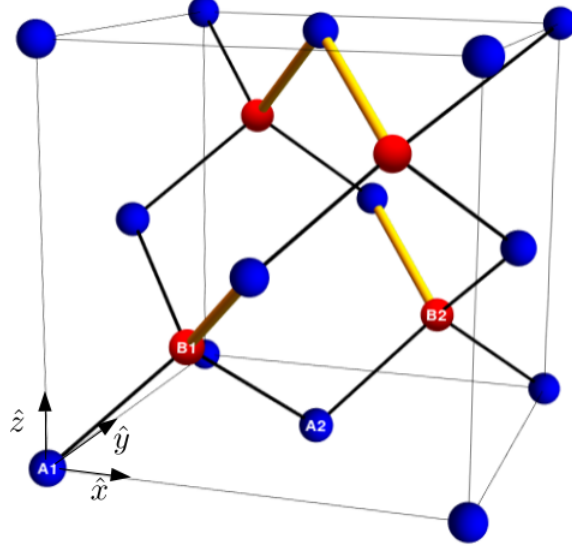
Figure B.1: **Unit cell of the diamond lattice with π-flux:** The gauge mean field is chosen such that $A_{\mathbf{r},\mathbf{r}+\mathbf{e}_\mu} = \pi$ on the yellow bonds and $A_{\mathbf{r},\mathbf{r}+\mathbf{e}_\mu} = 0$ on the black bonds. $A1, A2, B1, B2$ denote the four sublattices in the enlarged unit cell of the $\pi-$flux phase.

$$S_\pi = S_\pi^A + S_\pi^B$$

$$S_\pi^A = \sum_{\mathbf{k},\omega}(\phi_{\mathbf{k}\omega,A1}^* \ \phi_{\mathbf{k}\omega,A2}^*) \begin{pmatrix} \frac{\omega^2}{2J_{zz}} + \lambda + \frac{J_\pm}{4}d_A(\mathbf{k}) & \frac{J_\pm}{4}f_A(\mathbf{k}) \\ \frac{J_\pm}{4}f_A^*(\mathbf{k}) & \frac{\omega^2}{2J_{zz}} + \lambda - \frac{J_\pm}{4}d_A(\mathbf{k}) \end{pmatrix} \begin{pmatrix} \phi_{\mathbf{k}\omega,A1} \\ \phi_{\mathbf{k}\omega,A2} \end{pmatrix} \quad \text{(B.10)}$$

$$S_\pi^B = \sum_{\mathbf{k},\omega}(\phi_{\mathbf{k}\omega,B1}^* \ \phi_{\mathbf{k}\omega,B2}^*) \begin{pmatrix} \frac{\omega^2}{2J_{zz}} + \lambda + \frac{J_\pm}{4}d_B(\mathbf{k}) & \frac{J_\pm}{4}f_B(\mathbf{k}) \\ \frac{J_\pm}{4}f_B^*(\mathbf{k}) & \frac{\omega^2}{2J_{zz}} + \lambda - \frac{J_\pm}{4}d_B(\mathbf{k}) \end{pmatrix} \begin{pmatrix} \phi_{\mathbf{k}\omega,B1} \\ \phi_{\mathbf{k}\omega,B2} \end{pmatrix}$$

$$\text{(B.11)}$$

where,

$$d_A(\mathbf{k}) = 2\left(\cos\left(\mathbf{k}\cdot\mathbf{d_1}\right) + \cos\left(\mathbf{k}\cdot(\mathbf{d_1}-\mathbf{d_3})\right)\right)$$

$$f_A(\mathbf{k}) = 1 + e^{-i\mathbf{k}\cdot\mathbf{d_1}} + e^{-i\mathbf{k}\cdot\mathbf{d_2}} - e^{-i\mathbf{k}\cdot\mathbf{d_3}} + e^{-i\mathbf{k}\cdot(\mathbf{d_1}+\mathbf{d_2})} - e^{-i\mathbf{k}\cdot(\mathbf{d_3}-\mathbf{d_1})} + e^{-i\mathbf{k}\cdot(\mathbf{d_2}+\mathbf{d_3})}$$

$$+ e^{-i\mathbf{k}\cdot(\mathbf{d_2}+\mathbf{d_3}-\mathbf{d_1})}$$

$$d_B(\mathbf{k}) = 2\left(\cos\left(\mathbf{k}\cdot\mathbf{d_1}\right) - \cos\left(\mathbf{k}\cdot(\mathbf{d_1}-\mathbf{d_3})\right)\right)$$

$$f_B(\mathbf{k}) = 1 - e^{-i\mathbf{k}\cdot\mathbf{d_1}} + e^{-i\mathbf{k}\cdot\mathbf{d_2}} + e^{-i\mathbf{k}\cdot\mathbf{d_3}} + e^{-i\mathbf{k}\cdot(\mathbf{d_1}+\mathbf{d_2})} - e^{-i\mathbf{k}\cdot(\mathbf{d_3}-\mathbf{d_1})} + e^{-i\mathbf{k}\cdot(\mathbf{d_2}+\mathbf{d_3})}$$

$$+ e^{-i\mathbf{k}\cdot(\mathbf{d_2}+\mathbf{d_3}-\mathbf{d_1})}$$

$$\text{(B.12)}$$

λ is the global Lagrange multiplier introduced to take into account the constraint $\phi_{\mathbf{r}}^{\dagger} \phi_{\mathbf{r}} = 1$. $(A1, A2, B1, B2)$ denotes four sublattices of the enlarged unit cell. The above action can further be diagonalised to obtain the dispersion for four monopole bands.

$$\epsilon_{A\pm}^{\pi}(\mathbf{k}) = \sqrt{2J_{zz}\left(\lambda \pm \frac{J_{\pm}}{4}\sqrt{\mid d_A(\mathbf{k}) \mid^2 + \mid f_A(\mathbf{k}) \mid^2}\right)}$$

$$\epsilon_{B\pm}^{\pi}(\mathbf{k}) = \sqrt{2J_{zz}\left(\lambda \pm \frac{J_{\pm}}{4}\sqrt{\mid d_B(\mathbf{k}) \mid^2 + \mid f_B(\mathbf{k}) \mid^2}\right)} \tag{B.13}$$

where $A\pm(B\pm)$ denote two bands made out of linear combination of $A1$ and $A2$ ($B1$ and $B2$) to diagonalise the S_{π}^A (S_{π}^B). Since A and B monopoles do not mix under the above dynamics, their bands are degenerate.

$$\epsilon_{A\pm}^{\pi}(\mathbf{k}) = \epsilon_{B\pm}^{\pi}(\mathbf{k}) \equiv \epsilon_{\pm}^{\pi}(\mathbf{k}) \tag{B.14}$$

We can compute different Green's function for monopole from the above action of the monopoles. The Green's function is defined as,

$$\left[G_{\phi}^{\pi}\right]_{\mu\nu}(\mathbf{k}, A/B, i\omega) = \int_0^{\beta} d\tau \left\langle \hat{\mathcal{T}}\left(\phi_{\mathbf{k},A/B,\mu}(\tau)\phi_{\mathbf{k},A/B,\nu}^{\dagger}(0)\right)\right\rangle e^{i\omega\tau} \tag{B.15}$$

where, $\mu, \nu = 1, 2$. The different Green's function are given by,

$$\left[G_{\phi}^{\pi}\right]_{11}(\mathbf{k}, A/B, i\omega) = \frac{J_{zz}}{\sqrt{\mid d_{A/B}(\mathbf{k}) \mid^2 + \mid f_{A/B}(\mathbf{k}) \mid^2}}$$
$$\times \left[\frac{\sqrt{\mid d_{A/B}(\mathbf{k}) \mid^2 + \mid f_{A/B}(\mathbf{k}) \mid^2} + d_{A/B}(\mathbf{k})}{\omega^2 + \left(\epsilon_+^{\pi}(\mathbf{k})\right)^2} + \frac{\sqrt{\mid d_{A/B}(\mathbf{k}) \mid^2 + \mid f_{A/B}(\mathbf{k}) \mid^2} - d_{A/B}(\mathbf{k})}{\omega^2 + \left(\epsilon_-^{\pi}(\mathbf{k})\right)^2}\right]$$

$$\left[G_{\phi}^{\pi}\right]_{22}(\mathbf{k}, A/B, i\omega) = \frac{J_{zz}}{\sqrt{\mid d_{A/B}(\mathbf{k}) \mid^2 + \mid f_{A/B}(\mathbf{k}) \mid^2}}$$
$$\times \left[\frac{\sqrt{\mid d_{A/B}(\mathbf{k}) \mid^2 + \mid f_{A/B}(\mathbf{k}) \mid^2} - d_{A/B}(\mathbf{k})}{\omega^2 + \left(\epsilon_+^{\pi}(\mathbf{k})\right)^2} + \frac{\sqrt{\mid d_{A/B}(\mathbf{k}) \mid^2 + \mid f_{A/B}(\mathbf{k}) \mid^2} + d_{A/B}(\mathbf{k})}{\omega^2 + \left(\epsilon_-^{\pi}(\mathbf{k})\right)^2}\right]$$

$$\left[G_{\phi}^{\pi}\right]_{12}(\mathbf{k}, A/B, i\omega) = \frac{J_{zz}f_{A/B}(\mathbf{k})}{\sqrt{\mid d_{A/B}(\mathbf{k}) \mid^2 + \mid f_{A/B}(\mathbf{k}) \mid^2}}\left[\frac{1}{\omega^2 + \left(\epsilon_+^{\pi}(\mathbf{k})\right)^2} - \frac{1}{\omega^2 + \left(\epsilon_-^{\pi}(\mathbf{k})\right)^2}\right]$$

$$\tag{B.16}$$

B.3   Raman matrices for the $\mathbf{e_g}$ and $\mathbf{t_{2g}}$ phonon modes

Structures of the Raman matrices, $\nabla_{\zeta^{(\lambda)}}\Lambda$, which govern the coupling of the $\mathbf{e_g}$ and $\mathbf{t_{2g}}$ phonon modes to the Raman photons, are obtained by decomposing six dimensional space of second order [68] polynomials$(x^2, y^2, z^2, xy, yz, zx)$ into the irreducible representations of symmetry group T_d and constructing the Hessian matrices for different components. The decomposition is as follows:

$$\mathbf{a_1} \oplus \mathbf{e} \oplus \mathbf{t_2}$$

where the basis for the irreducible subspaces are

$$\mathbf{a_1} \ : \ x^2 + y^2 + z^2 \tag{B.17}$$

$$\mathbf{e} \ : \ (2z^2 - x^2 - y^2, x^2 - y^2) \tag{B.18}$$

$$\mathbf{t_2} \ : \ (xy, yz, zx) \tag{B.19}$$

Hence, the relevant polarizability matrices of the Raman scattering are given by,

$$\mathbf{e_g} \ : \ \left[\nabla_{\zeta_{1,g}^{(e)}}\Lambda\right]_{\zeta_{1,g}^{(e)}=0} \propto \begin{pmatrix} -1 & 0 & 0 \\ 0 & -1 & 0 \\ 0 & 0 & 2 \end{pmatrix}, \ \left[\nabla_{\zeta_{2,g}^{(e)}}\Lambda\right]_{\zeta_{2,g}^{(e)}=0} \propto \begin{pmatrix} 1 & 0 & 0 \\ 0 & -1 & 0 \\ 0 & 0 & 0 \end{pmatrix} \tag{B.20}$$

$$\mathbf{t_{2g}} \ : \ \left[\nabla_{\zeta_{1,g}^{(t_2)}}\Lambda\right]_{\zeta_{1,g}^{(t_2)}=0} \propto \begin{pmatrix} 0 & 1 & 0 \\ 1 & 0 & 0 \\ 0 & 0 & 0 \end{pmatrix}, \ \left[\nabla_{\zeta_{2,g}^{(t_2)}}\Lambda\right]_{\zeta_{2,g}^{(t_2)}=0} \propto \begin{pmatrix} 0 & 0 & 1 \\ 0 & 0 & 0 \\ 1 & 0 & 0 \end{pmatrix},$$

$$\left[\nabla_{\zeta_{3,g}^{(t_2)}}\Lambda\right]_{\zeta_{3,g}^{(t_2)}=0} \propto \begin{pmatrix} 0 & 0 & 0 \\ 0 & 0 & 1 \\ 0 & 1 & 0 \end{pmatrix} \tag{B.21}$$
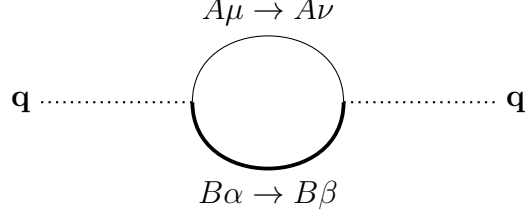
Figure B.2: **Self-energy bubble diagrams for phonon in π-flux phase:** The label $A\mu \to A\nu$ ($B\alpha \to B\beta$) implies the $A\mu$ ($B\alpha$) monopole is created in the left vertex and $A\nu$ ($B\beta$) monopole is annihilated at the right vertex. $\mu, \nu, \alpha, \beta = 1, 2$, hence, there are 16 possible distinct diagrams.

B.4 Raman response in $\pi-$flux phase

B.4.1 Vertex functions of magnetoelastic coupling

The vertex functions ($M_{\mathbf{k}}^{\mu\nu}$) of the magnetic monopole-phonon coupling in the π-flux phase (see in Eq. 4.35) are given by,

$$
\begin{aligned}
M_{\mathbf{k}}^{11} &= 2(1 + e^{i\mathbf{k}\cdot\mathbf{d_1}}) \\
M_{\mathbf{k}}^{12} &= 2(1 - e^{i\mathbf{k}\cdot(\mathbf{d_1}-\mathbf{d_3})}) \\
M_{\mathbf{k}}^{21} &= 2(e^{i\mathbf{k}\cdot(\mathbf{d_1}+\mathbf{d_2})} + e^{i\mathbf{k}\cdot(\mathbf{d_2}+\mathbf{d_3})}) \\
M_{\mathbf{k}}^{22} &= 2(1 - e^{i\mathbf{k}\cdot\mathbf{d_1}})
\end{aligned}
\tag{B.22}
$$

B.4.2 Self-energy of phonons due to magnetic monopoles

Similar to the zero flux case, the self-energy can be obtained by calculating the bubble diagrams appearing in the second-order perturbation theory. The only difference is that due to the larger unit cell, *sixteen* nonequivalent diagrams (see Fig. B.2) need to be taken care of.

For convenience, we introduce the following convention.

We now compute all the distinct contributions to the phonon self-energy. In the following equations, we group the distinct diagrams along with their Hermitian conjugate.

$$\begin{pmatrix} A1 \to A1 \\ B1 \to B1 \end{pmatrix} = \sum_{\mathbf{k}} \frac{M_{\mathbf{k}}^{11} M_{-\mathbf{k}}^{11} J_{zz}^2}{\sqrt{\mid d_A \mid^2 + \mid f_A \mid^2} \sqrt{\mid d_B \mid^2 + \mid f_B \mid^2}}$$

$$\times \left[\left(\sqrt{\mid d_A \mid^2 + \mid f_A \mid^2} + d_A \right) \left(\sqrt{\mid d_B \mid^2 + \mid f_B \mid^2} + d_B \right) W_{++} \right.$$

$$+ \left(\sqrt{\mid d_A \mid^2 + \mid f_A \mid^2} + d_A \right) \left(\sqrt{\mid d_B \mid^2 + \mid f_B \mid^2} - d_B \right) W_{+-}$$

$$+ \left(\sqrt{\mid d_A \mid^2 + \mid f_A \mid^2} - d_A \right) \left(\sqrt{\mid d_B \mid^2 + \mid f_B \mid^2} + d_B \right) W_{-+}$$

$$\left. + \left(\sqrt{\mid d_A \mid^2 + \mid f_A \mid^2} - d_A \right) \left(\sqrt{\mid d_B \mid^2 + \mid f_B \mid^2} - d_B \right) W_{--} \right]$$

$$\begin{pmatrix} A1 \to A1 \\ B1 \to B2 \end{pmatrix} + \begin{pmatrix} A1 \to A1 \\ B2 \to B1 \end{pmatrix} = \sum_{\mathbf{k}} \frac{\mathcal{R}e \left(M_{\mathbf{k}}^{11} M_{-\mathbf{k}}^{12} f_B(\mathbf{k}) \right) J_{zz}^2}{\sqrt{\mid d_A \mid^2 + \mid f_A \mid^2} \sqrt{\mid d_B \mid^2 + \mid f_B \mid^2}}$$

$$\times \left[\left(\sqrt{\mid d_A \mid^2 + \mid f_A \mid^2} + d_A \right) (W_{++} - W_{+-}) \right.$$

$$\left. + \left(\sqrt{\mid d_A \mid^2 + \mid f_A \mid^2} - d_A \right) (W_{-+} - W_{--}) \right]$$

$$\begin{pmatrix} A1 \to A1 \\ B2 \to B2 \end{pmatrix} = \sum_{\mathbf{k}} \frac{M_{\mathbf{k}}^{12} M_{-\mathbf{k}}^{12} J_{zz}^2}{\sqrt{\mid d_A \mid^2 + \mid f_A \mid^2} \sqrt{\mid d_B \mid^2 + \mid f_B \mid^2}}$$

$$\left[\left(\sqrt{\mid d_A \mid^2 + \mid f_A \mid^2} + d_A \right) \left(\sqrt{\mid d_B \mid^2 + \mid f_B \mid^2} - d_B \right) W_{++} \right.$$

$$+ \left(\sqrt{\mid d_A \mid^2 + \mid f_A \mid^2} + d_A \right) \left(\sqrt{\mid d_B \mid^2 + \mid f_B \mid^2} + d_B \right) W_{+-}$$

$$+ \left(\sqrt{\mid d_A \mid^2 + \mid f_A \mid^2} - d_A \right) \left(\sqrt{\mid d_B \mid^2 + \mid f_B \mid^2} - d_B \right) W_{-+}$$

$$\left. + \left(\sqrt{\mid d_A \mid^2 + \mid f_A \mid^2} - d_A \right) \left(\sqrt{\mid d_B \mid^2 + \mid f_B \mid^2} + d_B \right) W_{--} \right]$$

$$\begin{pmatrix} A1 \to A2 \\ B2 \to B1 \end{pmatrix} + \begin{pmatrix} A2 \to A1 \\ B1 \to B2 \end{pmatrix} = \sum_{\mathbf{k}} \frac{J_{zz}^2 \left(M_{\mathbf{k}}^{12} M_{-\mathbf{k}}^{21} f_A^* f_B + M_{\mathbf{k}}^{21} M_{-\mathbf{k}}^{12} f_A f_B^* \right)}{\sqrt{\mid d_A \mid^2 + \mid f_A \mid^2} \sqrt{\mid d_B \mid^2 + \mid f_B \mid^2}}$$

$$\times [W_{--} - W_{-+} - W_{+-} + W_{++}]$$

$$\begin{pmatrix} A2 \to A2 \\ B2 \to B2 \end{pmatrix} = \sum_{\mathbf{k}} \frac{M_{\mathbf{k}}^{22} M_{-\mathbf{k}}^{22} J_{zz}^2}{\sqrt{\mid d_A \mid^2 + \mid f_A \mid^2} \sqrt{\mid d_B \mid^2 + \mid f_B \mid^2}}$$

$$\times \left[\left(\sqrt{\mid d_A \mid^2 + \mid f_A \mid^2} + d_A \right) \left(\sqrt{\mid d_B \mid^2 + \mid f_B \mid^2} + d_B \right) W_{--} \right.$$

$$+ \left(\sqrt{\mid d_A \mid^2 + \mid f_A \mid^2} + d_A \right) \left(\sqrt{\mid d_B \mid^2 + \mid f_B \mid^2} - d_B \right) W_{-+}$$

$$+ \left(\sqrt{\mid d_A \mid^2 + \mid f_A \mid^2} - d_A \right) \left(\sqrt{\mid d_B \mid^2 + \mid f_B \mid^2} + d_B \right) W_{+-}$$

$$\left. + \left(\sqrt{\mid d_A \mid^2 + \mid f_A \mid^2} - d_A \right) \left(\sqrt{\mid d_B \mid^2 + \mid f_B \mid^2} - d_B \right) W_{++} \right]$$

$$
\begin{pmatrix} A2 \to A2 \\ B1 \to B2 \end{pmatrix} + \begin{pmatrix} A2 \to A2 \\ B2 \to B1 \end{pmatrix} = \sum_{\mathbf{k}} \frac{\mathcal{R}e\left(M_{\mathbf{k}}^{21} M_{-\mathbf{k}}^{22} f_B(\mathbf{k})\right) J_{zz}^2}{\sqrt{\mid d_A \mid^2 + \mid f_A \mid^2}\sqrt{\mid d_B \mid^2 + \mid f_B \mid^2}}
$$

$$
\times \left[\left(\sqrt{\mid d_A \mid^2 + \mid f_A \mid^2} + d_A\right)(W_{-+} - W_{--})\right.
$$

$$
\left. + \left(\sqrt{\mid d_A \mid^2 + \mid f_A \mid^2} - d_A\right)(W_{++} - W_{+-})\right]
$$

$$
\begin{pmatrix} A1 \to A2 \\ B1 \to B2 \end{pmatrix} + \begin{pmatrix} A2 \to A1 \\ B2 \to B1 \end{pmatrix} = \sum_{\mathbf{k}} \frac{J_{zz}^2\left(M_{\mathbf{k}}^{11} M_{-\mathbf{k}}^{22} f_A f_B^* + M_{-\mathbf{k}}^{11} M_{\mathbf{k}}^{22} f_A^* f_B\right)}{\sqrt{\mid d_A \mid^2 + \mid f_A \mid^2}\sqrt{\mid d_B \mid^2 + \mid f_B \mid^2}}
$$

$$
\times \left[W_{--} - W_{-+} - W_{+-} + W_{++}\right]
$$

There are five other distinct diagrams which can be obtained by replacing $A \to B$ in the above diagrams (more specifically, second, third and sixth expression). Adding up all the above contributions, we obtain,

$$
\Sigma_{\zeta^{(e)}}^{\pi}(\mathbf{q} = 0, i\Omega) = \frac{J_{sp}^{(e)2}}{N} \sum_{\mathbf{k}} \left[\mathcal{P}_1(\mathbf{k})W_{++}(\mathbf{k}, i\Omega) + \mathcal{P}_2(\mathbf{k})W_{--}(\mathbf{k}, i\Omega)\right.
$$

$$
\left. + \mathcal{P}_3(\mathbf{k})W_{+-}(\mathbf{k}, i\Omega) + \mathcal{P}_4(\mathbf{k})W_{-+}(\mathbf{k}, i\Omega)\right] \tag{B.23}
$$

where, $\mathcal{P}_1(\mathbf{k})$, $\mathcal{P}_2(\mathbf{k})$, $\mathcal{P}_3(\mathbf{k})$, $\mathcal{P}_4(\mathbf{k})$ are real functions of momentum and

$$
W_{mn}(\mathbf{k}, i\Omega) = -\frac{1}{\beta} \sum_{\omega} \frac{1}{(\Omega + \omega)^2 + (\epsilon_m^{\pi}(\mathbf{k}))^2} \frac{1}{\omega^2 + (\epsilon_n^{\pi}(\mathbf{k}))^2} \tag{B.24}
$$

The phonon linewidth is obtained from Eq. B.23 by calculating its imaginary part. Apart from the momentum dependent form factors, the contribution is mostly dominated by the four W_{mn} terms. Calculating their imaginary parts, we obtain,

$$
\lim_{\delta \to 0} \mathcal{I}m\left(W_{\pm\pm}(\mathbf{k}, \Omega + i\delta)\right) = \frac{\pi(1 + 2n(\epsilon_{\pm}^{\pi}(\mathbf{k})))}{4\epsilon_{\pm}^{\pi}(\mathbf{k})^2}\left[\delta\left(\Omega + 2\epsilon_{\pm}^{\pi}(\mathbf{k})\right) - \delta\left(\Omega - 2\epsilon_{\pm}^{\pi}(\mathbf{k})\right)\right]
$$

$$
\lim_{\delta \to 0} \mathcal{I}m\left(W_{+-}(\mathbf{k}, \Omega + i\delta)\right) = \mathcal{I}m\left(W_{-+}(\mathbf{k}, \Omega + i\delta)\right)
$$

$$
= \frac{\pi(1 + n(\epsilon_+^{\pi}(\mathbf{k})) + n(\epsilon_-^{\pi}(\mathbf{k})))}{4\epsilon_+^{\pi}(\mathbf{k})\epsilon_-^{\pi}(\mathbf{k})}\left[\delta\left(\Omega + \epsilon_+^{\pi}(\mathbf{k}) + \epsilon_-^{\pi}(\mathbf{k})\right) - \delta\left(\Omega - \epsilon_+^{\pi}(\mathbf{k}) - \epsilon_-^{\pi}(\mathbf{k})\right)\right]
$$

$$
+ \frac{\pi(n(\epsilon_+^{\pi}(\mathbf{k})) - n(\epsilon_-^{\pi}(\mathbf{k})))}{4\epsilon_+^{\pi}(\mathbf{k})\epsilon_-^{\pi}(\mathbf{k})}\left[\delta\left(\Omega + \epsilon_-^{\pi}(\mathbf{k}) - \epsilon_+^{\pi}(\mathbf{k})\right) - \delta\left(\Omega + \epsilon_+^{\pi}(\mathbf{k}) - \epsilon_-^{\pi}(\mathbf{k})\right)\right]
$$

$$
\tag{B.25}
$$

Substituting the above expressions in B.23, we obtain the linewidth of the phonon in the $\pi-$flux phase due to the phonon-magnetic monopole coupling which is given in Eq. 4.37 of the main text.

B.5 Effect of Gauge fluctuations for the magnetic monopoles

The vertex functions of the photon-magnetic monopole interaction of Eq. 4.38 are given by,

$$
\begin{aligned}
\gamma_B^{\mu\nu}(\mathbf{k}, \mathbf{k}') &= e^{-i\mathbf{k}\cdot\mathbf{d}_\mu} e^{i\mathbf{k}'\cdot\mathbf{d}_\nu} - e^{-i\mathbf{k}\cdot\mathbf{d}_\nu} e^{i\mathbf{k}'\cdot\mathbf{d}_\mu} \\
\gamma_A^{\mu\nu}(\mathbf{k}, \mathbf{k}') &= e^{-i\mathbf{k}\cdot(\mathbf{d}_\mu-\mathbf{d}_\nu)} - e^{i\mathbf{k}'\cdot(\mathbf{d}_\mu-\mathbf{d}_\nu)}
\end{aligned}
\tag{B.26}
$$

Due to the photon-monopole interaction, the interaction vertices of phonon-monopole coupling is modified. The leading order contribution to the vertex correction obtained from the perturbative expansion is given by,

$$
\delta\alpha^{(\rho)}(\mathbf{q}, \mathbf{p}, i\Omega, i\omega_m) = -\frac{J_\pm^2}{16N^{\frac{3}{2}}} \sum_{\mathbf{k}} \sum_{\mu,\nu} (\alpha_\mathbf{k}^{(\rho)} + \alpha_{\mathbf{k}+\mathbf{q}}^{(\rho)}) \gamma_B^\mu(\mathbf{p}, \mathbf{k}+\mathbf{q}) \gamma_A^\nu(\mathbf{k}, -\mathbf{q}+\mathbf{p})
$$
$$
\times \frac{1}{\beta} \sum_{\omega_n} G_\phi(\mathbf{k}+\mathbf{q}, B, i\Omega + i\omega_n) D_{\mu\nu}(\mathbf{k}+\mathbf{q}-\mathbf{p}, i\Omega + i\omega_n - i\omega_m) G_\phi(\mathbf{k}, A, i\omega_n)
$$

$$
\tag{B.27}
$$

where, $\gamma_{A,B}^\mu(\mathbf{k}, \mathbf{k}') = \sum_{\nu(\neq\mu)} \gamma_{A,B}^{\mu\nu}(\mathbf{k}, \mathbf{k}')$.

To further simplify the above expression, we first perform the frequency summation of the above expression using Matsubara method and then the momentum integrals are computed using the several approximations. The monopole band structure is expanded around the minima at $\mathbf{k} = 0$ up to first non-zero term.

$$
\epsilon_\mathbf{k}^0 \approx \Delta + m_0 k^2
\tag{B.28}
$$

where m_0 is a constant measuring the curvature of the band at $\mathbf{k} = 0$. Further, the vertex functions are also expanded in momentum and approximated to the leading term to obtain from

Eq. 4.24,

$$\mid \alpha_{\mathbf{k}}^{(e)} \mid \approx 2 \,, \quad \mid \alpha_{\mathbf{k}}^{(t_2)} \mid = \sqrt{\frac{\sum_{p=1}^{3} \mid \alpha_{p,\mathbf{k}}^{(t_2)} \mid^2}{3}} \approx \frac{k}{3} \tag{B.29}$$

and from Eq. B.26,

$$\gamma_A^{\mu\nu}(\mathbf{k}, \mathbf{k}') \approx i(\mathbf{k} + \mathbf{k}') \cdot (\mathbf{d}_{\boldsymbol{\nu}} - \mathbf{d}_{\boldsymbol{\mu}})$$
$$\gamma_B^{\mu\nu}(\mathbf{k}, \mathbf{k}') \approx i(\mathbf{k} + \mathbf{k}') \cdot (\mathbf{d}_{\boldsymbol{\nu}} - \mathbf{d}_{\boldsymbol{\mu}}) \tag{B.30}$$

We substitute the above expressions in Eq. B.27. Due to Raman criterion, only $\mathbf{q} = 0$ limit is considered. Further, we set $\Omega = \omega_m = 0$ to find the frequency independent correction. We redefine the notations as,

$$\delta\alpha^{(e)}(0, \mathbf{p}, 0, 0) = \delta\alpha_{\mathbf{p}}^{(e)}$$
$$\delta\alpha^{(t_2)}(0, \mathbf{p}, 0, 0) = \delta\alpha_{\mathbf{p}}^{(t_2)}$$

Finally, applying all the approximations described above, the leading corrections to the vertex functions are obtained which is given in Eq. 4.39.

B.6 Hamiltonian and form factors in the paramagnetic phase

For the convenience of calculation, we express the Hamiltonian given in Eq. 4.6 and 4.7 in momentum space representation.

$$H_{sp}^{(e)} = J_{sp}^{(e)} \sum_{\mathbf{k}} \sum_{\mu=0}^{3} \left(\zeta_{1,g}^{(e)}(\mathbf{k}) s_\mu^x(-\mathbf{k}) + \zeta_{2,g}^{(e)}(\mathbf{k}) s_\mu^y(-\mathbf{k}) \right) \left(1 + e^{i\mathbf{k}\cdot\mathbf{d}_{\boldsymbol{\mu}}} \right) \tag{B.31}$$

$$H_{sp}^{(t_2)} = J_{sp}^{(t_2)} \sum_{\mathbf{k}} \sum_{p=1}^{3} \sum_{\alpha=x,y} \sum_{\mu=0}^{3} L_{p,\alpha,\mu}^{(t_2)} \zeta_{p,g}^{(t_2)}(\mathbf{k}) s_\mu^\alpha(-\mathbf{k}) \left(1 + e^{i\mathbf{k}\cdot\mathbf{d}_{\boldsymbol{\mu}}} \right) \tag{B.32}$$

From the above Hamiltonians, we can obtain the self-energy of the phonon using similar kind of perturbation theory as applied to QSL phase. Again, the first non-zero contribution comes in the second order($\mathcal{O}(J_{sp}^{(\rho)2})$) in the perturbative series and it is given in Eq. 4.50 of the main text. The form factors in the Eq. 4.50 are given by,

$$\eta_{\mu\nu}^{(e)}(\mathbf{q}) = 1 + e^{i\mathbf{q}\cdot\mathbf{d}_{\boldsymbol{\nu}}} + e^{-i\mathbf{q}\cdot\mathbf{d}_{\boldsymbol{\mu}}} + e^{i\mathbf{q}\cdot(\mathbf{d}_{\boldsymbol{\mu}}-\mathbf{d}_{\boldsymbol{\nu}})}$$

$$\eta_{\mu\nu,\alpha}^{(t_2)}(\mathbf{q}) = (1 + e^{i\mathbf{q}\cdot\mathbf{d}_{\boldsymbol{\nu}}} + e^{-i\mathbf{q}\cdot\mathbf{d}_{\boldsymbol{\mu}}} + e^{i\mathbf{q}\cdot(\mathbf{d}_{\boldsymbol{\mu}}-\mathbf{d}_{\boldsymbol{\nu}})}) \sum_{p=1}^{3} L_{p,\alpha,\mu}^{(t_2)} L_{p,\alpha,\nu}^{(t_2)} \tag{B.33}$$

APPENDIX C

ANOMALOUS RAMAN SIGNATURES OF $Ca_{10}Cr_7O_{28}$

C.1 The phonon linewidth

The linewidth of the phonon can be perturbatively obtained from Eq. 5.16 by calculating the imaginary part of its self-energy. To the leading order, it is given by,

$$
\Pi_{orb}^{(p)} \propto \mathcal{I}m \left(\int_0^\beta d\tau \, e^{i\omega_n \tau} \langle\langle \hat{T} \left[\Gamma^{p,\beta} \tau_i^\beta(\tau) + \sum_j A_{ij}^{\beta\gamma;p} \tau_i^\beta(\tau) \tau_j^\gamma(\tau) \right] \right.
$$

$$
\left. \times \left[\Gamma^{p,\beta'} \tau_i^{\beta'}(0) + \sum_k A_{ik}^{\beta'\gamma';p} \tau_i^{\beta'}(0) \tau_k^{\gamma'}(0) \right] \rangle\rangle \right)_{i\omega_n \to \omega + i0^+}
$$

$$
= \mathcal{I}m \left(\int_0^\beta d\tau \, e^{i\omega_n \tau} \left[\Gamma^{p,\beta} \Gamma^{p,\beta'} \sum_{ij} \langle\langle \hat{T} \left(\tau_i^\beta(\tau) \tau_j^{\beta'}(0) \right) \rangle\rangle \right. \right.
$$

$$
+ \Gamma^{p,\beta} \sum_{ijk} A_{jk}^{\beta'\gamma';p} \langle\langle \hat{T} \left(\tau_i^\beta(t) \tau_j^{\beta'}(0) \tau_k^{\gamma'}(0) \right) \rangle\rangle
$$

$$
+ \sum_{ijk} A_{ij}^{\beta\gamma;p} \Gamma^{p,\beta'} \langle\langle \hat{T} \left(\tau_i^\beta(\tau) \tau_j^\gamma(\tau) \tau_k^{\beta'}(0) \right) \rangle\rangle
$$

$$
\left. \left. + \sum_{ijkl} A_{ij}^{\beta\gamma;p} A_{kl}^{\beta'\gamma';p} \langle\langle \hat{T} \left(\tau_i^\beta(\tau) \tau_j^\gamma(\tau) \tau_k^{\beta'}(0) \tau_l^{\gamma'}(0) \right) \rangle\rangle \right] \right)_{i\omega_n \to \omega + i0^+} \quad \text{(C.1)}
$$

There are four contributions which are given as follows :

Contribution-1 :

$$
\Pi_{(1)}^{(p)}(\mathbf{k}, \omega) = \frac{\Gamma^{p,\beta} \Gamma^{p,\beta'}}{N^2} \sum_{ij} \mathcal{I}m \left(\int_0^\beta d\tau \, e^{i\omega_n \tau} \langle\langle \hat{T} \left(\tau_i^\beta(\tau) \tau_j^{\beta'}(0) \right) \rangle\rangle e^{-i\mathbf{k}\cdot(\mathbf{r}_j - \mathbf{r}_i)} \right)_{i\omega_n \to \omega + i0^+}
$$

$$
= \Gamma^{p,\beta} \Gamma^{p,\beta'} \, \mathcal{I}m \left(\tilde{\mathcal{C}}_{\beta\beta'}(\mathbf{k}, \omega + i0^+) \right) \quad \text{(C.2)}
$$

$$\Pi_{(1)}^{(p)}(\mathbf{k}=\mathbf{0},\omega) = \mathcal{I}m\left[\Gamma^{p,x}\Gamma^{p,x}\tilde{\mathcal{C}}_{xx}(\mathbf{k}=\mathbf{0},\omega+i0^+) + \Gamma^{p,x}\Gamma^{p,z}\tilde{\mathcal{C}}_{xz}(\mathbf{k}=\mathbf{0},\omega+i0^+)\right.$$
$$\left. +\Gamma^{p,z}\Gamma^{p,x}\tilde{\mathcal{C}}_{zx}(\mathbf{k}=\mathbf{0},\omega+i0^+) + \Gamma^{p,z}\Gamma^{p,z}\tilde{\mathcal{C}}_{zz}(\mathbf{k}=\mathbf{0},\omega+i0^+)\right]$$

$$(\mathrm{C.3})$$

Contribution-2 : We assume the coupling constant $A_{ij}^{\beta\gamma;p}$ to be uniform, i.e., $A_{ij}^{\beta\gamma;p} = A^{\beta\gamma;p}$.

$$\Pi_{(2)}^{(p)}(\mathbf{k},\omega)$$
$$=\frac{\Gamma^{p,\beta}A^{\beta'\gamma';p}}{N^3}$$
$$\times \sum_{ijk}\int d\mathbf{k}'\, \mathcal{I}m\left(\int_0^\beta dt\, e^{i\omega_n\tau}\langle\langle\hat{T}\left(\tau_i^\beta(\tau)\tau_j^{\beta'}(0)\tau_k^{\gamma'}(0)\right)\rangle\rangle e^{-i\mathbf{k}\cdot(\mathbf{r}_i-\mathbf{r}_k)}e^{-i\mathbf{k}'\cdot(\mathbf{r}_j-\mathbf{r}_k)}\right)_{i\omega_n\to\omega+i0^+}$$
$$\approx\frac{\Gamma^{p,\beta}A^{\beta'\gamma';p}}{N^3}\sum_{ijk}\int d\mathbf{k}'\, \mathcal{I}m\left(\mathcal{C}_{ij}^{\beta\beta'}(\omega+i0^+)\langle\tau_k^{\gamma'}\rangle + \mathcal{C}_{ik}^{\beta\gamma'}(\omega+i0^+)\langle\tau_j^{\beta'}\rangle\right)$$
$$\times e^{-i\mathbf{k}\cdot(\mathbf{r}_i-\mathbf{r}_k)}e^{-i\mathbf{k}'\cdot(\mathbf{r}_j-\mathbf{r}_k)}$$
$$=\frac{\Gamma^{p,\beta}\left(A^{\beta'\gamma';p}+A^{\gamma'\beta';p}\right)}{N^2}\sum_{ij}\int d\mathbf{k}'\, \langle\tau_{\mathbf{k}+\mathbf{k}'}^{\gamma'}\rangle\mathcal{I}m\left(\mathcal{C}_{ij}^{\beta\beta'}(\omega+i0^+)\right)e^{-i\mathbf{k}\cdot\mathbf{r}_i}e^{-i\mathbf{k}'\cdot\mathbf{r}_j}$$
$$=\Gamma^{p,\beta}\left(A^{\beta'\gamma';p}+A^{\gamma'\beta';p}\right)\langle\tau^{\gamma'}\rangle\mathcal{I}m\left(\tilde{\mathcal{C}}_{\beta\beta'}(\mathbf{k},\omega+i0^+)\right) \qquad (\mathrm{C.4})$$

where in the second step we have applied the quadratic approximation by splitting the **3**-point correlator in **2**- and **1**-point correlators and at the last step in the mean field level we have used, $\langle\tau_{\mathbf{k}+\mathbf{k}'}^{\gamma'}\rangle = \langle\tau^{\gamma'}\rangle\delta_{\mathbf{k},-\mathbf{k}'}$. Adding all the contributions, we get,

$$\Pi_{(2)}^{(p)}(\mathbf{k}=0,\omega) = \left(2A^{xx;p}\Gamma^{p,x}\langle\tau^x\rangle + \Gamma^{p,x}\left(A^{xz;p}+A^{zx;p}\right)\langle\tau^z\rangle\right)\mathcal{I}m\left[\tilde{\mathcal{C}}_{xx}\left(\mathbf{k}=0,\omega+i0^+\right)\right]$$
$$+\left(2A^{xx;p}\Gamma^{p,z}\langle\tau^x\rangle + \Gamma^{p,z}\left(A^{xz;p}+A^{zx;p}\right)\langle\tau^z\rangle\right)\mathcal{I}m\left[\tilde{\mathcal{C}}_{zx}(\mathbf{k}=0,\omega+i0^+)\right]$$
$$+\left(2A^{zz;p}\Gamma^{p,x}\langle\tau^z\rangle + \Gamma^{p,x}\left(A^{zx;p}+A^{xz;p}\right)\langle\tau^x\rangle\right)\mathcal{I}m\left[\tilde{\mathcal{C}}_{xz}(\mathbf{k}=0,\omega+i0^+)\right]$$
$$+\left(2A^{zz;p}\Gamma^{p,x}\langle\tau^z\rangle + \Gamma^{p,z}\left(A^{zx;p}+A^{xz;p}\right)\langle\tau^x\rangle\right)\mathcal{I}m\left[\tilde{\mathcal{C}}_{zz}(\mathbf{k}=0,\omega+i0^+)\right]$$

$$(\mathrm{C.5})$$

Contribution-3 : Very similar to the contribution-2, it can be shown :

$$
\Pi^{(p)}_{(3)}(\mathbf{k}, \omega) = \frac{\Gamma^{p\beta} A^{\beta'\gamma';p}}{N^3}
$$
$$
\times \sum_{ijk} \int d\mathbf{k}' \, \mathcal{I}m \left(\int d\tau \, e^{i\omega_n \tau} \langle\langle \hat{T} \left(\tau_i^\beta(\tau) \tau_j^{\beta'}(0) \tau_k^{\gamma'}(0) \right) \rangle\rangle e^{-i\mathbf{k}\cdot(\mathbf{r}_i - \mathbf{r}_k)} e^{-i\mathbf{k}'\cdot(\mathbf{r}_j - \mathbf{r}_k)} \right)_{i\omega_n \to \omega + i0^+}
$$
$$
\approx \Gamma^{p\beta} \left(A^{\beta'\gamma';p} + A^{\gamma'\beta';p} \right) \langle \tau^{\gamma'} \rangle \mathcal{I}m \left(\tilde{\mathcal{C}}_{\beta'\beta}(\mathbf{k}, \omega + i0^+) \right) \tag{C.6}
$$

Adding all the contributions we get,

$$
\Pi^{(p)}_{(3)}(\mathbf{k} = 0, \omega) = (2A^{xx;p}\Gamma^{p,x}\langle\tau^x\rangle + \Gamma^{p,x}\left(A^{xz;p} + A^{zx;p}\right)\langle\tau^z\rangle)\, \mathcal{I}m\left[\tilde{\mathcal{C}}_{xx}\left(\mathbf{k}=0, \omega + i0^+\right)\right]
$$
$$
+ (2A^{xx;p}\Gamma^{p,z}\langle\tau^x\rangle + \Gamma^{p,z}\left(A^{xz;p} + A^{zx;p}\right)\langle\tau^z\rangle)\, \mathcal{I}m\left[\tilde{\mathcal{C}}_{xz}(\mathbf{k}=0, \omega + i0^+)\right]
$$
$$
+ (2A^{zz;p}\Gamma^{p,x}\langle\tau^z\rangle + \Gamma^{p,x}\left(A^{zx;p} + A^{xz;p}\right)\langle\tau^x\rangle)\, \mathcal{I}m\left[\tilde{\mathcal{C}}_{zx}(\mathbf{k}=0, \omega + i0^+)\right]
$$
$$
+ (2A^{zz;p}\Gamma^{p,x}\langle\tau^z\rangle + \Gamma^{p,z}\left(A^{zx;p} + A^{xz;p}\right)\langle\tau^x\rangle)\, \mathcal{I}m\left[\tilde{\mathcal{C}}_{zz}(\mathbf{k}=0, \omega + i0^+)\right]
$$
$$
\tag{C.7}
$$

Note that contribution-1, 2 and 3 have similar dependence on the imaginary part of the time-ordered two-point spin correlations.

Contribution-4

$$
\Pi^{(p)}_{(4)}(\mathbf{k}, \omega) = \frac{A^{\beta\gamma;(p)} A^{\beta'\gamma';(p)}}{N^4} \sum_{ijkl}
$$
$$
\times \int d\mathbf{k}' d\mathbf{k}'' \, \mathcal{I}m \left(\int_0^\beta d\tau \, e^{i\omega_n \tau} \langle\langle \hat{T} \left(\tau_i^\beta(\tau) \tau_j^\gamma(\tau) \tau_k^{\beta'}(0) \tau_l^{\gamma'}(0) \right) \rangle\rangle \right)_{i\omega_n \to \omega + i0^+}
$$
$$
\times e^{-i\mathbf{k}'\cdot(\mathbf{r_i} - \mathbf{r_j}) - i\mathbf{k}\cdot(\mathbf{r_l} - \mathbf{r_j}) - i\mathbf{k}''\cdot(\mathbf{r_k} - \mathbf{r_l})}
$$
$$
= \left(A^{\beta\gamma;p} A^{\beta'\gamma';p} + A^{\beta\gamma;p} A^{\gamma'\beta';p} \right) \left(\langle\tau^\gamma\rangle\langle\tau^{\gamma'}\rangle \mathcal{I}m\left[\tilde{\mathcal{C}}_{\beta\beta'}(\mathbf{k}, \omega + i0^+)\right] \right.
$$
$$
\left. + \frac{1}{2\pi}\mathcal{I}m\left[\int d\mathbf{k}' \sum_m \tilde{\mathcal{C}}_{\beta\beta'}(\mathbf{k} + \mathbf{k}', \omega_n + \Omega_m) \tilde{\mathcal{C}}_{\gamma\gamma'}(-\mathbf{k}', -\Omega_m)\right] \right)_{i\omega_n \to \omega + i0^+}
$$
$$
\tag{C.8}
$$

Therefore, adding all the contribution the phonon linewidth can be written as,

$$
\Pi_{orb}^{(p)} \left(\mathbf{k} = 0, \omega \right) = \sum_{\mu,\nu=x,z} \mathcal{M}_{\mu\nu} \mathcal{I}m \left[\tilde{\mathcal{C}}_{\mu\nu} \left(\mathbf{k} = 0, \omega + i0^{+} \right) \right]
$$
$$
+ \sum_{\mu,\nu=x,z} \sum_{\alpha,\beta=x,z} \mathcal{M}_{\alpha\beta\mu\nu} \mathrm{Im} \left[\int d\mathbf{k}' \sum_{m} \tilde{\mathcal{C}}_{\mu\nu}(\mathbf{k}', i\Omega_m + i\omega_n) \tilde{\mathcal{C}}_{\alpha\beta} \left(-\mathbf{k}', -i\Omega_m \right) \right]_{i\omega_n \to \omega + i0^{+}}
$$
$$
\tag{C.9}
$$

Here $\mathcal{M}_{\mu\nu}$ and $\mathcal{M}_{\alpha\beta\mu\nu}$ are in general temperature dependent coupling coefficients. It is clear from the above expression that the various contributions, within the the quadratic approximations are given by the various components of the two-spin correlation function $\tilde{\mathcal{C}}_{\mu\nu}(\mathbf{k}, i\omega_n)$ which we now calculate within quadratic approximation from the bare orbital Hamiltonian.

C.2 Time-ordered correlation functions for the orbital degrees of freedom in imaginary time formulation

The bare orbital part of the low energy Hamiltonian is given by,

$$
H_{orb} = \sum_{\langle ij \rangle} \bar{\mathcal{K}}^{xx} \tau_i^x \tau_j^x + \Delta_1 \sum_i \tau_i^z \tag{C.10}
$$

Equation of motion for the orbital degrees of freedom due to the above Hamiltonian in the imaginary time formulation is given by,

$$
\dot{\tau}_{\mathbf{r}}^x = 2i\Delta_1 \tau_{\mathbf{r}}^y \tag{C.11}
$$
$$
\dot{\tau}_{\mathbf{r}}^y = 2i\bar{\mathcal{K}}^{xx} \sum_{\mathbf{d}} \tau_{\mathbf{r}}^z \tau_{\mathbf{r}+\mathbf{d}}^x - 2i\Delta_1 \tau_{\mathbf{r}}^x \tag{C.12}
$$
$$
\dot{\tau}_{\mathbf{r}}^z = -2i\bar{\mathcal{K}}^{xx} \sum_{\mathbf{d}} \tau_{\mathbf{r}}^y \tau_{\mathbf{r}+\mathbf{d}}^x \tag{C.13}
$$

Equations of motion for the correlators:

$$\dot{\mathcal{C}}_{xx}(\mathbf{r}, t) = 2i\Delta_1 \mathcal{C}_{yx}(\mathbf{r}, t) \tag{C.14}$$

$$\dot{\mathcal{C}}_{yx}(\mathbf{r}, t) + 2i\Delta_1 \mathcal{C}_{xx}(\mathbf{r}, t) = -2i\delta(t)\delta(\mathbf{r})\langle\tau^z\rangle - 2i\Delta_1\langle\tau^x\rangle^2 + 2i\bar{\mathcal{K}}^{xx}\sum_{\mathbf{d}}\langle\hat{T}\left(\tau_{\mathbf{r}}^z(t)\tau_{\mathbf{r+d}}^x(t)\tau_0^x(0)\right)\rangle \tag{C.15}$$

$$\dot{\mathcal{C}}_{zx}(\mathbf{r}, t) = -2i\bar{\mathcal{K}}^{xx}\sum_{\mathbf{d}}\langle\hat{T}\left(\tau_{\mathbf{r}}^y(t)\tau_{\mathbf{r+d}}^x(t)\tau_0^x(0)\right)\rangle \tag{C.16}$$

$$\dot{\mathcal{C}}_{yz}(\mathbf{r}, t) = 2i\delta(t)\delta(\mathbf{r})\langle\tau^x\rangle + 2i\bar{\mathcal{K}}^{xx}\sum_{\mathbf{d}}\langle\hat{T}\left(\tau_{\mathbf{r}}^z(t)\tau_{\mathbf{r+d}}^x(t)\tau_0^z(0)\right)\rangle - 2i\Delta_1\left(\mathcal{C}_{xz}(\mathbf{r}, t) + \langle\tau^x\rangle\langle\tau^z\rangle\right) \tag{C.17}$$

$$\dot{\mathcal{C}}_{zz}(\mathbf{r}, t) = -2i\bar{\mathcal{K}}^{xx}\sum_{\mathbf{d}}\langle\hat{T}\left(\tau_{\mathbf{r}}^y(t)\tau_{\mathbf{r+d}}^x(t)\tau_0^z(0)\right)\rangle \tag{C.18}$$

$$\dot{\mathcal{C}}_{xz}(\mathbf{r}, t) = 2i\Delta_1 \mathcal{C}_{yz}(\mathbf{r}, t) \tag{C.19}$$

C.2.1 Quadratic Approximations and solving the equations of motion of Green's function

Approximation 1: To solve the above equations of motion, we approximate the 3-point correlators in the above equations of motion by splitting into 2-point and 1-point correlations. A typical example looks like as follows.

$$\bar{\mathcal{K}}^{xx}\sum_{\mathbf{d}}\langle\hat{T}\left(\tau_{\mathbf{r}}^z(t)\tau_{\mathbf{r+d}}^x(t)\tau_0^x(0)\right)\rangle \approx \tilde{\mathcal{K}}^{xx}\left(\langle\langle\tau_{\mathbf{r}}^z\tau_{\mathbf{r+d}}^x\rangle\rangle\langle\tau^x\rangle + \mathcal{C}_{zx}(\mathbf{r}, t)\langle\tau^x\rangle\right.$$
$$\left. + \mathcal{C}_{xx}(\mathbf{r}, t)\langle\tau^z\rangle + \langle\tau^z\rangle\langle\tau^x\rangle^2\right) \tag{C.20}$$

where, $\tilde{\mathcal{K}}^{xx} = \bar{\mathcal{K}}^{xx}D$ with D being being the coordination number. The first term is time-independent, hence do not contribute to finite frequency response.

Approximation 2: We further do a second approximation by setting the nearest neighbour 2-point correlator in Eq. C.20 to its mean field value, such that, $\langle\langle\tau_{\mathbf{r}}^z\tau_{\mathbf{r+d}}^x\rangle\rangle = \langle\tau_{\mathbf{r}}^z\tau_{\mathbf{r+d}}^x\rangle - \langle\tau_{\mathbf{r}}^z\rangle\langle\tau_{\mathbf{r+d}}^x\rangle \approx 0$.

With these approximations, the equation of motions can be simplified to,

$$\dot{C}_{xx}(\tau, \mathbf{r}) = 2i\Delta_1 C_{yx}(\tau, \mathbf{r}) \tag{C.21}$$

$$\dot{C}_{zx}(\tau, \mathbf{r}) = -2i\tilde{\mathcal{K}}\langle\tau^x\rangle C_{yx}(\tau, \mathbf{r}) \tag{C.22}$$

$$\dot{C}_{yx}(\tau, \mathbf{r}) + 2i\left(\Delta_1 - \tilde{\mathcal{K}}\langle\tau^z\rangle\right)C_{xx}(\tau, \mathbf{r}) - 2i\tilde{\mathcal{K}}\langle\tau^x\rangle C_{zx}(\tau, \mathbf{r}) = C_2(\tau, \mathbf{r}) \tag{C.23}$$

$$\dot{C}_{xz}(\tau, \mathbf{r}) = 2i\Delta_1 C_{yz}(\tau, \mathbf{r}) \tag{C.24}$$

$$\dot{C}_{zz}(\tau, \mathbf{r}) = -2i\tilde{\mathcal{K}}\langle\tau^x\rangle C_{yz}(\tau, \mathbf{r}) \tag{C.25}$$

$$\dot{C}_{yz}(\tau, \mathbf{r}) + 2i\left(\Delta_1 - \tilde{\mathcal{K}}\right)C_{xz}(\tau, \mathbf{r}) - 2i\tilde{\mathcal{K}}\langle\tau^x\rangle C_{zz}(\tau, \mathbf{r}) = C_1(\tau, \mathbf{r}) \tag{C.26}$$

where,

$$C_1(\tau, \mathbf{r}) = 2i\langle\tau^x\rangle\delta(\tau)\delta(\mathbf{r}) + 2i\langle\tau^x\rangle\langle\tau^z\rangle\left(\tilde{\mathcal{K}}\langle\tau^z\rangle - \Delta_1\right)$$

$$C_2(\tau, \mathbf{r}) = -2i\langle\tau^z\rangle\delta(\tau)\delta(\mathbf{r}) + 2i\langle\tau^x\rangle^2\left(\tilde{\mathcal{K}}\langle\tau^z\rangle - \Delta_1\right)$$

The above equations can be easily solved by going to the frequency space. The frequency space correlations are then given by,

$$\tilde{C}_{yz}(i\omega_n, \mathbf{k} = 0) = -\frac{i\omega_n \tilde{C}_1(i\omega_n, \mathbf{k} = 0)}{(i\omega_n)^2 - \left(4\Delta_1^2 + 4\tilde{\mathcal{K}}^2\langle\tau^x\rangle^2 - 4\tilde{\mathcal{K}}\Delta_1\langle\tau^z\rangle\right)} \tag{C.27}$$

$$\tilde{C}_{xz}(i\omega_n, \mathbf{k} = 0) = \frac{2i\Delta_1 \tilde{C}_1(i\omega_n, \mathbf{k} = 0)}{(i\omega_n)^2 - \left(4\Delta_1^2 + 4\tilde{\mathcal{K}}^2\langle\tau^x\rangle^2 - 4\tilde{\mathcal{K}}\Delta_1\langle\tau^z\rangle\right)} \tag{C.28}$$

$$\tilde{C}_{zz}(i\omega_n, \mathbf{k} = 0) = -\frac{2i\tilde{\mathcal{K}}\langle\tau^x\rangle\tilde{C}_1(i\omega_n, \mathbf{k} = 0)}{(i\omega_n)^2 - \left(4\Delta_1^2 + 4\tilde{\mathcal{K}}^2\langle\tau^x\rangle^2 - 4\tilde{\mathcal{K}}\Delta_1\langle\tau^z\rangle\right)} \tag{C.29}$$

$$\tilde{C}_{yx}(i\omega_n, \mathbf{k} = 0) = -\frac{i\omega_n \tilde{C}_2(i\omega_n, \mathbf{k} = 0)}{(i\omega_n)^2 - \left(4\Delta_1^2 + 4\tilde{\mathcal{K}}^2\langle\tau^x\rangle^2 - 4\tilde{\mathcal{K}}\Delta_1\langle\tau^z\rangle\right)} \tag{C.30}$$

$$\tilde{C}_{xx}(i\omega_n, \mathbf{k} = 0) = \frac{2i\Delta_1 \tilde{C}_2(i\omega_n, \mathbf{k} = 0)}{(i\omega_n)^2 - \left(4\Delta_1^2 + 4\tilde{\mathcal{K}}^2\langle\tau^x\rangle^2 - 4\tilde{\mathcal{K}}\Delta_1\langle\tau^z\rangle\right)} \tag{C.31}$$

$$\tilde{C}_{zx}(i\omega_n, \mathbf{k} = 0) = -\frac{2i\tilde{\mathcal{K}}\langle\tau^x\rangle\tilde{C}_2(i\omega_n, \mathbf{k} = 0)}{(i\omega_n)^2 - \left(4\Delta_1^2 + 4\tilde{\mathcal{K}}^2\langle\tau^x\rangle^2 - 4\tilde{\mathcal{K}}\Delta_1\langle\tau^z\rangle\right)} \tag{C.32}$$

where,

$$\tilde{C}_1(i\omega_n, \mathbf{k} = 0) = \frac{2i}{N}\langle\tau^x\rangle + 2i\beta\langle\tau^x\rangle\langle\tau^z\rangle\left(\tilde{\mathcal{K}}\langle\tau^z\rangle - \Delta_1\right)\delta_{n,0}$$

$$\tilde{C}_2(i\omega_n, \mathbf{k} = 0) = -\frac{2i}{N}\langle\tau^z\rangle + 2i\beta\langle\tau^x\rangle^2 \left(\tilde{\mathcal{K}}\langle\tau^z\rangle - \Delta_1\right)\delta_{n,0}$$

The correlators in the real frequency space can be obtained from the above by the standard procedure of analytic continuation, $i\omega_n \rightarrow \omega + i0^+$.

C.2.2 Phenomenological damping of the correlation functions

We add a phenomenological term to the equations of motion given in Eqs. C.21 – C.26 which causes the decay of the correlation functions with time.

$$\dot{C}_{xx}(\tau, \mathbf{r}) - i\Gamma\, C_{xx}(\tau, \mathbf{r}) = 2i\Delta_1 C_{yx}(\tau, \mathbf{r}) \tag{C.33}$$

$$\dot{C}_{zx}(\tau, \mathbf{r}) - i\Gamma\, C_{zx}(\tau, \mathbf{r}) = -2i\tilde{\mathcal{K}}\langle\tau^x\rangle C_{yx}(\tau, \mathbf{r}) \tag{C.34}$$

$$\dot{C}_{yx}(\tau, \mathbf{r}) - i\Gamma\, C_{yx}(\tau, \mathbf{r}) + 2i\left(\Delta_1 - \tilde{\mathcal{K}}\langle\tau^z\rangle\right)C_{xx}(\tau, \mathbf{r}) - 2i\tilde{\mathcal{K}}\langle\tau^x\rangle C_{zx}(\tau, \mathbf{r}) = C_2(\tau, \mathbf{r}) \tag{C.35}$$

$$\dot{C}_{xz}(\tau, \mathbf{r}) - i\Gamma\, C_{xz}(\tau, \mathbf{r}) = 2i\Delta_1 C_{yz}(\tau, \mathbf{r}) \tag{C.36}$$

$$\dot{C}_{zz}(\tau, \mathbf{r}) - i\Gamma\, C_{zz}(\tau, \mathbf{r}) = -2i\tilde{\mathcal{K}}\langle\tau^x\rangle C_{yz}(\tau, \mathbf{r}) \tag{C.37}$$

$$\dot{C}_{yz}(\tau, \mathbf{r}) - i\Gamma\, C_{yz}(\tau, \mathbf{r}) + 2i\left(\Delta_1 - \tilde{\mathcal{K}}\right)C_{xz}(\tau, \mathbf{r}) - 2i\tilde{\mathcal{K}}\langle\tau^x\rangle C_{zz}(\tau, \mathbf{r}) = C_1(\tau, \mathbf{r}) \tag{C.38}$$

The relevant correlators to the linewidth calculations now become,

$$\tilde{C}_{xx}(i\omega_n, \mathbf{k}) = \frac{2i\Delta_1\tilde{C}_2(i\omega_n, \mathbf{k})}{(i\omega_n)^2 - \left(4\Delta_1^2 + 4\tilde{\mathcal{K}}^2\langle\tau^x\rangle^2 - 4\tilde{\mathcal{K}}\Delta_1\langle\tau^z\rangle\right) - \Gamma^2 - 2\omega_n\Gamma} \tag{C.39}$$

$$\tilde{C}_{xz}(i\omega_n, \mathbf{k}) = \frac{2i\Delta_1\tilde{C}_1(i\omega_n, \mathbf{k})}{(i\omega_n)^2 - \left(4\Delta_1^2 + 4\tilde{\mathcal{K}}^2\langle\tau^x\rangle^2 - 4\tilde{\mathcal{K}}\Delta_1\langle\tau^z\rangle\right) - \Gamma^2 - 2\omega_n\Gamma} \tag{C.40}$$

$$\tilde{C}_{zz}(i\omega_n, \mathbf{k}) = -\frac{2i\,\tilde{\mathcal{K}}\langle\tau^x\rangle\,\tilde{C}_1(i\omega_n, \mathbf{k})}{(i\omega_n)^2 - \left(4\Delta_1^2 + 4\tilde{\mathcal{K}}^2\langle\tau^x\rangle^2 - 4\tilde{\mathcal{K}}\Delta_1\langle\tau^z\rangle\right) - \Gamma^2 - 2\omega_n\Gamma} \tag{C.41}$$

The imaginary part of the above correlation functions contribute to the phonon linewidth as described in Eq. 5.21. Since the numerators of the above expressions are purely real, the contribution completely comes from the denominator. Generically, all the contribution looks like as follows,

$$\mathcal{I}m\left[\tilde{C}_{\mu\nu}(\omega+i0^+,\mathbf{k}=0)\right] \propto -\frac{2\omega\Gamma}{\left(\omega^2 - \left(4\Delta_1^2 + 4\tilde{\mathcal{K}}^2\langle\tau^x\rangle^2 - 4\tilde{\mathcal{K}}\Delta_1\langle\tau^z\rangle\right) - \Gamma^2\right)^2 + 4\omega^2\Gamma^2}$$

<div align="right">(C.42)</div>

Substituting the above in Eq. C.9, we obtain the renormalisation of the linewidth of the phonons.

APPENDIX D

SPIN-3/2 ICE

D.1 The wave functions

The magnetic contribution of the material comes from $Tb^{3+}([Xe]4f^8)$ ion. Due to strong spin-orbit coupling of the rare-earth family, the outer shell forms $J = 6(L = 3, S = 3)$ Hilbert space. Because of the D_{3d} crystal field of the Oxygen, the 13 dimensional space splits in the following way [104]

$$\Gamma_{13} = 4\mathbf{e_g} \oplus 3\mathbf{a_{1g}} \oplus 2\mathbf{A_{2g}} \tag{D.1}$$

The lowest two CEF states are doublets and in the case of Tb^{3+}, these wave-function have been determined from the experiments and are given as follows [104]:

$$\mid \sigma_\pm/\tau_\pm \rangle = A_{\sigma/\tau} \mid \pm 4 \rangle \mp B_{\sigma/\tau} \mid \pm 1 \rangle + C_{\sigma/\tau} \mid \mp 2 \rangle \pm D_{\sigma/\tau} \mid \mp 5 \rangle \tag{D.2}$$

where $A_\sigma = 0.912$, $B_\sigma = 0.119$, $C_\sigma = 0.176$, $D_\sigma = 0.352$, $A_\tau = 0.374$, $B_\tau = 0.108$, $C_\tau = -0.232$, $D_\tau = -0.891$ (our choice differs by a phase from the description given in the reference). Both the doublets form E_g irreducible representation under the symmetry group of the anionic crystal field environment.

D.2 Symmetry transformation of $S = \frac{3}{2}$ states

The transformation properties of the $S = \frac{3}{2}$ states under symmetry of a tetrahedron (T_d) and time-reversal (TR) is given by

$$C_3[111]: \quad |\sigma_\pm\rangle_i \longrightarrow e^{\mp i\frac{2\pi}{3}} |\sigma_\pm\rangle_j$$

$$|\tau_\pm\rangle_i \longrightarrow e^{\mp i\frac{2\pi}{3}} |\tau_\pm\rangle_j$$

$$C_2[\hat{z}]: \quad |\sigma_\pm\rangle_i \longrightarrow |\sigma_\pm\rangle_j$$

$$|\tau_\pm\rangle_i \longrightarrow |\tau_\pm\rangle_j$$

$$\sigma_d[x=y]: \quad |\sigma_\pm\rangle_i \longrightarrow e^{\pm i\frac{2\pi}{3}} |\sigma_\mp\rangle_j$$

$$|\tau_\pm\rangle_i \longrightarrow e^{\pm i\frac{2\pi}{3}} |\tau_\mp\rangle_j$$

$$S_4[\hat{z}]: \quad |\sigma_\pm\rangle_i \longrightarrow e^{\pm i\frac{2\pi}{3}} |\sigma_\mp\rangle_j$$

$$|\tau_\pm\rangle_i \longrightarrow e^{\pm i\frac{2\pi}{3}} |\tau_\mp\rangle_j$$

$$TR: \quad |\sigma_\pm\rangle_i \longrightarrow |\sigma_\mp\rangle_i$$

$$|\tau_\pm\rangle_i \longrightarrow |\tau_\mp\rangle_i$$

Here, $|\ldots\rangle_i$ denotes the CEF state at site i of a tetrahedron. Transformation of the site index can be fixed from the transformation of the vertices of the tetrahedron (see Fig. D.1) under corresponding symmetry element. It can be easily represented by the following cycles:

$$C_3[111] \longrightarrow (243), \quad C_2[\hat{z}] \longrightarrow (12)(34)$$

$$\sigma_d[x=y] \longrightarrow (34), \quad S_4[\hat{z}] \longrightarrow (1324)$$

D.3 The on-site operators

The $S = 3/2$ spins allow for a 4 dimensional Hilbert space that is spanned by 4×4 matrices. Therefore, there are 15 non-trivial on-site operators. These are given by the dipole (three)

$$\{S_i^x, S_i^y, S_i^z\} \tag{D.3}$$
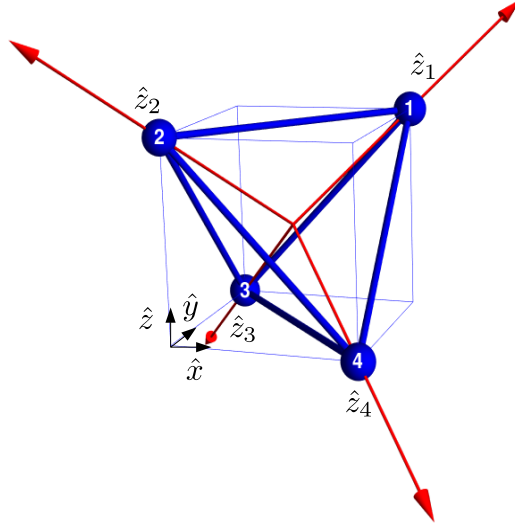
Figure D.1: Local basis for the up tetrahedron

quadrupole (five)

$$\{Q_i^{zz}, Q_i^{yy}, Q_i^{xy}, Q_i^{yz}, Q_i^{zx}\} \tag{D.4}$$

and octupole (seven)

$$\{T_i^{xxx}, T_i^{yyy}, T_i^{zzz}, T_i^{xxy}, T_i^{xxz}, T_i^{yyx}, T_i^{xyz}\} \tag{D.5}$$

operators. In terms of spins, the quadrupoles and octupoles are defined as,

$$Q_i^{\alpha\beta} = \frac{1}{2}\mathcal{S}\left[S_i^\alpha S_i^\beta\right] - \frac{5}{4}\delta^{\alpha\beta}\mathcal{I}_i \tag{D.6}$$

$$T_i^{\alpha\beta\gamma} = \frac{1}{6}\mathcal{S}\left[S_i^\alpha S_i^\beta S_i^\gamma\right] \tag{D.7}$$

where the operator $\mathcal{S}$ symmetrises the spin indices.

D.3.1   Transformation of $S = \frac{3}{2}$ operators

Under the above transformations of the states, the dipole operators mixes with the octupole operators and quadrupole operators mixes among themselves. as follows :

Transformation of quadrupolar operators :

$$C_3[111] : \begin{cases} Q_i^{yz} \longrightarrow Q_j^{yz} \\ Q_i^{zx} \longrightarrow Q_j^{zx} \\ Q_i^{zz} \longrightarrow Q_j^{zz} \\ Q_i^{yy} \longrightarrow -\frac{1}{2}Q_j^{yy} - \frac{3}{4}Q_j^{zz} + \frac{\sqrt{3}}{2}Q_j^{xy} \\ Q_i^{xy} \longrightarrow -\frac{\sqrt{3}}{2}Q_j^{yy} - \frac{\sqrt{3}}{4}Q_j^{zz} - \frac{1}{2}Q_j^{xy} \end{cases} \tag{D.8}$$

$$C_2[\hat{z}] : \begin{cases} Q_i^{yz} \longrightarrow Q_j^{yz} \\ Q_i^{zx} \longrightarrow Q_j^{zx} \\ Q_i^{zz} \longrightarrow Q_j^{zz} \\ Q_i^{yy} \longrightarrow Q_j^{yy} \\ Q_i^{xy} \longrightarrow Q_j^{xy} \end{cases} \tag{D.9}$$

$$\sigma_d[x=y] \ \& \ S_4[\hat{z}] : \begin{cases} Q_i^{yz} \longrightarrow Q_j^{yz} \\ Q_i^{zx} \longrightarrow -Q_j^{zx} \\ Q_i^{zz} \longrightarrow Q_j^{zz} \\ Q_i^{yy} \longrightarrow -\frac{1}{2}Q_j^{yy} - \frac{3}{4}Q_j^{zz} + \frac{\sqrt{3}}{2}Q_j^{xy} \\ Q_i^{xy} \longrightarrow \frac{\sqrt{3}}{2}Q_j^{yy} + \frac{\sqrt{3}}{4}Q_j^{zz} + \frac{1}{2}Q_j^{xy} \end{cases} \tag{D.10}$$

The twenty dimensional space of quadrupole operators on a single tetrahedron can be decomposed into irreps of T_d.

$$\Gamma_{quadrupole} = 2\mathbf{a_1} \oplus \mathbf{a_2} \oplus \mathbf{e} \oplus 2\mathbf{t_1} \oplus 3\mathbf{t_2} \tag{D.11}$$

Transformation of dipole and octupole operators

$$
C_3[111]: \begin{cases}
S_i^z \longrightarrow S_j^z, \\[4pt]
T_i^{zzz} \longrightarrow T_j^{zzz} \\[4pt]
S_i^x \longrightarrow \frac{9}{2}S_j^x + \frac{7}{2\sqrt{3}}S_j^y - \frac{3}{2}T_j^{xxx} - \frac{\sqrt{3}}{2}T_j^{yyy} - \frac{\sqrt{3}}{2}T_j^{xxy} - \frac{3}{2}T_j^{yyx} \\[4pt]
S_i^y \longrightarrow -\frac{7}{2\sqrt{3}}S_j^x + \frac{9}{2}S_j^y + \frac{\sqrt{3}}{2}T_j^{xxx} - \frac{3}{2}T_j^{yyy} - \frac{3}{2}T_j^{xxy} + \frac{\sqrt{3}}{2}T_j^{yyx} \\[4pt]
T_i^{xyz} \longrightarrow -\frac{41}{16\sqrt{3}}S_j^z + \frac{\sqrt{3}}{4}T_j^{zzz} + \frac{\sqrt{3}}{2}T_j^{xxz} - \frac{1}{2}T_j^{xyz} \\[4pt]
T_i^{xxz} \longrightarrow \frac{41}{16}S_j^z - \frac{3}{4}T_j^{zzz} - \frac{1}{2}T_j^{xxz} - \frac{\sqrt{3}}{2}T_j^{xyz} \\[4pt]
T_i^{xxx} \longrightarrow \frac{35}{4}S_j^x + \frac{35}{4\sqrt{3}}S_j^y - \frac{25}{8}T_j^{xxx} - \frac{9\sqrt{3}}{8}T_j^{yyy} - \frac{13\sqrt{3}}{8}T_j^{xxy} - \frac{21}{8}T_j^{yyx} \\[4pt]
T_i^{yyy} \longrightarrow -\frac{35}{4\sqrt{3}}S_j^x + \frac{35}{4}S_j^y + \frac{9\sqrt{3}}{8}T_j^{xxx} - \frac{25}{8}T_j^{yyy} - \frac{21}{8}T_j^{xxy} + \frac{13\sqrt{3}}{8}T_j^{yyx} \\[4pt]
T_i^{xxy} \longrightarrow -\frac{35}{12\sqrt{3}}S_j^x + \frac{35}{12}S_j^y + \frac{13}{8\sqrt{3}}T_j^{xxx} - \frac{7}{8}T_j^{yyy} - \frac{11}{8}T_j^{xxy} + \frac{1}{8\sqrt{3}}T_j^{yyx} \\[4pt]
T_i^{yyx} \longrightarrow \frac{35}{12}S_j^x + \frac{35}{12\sqrt{3}}S_j^y - \frac{7}{8}T_j^{xxx} - \frac{13}{8\sqrt{3}}T_j^{yyy} - \frac{1}{8\sqrt{3}}T_j^{xxy} - \frac{11}{8}T_j^{yyx}
\end{cases}
\tag{D.12}
$$

$$
C_2[\hat{z}]: \begin{cases}
S_i^z \longrightarrow S_j^z \\[4pt]
S_i^x \longrightarrow S_j^x \\[4pt]
S_i^y \longrightarrow S_j^y \\[4pt]
T_i^{zzz} \longrightarrow T_j^{zzz} \\[4pt]
T_i^{xyz} \longrightarrow T_j^{xyz} \\[4pt]
T_i^{xxz} \longrightarrow T_j^{xxz} \\[4pt]
T_i^{xxx} \longrightarrow T_j^{xxx} \\[4pt]
T_i^{yyy} \longrightarrow T_j^{yyy} \\[4pt]
T_i^{xxy} \longrightarrow T_j^{xxy} \\[4pt]
T_i^{yyx} \longrightarrow T_j^{yyx}
\end{cases}
\tag{D.13}
$$

$$\sigma_d[\hat{z}] \ \& \ S_4[\hat{z}]: \begin{cases} S_i^z \longrightarrow -S_j^z, \\[4pt] T_i^{zzz} \longrightarrow -T_j^{zzz} \\[4pt] S_i^x \longrightarrow \frac{9}{2}S_j^x + \frac{7}{2\sqrt{3}}S_j^y - \frac{3}{2}T_j^{xxx} - \frac{\sqrt{3}}{2}T_j^{yyy} - \frac{\sqrt{3}}{2}T_j^{xxy} - \frac{3}{2}T_j^{yyx} \\[4pt] S_i^y \longrightarrow \frac{7}{2\sqrt{3}}S_j^x - \frac{9}{2}S_j^y - \frac{\sqrt{3}}{2}T_j^{xxx} + \frac{3}{2}T_j^{yyy} + \frac{3}{2}T_j^{xxy} - \frac{\sqrt{3}}{2}T_j^{yyx} \\[4pt] T_i^{xyz} \longrightarrow -\frac{41}{16\sqrt{3}}S_j^z + \frac{\sqrt{3}}{4}T_j^{zzz} + \frac{\sqrt{3}}{2}T_j^{xxz} - \frac{1}{2}T_j^{xyz} \\[4pt] T_i^{xxz} \longrightarrow -\frac{41}{16}S_j^z + \frac{3}{4}T_j^{zzz} + \frac{1}{2}T_j^{xxz} + \frac{\sqrt{3}}{2}T_j^{xyz} \\[4pt] T_i^{xxx} \longrightarrow \frac{35}{4}S_j^x + \frac{35}{4\sqrt{3}}S_j^y - \frac{25}{8}T_j^{xxx} - \frac{9\sqrt{3}}{8}T_j^{yyy} - \frac{13\sqrt{3}}{8}T_j^{xxy} - \frac{21}{8}T_j^{yyx} \\[4pt] T_i^{yyy} \longrightarrow \frac{35}{4\sqrt{3}}S_j^x - \frac{35}{4}S_j^y - \frac{9\sqrt{3}}{8}T_j^{xxx} + \frac{25}{8}T_j^{yyy} + \frac{21}{8}T_j^{xxy} - \frac{13\sqrt{3}}{8}T_j^{yyx} \\[4pt] T_i^{xxy} \longrightarrow \frac{35}{12\sqrt{3}}S_j^x - \frac{35}{12}S_j^y - \frac{13}{8\sqrt{3}}T_j^{xxx} + \frac{7}{8}T_j^{yyy} + \frac{11}{8}T_j^{xxy} - \frac{1}{8\sqrt{3}}T_j^{yyx} \\[4pt] T_i^{yyx} \longrightarrow \frac{35}{12}S_j^x + \frac{35}{12\sqrt{3}}S_j^y - \frac{7}{8}T_j^{xxx} - \frac{13}{8\sqrt{3}}T_j^{yyy} - \frac{1}{8\sqrt{3}}T_j^{xxy} - \frac{11}{8}T_j^{yyx} \end{cases} \tag{D.14}$$

The 40 dimensional subspace of dipole and octupole operators can be decomposed in the following way.

$$\Gamma_{dipole+octupole} = \mathbf{a_1} \oplus 3\mathbf{a_2} \oplus 3\mathbf{e} \oplus 6\mathbf{t_1} \oplus 4\mathbf{t_2} \tag{D.15}$$

D.4 Diagonalisation of complete onsite Hamiltonian in presence of magnetoelastic coupling

As mentioned in the main text, the complete onsite Hamiltonian is given by,

$$\begin{aligned} H_{onsite} &= H_0 + H_{\sigma,\tau} \\ &= \frac{\tilde{\Delta}}{2}\sum_i (S_i^z)^2 + \sum_i \Gamma_2 \left(\frac{10}{3}S_i^x - T_i^{xxx} - T_i^{yyx} \right) \end{aligned} \tag{D.16}$$

This complete onsite Hamiltonian can then be rewritten as,

$$H_{onsite} = H_0 + H_{\sigma,\tau} = \sum_i \frac{\tilde{\tilde{\Delta}}}{2} \left(\bar{S}_i^z \left[\Gamma_2/\tilde{\Delta} \right] \right)^2 + \text{Constant} \tag{D.17}$$

where, $\tilde{\tilde{\Delta}} = \frac{\sqrt{\tilde{\Delta}^2 + 3\Gamma_2^2}}{2}$ and the $\bar{S}_i^z \left[\Gamma_2/\tilde{\Delta} \right]$ are such that it looks exactly same as S_i^z, but in the transformed basis where H_{onsite} is diagonal. In fact, we can define all the 15 operators in this

new basis having the same structure, and the rest of the analysis remains as it is. If $U[\Gamma_2/\tilde{\Delta}]$ is the unitary transformation makes H_{onsite} diagonal, the *rotated* operators are then given by,

$$\bar{S}_i^z\left[\Gamma_2/\tilde{\Delta}\right] = U\left[\Gamma_2/\tilde{\Delta}\right]^\dagger S_i^z\, U\left[\Gamma_2/\tilde{\Delta}\right] \approx S_i^z + \frac{\Gamma_2}{\tilde{\Delta}}Q_i^{zx} + \mathcal{O}\left[(\Gamma_2/\tilde{\Delta})^2\right] \tag{D.18}$$

$$\bar{S}_i^x\left[\Gamma_2/\tilde{\Delta}\right] = U\left[\Gamma_2/\tilde{\Delta}\right]^\dagger S_i^x\, U\left[\Gamma_2/\tilde{\Delta}\right] \approx S_i^x + \frac{\Gamma_2}{\tilde{\Delta}}Q_i^{yy} - \frac{\Gamma_2}{\tilde{\Delta}}Q_i^{zz} + \mathcal{O}\left[(\Gamma_2/\tilde{\Delta})^2\right] \tag{D.19}$$

$$\bar{S}_i^y\left[\Gamma_2/\tilde{\Delta}\right] = U\left[\Gamma_2/\tilde{\Delta}\right]^\dagger S_i^y\, U\left[\Gamma_2/\tilde{\Delta}\right] \approx S_i^y - \frac{\Gamma_2}{\tilde{\Delta}}Q_i^{xy} + \mathcal{O}\left[(\Gamma_2/\tilde{\Delta})^2\right] \tag{D.20}$$

$$\bar{Q}_i^{zz}\left[\Gamma_2/\tilde{\Delta}\right] = U\left[\Gamma_2/\tilde{\Delta}\right]^\dagger Q_i^{zz}\, U\left[\Gamma_2/\tilde{\Delta}\right]$$
$$\approx Q_i^{zz} + \frac{20\Gamma_2}{3\tilde{\Delta}}S^x - \frac{2\Gamma_2}{\tilde{\Delta}}T_i^{xxx} - \frac{2\Gamma_2}{\tilde{\Delta}}T_i^{yyx} + \mathcal{O}\left[(\Gamma_2/\tilde{\Delta})^2\right] \tag{D.21}$$

$$\bar{T}_i^{zzz}\left[\Gamma_2/\tilde{\Delta}\right] = U\left[\Gamma_2/\tilde{\Delta}\right]^\dagger T_i^{zzz}\, U\left[\Gamma_2/\tilde{\Delta}\right] \approx T_i^{zzz} + \frac{13\Gamma_2}{4\tilde{\Delta}}Q_i^{zx} + \mathcal{O}\left[(\Gamma_2/\tilde{\Delta})^2\right] \tag{D.22}$$

Similarly, all the other operators can also be found by applying the unitary transformation.

D.5 Frozen δ-excitations inside the sea of $S = 1/2$ CSI

As noted in the main text, the dynamical arrest of δ-excitations at low temperatures can be implemented energetically via the term

$$U\sum_{i\in"\delta"}(\mathbf{B}\cdot\hat{\mathbf{e}}_{i\alpha} - \mu_{i\alpha}3/2)^2 \tag{D.23}$$

Expanding the square, we get

$$U\sum_{i\alpha\in"\delta"}\left((\mathbf{B}\cdot\hat{\mathbf{e}}_{i\alpha})^2 - 3\mu_{i\alpha}\mathbf{B}\cdot\hat{\mathbf{e}}_{i\alpha} + 9/4\right) \tag{D.24}$$

Leaving out the constant term, on coarse-graining, the first term renormalises the usual magnetostatic energy $\sim \mathbf{B}^2$ while the second term – linear in $\mathbf{B}$ becomes

$$\sim -U\int d^3\mathbf{r}\,\mathbf{M}\cdot\mathbf{B} \tag{D.25}$$

where we define a new magnetisation vector, $\mathbf{M}(\mathbf{r})$ (see the main text for the details of the expression), to capture the presence of δ-excitations. The partition function is then given by

(ignoring the constant term),

$$\mathcal{Z}\left[\{\mu\}\right] = \int \mathcal{D}\mathbf{B} \, \exp\left[-\int d^3\mathbf{r} \, \left(\tilde{U}\,\mathbf{B}^2 - U\mathbf{M}\cdot\mathbf{B}\right)\right]\delta\left(\nabla\cdot\mathbf{B}\right) \qquad \text{(D.26)}$$

Note that the divergenceless condition is satisfied throughout the space including the almost frozen locations, as δ-excitations are gauge neutral by construction. We now integrate out the $\mathbf{B}$ field to obtain the effective partition for these excitaions as

$$
\begin{aligned}
\mathcal{Z}\left[\{\mu\}\right] &= \exp\left[\frac{U^2}{4\tilde{U}}\sum_{i\alpha,j\beta\in"\delta"}\int d^3\mathbf{k}\left(\delta_{\alpha\beta} - \frac{k^\alpha k^\beta}{k^2}\right)M^\alpha(-\mathbf{k})M^\beta(\mathbf{k})\right] \\
&= \exp\left[\frac{9U^2}{4\tilde{U}}\sum_{i\alpha,j\beta\in"\delta"}\left(\delta_{\alpha\beta}\delta(\mathbf{r}_i-\mathbf{r}_j) - \frac{r_{ij}^2\hat{\mathbf{e}}_{i\alpha}\cdot\hat{\mathbf{e}}_{j\beta} - 3\left(\mathbf{r}_{ij}\cdot\hat{\mathbf{e}}_{i\alpha}\right)\left(\mathbf{r}_{ij}\cdot\hat{\mathbf{e}}_{j\beta}\right)}{4\pi r_{ij}^5}\right)\mu_{i\alpha}\mu_{j\beta}\right]
\end{aligned}
$$
$$\text{(D.27)}$$

$$= \exp\left[-\frac{9U^2}{4\tilde{U}}\sum_{i\alpha,j\beta\in"\delta"}\frac{r_{ij}^2\hat{\mathbf{e}}_{i\alpha}\cdot\hat{\mathbf{e}}_{j\beta} - 3\left(\mathbf{r}_{ij}\cdot\hat{\mathbf{e}}_{i\alpha}\right)\left(\mathbf{r}_{ij}\cdot\hat{\mathbf{e}}_{j\beta}\right)}{4\pi r_{ij}^5}\mu_{i\alpha}\mu_{j\beta}\right] \qquad \text{(D.28)}$$

where $\mathbf{r}_{ij} = \mathbf{r}_i - \mathbf{r}_j$. One can clearly see that the almost frozen excitations behaves like source of magnetic dipole moments and hence interact by effective dipolar potential.

D.5.1 Correlation between two S=1/2 spins from the ice manifold

The spin-spin correlation of the ice manifold is given by,

$$\langle S_{\mathbf{r}\alpha}^z S_{\mathbf{r}'\beta}^z\rangle = \frac{\int \mathcal{D}\mathbf{B} \, \left(\mathbf{B}\cdot\hat{\mathbf{e}}_{\mathbf{r}\alpha}\right)\left(\mathbf{B}\cdot\hat{\mathbf{e}}_{\mathbf{r}'\beta}\right)\delta\left(\nabla\cdot\mathbf{B}\right)\exp\left[-\int d^3\mathbf{r}\left(\tilde{U}\,\mathbf{B}^2 - U\,\mathbf{M}\cdot\mathbf{B}\right)\right]}{\mathcal{Z}[\{\mu\}]}$$
$$\text{(D.29)}$$

We introduce a source term to compute the above correlation function.

$$\mathcal{Z}\left[\{\mu\},\mathbf{J}\right] = \int \mathcal{D}\mathbf{B}\,\delta\left(\nabla\cdot\mathbf{B}\right)\exp\left[-\int d^3\mathbf{r}\left(\tilde{U}\,\mathbf{B}^2 - U\,\mathbf{M}\cdot\mathbf{B} + i\mathbf{J}(\mathbf{r})\cdot\mathbf{B}(\mathbf{r})\right)\right] \qquad \text{(D.30)}$$

where, $\mathbf{J}(\mathbf{r}) = \sum_{\mathbf{R}\alpha}\mathcal{J}_{\mathbf{R}\alpha}\hat{\mathbf{e}}_{\mathbf{R}\alpha}\delta\left(\mathbf{r}-\mathbf{R}\right)$. Then, the correlation function can be rewritten as,

$$\langle S_{\mathbf{r}\alpha}^z S_{\mathbf{r}'\beta}^z\rangle = -\left[\frac{\partial}{\partial\mathcal{J}_{\mathbf{r}\alpha}}\frac{\partial}{\partial\mathcal{J}_{\mathbf{r}'\beta}}\frac{\mathcal{Z}[\{\mu\},\mathbf{J}]}{\mathcal{Z}[\{\mu\}]}\right]_{\mathbf{J}=\mathbf{0}} \qquad \text{(D.31)}$$

131

Using $\mathbf{B} = \nabla \times \mathbf{A}$ and rewriting everything in the momentum space, we obtain,

$$\mathcal{Z}\left[\{\mu\}, \mathbf{J}\right] = \int \mathcal{D}\mathbf{A} \, \exp\left[-\int d^3\mathbf{k} \left(\tilde{U} \, \mathbf{k}^2 \mathbf{A}(-\mathbf{k}) \cdot \mathbf{A}(\mathbf{k}) - i \, \mathbf{j}(-\mathbf{k}) \cdot \mathbf{A}(\mathbf{k})\right)\right] \qquad \text{(D.32)}$$

where, $j^c(-\mathbf{k}) = \epsilon_{abc}\left(U \, M^a(-\mathbf{k}) - iJ^a(-\mathbf{k})\right)k^b$. Integrating out $\mathbf{A}$, we get,

$$
\begin{aligned}
&\mathcal{Z}[\{\mu\}, \mathbf{J}] \\
&= N \exp\left[-\frac{1}{4\tilde{U}} \int d^3\mathbf{k} \, \frac{\mathbf{j}(-\mathbf{k}) \cdot \mathbf{j}(\mathbf{k})}{\mathbf{k}^2}\right] \\
&= N \exp\left[\frac{1}{4\tilde{U}} \int d^3\mathbf{k} \left(\delta_{ab} - \frac{k^a k^b}{\mathbf{k}^2}\right)\left(U^2 M^a(-\mathbf{k})M^b(\mathbf{k}) + J^a(-\mathbf{k})J^b(\mathbf{k})\right.\right. \\
&\hspace{8cm} \left.\left. + iU M^a(-\mathbf{k})J^b(\mathbf{k})\right)\right] \qquad \text{(D.33)}
\end{aligned}
$$

where N is a constant number. $\exp[\frac{U^2}{4\tilde{U}} \int \frac{d^3\mathbf{k}}{(2\pi)^3}\left(\delta_{ab} - \frac{k^a k^b}{\mathbf{k}^2}\right) M^a(-\mathbf{k})M^b(\mathbf{k})]$ term in the above expression gets canceled by the $\mathcal{Z}[\{\mu\}]$ term in the denominator of the correlation function. Therefore, to obtain the correlation function, we need to evaluate,

$$
\begin{aligned}
&\langle S^z_{\mathbf{r}\alpha} S^z_{\mathbf{r}'\beta}\rangle \\
&= -N\left[\frac{\partial}{\partial \mathcal{J}_{\mathbf{r}\alpha}} \frac{\partial}{\partial \mathcal{J}_{\mathbf{r}'\beta}}\right. \\
&\qquad\quad \left.\exp\left[-\frac{1}{4\tilde{U}} \int d^3\mathbf{k} \left(\delta_{ab} - \frac{k^a k^b}{\mathbf{k}^2}\right)\left(J^a(-\mathbf{k})J^b(\mathbf{k}) + iU \, M^a(-\mathbf{k})J^b(\mathbf{k})\right)\right]\right]_{\mathbf{J}=\mathbf{0}} \\
&= -N\left[\frac{\partial}{\partial \mathcal{J}_{\mathbf{r}\alpha}} \frac{\partial}{\partial \mathcal{J}_{\mathbf{r}'\beta}}\right. \\
&\qquad\quad \exp\left[-\frac{1}{4\tilde{U}} \sum_{\mathbf{R_1 R_2}\mu\nu}\left(\delta_{ab}\delta(\mathbf{R_1} - \mathbf{R_2}) - \frac{R_{12}^2 \delta_{ab} - 3R_{12}^a R_{12}^b}{4\pi R_{12}{}^5}\right) \mathcal{J}_{\mathbf{R_1}\alpha}\mathcal{J}_{\mathbf{R_2}\beta}\hat{e}^a_{\mathbf{R_1}\mu}\hat{e}^b_{\mathbf{R_2}\nu}\right. \\
&\qquad\qquad \left.\left.- \frac{iU}{4\tilde{U}} \sum_{\mathbf{R_1}\beta} \sum_{i\beta\in"\delta"}\left(\delta_{ab}\delta(\mathbf{R_1} - \mathbf{R_i}) - \frac{R_{1i}^2 \delta_{ab} - 3R_{1i}^a R_{1i}^b}{4\pi R_{1i}^5}\right) \mathcal{J}_{\mathbf{R_1}\alpha}\mu_{i\beta}\hat{e}^a_{\mathbf{R_1}\mu}\hat{e}^b_{i\nu}\right]\right]_{\mathbf{J}=\mathbf{0}} \\
&= -N\left[\frac{\partial}{\partial \mathcal{J}_{\mathbf{r}\alpha}} \frac{\partial}{\partial \mathcal{J}_{\mathbf{r}\beta}}\right. \hspace{6.5cm} \text{(D.34)} \\
&\qquad\quad \left.\exp\left[-\frac{1}{4\,\tilde{U}} \sum_{\mathbf{R_1},\mathbf{R_2}\mu\nu} \mathcal{V}^{\mu\nu}_{\mathbf{R_1 R_2}}\mathcal{J}_{\mathbf{R_1}\mu}\mathcal{J}_{\mathbf{R_2}\nu} - \frac{iU}{4\,\tilde{U}} \sum_{\mathbf{R_1}\mu} \sum_{i\nu\in"\delta"} \mathcal{V}^{\mu\nu}_{\mathbf{R_1 R_i}}\mathcal{J}_{\mathbf{R_1}\mu}\mu_{i\nu}\right]\right]_{\mathbf{J}=\mathbf{0}}
\end{aligned}
$$

$$\text{(D.35)}$$

where,

$$
\mathcal{V}^{\alpha\beta}_{\mathbf{R}_i \mathbf{R}_j} = \delta_{ab}\delta\left(\mathbf{R}_i - \mathbf{R}_j\right) - \frac{R_{ij}^2 \delta_{ab} - 3R_{ij}^a R_{ij}^b}{R_{ij}^{\,5}} \hat{e}^a_{\mathbf{R}_i \alpha} \hat{e}^b_{\mathbf{R}_j \beta}
\tag{D.36}
$$

$$
\langle S^z_{\mathbf{r}\alpha} S^z_{\mathbf{r}'\beta} \rangle = \frac{C_1}{2\tilde{U}} \mathcal{V}^{\alpha\beta}_{\mathbf{r}\mathbf{r}'} + \frac{C_2 U^2}{4\tilde{U}^2} \sum_{i\mu, j\nu \in "\delta"} \mathcal{V}^{\alpha\mu}_{\mathbf{r}i} \mathcal{V}^{\beta\nu}_{\mathbf{r}'j} \mu_{i\mu} \mu_{j\nu}
\tag{D.37}
$$

where C_1 and C_2 are two constant numbers.

D.6 Hopping of δ-excitations

In the zero flux phase, the electric field piercing through each hexagon can be set to zero at the mean field level. The above Hamiltonian reduces to the simple hopping Hamiltonian on the pyrochlore lattice. It is then given by,

$$
H_\delta = -t \sum_{\mathbf{k}} \sum_{\mu\nu} \mathcal{H}_{\mu\nu}(\mathbf{k}) a^\dagger_{\mathbf{k},\mu} a_{\mathbf{k},\nu}
\tag{D.38}
$$

where

$$
\mathcal{H}_{\mu\nu}(\mathbf{k}) = \mathcal{H}^{2NN}_{\mu\nu}(\mathbf{k}) + \mathcal{H}^{3NN}_{\mu\nu}(\mathbf{k})
\tag{D.39}
$$

where

$$
\mathcal{H}^{2NN}_\delta = \begin{pmatrix}
0 & 2\cos\frac{2k_x}{\sqrt{3}}\cos\frac{k_y-k_z}{\sqrt{3}} & 2\cos\frac{2k_y}{\sqrt{3}}\cos\frac{k_x-k_z}{\sqrt{3}} & 2\cos\frac{2k_z}{\sqrt{3}}\cos\frac{k_x-k_y}{\sqrt{3}} \\
2\cos\frac{2k_x}{\sqrt{3}}\cos\frac{k_y-k_z}{\sqrt{3}} & 0 & 2\cos\frac{2k_z}{\sqrt{3}}\cos\frac{k_x+k_y}{\sqrt{3}} & 2\cos\frac{2k_y}{\sqrt{3}}\cos\frac{k_x+k_z}{\sqrt{3}} \\
2\cos\frac{2k_y}{\sqrt{3}}\cos\frac{k_x-k_z}{\sqrt{3}} & 2\cos\frac{2k_z}{\sqrt{3}}\cos\frac{k_x+k_y}{\sqrt{3}} & 0 & 2\cos\frac{2k_x}{\sqrt{3}}\cos\frac{k_y+k_z}{\sqrt{3}} \\
2\cos\frac{2k_z}{\sqrt{3}}\cos\frac{k_x-k_y}{\sqrt{3}} & 2\cos\frac{2k_y}{\sqrt{3}}\cos\frac{k_x+k_z}{\sqrt{3}} & 2\cos\frac{2k_x}{\sqrt{3}}\cos\frac{k_y+k_z}{\sqrt{3}} & 0
\end{pmatrix}
\tag{D.40}
$$

$$\mathcal{H}_\delta^{3NN} = \begin{pmatrix} 2\left(C_{\bar{x}y} + C_{\bar{x}z} + C_{\bar{y}z}\right) & 0 & 0 & 0 \\ 0 & 2\left(C_{xy} + C_{\bar{y}z} + C_{xz}\right) & 0 & 0 \\ 0 & 0 & 2\left(C_{xy} + C_{\bar{x}z} + C_{yz}\right) & 0 \\ 0 & 0 & 0 & 2\left(C_{\bar{x}y} + C_{xz} + C_{yz}\right) \end{pmatrix}$$

$$(D.41)$$

where $C_{xy} = \cos\frac{2(k_x+k_y)}{\sqrt{3}}$ and $C_{\bar{x}y} = \cos\frac{2(k_x-k_y)}{\sqrt{3}}$

The dispersion of the above Hamiltonian is shown in Fig. 6.9(a) in the main text. In the π-flux phase, similar hopping Hamiltonian appears with an overall negative sign, that inverts the band structure (see Fig. 6.9(b) in the main text). Clearly, such hopping renormalises the bare gap of the δ-excitations, and might lead to condensation of them if the quantum fluctuation is significantly high.

BIBLIOGRAPHY

[1] L. Savary and L. Balents, "Quantum spin liquids: A review," *Reports on Progress in Physics*, vol. 80, no. 1, p. 016 502, 2016.

[2] X.-G. Wen, "Quantum orders and symmetric spin liquids," *Phys. Rev. B*, vol. 65, p. 165 113, 16 2002.

[3] T. Tarun Grover, Y. Zhang, and A. Vishwanath, "Entanglement entropy as a portal to the physics of quantum spin liquids," *New J. Phys.*, vol. 15, p. 025 002, 2013.

[4] N. Goldenfeld, *Lectures on Phase Transitions and the Renormalization Group*, 1st ed. CRC Press, 1992.

[5] T. Senthil, "Symmetry-protected topological phases of quantum matter," *Annual Review of Condensed Matter Physics*, vol. 6, no. 1, pp. 299–324, 2015.

[6] B. A. Bernevig, *Topological Insulators and Topological Superconductors*. Princeton university press, Princeton, 2013.

[7] A. Kitaev and J. Preskill, "Topological entanglement entropy," *Phys. Rev. Lett.*, vol. 96, p. 110 404, 11 2006.

[8] M. Pretko and T. Senthil, "Entanglement entropy of $U(1)$ quantum spin liquids," *Phys. Rev. B*, vol. 94, p. 125 112, 12 2016.

[9] M. A. Levin and X.-G. Wen, "String-net condensation: A physical mechanism for topological phases," *Phys. Rev. B*, vol. 71, p. 045 110, 4 2005.

[10] X. G. Wen, *Quantum Field Theory of Many-Body Systems: From the Origin of Sound to an Origin of Light and Electrons*. Oxford University Press, Oxford, 2007.

[11] G. Baskaran and P. W. Anderson, "Gauge theory of high-temperature superconductors and strongly correlated fermi systems," *Phys. Rev. B*, vol. 37, pp. 580–583, 1 1988.

[12] M. Hermele, M. P. A. Fisher, and L. Balents, "Pyrochlore photons: The $U(1)$ spin liquid in a $S = \frac{1}{2}$ three-dimensional frustrated magnet," *Phys. Rev. B*, vol. 69, p. 064 404, 6 2004.

[13] A. Kitaev, "Anyons in an exactly solved model and beyond," *Annals of Physics*, vol. 321, no. 1, pp. 2–111, 2006, January Special Issue.

[14] J. B. Kogut, "An introduction to lattice gauge theory and spin systems," *Rev. Mod. Phys.*, vol. 51, pp. 659–713, 4 1979.

[15] E. Fradkin and S. H. Shenker, "Phase diagrams of lattice gauge theories with higgs fields," *Phys. Rev. D*, vol. 19, pp. 3682–3697, 12 1979.

[16] E. Fradkin, *Field Theories of Condensed Matter Physics*, 2nd ed. Cambridge University Press, Cambridge, 2013.

[17] G. A. F. Doron L. Bergman and L. Balents, "Ordering in a frustrated pyrochlore antiferromagnet proximate to a spin liquid," *Phys. Rev. B*, vol. 73, p. 134 402, 2006.

[18] G. Chen, ""magnetic monopole" condensation of the pyrochlore ice u(1) quantum spin liquid: Application to $Pr_2Ir_2O_7$ and $Yb_2Ti_2O_7$," *Phys. Rev. B*, vol. 94, p. 205 107, 20 2016.

[19] L. Savary and L. Balents, "Coulombic quantum liquids in spin-1/2 pyrochlores," *Phys. Rev. Lett.*, vol. 108, p. 037 202, 2012.

[20] C. Xu, "Gapless bosonic excitation without symmetry breaking: An algebraic spin liquid with soft gravitons," *Phys. Rev. B*, vol. 74, p. 224 433, 22 2006.

[21] A. Prem, S. Vijay, Y.-Z. Chou, M. Pretko, and R. M. Nandkishore, "Pinch point singularities of tensor spin liquids," *Phys. Rev. B*, vol. 98, p. 165 140, 16 2018.

[22] W. Witczak-Krempa, G. Chen, Y. B. Kim, and L. Balents, "Correlated quantum phenomena in the strong spin-orbit regime," *Annual Review of Condensed Matter Physics*, vol. 5, no. 1, pp. 57–82, 2014.

[23] J. G. Rau, E. K.-H. Lee, and H.-Y. Kee, "Spin-orbit physics giving rise to novel phases in correlated systems: Iridates and related materials," *Annu. Rev. Condens. Matter Phys.*, vol. 7, no. 1, pp. 195–221, 2016.

[24] J. G. Rau and M. J. P. Gingras, "Frustrated quantum rare-earth pyrochlores," *Annu. Rev. Condens. Matter Phys.*, vol. 10, pp. 357–386, 2019.

[25] A. P. Ramirez, "Strongly geometrically frustrated magnets," *Annu. Rev. Mater. Sci.*, vol. 24, no. 1, pp. 453–480, 1994.

[26] J. Chalker, "Spin liquids and frustrated magnetism," *Oxford University Press, Oxford*, 2015.

[27] O. A. Starykh, "Unusual ordered phases of highly frustrated magnets: A review," *Reports on Progress in Physics*, vol. 78, no. 5, p. 052 502, 2015.

[28] J. S. Gardner *et al.*, "Cooperative paramagnetism in the geometrically frustrated pyrochlore antiferromagnet $Tb_2Ti_2O_7$," *Phys. Rev. Lett.*, vol. 82, pp. 1012–1015, 5 1999.

[29] K. Kimura *et al.*, "Quantum fluctuations in spin-ice-like $Pr_2Zr_2O_7$," *Nat. Commun.*, vol. 4, p. 1934, 2013.

[30] K. A. Ross, L. Savary, B. D. Gaulin, and L. Balents, "Quantum excitations in quantum spin ice," *Phys. Rev. X*, vol. 1, p. 021 002, 2 2011.

[31] L. J. Sandilands, Y. Tian, K. W. Plumb, Y.-J. Kim, and K. S. Burch, "Scattering continuum and possible fractionalized excitations in $\alpha - RuCl_3$," *Phys. Rev. Lett.*, vol. 114, p. 147 201, 2015.

[32] S. H. Do *et al.*, "Majorana fermions in the Kitaev quantum spin system α-$RuCl_3$," Nat. Phys., vol. 13, p. 1079, 2017.

[33] K. Mehlawat, A. Thamizhavel, and Y. Singh, "Heat capacity evidence for proximity to the Kitaev quantum spin liquid in A_2IrO_3 (A = Na, Li)," Phys. Rev. B, vol. 95, p. 144 406, 2017.

[34] A Glamazda, P Lemmens, S. H. Do, Y. S. Choi, and K. Y. Choi, "Raman spectroscopic signature of fractionalized excitations in the harmonic-honeycomb iridates $\beta-$ and $\gamma- Li_2IrO_3$," *Nat. Commun.*, p. 12 286, 2016.

[35] M. Abramchuk, C. O. Keskinbora, J. W. Krizan, K. R. Metz, D. C. Bell, and F. Tafti, "Cu_2IrO_3: A New Magnetically Frustrated Honeycomb Iridate," J. Am. Chem. Soc., vol. 139, p. 15 371, 2017.

[36] Z. Nussinov and J. van den Brink, "Compass models: Theory and physical motivations," Rev. Mod. Phys., vol. 87, p. 1, 1 2015.

[37] G. Jackeli and G. Khaliullin, "Mott Insulators in the Strong Spin-Orbit Coupling Limit: From Heisenberg to a Quantum Compass and Kitaev Models," Phys. Rev. Lett., vol. 102, p. 017 205, 2009.

[38] A. Seth, S. Bhattacharjee, and R. Moessner, *Manuscript under preparation.*

[39] A. Seth, S. Bhattacharjee, and R. Moessner, "Probing emergent qed in quantum spin ice via raman scattering of phonons: Shallow inelastic scattering and pair production," *arXiv:2202.03455*, 2022 (*Accepted in Phys. Rev. B*).

[40] B. Lake, A. Tsvelik, and S. e. a. Notbohm, "Confinement of fractional quantum number particles in a condensed-matter system," *Nat. Phys.*, vol. 6, pp. 50–55, 2010.

[41] S. T. Bramwell *et al.*, "Spin correlations in $Ho_2Ti_2O_7$: A dipolar spin ice system," *Phys. Rev. Lett.*, vol. 87, p. 047 205, 4 2001.

[42] S. T. Bramwell and M. J. P. Gingras, "Spin Ice State in Frustrated Magnetic Pyrochlore Materials," *Science*, vol. 294, no. 5546, pp. 1495–1501, Nov. 2001.

[43] B. C. Melot *et al.*, "Large low-temperature specific heat in pyrochlore $Bi_2Ti_2O_7$," *Phys. Rev. B*, vol. 79, p. 224 111, 22 2009.

[44] P. A. Lee, "An end to the drought of quantum spin liquids," *Science*, vol. 321, no. 5894, pp. 1306–1307, 2008.

[45] S. Yamashita, Y. Nakazawa, and M. e. a. Oguni, "Thermodynamic properties of a spin-1/2 spin-liquid state in a κ-type organic salt," *Nat. Phys.*, vol. 4, 459–462, 2008.

[46] Y. Kasahara *et al.*, "Unusual thermal hall effect in a kitaev spin liquid candidate $\alpha-RuCl_3$," *Phys. Rev. Lett.*, vol. 120, p. 217 205, 21 2018.

[47] Y. Nakamura, N. Yoneyama, T. Sasaki, T. Tohyama, A. Nakamura, and H. Kishida, "Magnetic raman scattering study of spin frustrated systems, κ-(bedt-ttf)2x," *J. Phys. Soc. Jpn.*, vol. 83, no. 7, p. 074 708, 2014.

[48] S. Pal *et al.*, "Probing signatures of fractionalisation in candidate quantum spin liquid Cu_2IrO_3 via anomalous raman scattering," *Phys. Rev. B*, vol. 104, p. 184 420, 18 2021.

[49] C. Castelnovo, R. Moessner, and S. L. Sondhi, "Magnetic monopoles in spin ice," *Nature*, vol. 451, pp. 42–45, 2008.

[50] P. A. Fleury and R. Loudon, "Scattering of light by one- and two-magnon excitations," *Phys. Rev.*, vol. 166, pp. 514–530, 2 1968.

[51] B. S. Shastry and B. I. Shraiman, "Theory of raman scattering in mott-hubbard systems," *Phys. Rev. Lett.*, vol. 65, p. 1068, 1990.

[52] J. Knolle, G.-W. Chern, D. L. Kovrizhin, R. Moessner, and N. B. Perkins, "Raman scattering signatures of kitaev spin liquids in A_2IrO_3 iridates with $A = Na$ or Li," *Phys. Rev. Lett.*, vol. 113, p. 187 201, 18 2014.

[53] B. Perreault, J. Knolle, N. B. Perkins, and F. J. Burnell, "Theory of raman response in three-dimensional kitaev spin liquids: Application to β- and $\gamma - Li_2IrO_3$ compounds," *Phys. Rev. B*, vol. 92, p. 094 439, 9 2015.

[54] B. Perreault, J. Knolle, N. B. Perkins, and F. J. Burnell, "Resonant raman scattering theory for kitaev models and their majorana fermion boundary modes," *Phys. Rev. B*, vol. 94, p. 104 427, 10 2016.

[55] J. Nasu, J. Knolle, D. L. Kovrizhin, Y. Motome, and R. Moessner, "Fermionic response from fractionalization in an insulating two-dimensional magnet," Nat. Phys., vol. 12, p. 912, 2016.

[56] B. Perreault, J. Knolle, N. B. Perkins, and F. J. Burnell, "Raman scattering in correlated thin films as a probe of chargeless surface states," *Phys. Rev. B*, vol. 94, p. 060 408, 6 2016.

[57] A. Sokolik *et al.*, "Spinons and damped phonons in spin-1/2 quantum-liquid $Ba_4Ir_3O_{10}$ observed by raman scattering," *arXiv:2110.15916*, 2021.

[58] A. S. Patri, M. Hosoi, S. B. Lee, and Y. B. Kim, "Theory of magnetostriction for multipolar quantum spin ice in pyrochlore materials," *Phys. Rev. Research*, vol. 2, p. 033 015, 2020.

[59] C. Balz *et al.*, "Physical realization of a quantum spin liquid based on a complex frustration mechanism," *Nat. Phys.*, vol. 12, p. 942, 2016.

[60] S. Pal *et al.*, *Manuscript under preparation*.

[61] H. A. Jahn and E. Teller, "Stability of polyatomic molecules in degenerate electronic states - I—Orbital degeneracy," Proc. R. Soc. London A, vol. 161, no. 905, p. 220, 1937.

[62] D. Gyepesová and V. Langer, "$Ca_{10}(Cr^VO_4)_6(Cr_{VI}O_4)$, a disordered mixed-valence chromium compound exhibiting inversion twinning," Acta Cryst., vol. C69, p. 111, 2013.

[63] Y. Xu *et al.*, "Importance of dynamic lattice effects for crystal field excitations in quantum spin ice candidate $Pr_2Zr_2O_7$," *Phys. Rev. B*, vol. 104, p. 075 125, 2021.

[64] J. Fu, J. G. Rau, M. J. P. Gingras, and N. B. Perkins, "Fingerprints of quantum spin ice in raman scattering," *Phys. Rev. B*, vol. 96, p. 035 136, 3 2017.

[65] A. Smekal, "Zur quantentheorie der dispersion," *Naturwissenschaften*, pp. 873–875, 43 1923.

[66] C. Raman, "A new radiation," *Indian J. Phys.*, vol. 2, p. 387,

[67] T. P. Devereaux and R. Hackl, "Inelastic light scattering from correlated electrons," *Rev. Mod. Phys.*, vol. 79, pp. 175–233, 1 2007.

[68] G. B. Wright, *Light Scattering Spectra of Solids*. Springer Berlin, Heidelberg, 1969.

[69] M. Cardona, "Raman scattering in high tc superconductors: Phonons, electrons, and electron–phonon interaction," *Physica C: Superconductivity*, vol. 317-318, pp. 30–54, 1999.

[70] T. P. Devereaux and A. P. Kampf, "Raman scattering in cuprate superconductors," *International Journal of Modern Physics B*, vol. 11, no. 18, pp. 2093–2118, 1997.

[71] C. Thomsen and G. Kaczmarczyk, *In Handbook of Vibrational Spectroscopy: Vibrational Raman spectroscopy of high-temperature superconductors*. Wiley, 2006.

[72] A. Auerbach, *Interacting Electrons and Quantum Magnetism*, 1st ed. Springer New York, NY, 1994.

[73] U. Fano, "Effects of configuration interaction on intensities and phase shifts," *Phys. Rev.*, vol. 124, pp. 1866–1878, 6 1961.

[74] A. Metavitsiadis and W. Brenig, "Phonon renormalization in the kitaev quantum spin liquid," *Phys. Rev. B*, vol. 101, p. 035 103, 3 2020.

[75] S. Pal, "Spectroscopic and diffraction signatures of quantum spin liquids, skyrmion lattices and transition metal dichalcogenides at low temperatures and high pressures," *PhD thesis*, Indian Institute of Science, Bangalore, India, 2022.

[76] Y. S. Choi *et al.*, "Exotic Low-Energy Excitations Emergent in the Random Kitaev Magnet Cu_2IrO_3," Phys. Rev. Lett., vol. 122, p. 167 202, 2019.

[77] E. M. Kenney *et al.*, "Coexistence of static and dynamic magnetism in the Kitaev spin liquid material Cu_2IrO_3," Phys. Rev. B, vol. 100, p. 094 418, 2019.

[78] S. K. Takahashi *et al.*, "Spin Excitations of a Proximate Kitaev Quantum Spin Liquid Realized in Cu_2IrO_3," Phys. Rev. X, vol. 9, p. 031 047, 2019.

[79] G. Baskaran, S. Mandal, and R. Shankar, "Exact results for spin dynamics and fractionalization in the kitaev model," *Phys. Rev. Lett.*, vol. 98, p. 247 201, 24 2007.

[80] E. H. Lieb, "Flux phase of the half-filled band," *Phys. Rev. Lett.*, vol. 73, pp. 2158–2161, 16 1994.

[81] J. Knolle, S. Bhattacharjee, and R. Moessner, "Dynamics of a quantum spin liquid beyond integrability: The Kitaev-Heisenberg-Γ model in an augmented parton mean-field theory," Phys. Rev. B, vol. 97, p. 134 432, 2018.

[82] J. Nasu, M. Udagawa, and Y. Motome, "Thermal fractionalization of quantum spins in a Kitaev model: Temperature-linear specific heat and coherent transport of Majorana fermions," Phys. Rev. B, vol. 92, p. 115 122, 2015.

[83] S. Bhattacharjee *et al.*, "Interplay of spin and lattice degrees of freedom in the frustrated antiferromagnet $CdCr_2O_4$: High-field and temperature-induced anomalies of the elastic constants," Phys. Rev. B, vol. 83, p. 184 421, 2011.

[84] A. M. Polyakov, *Gauge fields and strings*. 1987.

[85] J. S. Gardner, M. J. P. Gingras, and J. E. Greedan, "Magnetic pyrochlore oxides," *Rev. Mod. Phys.*, vol. 82, pp. 53–107, 1 2010.

[86] M. J. P. Gingras and P. A. McClarty, "Quantum spin ice: A search for gapless quantum spin liquids in pyrochlore magnets," *Rep. Prog. Phys.*, vol. 77, p. 056 501, 2014.

[87] A. P. Ramirez, A Hayashi, R. J. Cava, R Siddharthan, and B. Shastry, "Zero-point entropy in 'spin ice'," *Nature*, vol. 399, no. 6734, pp. 333–335, 1999.

[88] C. Castelnovo, R. Moessner, and S. Sondhi, "Spin ice, fractionalization, and topological order," *Annu. Rev. Condens. Matter Phys.*, vol. 3, pp. 35–55, 2012.

[89] S. T. Bramwell and M. J. Harris, "The history of spin ice," *J. Phys. Condens. Matter*, vol. 32, p. 374 010, 2020.

[90] M. J. Harris, S. T. Bramwell, D. F. McMorrow, T. Zeiske, and K. W. Godfrey, "Geometrical frustration in the ferromagnetic pyrochlore $Ho_2Ti_2O_7$," *Phys. Rev. Lett.*, vol. 79, pp. 2554–2557, 13 1997.

[91] R. Moessner and J. T. Chalker, "Properties of a Classical Spin Liquid: The Heisenberg Pyrochlore Antiferromagnet," *Phys. Rev. Lett.*, vol. 80, no. 13, pp. 2929–2932, Mar. 1998.

[92] C. L. Henley, "The "coulomb phase" in frustrated systems," *Annu. Rev. Condens. Matter Phys.*, vol. 1, no. 1, pp. 179–210, 2010.

[93] R. Applegate, N. R. Hayre, R. R. P. Singh, T. Lin, A. G. R. Day, and M. J. P. Gingras, "Vindication of $Yb_2Ti_2O_7$ as a model exchange quantum spin ice," *Phys. Rev. Lett.*, vol. 109, p. 097 205, 9 2012.

[94] S. B. Lee, S. Onoda, and L. Balents, "Generic quantum spin ice," *Phys. Rev. B*, vol. 86, p. 104 412, 2012.

[95] N. Shannon, O. Sikora, F. Pollmann, K. Penc, and P. Fulde, "Quantum ice: A quantum monte carlo study," *Phys. Rev. Lett.*, vol. 108, p. 067 204, 6 2012.

[96] O. Benton, O. Sikora, and N. Shannon, "Seeing the light: Experimental signatures of emergent electromagnetism in a quantum spin ice," *Phys. Rev. B*, vol. 86, p. 075 154, 7 2012.

[97] S. V. Isakov, R. Moessner, and S. L. Sondhi, "Why spin ice obeys the ice rules," *Phys. Rev. Lett.*, vol. 95, p. 217 201, 21 2005.

[98] S. V. Isakov, K. Gregor, R. Moessner, and S. L. Sondhi, "Dipolar spin correlations in classical pyrochlore magnets," *Phys. Rev. Lett.*, vol. 93, p. 167 204, 16 2004.

[99] C. L. Henley, "Power-law spin correlations in pyrochlore antiferromagnets," *Phys. Rev. B*, vol. 71, p. 014 424, 1 2005.

[100] Y. Kato and S. Onoda, "Numerical evidence of quantum melting of spin ice: Quantum-to-classical crossover," *Phys. Rev. Lett.*, vol. 115, p. 077 202, 7 2015.

[101] R. Sibille *et al.*, "Candidate quantum spin ice in the pyrochlore $Pr_2Hf_2O_7$," *Phys. Rev. B*, vol. 94, p. 024 436, 2 2016.

[102] S. Petit *et al.*, "Antiferroquadrupolar correlations in the quantum spin ice candidate $Pr_2Zr_2O_7$," *Phys. Rev. B*, vol. 94, p. 165 153, 16 2016.

[103] A. J. Princep, H. C. Walker, D. T. Adroja, D. Prabhakaran, and A. T. Boothroyd, "Crystal field states of Tb^{3+} in the pyrochlore spin liquid $Tb_2Ti_2O_7$ from neutron spectroscopy," *Phys. Rev. B*, vol. 91, p. 224 430, 22 2015.

[104] M. Ruminy *et al.*, "Crystal-field parameters of the rare-earth pyrochlores $R_2Ti_2O_7$ (R = Tb, Dy, and Ho)," *Phys. Rev. B*, vol. 94, p. 024 430, 2 2016.

[105] T. Fennell *et al.*, "Magnetoelastic excitations in the pyrochlore spin liquid $Tb_2Ti_2O_7$," *Phys. Rev. Lett.*, vol. 112, p. 017 203, 2014.

[106] S. H. Curnoe, "Structural distortion and the spin liquid state in $Tb_2Ti_2O_7$," *Phys. Rev. B*, vol. 78, p. 094 418, 9 2008.

[107] J. S. Gardner *et al.*, "Neutron scattering studies of the cooperative paramagnet pyrochlore $Tb_2Ti_2O_7$," *Phys. Rev. B*, vol. 64, p. 224 416, 22 2001.

[108] J. P. C. Ruff *et al.*, "Structural fluctuations in the spin-liquid state of $Tb_2Ti_2O_7$," *Phys. Rev. Lett.*, vol. 99, p. 237 202, 23 2007.

[109] M. J. P. Gingras *et al.*, "Thermodynamic and single-ion properties of Tb^{3+} within the collective paramagnetic-spin liquid state of the frustrated pyrochlore antiferromagnet $Tb_2Ti_2O_7$," *Phys. Rev. B*, vol. 62, pp. 6496–6511, 10 2000.

[110] H. R. Molavian, M. J. P. Gingras, and B. Canals, "Dynamically induced frustration as a route to a quantum spin ice state in $Tb_2Ti_2O_7$ via virtual crystal field excitations and quantum many-body effects," *Phys. Rev. Lett.*, vol. 98, p. 157 204, 2007.

[111] J. G. Rau and M. J. P. Gingras, "Magnitude of quantum effects in classical spin ices," *Phys. Rev. B*, vol. 92, p. 144 417, 14 2015.

[112] J.-J. Wen *et al.*, "Disordered route to the coulomb quantum spin liquid: Random transverse fields on spin ice in $Pr_2Zr_2O_7$," *Phys. Rev. Lett.*, vol. 118, p. 107 206, 2017.

[113] S. Nakatsuji, *Private communications*.

[114] S. Onoda and Y. Tanaka, "Quantum fluctuations in the effective pseudospin-$\frac{1}{2}$ model for magnetic pyrochlore oxides," *Phys. Rev. B*, vol. 83, p. 094 411, 9 2011.

[115] S. Onoda and Y. Tanaka, "Quantum melting of spin ice: Emergent cooperative quadrupole and chirality," *Phys. Rev. Lett.*, vol. 105, p. 047 201, 4 2010.

[116] Z. Hao, A. G. R. Day, and M. J. P. Gingras, "Bosonic many-body theory of quantum spin ice," *Phys. Rev. B*, vol. 90, p. 214 430, 21 2014.

[117] J. O. Jensen, "Vibrational frequencies and structure of B_4Cl_4: An ab intio quantum chemical study," *Spectrochimica Acta Part A: Molecular and Biomolecular Spectroscopy*, vol. 58, no. 10, pp. 2299–2309, 2002.

[118] O. Tchernyshyov, R. Moessner, and S. L. Sondhi, "Spin-peierls phases in pyrochlore antiferromagnets," *Phys. Rev. B*, vol. 66, p. 064 403, 6 2002.

[119] K Matsuhira *et al.*, "Spin freezing in the pyrochlore antiferromagnet $Pr_2Zr_2O_7$," in *J. Phys.: Conf. Ser.*, IOP Publishing, vol. 145, 2009, p. 012 031.

[120] S. D. Pace, S. C. Morampudi, R. Moessner, and C. R. Laumann, "Emergent fine structure constant of quantum spin ice is large," *Phys. Rev. Lett.*, vol. 127, p. 117 205, 11 2021.

[121] O. I. Motrunich and T. Senthil, "Origin of artificial electrodynamics in three-dimensional bosonic models," *Phys. Rev. B*, vol. 71, p. 125 102, 2005.

[122] E. Lantagne-Hurtubise, S. Bhattacharjee, and R. Moessner, "Electric field control of emergent electrodynamics in quantum spin ice," *Phys. Rev. B*, vol. 96, p. 125 145, 12 2017.

[123] I. Mandal, "Electric field response in breathing pyrochlores," *Eur. Phys. J. B*, vol. 92, p. 187, 2019.

[124] G. D. Mahan, *Many-Particle Physics*. Springer New York, NY, 2000.

[125] R. P. Feynman, "The behavior of hadron collisions at extreme energies," in *Special Relativity and Quantum Theory*, Springer, Dordrecht, 1988, pp. 289–304.

[126] J. D. Bjorken and E. A. Paschos, "Inelastic electron-proton and γ-proton scattering and the structure of the nucleon," *Phys. Rev.*, vol. 185, pp. 1975–1982, 5 1969.

[127] E. D. Bloom *et al.*, "High-energy inelastic $e - p$ scattering at 6° and 10°," *Phys. Rev. Lett.*, vol. 23, pp. 930–934, 16 1969.

[128] M. Breidenbach *et al.*, "Observed behavior of highly inelastic electron-proton scattering," *Phys. Rev. Lett.*, vol. 23, pp. 935–939, 16 1969.

[129] S. Lee and E.-G. Moon, "Spin-lattice coupling in $U(1)$ quantum spin liquids," *Phys. Rev. B*, vol. 99, p. 014 412, 2019.

[130] Y. Xu *et al.*, "Phonon spectrum of $Pr_2Zr_2O_7$ and $Pr_2Ir_2O_7$ as evidence of coupling of the lattice with electronic and magnetic degrees of freedom," *Phys. Rev. B*, vol. 105, p. 075 137, 7 2022.

[131] M. Ruminy *et al.*, "First-principles calculation and experimental investigation of lattice dynamics in the rare-earth pyrochlores $R_2Ti_2O_7$ (R = Tb, Dy, Ho)," *Phys. Rev. B*, vol. 93, p. 214 308, 21 2016.

[132] C. Balz *et al.*, "Crystal growth, structure and magnetic properties of $Ca_{10}Cr_7O_{28}$," *J. Phys.: Condens. Matter*, vol. 29, p. 225 802, 2017.

[133] C. Balz *et al.*, "Magnetic Hamiltonian and phase diagram of the quantum spin liquid $Ca_{10}Cr_7O_{28}$," *Phys. Rev. B*, vol. 95, no. 17, p. 174 414, 2017.

[134] I. Arčon, B. Mirtič, and A. Kodre, "Determination of Valence States of Chromium in Calcium Chromates by Using X-ray Absorption Near-Edge Structure (XANES) Spectroscopy," *J. Am. Ceram. Soc.*, vol. 81, p. 222, 1998.

[135] A. Balodhi and Y. Singh, "Synthesis and pressure and field-dependent magnetic properties of the kagome-bilayer spin liquid $Ca_{10}Cr_7O_{28}$," Phys. Rev. Mater., vol. 1, no. 2, p. 024 407, 2017.

[136] J. M. Ni *et al.*, "Ultralow-temperature heat transport in the quantum spin liquid candidate $Ca_{10}Cr_7O_{28}$ with a bilayer kagome lattice," Phys. Rev. B, vol. 97, no. 10, p. 104 413, 2018.

[137] J. Sonnenschein *et al.*, "Signatures for spinons in the quantum spin liquid candidate $Ca_{10}Cr_7O_{28}$," Phys. Rev. B, vol. 100, no. 17, p. 174 428, 2019.

[138] S. Biswas and K. Damle, "Magnetic Hamiltonian and phase diagram of the quantum spin liquid $Ca_{10}Cr_7O_{28}$," Phys. Rev. B, vol. 97, no. 11, p. 115 102, 2018.

[139] R. Pohle, H. Yan, and N. Shannon, "Theory of $Ca_{10}Cr_7O_{28}$ as a bilayer breathing-kagome magnet: Classical thermodynamics and semiclassical dynamics," Phys. Rev. B, vol. 104, no. 2, p. 024 426, 2021.

[140] V. Dediu, C. Ferdeghini, F. C. Matacotta, P. Nozar, and G. Ruani, "Jahn-Teller Dynamics in Charge-Ordered Manganites from Raman Spectroscopy," Phys. Rev. Lett., vol. 84, no. 19, p. 4489, 2000.

[141] J. Zhang, P. Dai, J. A. Fernandez-Baca, E. W. Plummer, Y. Tomioka, and Y. Tokura, "Jahn-Teller Phonon Anomaly and Dynamic Phase Fluctuations in $La_{0.7}Ca_{0.3}MnO_3$," Phys. Rev. Lett., vol. 86, no. 17, p. 3823, 2001.

[142] L. Martín-Carrón and A. de Andrés, "Raman phonons and the Jahn–Teller transition in $RMnO_3$ manganites," *J. Alloys Compd.*, vol. 323-324, p. 417, 2001.

[143] L. Martín-Carrón and A. de Andrés, "Melting of the cooperative jahn-teller distortion in $LaMnO_3$ single crystal studied by raman spectroscopy," *Eur. Phys. J. B*, vol. 22, p. 11, 2001.

[144] T. Malcherek, B. Mihailova, and M. D. Welch, "Structural phase transitions of clinoatacamite and the dynamic Jahn–Teller effect," Phys. Chem. Minerals, vol. 44, p. 307, 2017.

[145] G. Gehring and K. Gehring, "Co-operative Jahn-Teller effects," Rep. Prog. Phys., vol. 38, p. 1, 1975.

[146] P. G. Klemens, "Anharmonic Decay of Optical Phonons," Phys. Rev., vol. 148, p. 845, 1966.

[147] O. Benton, L. Jaubert, H. Yan, and N. Shannon, "A spin-liquid with pinch-line singularities on the pyrochlore lattice," *Nat. Comm.*, vol. 7, p. 11 572, 1 2016.

[148] H. Yan, O. Benton, L. D. C. Jaubert, and N. Shannon, "Rank–2 $U(1)$ spin liquid on the breathing pyrochlore lattice," *Phys. Rev. Lett.*, vol. 124, p. 127 203, 12 2020.

[149] S. Han, A. S. Patri, and Y. B. Kim, "Realization of fractonic quantum phases in the breathing pyrochlore lattice," *Phys. Rev. B*, vol. 105, p. 235 120, 23 2022.

[150] I. Affleck, T. Kennedy, E. H. Lieb, and H. Tasaki, "Rigorous results on valence-bond ground states in antiferromagnets," *Phys. Rev. Lett.*, vol. 59, pp. 799–802, 7 1987.

[151] H. Abdul-Rahman, M. Lemm, A. Lucia, B. Nachtergaele, and A. Young, "A class of two-dimensional aklt models with a gap," *arXiv:1901.09297*, 2019.

[152] G. Chen, M. Hermele, and L. Radzihovsky, "Frustrated quantum critical theory of putative spin-liquid phenomenology in $6H-B-Ba_3NiSb_2O_9$," *Phys. Rev. Lett.*, vol. 109, p. 016 402, 1 2012.

[153] A. Koga, T. Minakawa, Y. Murakami, and J. Nasu, "Spin transport in the quantum spin liquid state in the s = 1 kitaev model: Role of the fractionalized quasiparticles," *J. Phys. Soc. Jpn.*, vol. 89, no. 3, p. 033 701, 2020.

[154] C. Xu *et al.*, "Possible kitaev quantum spin liquid state in 2d materials with $S = 3/2$," *Phys. Rev. Lett.*, vol. 124, p. 087 205, 8 2020.

[155] H.-K. Jin, W. M. H. Natori, F. Pollmann, and J. Knolle, "Unveiling the s=3/2 kitaev honeycomb spin liquids," *arXiv:2107.13364*, 2021.

[156] J. Zhang *et al.*, "Neutron spectroscopic study of crystal field excitations in $Tb_2Ti_2O_7$ and $Tb_2Sn_2O_7$," *Phys. Rev. B*, vol. 89, p. 134 410, 13 2014.

[157] H. Aoki, T. Sakakibara, K. Matsuhira, and Z. Hiroi, "Magnetocaloric effect study on the pyrochlore spin ice compound dy2ti2o7 in a [111] magnetic field," *J. Phys. Soc. Jpn.*, vol. 73, pp. 2851–2856, 2004.

[158] C. Castelnovo, R. Moessner, and S. L. Sondhi, "Thermal quenches in spin ice," *Phys. Rev. Lett.*, vol. 104, p. 107 201, 10 2010.

[159] A. Sen and R. Moessner, "Topological spin glass in diluted spin ice," *Phys. Rev. Lett.*, vol. 114, p. 247 207, 24 2015.

[160] T. K. Bose, R. Moessner, and A. Sen, "Dipolar spin glass transition in three dimensions," *Phys. Rev. B*, vol. 100, p. 064 425, 6 2019.

[161] C. M. Newman and D. L. Stein, "Metastable states in spin glasses and disordered ferromagnets," *Phys. Rev. E*, vol. 60, pp. 5244–5260, 5 1999.

[162] S. Rosenkranz, A. P. Ramirez, A. Hayashi, R. J. Cava, R. Siddharthan, and B. S. Shastry, "Crystal-field interaction in the pyrochlore magnet ho2ti2o7," *J. Appl. Phys.*, vol. 87, p. 5914, 2000.